

**From Molecular Parameters to
Electronic Properties of Organic Thin Films:
A Photoelectron Spectroscopy Study**

Dissertation
zur Erlangung des wissenschaftlichen Grades
Dr. rer. nat.

vorgelegt von

Martin Schwarze
geboren am 30.09.1986 in Leonberg

Dresden Integrated Center for Applied Physics and Photonic Materials
Fakultät Physik
Bereich Mathematik und Naturwissenschaften
Technische Universität Dresden

2018

Eingereicht am 22.02.2018

Verteidigt am 05.06.2018

1. Gutachter: Prof. Dr. Karl Leo

2. Gutachterin: Prof. Dr. Elizabeth von Hauff

Abstract

The field of organic semiconductors considerably gained research interest due to promising applications in flexible, large-area, lightweight and semitransparent electronic devices, such as light-emitting diodes, solar cells, or transistors. The working mechanism of such devices depends on the combination of different neat or blended organic films, whose physical properties substantially differ from those of inorganic semiconductors. Weak intermolecular electronic coupling and large energetic disorder result in a thermally activated charge carrier hopping between localized electronic states. Therefore, many processes in organic devices are determined by properties of single molecules. The major goal of this thesis is to disclose relationships between electronic properties of organic thin films and molecular parameters, helping to provide specific design rules for new molecules.

In the first part of this thesis, the impact of molecular quadrupole moments on the transport energies of charge carriers is investigated by photoelectron spectroscopy. The results reveal for a variety of planar small molecules that charge-quadrupole interactions along the π - π -stacking geometry induce large energy changes with molecular orientation at surfaces and interfaces of crystalline films. Furthermore, these electrostatic interactions enable a continuous tuning of energy levels in crystalline intermixed blends by more than 1 eV. In blends exhibiting separated phases, quadrupole moments induce electrostatic gradients from the interface to the bulk phase. These two effects are exploited in organic solar cells consisting of a ternary blend of two intermixed donors blended with one acceptor. By changing the mixing ratio of the two donors, the open-circuit voltage can be continuously tuned. Additionally, the dissociation barrier of electron-hole pairs at the interface can be varied, reflecting in a change in photocurrent.

In the second part, molecular n-doping is investigated, facing the particular issue of air sensitivity. The analysis of two air stable precursor molecules of n-dopants reveals very good doping properties after their thermal evaporation, partly even better than for a reference air sensitive dopant. For high doping concentrations, temperature-dependent conductivity measurements show that the thermal activation energy of many compounds can be described by an empirical function of two molecular parameters, the relaxation energy of matrix anions and the Coulomb binding energy of integer charge transfer complexes (ICTCs) between matrix anions and dopant cations. The investigation of the density of states indicates that charge transport at high doping concentrations predominantly occurs by a rearrangement between different ICTC configurations and is limited by their energetic disorder, which can be reduced substantially by adding electron withdrawing side groups to the matrix molecules. The exposure of several n-doped semiconductors to air reveals that the air stability increases with larger ionization energies of ICTCs. This effect is attributed to an universal trap introduced upon air exposure. Its energy is estimated to be 3.9 eV, setting a general limit for air stable n-doping.

Kurzfassung

Organische Halbleiter bieten vielversprechende Anwendungsmöglichkeiten in ultraleichten, flexiblen, großflächigen und semitransparenten elektronischen Bauteilen wie beispielsweise in Leuchtdioden, Solarzellen oder Transistoren. Die Funktionsweise solcher Bauteile basiert auf der Kombination verschiedener organischer Moleküle in dünnen Schichten, deren physikalische Eigenschaften sich stark von herkömmlichen anorganischen Halbleitern unterscheiden. Die schwache elektronische Kopplung zwischen einzelnen Molekülen und die große energetische Unordnung in organischen Halbleitern bewirken einen temperaturaktivierten Transport von Ladungsträgern zwischen lokalisierten elektronischen Zuständen. Daher werden viele Prozesse in organischen Halbleiterbauelementen von molekularen Eigenschaften bestimmt. Das Hauptziel dieser Dissertation ist es, verschiedene elektronische Eigenschaften dünner organischer Filme mit molekularen Parametern in Verbindung zu bringen, was als Grundlage für die gezielte Entwicklung neuer Moleküle dienen soll.

Im ersten Teil dieser Arbeit wird mittels Photoelektronenspektroskopie der Einfluss molekularer Quadrupolmomente auf die Transportenergien von Ladungsträgern untersucht. Für eine große Anzahl verschiedener planarer Moleküle zeigt sich, dass die Wechselwirkung von Ladungen mit Quadrupolmomenten entlang der π - π -Stapelrichtung große Veränderungen der Energieniveaus an der Oberfläche und der Grenzfläche von kristallinen Filmen bewirkt, beispielsweise wenn sich die Molekülorientierung ändert. Dieser elektrostatische Effekt ermöglicht es, die Energieniveaus in einer homogen durchmischten Schicht zweier Molekülarten kontinuierlich über eine Größenordnung von mehr als 1 eV durchzustimmen. In Mischungen mit einer Phasentrennung können molekulare Quadrupolmomente einen elektrostatischen Gradienten an der Grenzfläche zwischen den Phasen ausbilden. Diese beiden Effekte werden in Solarzellen ausgenutzt, die aus einer Mischung von zwei Donatormolekülen und einem Akzeptormolekül bestehen. Durch Variation des Mischverhältnisses der zwei Donatoren lässt sich die Leerlaufspannung kontinuierlich anpassen. Zusätzlich lässt sich die Energiebarriere für die Ladungsträgertrennung an der Grenzfläche reduzieren, was zu einem höheren Photostrom führt.

Im zweiten Teil wird molekulare n-Dotierung untersucht, bei der das spezielle Problem der Luftsensitivität berücksichtigt werden muss. Zwei luftstabile Ausgangsmoleküle von n-Dotanden weisen nach ihrer thermischen Verdampfung sehr gute Dotiereigenschaften auf, welche für ein Molekül sogar besser als bei entsprechenden luftsensitiven Referenzdotanden sind. Temperaturabhängige Leitfähigkeitsmessungen zeigen, dass die thermische Aktivierungsenergie bei hohen Dotierkonzentrationen durch eine empirische Funktion von zwei molekularen Parametern beschrieben werden kann, welche die Relaxationsenergie von Anionen des Matrixmoleküls und die Coulombbindungsenergie des Ionenpaars aus Matrix- und Dotandenmolekül sind. Die Untersuchung der Zustandsdichte dieser hochdotierten Halbleiter deutet darauf hin, dass sich der Ladungstransport durch

eine Umbesetzung dieser Ionenpaare beschreiben lässt. Der Transport ist dabei durch die energetische Unordnung der Ionenpaare limitiert, welche sich allerdings durch das Hinzufügen von elektronenziehenden Seitengruppen an die Matrixmoleküle deutlich reduzieren lässt. Der Kontakt verschiedener n-dotierter Halbleiter mit Luft zeigt, dass sich die Luftstabilität dieser mit größerer Ionisationsenergie der Anionen des Matrixmaterials verbessert. Diese Beobachtung wird dadurch erklärt, dass durch den Kontakt mit Luft ein universeller Fallenzustand mit der Energie von 3.9 eV entsteht. Dieser setzt eine allgemeine Grenze für luftstabile n-Dotierung.

List of Publications

Articles

- [A1] E. Siebert-Henze, V. G. Lyssenko, J. Fischer, M. Tietze, R. Brueckner, M. Schwarze, K. Vandewal, D. Ray, M. Riede, and K. Leo: “Built-in voltage of organic bulk heterojunction pin solar cells measured by electroabsorption spectroscopy”. *AIP Advances* **4** (4), 7134 (2014).
- [A2] L. E. Polander, P. Pahner, M. Schwarze, M. Saalfrank, C. Koerner, and K. Leo: “Hole-transport material variation in fully vacuum deposited perovskite solar cells”. *APL Materials* **2** (8), 81503 (2014).
- [A3] J. Fischer, D. Ray, H. Kleemann, P. Pahner, M. Schwarze, C. Koerner, K. Vandewal, and K. Leo: “Density of states determination in organic donor-acceptor blend layers enabled by molecular doping”. *Journal of Applied Physics* **117** (24), 245501 (2015).
- [A4] M. Schwarze, W. Tress, B. Beyer, F. Gao, R. Scholz, C. Poelking, K. Ortstein, A. A. Günther, D. Kasemann, D. Andrienko, and K. Leo: “Band structure engineering in organic semiconductors”. *Science* **352** (6292), 1446 (2016).
- [A5] L. Fang, F. Holzmueller, T. Matulaitis, A. Baasner, C. Hauenstein, J. Benduhn, M. Schwarze, A. Petrich, F. Piersimoni, R. Scholz, O. Zeika, C. Koerner, D. Nehler, K. Vandewal, and K. Leo: “Fluorine-containing low-energy-gap organic dyes with low voltage losses for organic solar cells”. *Synthetic Metals* **222**, 232 (2016).
- [A6] M. L. Tietze, B. D. Rose, M. Schwarze, A. Fischer, S. Runge, J. Blochwitz-Nimoth, B. Lüssem, K. Leo, and J.-L. Bredas: “Passivation of Molecular n-Doping: Exploring the Limits of Air Stability”. *Advanced Functional Materials* **26** (21), 3730 (2016).

- [A7] M. Schwarze, B. D. Naab, M. L. Tietze, R. Scholz, P. Pahner, F. Bussolotti, S. Kera, D. Kasemann, Z. Bao, and K. Leo: “Analyzing the n-Doping Mechanism of an Air-Stable Small-Molecule Precursor”. *ACS Applied Materials & Interfaces* **10** (1), 1340 (2018).
- [A8] C. Gaul*, S. Hutsch*, M. Schwarze*, K. S. Schellhammer*, F. Bussolotti, S. Kera, G. Cuniberti, K. Leo, and F. Ortman: “Insight into doping efficiency of organic semiconductors from the analysis of the density of states in n-doped C₆₀ and ZnPc”. *Nature Materials* **17** (5), 439 (2018). *Equal author contribution.
- [A9] M. L. Tietze, J. Benduhn, P. Pahner, B. Nell, M. Schwarze, H. Kleemann, M. Kramer, K. Zojer, K. Vandewal, and K. Leo: “Elementary steps in electrical doping of organic semiconductors”. *Nature Communications* **9**, 1182 (2018).
- [A10] M. Schwarze, K. S. Schellhammer, C. Gaul, K. Ortstein, M. Lau, G. Cuniberti, C. Poelking, D. Andrienko, F. Ortman, and K. Leo: “Engineering of Device Energy Levels at Organic Heterojunctions by Charge-Quadrupole Interactions”, *submitted*.
- [A11] M. Schwarze, F. Bussolotti, C. Gaul, R. Scholz, A. Hofacker, K. S. Schellhammer, B. D. Naab, Z. Bao, D. Spoltore, B. Nell, K. Vandewal, S. Kera, N. Ueno, J. Widmer, F. Ortman, and K. Leo: “Molecular Parameters Responsible for Thermally Activated Transport in Doped Organic Semiconductors”, *submitted*.
- [A12] M. Schwarze, A. Hofacker, and K. Leo: “Universal Electron Trap as a Limit for Air Stable n-Doping in Organic Semiconductors”, *in preparation*.
- [A13] P. Pahner, M. Schwarze, M. L. Tietze, H. Kleemann, and K. Leo: “Global oxygen-induced trap levels in organic hole transport materials”, *in preparation*.

Conference Contributions (Presenting Author only)

- [C1] M. Schwarze, M. L. Tietze, P. Pahner, B. D. Naab, Z. Bao, B. Lüssem, D. Kasemann, and K. Leo: “Photoelectron spectroscopy studies on two air-stable molecular n-dopants”, Oral Presentation. *DPG Spring Meeting, Dresden, Germany* (2014).
- [C2] M. Schwarze, M. L. Tietze, P. Pahner, B. D. Naab, Z. Bao, B. Lüssem, D. Kasemann, and K. Leo: “Photoelectron spectroscopy studies on efficient air-stable molecular n-dopants”, Oral Presentation. *DPG Spring Meeting, Berlin, Germany* (2015).

- [C3] M. Schwarze, M. L. Tietze, P. Pahner, B. D. Naab, Z. Bao, D. Kasemann, and K. Leo: “Photoelectron spectroscopy studies on efficient air-stable molecular n-dopants for organic semiconductors”, Oral Presentation. *E-MRS Spring Meeting, Lille, France* (2015).
- [C4] M. Schwarze, M. L. Tietze, B. D. Naab, Z. Bao, D. Kasemann, and K. Leo: “Correlation of Air Stability and Energetic States in n-Doped Organic Semiconductors”, Oral Presentation. *MRS Fall Meeting, Boston, MA-US* (2015).
- [C5] M. Schwarze, C. Gaul, K. Ortstein, F. Ortmann, and K. Leo: “How molecular quadrupole moments affect the energetics in organic thin films”, Oral Presentation. *DPG Spring Meeting, Dresden, Germany* (2017).
- [C6] M. Schwarze, S. Schellhammer, C. Gaul, K. Ortstein, F. Ortmann, and K. Leo: “Molecular-Scale Calibration of Device Energy Levels by Charge-Quadrupole Interactions”, Poster Presentation. *European Conference on Molecular Electronics (ECME), Dresden, Germany* (2017).
- [C7] M. Schwarze, C. Gaul, R. Scholz, F. Ortmann, and K. Leo: “Conductivity in Doped Organic Semiconductors: Impact of Electrostatic Disorder Induced by Charge Transfer Complexes”, Poster Presentation. *European Conference on Molecular Electronics (ECME), Dresden, Germany* (2017).
- [C8] V. Scholz, F. Selzer, W. Haq, E. Zrenner, C. Kern, F. Hennrich, M. Kappes, M. Wegener, M. Schwarze, H. Kleemann, and K. Leo: “Functionalized PEDOT as Biocompatible Electrode Material for Medical Applications”, Poster Presentation. *LOPEC, München, Germany* (2018).

Contents

| | |
|--|-----------|
| List of Publications | v |
| 1 Introduction | 1 |
| 2 Physics of Organic Semiconductors | 5 |
| 2.1 Molecular Solids | 5 |
| 2.1.1 Single Molecules | 5 |
| 2.1.2 Electrostatic Interactions in Molecular Solids | 9 |
| 2.1.3 Energetic Disorder | 12 |
| 2.2 Charge Transport | 13 |
| 2.2.1 Marcus Theory for Electron Transfer | 13 |
| 2.2.2 Gaussian Disorder Model | 15 |
| 2.2.3 Impact of Charge Carrier Traps | 17 |
| 2.3 Molecular Doping | 18 |
| 2.3.1 Introduction | 18 |
| 2.3.2 Generation of Mobile Charge Carriers | 19 |
| 2.3.3 Transport in Doped Organic Semiconductors | 22 |
| 2.3.4 Air-stable n-Doping | 24 |
| 2.4 Organic Solar Cells | 25 |
| 2.4.1 p-n-Junction | 25 |
| 2.4.2 Basic Mechanism of Organic Solar Cells | 26 |
| 2.4.3 Solar Cell Parameters | 27 |
| 3 Experimental Methods | 31 |
| 3.1 Materials and Sample Preparation | 31 |
| 3.2 Photoelectron Spectroscopy | 33 |
| 3.2.1 Ultraviolet Photoelectron Spectroscopy | 36 |
| 3.2.2 X-ray Photoelectron Spectroscopy | 38 |
| 3.2.3 Inverse Photoelectron Spectroscopy | 39 |
| 3.3 Conductivity Measurements | 40 |
| 3.4 Solar Cells | 41 |

| | | |
|----------|---|------------|
| 3.5 | Density Functional Theory | 42 |
| 4 | Impact of Quadrupole Moments on Thin Film Energy Levels | 43 |
| 4.1 | Model System of F_nZnPc | 44 |
| 4.2 | Energy Level Dependence on Molecular Orientation | 45 |
| 4.2.1 | Connection to the Quadrupole Component Q_π | 46 |
| 4.2.2 | Extension to other Systems | 50 |
| 4.3 | Impact of Mixing Ratio on Blend Energy Levels | 52 |
| 4.3.1 | Intermixed Blends | 52 |
| 4.3.2 | Blends with Phase Separation | 55 |
| 4.4 | Application to Organic Solar Cells | 59 |
| 4.4.1 | Energy Levels in Ternary Blends | 60 |
| 4.4.2 | Tuning of Open-Circuit Voltage | 61 |
| 4.4.3 | Splitting Efficiency of CT States | 63 |
| 4.5 | Summary | 66 |
| 5 | Investigations on Molecular n-Doping | 67 |
| 5.1 | Comparison of Different n-Dopants | 67 |
| 5.1.1 | Doping Characteristics | 69 |
| 5.1.2 | Doping Mechanism of o-MeO-DMBI-Cl | 73 |
| 5.2 | Analysis of Electronic States | 78 |
| 5.2.1 | Integer Charge Transfer Complexes | 78 |
| 5.2.2 | Example of n-Doped ZnPc and C_{60} | 80 |
| 5.2.3 | Highly Efficient Charge Transfer from 2-Cyc-DMBI | 83 |
| 5.2.4 | Importance of Energetic Disorder at 10 mol% | 84 |
| 5.3 | Electrical Conductivity | 88 |
| 5.3.1 | Arrhenius-type Thermal Activation of the Conductivity | 88 |
| 5.3.2 | Concentration Dependence of the Activation Energy | 90 |
| 5.3.3 | Important Molecular Parameters at 10 mol% | 94 |
| 5.4 | Air Stability of n-Doped Semiconductors | 99 |
| 5.4.1 | Conductivity Decrease Upon Air Exposure | 99 |
| 5.4.2 | Analysis of Fermi Level Shift Upon Air Exposure | 101 |
| 5.4.3 | Universal Air Trap as a Limit for Air Stable n-Doping | 104 |
| 5.5 | Summary | 106 |
| 6 | Conclusion and Outlook | 107 |

| | | |
|----------|---|------------|
| 6.1 | Conclusion | 107 |
| 6.2 | Outlook | 108 |
| 7 | Appendix | 113 |
| 7.1 | List of Abbreviations and Symbols | 113 |
| 7.2 | List of Materials | 115 |
| 7.2.1 | Chemical Structures and Names | 115 |
| 7.2.2 | Material Properties | 121 |
| 7.3 | Simulation Results | 123 |
| 7.4 | Stack Details for UPS samples | 125 |
| | Bibliography | 129 |

1. Introduction

Electronic devices based mostly on inorganic semiconductors like silicon play an important role in our daily life. In addition to these well-established electronic applications, the unique properties of organic semiconductors facilitate the development of a novel class of flexible, large-area, lightweight, and semitransparent electronic devices [1–5], which can potentially be produced at low cost with roll-to-roll printing processes [6]. Within the past decade, organic light-emitting diodes (OLEDs) [7] already have been established in the market of display applications, particularly in smart phones, due to their good color quality, low power consumption, and small thickness. Further promising applications of organic semiconductors comprise optoelectronic devices such as solar cells, photodetectors, and lasers [8–10] as well as the use of organic electronics for medical applications and bioelectronics [11–13].

Organic semiconductors consist of molecules with delocalized π -electron systems with the electronic coupling between single molecules being typically much weaker compared to covalently bonded inorganic semiconductors. Together with the low dielectric constants, this results in a thermally activated hopping transport of charge carriers between localized electronic states in most organic semiconductors, with charge carrier mobilities being much lower than in inorganic semiconductors. Organic semiconductors are typically divided into two classes, namely small molecules and conjugated polymers. Polymers are processed from solution, for example by printing or coating techniques, and usually exhibit higher charge carrier mobilities than the respective small molecules due to their larger conjugation length [14, 15]. In addition to the fabrication from solution, small molecules can also be sublimed in ultra-high vacuum, allowing a reliable production of complex device architectures exhibiting multilayer structures. The basic investigations of this thesis focus on small molecules due to their defined chemical structure and high degree of purity.

The working mechanism of most organic electronic devices depends on the combination of different organic thin films, consisting each of one or more types of organic molecules. It is therefore crucial to understand the relationship between molecular parameters, thin film properties, and device characteristics to enable a targeted optimization of organic devices by systematically varying the chemical structure of organic molecules. Two of the most important thin film parameters are the transport energies of holes and electrons, which are associated to the ionization energy (IE) and the electron affinity (EA) of organic semiconductors, respectively [16, 17]. For example, the open-circuit voltage in organic solar cells directly depends on the magnitudes of IE and EA at the heterojunction of two materials [18, 19]. However, IE and EA of molecules in organic films are not uni-

versal, but vary with film morphology and composition [20–22] and also differ between the bulk, the surface, and the interface of organic films due to the different electrostatic environments [23–26]. Simulations in previous studies showed for crystalline films that charge-quadrupole interactions can induce large changes to IE and EA [27–29]. Further simulations demonstrated for flat heterojunctions that molecular quadrupole moments can help to overcome the large Coulomb binding energy of electron-hole pairs at the interface, so-called charge transfer states [30, 31]. Apart from neat films and flat heterojunctions, the impact of quadrupole moments in blends of different molecules was not systematically investigated so far.

Molecular electrical doping is a powerful method to optimize device architectures [7, 9, 32, 33]. Efficient dopants transfer electrons or holes to the matrix material, allowing to control charge carrier density, Fermi level position, and electrical conductivity [34, 35]. Furthermore, doping can provide ohmic injection or extraction of charge carriers at metal-organic contacts by carrier tunneling through narrow depletion zones, being independent of the work function of the metal [34, 36]. Although molecular doping is standardly employed in most small molecule devices, the doping process and the charge transport mechanism is not fully understood yet, making molecular design of new efficient dopants challenging. In particular, the reason why large doping concentrations of 1-10 mol% are necessary to achieve reasonable Fermi level shifts and high conductivities was controversially discussed. Possible explanations comprise the increase of doping efficiency and mobility at large doping concentrations due to the overlap of deep Coulomb potentials at reduced distances between dopant ions [37–39] or due to the filling of intrinsic deep trap states within the transport gap of the matrix, originating from chemical impurities or structural disorder [40–42]. Recently, a reduction of doping efficiency due to the formation of new hybrid orbitals of matrix and dopant molecules was intensely discussed [43, 44]. In contrast to p-doping, n-doping of organic semiconductors often faces the issue of air sensitivity because it necessitates dopants with low ionization energies, which degrade under air exposure [20]. A workaround is the usage of air stable precursor molecules, which provide the actual n-doping species upon thermal evaporation, exposure to light, or in solution [45–50]. Nevertheless, the air sensitivity of the actual n-doped layers was not systematically investigated in the past.

This thesis addresses two topics, the impact of molecular quadrupole moments on the energy levels of organic films and the physics of molecular n-doping. After this introduction, Chapter 2 and 3 briefly summarize the physical basics of organic semiconductors as well as the experimental and simulation methods used for this thesis, respectively. In Chapter 4, the energy levels of neat films of ZnPc and its fluorinated derivatives are probed with ultraviolet photoelectron spectroscopy (UPS) at varying molecular orientation and film thickness. Furthermore, the energies of crystalline intermixed blends and of donor/acceptor blends exhibiting some degree of phase separation are investigated for different mixing ratios. The observed change of energy levels with morphology or mixing

ratio is then compared to the quadrupole moments of single molecules, obtained from density functional theory (DFT) simulations. These findings are applied to organic solar cells to study the impact of single molecule parameters on device characteristics, i.e. the open-circuit voltage and the short-circuit current.

In Chapter 5, the doping properties of two newly developed air stable n-dopants are compared to established dopants. Due to its reduced doping efficiency, the decomposition mechanism of the air stable n-dopant precursor o-MeO-DMBI-Cl is investigated in more detail with photoelectron spectroscopy and mass spectroscopy. The highly efficient and air stable n-dopant precursor (2-Cyc-DMBI)₂ is used to analyze the electronic states and the transport properties in different n-doped semiconductors with UPS and temperature-dependent conductivity measurements, respectively. The variation in conductivity among different compounds is correlated with molecular parameters directly obtained from the chemical structures of matrix and dopant molecules using DFT simulations. Finally, the sensitivity of the electronic properties of different n-doped organic semiconductors to air exposure is compared to investigate whether there is an universal energetic limit for air stable n-doping. The main results of this thesis are summarized in Chapter 6 and concepts for future scientific studies based on these results are suggested.

2. Physics of Organic Semiconductors

This chapter serves as a brief introduction to the physics of organic semiconductors and provides a basis for the discussion of the experimental results presented in Chapters 4 and 5 of this thesis. After the introduction into the electronic properties of molecules in solids in Section 2.1, common models describing charge transport in organic semiconductors are presented in Section 2.2. Section 2.3 introduces common models on the underlying mechanism of molecular doping and summarizes previous considerations on charge transport in doped organic semiconductors. Finally, Section 2.4 briefly describes the basic mechanisms of organic solar cells and relationships of device parameters with physical properties.

2.1 Molecular Solids

Organic semiconductor devices are based on thin solid films consisting of organic materials with conjugated π -systems. There are two different classes of organic semiconductors, namely small molecules and polymers. While polymers are employed in various efficient organic devices and are an important subject of current research, this thesis concentrates on the class of small molecules. Their defined molecular structure and the possibility of controlled processing by thermal evaporation in vacuum makes them more suitable for a basic study on electronic properties. This section briefly introduces the particular properties of the electronic structure in organic molecules. After highlighting the importance of conjugated π -systems in Section 2.1.1, Section 2.1.2 describes electrostatic and disorder effects in a molecular solid and their impact on the electronic levels. This section is based on references [28, 51, 52].

2.1.1 Single Molecules

The energetic states of organic molecules, i.e. the molecular orbital energies, define the electronic properties of organic semiconductor devices. In terms of quantum mechanics, a molecule is a complex many particle system and an exact analytical calculation of the molecular orbitals is not possible. The LCAO ("linear combination of atomic orbitals") method delivers an approximation of the molecular orbitals by a linear combination of the electron wave functions of the single atomic orbitals where the number of hybrid orbitals is equal to the number of atoms. The most frequently occurring element in organic molecules is carbon and exemplifies the LCAO concept in the following. The ground state electron configuration of a carbon atom is: $1s^2 2s^2 2p_x^1 2p_y^1$ (Figure 2.1a). In order to create

a molecular bond, one of the 2s-electrons is first excited to the empty 2p state, leading to the following electron configuration of the excited state: $1s^2 2s^1 2p_x^1 2p_y^1 2p_z^1$ (Figure 2.1b). As a next step, new hybrid orbitals can form whose wave functions are approximated by a linear combination of the wave functions of the atomic orbitals:

$$\psi_i = c_s\psi_s + c_{p_x}\psi_{p_x} + c_{p_y}\psi_{p_y} + c_{p_z}\psi_{p_z}. \quad (2.1)$$

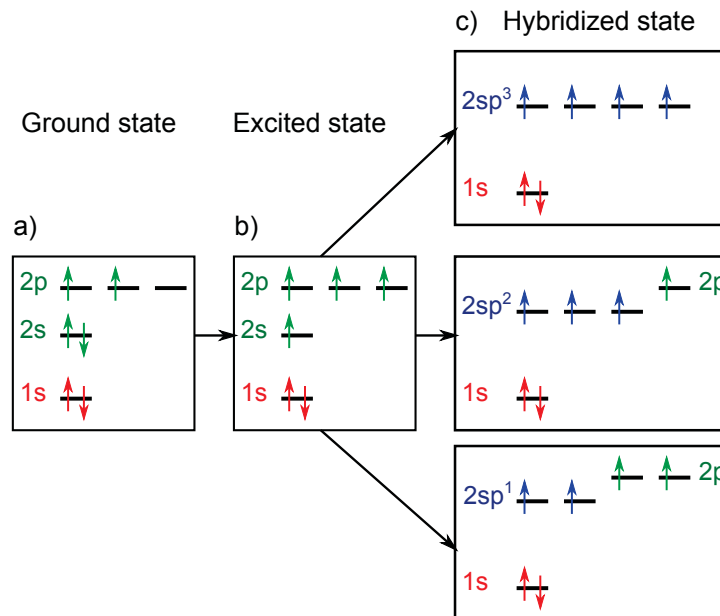


Figure 2.1: Electron configuration of carbon: (a) Ground state configuration of carbon. (b) Electron configuration of the excited state. (c) Electron configuration of the sp^1 -, sp^2 - and sp^3 -hybridization (top to bottom). Red, green, and blue colors indicate core levels, valence levels, and hybrid orbitals, respectively. Figure is adapted from reference [53].

The sp^1 -hybridization forms two equal hybrid orbitals rotated by an angle of 180° to each other and two p-orbitals remain. One example for the sp^1 -hybridization is ethyne, where a triple bond is formed between the two carbon atoms. The sp^3 -hybridization results in four equal orbitals that are separated by an angle of 109.5° . Two sp^3 -orbitals can form bonds with high binding energies, as seen for example in diamond with its rigid cubic crystal structure. The sp^2 -hybridization, being the most important hybridization for organic semiconductors, forms three equal sp^2 -orbitals separated by an angle of 120° and one remaining p-orbital which is perpendicular to the sp^2 -orbitals and often is denoted by p_z . Two sp^2 -orbitals form strong σ -bonds where the electron density is on the bonding axis and strongly localized between the two carbon atoms. The linear combination of the atomic orbitals results in bonding and antibonding orbitals denoted as σ - and σ^* -orbitals. The remaining p-orbitals form considerably weaker π -bonds with the electron density being not between two carbon atoms. In conjugated π -systems with an alternation

of single and double carbon bonds, the electron wave functions can be delocalized over many atoms. Equally to the σ -bonds, π -bonds exhibit also bonding (π) and antibonding (π^*) orbitals.

The most important molecular orbitals are the *highest occupied molecular (π -)orbital* (HOMO) and the *lowest unoccupied molecular (π^* -)orbital* (LUMO) as they control the electronic and optical properties of organic semiconductors. The *ionization energy* (IE) of a molecule is the energy required to remove an electron from the HOMO, while the *electron affinity* (EA) is the energy gained by adding one electron to the LUMO of the molecule. Note that both quantities are defined positively in this thesis, which means that a decrease of the absolute energies of HOMO and LUMO results in an increase of IE and EA . IE and EA correlate with the transport energies of positive and negative charge carriers, respectively, and are very important measures to characterize the electronic properties of organic semiconductors. Although HOMO and LUMO energies should refer to the orbital energies of neutral molecules, the common usage is different. HOMO and LUMO energies published in literature often refer to energies necessary to generate holes in the HOMO and electrons in the LUMO, respectively [54, 55]. This thesis stays to this nomenclature because photoelectron spectroscopy measures exactly these energies. The difference between IE and EA is called *transport gap* and is typically larger than the optical gap, which is the energy necessary to excite an electron from the HOMO to the LUMO in the neutral molecule.

Conjugated π -systems are essential for the electrical and optical properties of organic semiconductors. One of the most simple example for an organic molecule with a conjugated π -system is benzene, consisting of a ring of six carbon and six hydrogen atoms. The six carbon atoms are connected by strong σ -bonds and weak π -bonds with the states of the π -electrons being delocalized over the whole ring (Fig. 2.2). In the ground state, the three (bonding) π -orbitals with the lowest energies are occupied by two electrons each due to spin degeneracy, while the orbitals with higher energies remain empty. The delocalization range of the electronic states within conjugated π -systems can be very large and can lead to very high charge carrier mobilities, as for example observed in graphene. The energy gap between the HOMO and LUMO level depends strongly on the extension of the π -electron system. The larger the conjugated system, i.e. the delocalization length, the smaller is the energy splitting between the orbitals, i.e. the energy gap. For example, from anthracene to pentacene the HOMO-LUMO gap substantially decreases with the number of carbon rings [56]. A possibility to manipulate the electronic levels of organic molecules is to attach electron donating or withdrawing moieties to the π -system. For example, a replacement of hydrogen atoms by fluorine atoms can shift HOMO and LUMO levels to lower energies while the HOMO-LUMO gap remains similar [57].

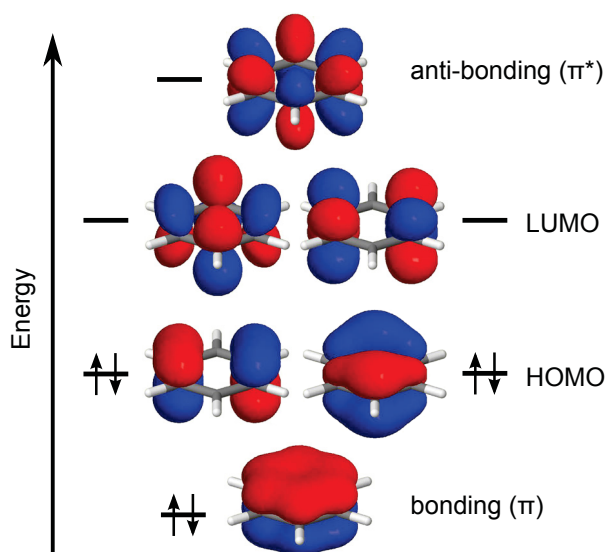


Figure 2.2: Hybrid molecular π -orbitals of benzene: All bonding states are occupied by electrons in the ground state, where the HOMO and LUMO levels are degenerated twice due to the symmetry of the molecule. Figure is adapted from reference [53].

Molecular Relaxation Energy

Ionization of a molecule leads to a transition from the neutral state to the ionized state of the molecule, whose transition probability is given by Fermi's Golden Rule. It can be assumed that the geometry of the molecule does not change during ionization because the timescale of the ionization is much faster than the timescale of any geometrical changes (Franck-Condon principle). The energy needed to positively charge a molecule being in its (geometric) ground state is called IE_0 and is depicted as a vertical line in Fig. 2.3. Since the transition probability depends on the overlap integral of the wave functions of the respective vibrational modes, the final state of this transition is, in general, not the vibrational ground state of the cation. After charging it positively, the cation relaxes energetically from the ground state geometry of the neutral molecule to its new ground state geometry and loses the *molecular relaxation energy* λ_+ .

Adding an electron to the relaxed cation, i.e. the half-filled HOMO state, increases the total energy of the molecule by the electron affinity of the cation (EA_+). Again, the final state of this process is, in general, not the vibrational ground state, leading to geometrical relaxation of the neutral molecule from the geometrical ground state of the cation to the neutral ground state by $\lambda_{0,+}$. For simplicity, it is assumed in this thesis that the magnitudes of λ_+ and $\lambda_{0,+}$ are equal [58]. The consequence of the two relaxation processes after charging and discharging is that EA_+ is smaller IE_0 [59, 60]:

$$IE_0 - EA_+ = 2\lambda_+ \quad (2.2)$$

For negatively charging, the EA of a neutral molecule in its ground state (EA_0) is smaller than the IE of the relaxed molecular anion (IE_-):

$$IE_- - EA_0 = 2\lambda_- \quad (2.3)$$

As described in Section 2.2.1, geometric relaxation plays a crucial role during charge transfer between two molecules. Furthermore, geometrical relaxation of molecules also affects emission and absorption wavelength of organic molecules. While photon absorption induces a transition of an electron from the HOMO to the LUMO, emission is the reversed process. Due to the geometrical relaxation after photon absorption, the emission wavelength is always redshifted compared to the absorption wavelength (Stokes-shift).

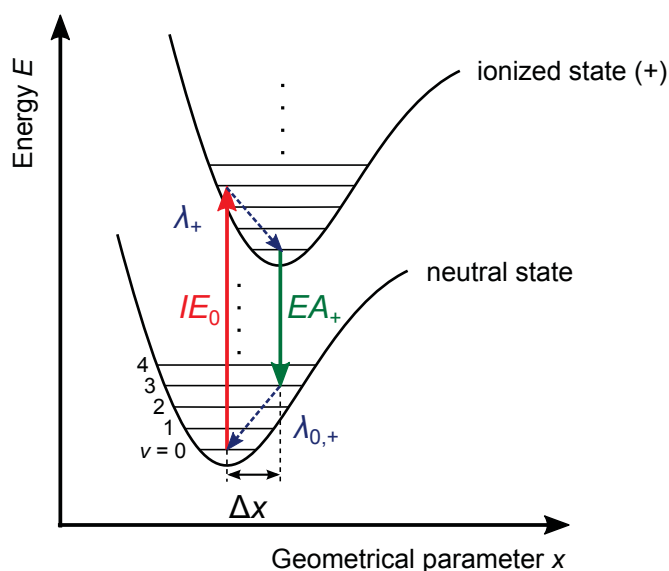


Figure 2.3: Electronic potential curves of a neutral molecule and its cation: The molecular relaxation energies λ_+ and $\lambda_{0,+}$ describe the losses in energy during geometric relaxation after removing an electron from the neutral molecule or adding an electron to the (relaxed) cation, respectively. ν denotes vibrational sublevels of neutral and ionized state. x denotes a geometrical parameter that changes with distortion of the molecule. Figure is adapted from reference [61].

2.1.2 Electrostatic Interactions in Molecular Solids

In contrast to the strong covalent coupling in inorganic semiconductors, the wave functions of different molecules only weakly overlap and the electronic states usually strongly localize in organic semiconductors. Despite the weak wave function overlap, the electronic states of charged molecules considerably change when embedded in a polarizable medium (Figure 2.4). Indeed, charge carriers in a molecular solid form quasi-particles, so-called *polarons*, whose energy is given by the energy of single molecule levels and induced changes due to interactions with surrounding molecules. Although the IE and EA can change due to intermolecular coupling of the electron wave functions [29], such effects can be neglected for the majority of the small molecules investigated in this thesis.

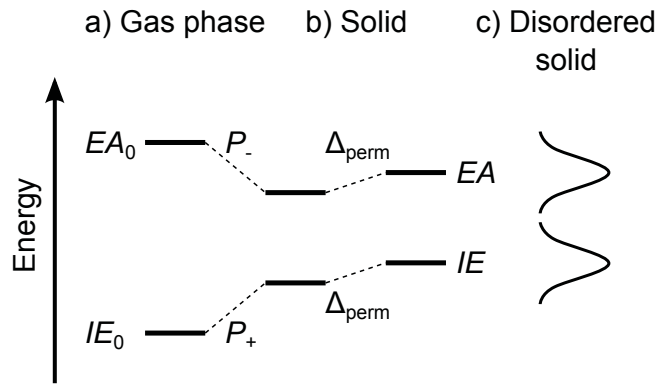


Figure 2.4: Change of molecular energies by electrostatic interactions in molecular solids: (a,b) While polarization (P_+ , P_-) reduces the gap between IE and EA , the permanent contribution (Δ_{perm}) leads to a similar change of IE and EA . **(c)** Energetic disorder leads to a broadening of the density of states.

The difference between the IE/EA of a molecule in the solid and a molecule in gas-phase is approximately given by the *electrostatic correction* of holes and electrons, consisting of a polarization (P_+ , P_-) and a permanent contribution (Δ_{perm}):

$$\Delta_+ = IE - IE_0 = P_+ + \Delta_{perm} \quad (2.4)$$

$$\Delta_- = EA - EA_0 = P_- + \Delta_{perm}. \quad (2.5)$$

The largest contribution to the electrostatic correction is usually the *polarization energy* (P_+ , P_-). A charged molecule in a solid induces a change in charge distribution on surrounding molecules, sketched as induced dipoles in Fig. 2.5a. If an induced dipole is aligned along the connection line with the (point) charge, the interaction energy between the charge and the induced dipole is:

$$\Delta_{ind} = \left(\frac{e}{4\pi\epsilon_r\epsilon_0} \right)^2 \frac{\alpha}{r^4}, \quad (2.6)$$

with α as the molecular polarizability and r as the distance between the charge and the induced dipole [52]. Although the approximation by a charge-dipole interaction illustrates the mechanism, it oversimplifies the actual physics because molecules exhibit more complex charge distributions [62, 63]. The interaction of the charged molecule with the induced charge distribution stabilizes the charge and reduces IE and increases EA with similar magnitude in the solid (Figure 2.4). The polarization energy of a hole or an electron increases with increasing polarizability of surrounding molecules and is typically around 0.5 eV in organic semiconductors [28].

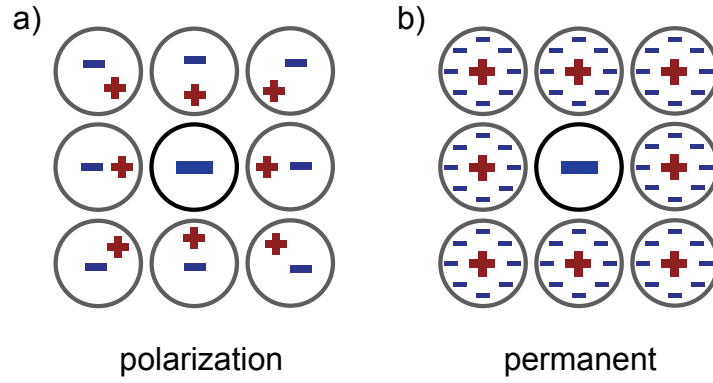


Figure 2.5: Sketch of electrostatic interactions in solids: (a) Induced dipole moments on the surrounding molecules stabilize the charge on the ion. (b) Permanent quadrupole moments on the surrounding molecules shift IE and EA to lower or higher values. In the sketched case, the charge is destabilized by the surrounding molecules.

Another contribution to the electrostatic correction is the *permanent* contribution Δ_{perm} , which describes the interaction of excess charges on molecules with permanent charge distributions on other molecules within the solid (Figure 2.5b). In some cases, this contribution can be very large and can even exceed the polarization energy. The interaction energy of an excess charge with the permanent electrostatic potential of surrounding molecules is

$$\Delta_{\text{perm}} = \frac{q}{4\pi\epsilon_0\epsilon_r} \int \frac{\rho(\vec{r})}{r} d\vec{r}, \quad (2.7)$$

with the charge distribution $\rho(\vec{r})$ and the excess charge q located at $\vec{r} = 0$. The charge distribution of the molecules can be approximated by a multipole expansion:

$$\Delta_{\text{perm}} = \frac{q}{4\pi\epsilon_0\epsilon_r} \sum_i \left[\frac{q_i}{r_i} + \frac{\vec{p}_i \cdot \vec{r}_i}{r_i^3} + \frac{1}{2} \frac{\vec{r}_i \cdot \mathbf{Q} \cdot \vec{r}_i}{r_i^5} \right], \quad (2.8)$$

where \sum_i sums over all molecules in the surrounding. The dipole moment \vec{p} is a vector and the quadrupole moment \mathbf{Q} is a tensor. Although ϵ_r can vary locally, it is used as a macroscopic constant in this thesis. Similarly, the multipole expansion breaks down at short distances and leads to an incorrect description of interactions between neighboring molecules. Nevertheless, the results in Section 5.2.4 indicate that the interaction between two molecules can be at least qualitatively explained by Equation 2.8.

For neutral molecules, the charge monopole q is always zero. Molecules with a large permanent dipole moment \vec{p} preferably arrange with an alternating orientation in a solid, decreasing their impact [27, 28]. Therefore, the leading component in Equation 2.8 is often the interaction of charges with permanent quadrupole moments. The charge-quadrupole interaction energy Δ_{q-Q} scales with r^{-3} and therefore strongly reduces with distance. Accordingly, the experimental results of this thesis are discussed in a short-range scheme

where the interaction of charges with the closest neighbors dominate. However, previous studies on DCV5T-Me(3,3) films showed that the magnitude of Δ_{q-Q} strongly depends on the integration limit for that system [27]. They were only able to correctly simulate the thin film energy levels when they integrated over the whole thin film geometry. Up to now, it is not clear for which systems such long-range effects become relevant.

In crystalline thin organic films, large molecular quadrupole moments can strongly shift the energy levels and can for example lead to an dependence of thin film energy levels on molecular orientation or induce electrostatic gradients at planar heterojunctions of different organic materials [27, 29, 64]. Chapter 4 of this thesis shows how electrostatic interactions influence electronic energies in neat and mixed solid films and how such electrostatic effects can be applied in electronic devices.

As already discussed in the last section, organic molecules geometrically relax after charging, which decreases their energy by the reorganization energy. In a molecular solid, not only the charged molecule itself relaxes but also its surrounding molecules. Thus, the reorganization energy in a molecular solid is generally different from a single molecules and consists of the molecular reorganization energy and the reorganization energy of its surrounding. However, previous studies showed that the contribution of intramolecular relaxation to the reorganization energy dominates in most molecular solids [52, 65].

2.1.3 Energetic Disorder

Energetic disorder has a huge impact on the electrical properties of organic semiconductors. The distribution of energy levels is typically assumed to be Gaussian with the standard deviation σ as a measure for energetic disorder present in the molecular solid. Most organic thin films, especially amorphous films and blends, exhibit a significant degree of *static disorder* (σ) originating from structural disorder. Even in neat films, fluctuations in the relative orientations and intermolecular distances between molecules lead to a local variation of the electrostatic potential and intermolecular coupling of the electron wave functions. In blends, molecular species can differ for example in their size, charge distribution or molecular polarizability, which results in a further variation of the electronic levels.

In a highly ordered molecular crystals, the energetic distribution is dominated by *dynamic disorder*, leading to time-dependent energy levels at finite temperatures. Particular in crystalline organic semiconductors with low static energetic disorder, dynamic disorder can lead to localized charge carriers and substantially decrease charge carrier mobilities [66]. Strong intermolecular coupling of the electron wave functions can form relatively broad energy bands in some organic crystals, such as pentacene, rubrene, and durene [67–69] exceeding the magnitude of energetic disorder. However, for most of the materials covered in this thesis, the intermolecular wave function overlap is comparably weak and its impact on electronic levels can be neglected for these materials.

2.2 Charge Transport

This section provides an overview of the most important charge transport models for disordered organic semiconductors. In crystalline inorganic semiconductors having broad electronic bands due to a strong covalent coupling between atoms, coherent band transport results in high charge carrier mobilities. A few studies also described the formation of electronic bands and a band-like transport in highly ordered crystalline organic semiconductors [67, 68, 70, 71]. However, in most organic semiconductors relevant for application in organic devices, weak intermolecular electronic coupling and energetic disorder lead to a thermally activated hopping between localized electronic states. This section concentrates on two important models describing hopping transport: Section 2.2.1 outlines the Marcus theory for electron transfer between molecules. Section 2.2.2 summarizes the Gaussian disorder model on hopping transport in a disordered medium. Finally, Section 2.2.3 briefly describes the impact of deep traps on charge carrier transport. This section is mainly based on the references [52, 65].

2.2.1 Marcus Theory for Electron Transfer

This section focuses on charge transport which is dominated by polaronic effects, i.e. when relaxation energies of charge carriers dominate the static energetic disorder. *Marcus theory* for electron transfer was originally used for the description of charge transfer between molecules in solution, but can be also applied to molecular solids [72, 73]. An important parameter for describing polaron transport is the *reorganization energy* (λ), which describes the energetic relaxation of the two involved molecules and its surrounding after charge transfer. While in solution the contribution of the surrounding to λ is usually large due to the high dielectric constant, molecular reorganization dominates λ in molecular solids [52, 65]. After electron transfer from a donating anion to an accepting neutral molecule, both molecules relax to their new ground state geometry. In a solid that consists only of one type of molecules, the molecular relaxation energies of donating and accepting molecule are similar. In such a case, λ after charge transfer in a molecular solid is approximately $2\lambda_-$ for electron transport and $2\lambda_+$ for hole transport (see Section 2.1.1). The sketch in Figure 2.6 illustrates the basic idea of Marcus theory. For the example of electron transport, the initial state of the system consists of a negatively charged donating and a neutral accepting molecule. Both molecules are in their ground state geometry characterized by their joint configuration coordinate q_i . In the final state, the joint ground-state geometry of the neutral donating and negatively charged accepting molecule is given by q_f . The potential curves of initial and final state are approximated by parabolas: $E_i(q) \propto (q - q_i)^2$ and $E_f(q) \propto (q - q_f)^2$. The intersection point of both parabolas gives directly the activation energy E_a for the electron transfer, which is $\lambda/4$ for systems without static energetic disorder ($E_f(q_f) = E_i(q_i)$, $\Delta G^0 = 0$ in Figure 2.6).

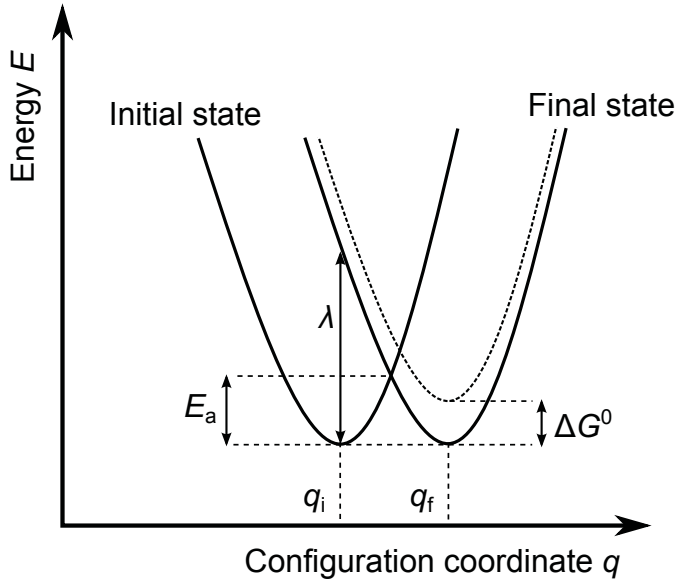


Figure 2.6: Illustration of Marcus theory for electron transfer: The electron transfer, i.e. transition from initial to final state, is thermally activated with an activation energy of E_a . If the ground state energy of the final system is increased by ΔG^0 compared to the initial system (dashed parabola), E_a becomes larger. Figure is adapted from reference [52].

In a quantum-mechanical approach, Marcus theory yields an electron transfer rate for small electronic coupling and phonon energies that are below the thermal energy ($k_B T$):

$$\kappa_{\text{ET}} = \frac{J^2}{\hbar} \sqrt{\frac{\pi}{\lambda k_B T}} \exp \left[-\frac{\lambda}{4k_B T} \right], \quad (2.9)$$

with J^2 as the transfer matrix element, describing the electronic coupling between initial and final state [72]. Equation 2.9 and the Einstein relation, $\mu = eD/k_B T$, with $D = (1/6)\kappa_{\text{ET}}a^2$ yield for the mobility in a three-dimensional system:

$$\mu = \frac{ea^2 J^2}{6\hbar(k_B T)^{3/2}} \sqrt{\frac{\pi}{\lambda}} \exp \left[-\frac{\lambda}{4k_B T} \right], \quad (2.10)$$

with a as the distance between two lattice sites [52]. The temperature dependence of the mobility varies with temperature. Whereas the mobility shows an Arrhenius-type temperature dependence at low temperatures, it decreases with $T^{-3/2}$ at high temperatures when $4k_B T \gg \lambda$. This results in an Arrhenius-type dependence below 600 K for a typical reorganization energy of 200 meV.

Equations 2.9 and 2.10 are only valid for systems without any static disorder. For a disordered system, the difference between the ground state energies of initial and final state (ΔG^0) is, in general, not zero and can have negative and positive values (see dashed parabola in Figure 2.6). In this case, the activation energy as obtained from the intersection point of the parabolas is: $E_a = (\lambda + \Delta G^0)^2/4\lambda$. Accordingly, the Marcus rate for electron transfer in Equation 2.9 changes to

$$\kappa_{\text{ET}} = \frac{J^2}{\hbar} \sqrt{\frac{\pi}{\lambda k_B T}} \exp \left[-\frac{(\lambda + \Delta G^0)^2}{4\lambda k_B T} \right]. \quad (2.11)$$

2.2.2 Gaussian Disorder Model

As already mentioned in Section 2.1.3, most organic semiconductors exhibit a substantial degree of energetic disorder, which strongly affects the charge carrier transport. One of the most established descriptions of hopping transport in disordered systems is the *Gaussian disorder model* (GDM) or *Bässler model* [74], where the energetic distribution of transport sites is assumed to be Gaussian:

$$g(E) = \frac{1}{\sqrt{2\pi}\sigma} \cdot \exp\left[-\frac{(E - E_0)^2}{2\sigma^2}\right], \quad (2.12)$$

where E_0 and σ describe the center and the standard deviation of the Gaussian distribution, respectively.

The GDM assumes localized transport sites and neglects any polaronic relaxation effects. Figure 2.7 shows a sketch of such a thermally activated and field assisted hopping transport. The hopping rate between two sites i and j can be described in terms of a *Miller-Abrahams rate*:

$$\nu_{i,j} = \nu_0 \cdot \exp(-2\gamma\Delta r_{i,j}) \cdot \begin{cases} \exp\left[-\frac{\Delta E_{i,j} - eF\Delta r_{i,j}}{k_B T}\right], & \Delta E_{i,j} - eF\Delta r_{i,j} > 0 \\ 1, & \Delta E_{i,j} - eF\Delta r_{i,j} < 0 \end{cases} \quad (2.13)$$

where $\Delta r_{i,j}$ and $\Delta E_{i,j}$ are distance and energy difference between the two sites, respectively. γ is the inverse localization radius of the electron wave function and is related to the strength of the electronic coupling between two hopping sites [75]. ν_0 describes the attempt-to-jump-frequency and is typically assumed to be around 10^{-12} s^{-1} [76, 77]. F is the applied electric field. The first part of Equation 2.13 describes the tunneling probability, depending on the strength of the electronic coupling of two sites. The Boltzmann factor in the second part assumes that thermal energy is required for jumps to final states with higher energies. For downward jumps, the probability is 1 and it is assumed within this model that the excess energy dissipates.

At low electric fields, single charge carriers generated at an arbitrary site within a Gaussian density of states (DOS) relax step-by-step to a quasi-equilibrium energy below the center of the DOS. This equilibrium energy reaches $-\sigma^2/(k_B T)$ by using quasi Boltzmann statistics [74]. For charge transport at low carrier concentrations, charge carriers need to be thermally activated from this quasi-equilibrium level to the effective transport level. This leads to the following temperature dependence of the mobility:

$$\mu = \mu_\infty \cdot \exp\left[-C \left(\frac{\sigma}{k_B T}\right)^2\right], \quad (2.14)$$

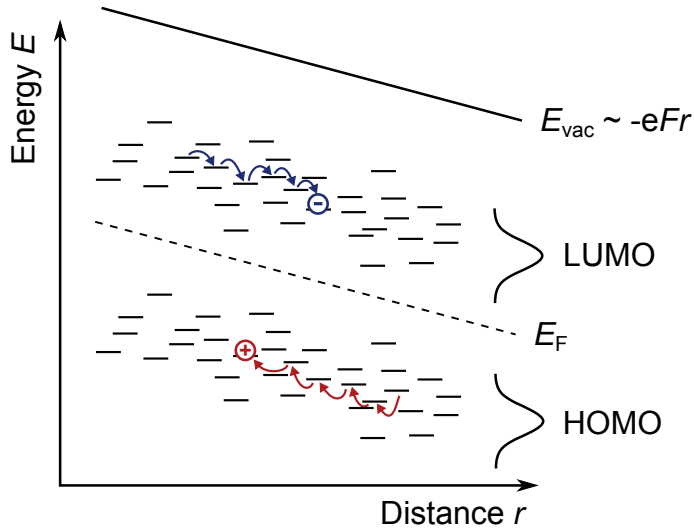


Figure 2.7: Sketch of the field assisted hopping transport within a disordered system with localized electronic states: The hopping process consists of a tunneling from initial to final state and a Boltzmann activated energy hop. The distribution of transport sites is assumed to be Gaussian. The figure is adapted from reference [61].

where the scaling parameter C is 0.44 for a three-dimensional system [52].

Equation 2.14 only holds true if the energetic disorder is large and polaronic relaxation effects can be neglected. However, the energetic relaxation after charge transfer can play an important role for charge transport. Due to this polaron relaxation, charge transfer is thermally activated by the *polaron binding energy* E_p . Fishchuk *et al.* combined the Marcus formalism and the GDM, leading to the following dependence of the mobility:

$$\mu \propto \exp \left[-\frac{E_p}{2k_B T} - C \left(\frac{\sigma}{k_B T} \right)^2 \right], \quad (2.15)$$

where C depends on the ratio of σ and E_p [78].

At high charge carrier densities, the Fermi level E_F crosses the equilibrium energy at $-\sigma^2/(k_B T)$, resulting in an Arrhenius-type dependence of the mobility on energetic disorder [79–82]. This dependence is for example observed experimentally in organic transistors [83], space-charge limited (SCL) diodes [80], or doped organic semiconductors [40, 84, 85]. Similar to Equation 2.15, a sum of a polaronic contribution and a disorder contribution can describe the temperature dependence of the mobility [82]:

$$\mu \propto \exp \left[-\frac{E_p}{2k_B T} - C \left(\frac{\sigma_{st}}{k_B T} \right) \right]. \quad (2.16)$$

In accordance to Marcus theory (see Section 2.2.1), the polaron binding energy E_p can be described by the relaxation energies of anions and cations. Neglecting external contribu-

tions to E_p , it is equal to the molecular relaxation energies λ_- and λ_+ for electron and hole transport, respectively.

2.2.3 Impact of Charge Carrier Traps

Charge carrier traps, which can originate from structural defects or chemical impurities, often hinder charge transport in organic semiconductors. The exact impact of traps on charge transport depends strongly on their energy and density. If the EA of an impurity is larger than the EA of the organic semiconductor, this impurity forms an electron trap and deteriorates electron transport. Similarly, a hole trap is introduced when the IE of an impurity is smaller than the IE of the organic semiconductor. The introduction of such traps leads to a thermal activation of the charge carrier mobility. The *Hoesterey-Letson* formula was developed to describe the charge carrier mobility in organic crystals with low energetic disorder [86]. For traps with the relative concentration c and the trap energy E_T with respect to the transport level, the mobility reduces like:

$$\mu(c) = \mu_0 \left[1 + c \cdot \exp\left(\frac{E_T}{k_B T}\right) \right]^{-1}, \quad (2.17)$$

where μ_0 is the mobility without traps ($c = 0$). For disordered organic semiconductors, the reduction of the mobility deviates from the behavior in Equation 2.17 and for example depends on the energetic distribution of transport states and trap states [87, 88].

The origin of charge carrier traps varies between different compounds. Organic semiconductors, especially solution-processed polymers, are often handled at ambient air during the production process, which can introduce charge carrier traps. *Nicolai et. al* identified in a recent study on several polymers with varying EA an universal electron trap with a distinct energy, which was supposed to originate from hydrated oxygen complexes [89]. Another study observed emerging tail states in the Gaussian DOS after exposure of the organic semiconductor to inert gas, which was attributed to the introduction of structural defects [90]. The results in Section 5.4.3 of this thesis indicate that a universal trap level introduced by air exposure reduces the conductivity in n-doped organic semiconductors.

2.3 Molecular Doping

The implementation of molecularly doped transport layers into organic optoelectronic devices, such as solar cells or light-emitting diodes, substantially increased their efficiencies [34, 35]. Furthermore, molecular doping can be employed to precisely tune device characteristics of organic transistors, which are supposed to be a key component of future flexible electronics [33, 91]. The aim of doping is the increase of the electrical conductivity and the shift of the Fermi level towards the transport level, enabling ohmic charge injection and extraction at metal/organic interfaces [34, 36] or the control of organic/organic interfaces [92, 93]. Although molecular doping was intensely investigated in the past, a complete picture of the doping process and the charge transport mechanism has not been established yet. This section introduces common concepts of the doping process (Section 2.3.2), prevailing considerations on charge transport in doped organic semiconductors (Section 2.3.3) and the issue of air sensitivity for n-doping (Section 2.3.4). It is mainly based on the ideas and thoughts of references [35, 94–96].

2.3.1 Introduction

Inspired by doped inorganic semiconductors, early doping attempts of organic semiconductors utilized elemental dopants. Both, p-doping by halogen gases [97, 98] and n-doping by alkali metals [99, 100] yielded an increase of the conductivity by several orders of magnitude. However, due to their small size, elemental dopants exhibit only a low stability and diffuse within the organic layers, making device fabrication with a controlled layer sequence challenging. With their larger molecular weight, organic molecules have a higher thermal stability and a smaller diffusivity, making them suitable for the use in organic devices. Nowadays, molecular doping is successfully employed in the majority of organic devices based on small molecules.

Molecular doping usually aims to increase the electrical conductivity (σ_e) of organic semiconductor films. σ_e is often described by the product of charge carrier concentration (n for electrons and p for holes) and charge carrier mobility (μ): $\sigma_e = \mu n e$, with e as the elementary charge [40]. The charge carrier concentration is directly connected to the dopant concentration (N_d) by the doping efficiency (η): $n = N_d \eta$. Figure 2.8 exemplary shows the concentration dependence of σ_e for bis-HFI-NTCDI layers n-doped with (2-Cyc-DMBI)₂. σ_e increases strongly above 0.1 mol% and reaches its maximum at very large concentrations between 10...20 mol%. Previous studies on different doped organic semiconductors also observed a superlinear increase of σ_e with N_d [40, 42, 84, 101–103], which implies that μ and/or η increases with doping concentration in this concentration regime. In the past, several studies provided explanations for the reduced conductivities at low doping concentrations and the strong increase towards high concentrations. The next section

summarizes proposed mechanisms of charge carrier generation and proposed origins of the superlinear increase of σ_e .

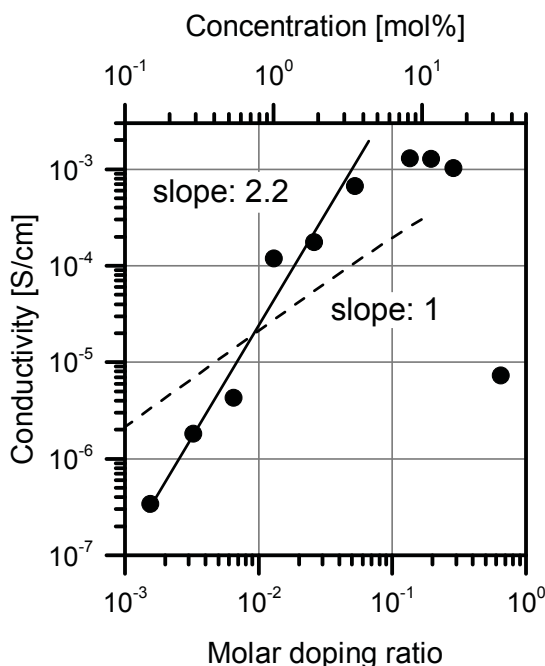


Figure 2.8: Superlinear increase of conductivity with doping concentration: The conductivity of bis-HFI-NTCDI n-doped with $(2\text{-Cyc-DMBI})_2$ is shown. The dashed line depicts the expected trend for a doping efficiency of 100% and a constant mobility, which was obtained in an undoped organic field-effect transistor.

2.3.2 Generation of Mobile Charge Carriers

The doping efficiency in organic semiconductors is often defined as the ratio between the concentration of *free* charge carriers and the concentration of dopant molecules. However, it might be misleading to transfer the terminology of *free* charge carriers typically used for band transport to doped organic semiconductors with localized electronic states and energetic disorder. Therefore, this thesis uses *mobile* instead of *free* carriers as a description of charge carriers predominantly contributing to (hopping) transport. In a simple picture, the generation of mobile charge carriers by molecular doping is often described by a two step process [41, 104, 105]. In the first step, the dopant releases a charge (an electron for n-doping and a hole for p-doping) to a matrix molecule, which leads to the formation of a charge transfer complex (CTC) between the matrix and the dopant molecule. In order to generate mobile charge carriers for transport, the charges in the CTC need to be separated by overcoming their Coulomb attraction. Accordingly, the doping efficiency of a matrix/dopant combination can be described by the product of the initial charge transfer efficiency and the generation efficiency of mobile carriers from bound CTCs. It is discussed below that the distinction between bound and mobile charge carriers becomes

difficult particularly at high doping concentrations. First, two common models for the initial charge transfer from dopant to matrix molecule are discussed.

Intital charge transfer: Integer vs. Partial Charge Transfer

The *integer charge transfer* (ICT) model neglects the impact of overlapping electron wave functions between matrix and dopant molecule and assumes a full charge transfer from dopant to matrix molecule [44, 105]. Upon n-doping, the neutral dopant turns into a cation and the matrix molecule turns into an anion, resulting in the formation of an *interger charge transfer complex* (ICTC). The efficiency of this charge transfer depends predominantly on the relative positions of the energy levels of matrix and dopant. As illustrated in Figure 2.9a, efficient n-doping requires the ionization energy of the dopant (IE_D) to be smaller than the electron affinity of the matrix molecule (EA_M), while EA_D should be larger than IE_M for efficient p-doping. In case of only weakly donating or accepting dopants, the charge transfer efficiency is thermally activated and depends on the difference between IE_D and EA_M for n-doping and between IE_M and EA_D for p-doping. Salzman *et al.* calculated the charge transfer efficiency in dependence of the doping concentration and energy level offset by assuming a Gaussian broadening of the density of states and using Fermi-Dirac statistics [44]. They revealed a decreasing charge transfer efficiency with increasing doping concentrations, where the effect is larger for weak electron donating and accepting dopant molecules. Apart from the relative energies, an unfavorable morphology can decrease the charge transfer efficiency when the dopants are not homogeneously distributed within the film [104, 106].

The hybridization model, proposed by the group of Norbert Koch, assumes a significant intermolecular coupling of the electron wave functions of matrix and dopant molecule [43, 107–109]. In the *charge transfer complex* (CTC), the frontier orbitals of matrix and dopant hybridize and form new orbitals. Accordingly, the charge transfer is not complete and the charge is localized on both the matrix and the dopant molecule [110]. Figure 2.9b shows a simplified sketch of the hybridization of the HOMO of an n-dopant and the LUMO of a matrix molecule. The hybridization forms a bonding and an antibonding orbital in which the former one determines the ionization energy of the CTC. This ionization energy is larger than the ionization energy of the remaining matrix molecules, which leads to an energy barrier for the charge transfer from the CTC to another matrix molecule. Accordingly, the CTC acts as a weak molecular dopant, as discussed for the case of an integer charge transfer [44]. Which preconditions are necessary for intermolecular hybridization of matrix and dopant is still under scientific discussion. Apart from a relatively strong coupling of the electron wave functions, the relative orientation of the matrix and the dopant molecule, i.e. the film morphology, is a crucial issue. Mendez *et al.* explained low conductivities in quaterthiophene doped by F_4TCNQ with intermolecular hybridization of matrix and dopant and showed that both molecules form a new

co-crystal within the doped layer [109]. As intermolecular hybridization was only observed in a few matrix/dopant combinations, the model seems to describe a special case of molecular doping. Therefore, further discussions in this thesis are based on the ICT model.

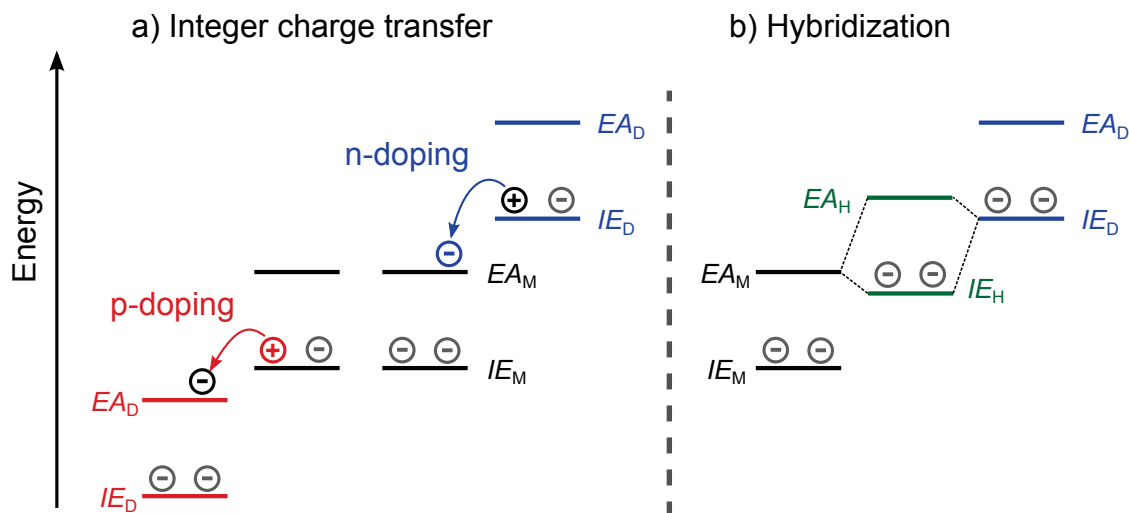


Figure 2.9: Common models for the initial charge transfer: (a) The integer charge transfer (ICT) model assumes a weak overlap of the electron wave functions of matrix and dopant molecule as well as a complete transfer of a single electron. (b) The hybridization model assumes a stronger overlap of the wave functions and a formation of a charge transfer complex (CTC), where the hybrid electron wave functions are localized on both the matrix and the dopant molecule. Such a complex exhibits new electronic levels (green) compared to the single matrix and dopant molecules. For simplicity, only ionization energies and electron affinities are shown in this sketch.

Dissociation of Integer Charge Transfer States

For the case of an integer charge transfer from dopant to matrix molecule, the two ions form an ICTC consisting of a donor cation and an acceptor anion for the case of n-doping. The Coulomb binding energy of ICTC is typically expected to be a few 100 meV due to the small dielectric constant in organic semiconductors [39, 104, 111]. This barrier is much larger than the thermal energy at room temperature and efficient ICTC dissociation and generation of mobile charge carriers seems unlikely. However, this simple scheme neglects further contributions to the ICTC dissociation barrier originating from the environment of the ICTC.

Several theoretical studies on organic interfaces showed that a different electrostatic environment at the interface can lead to energy level gradients which favor charge separation [23, 26, 64, 112, 113]. The experimental results of this thesis indicate that charge-quadrupole interactions can reduce the dissociation barriers of bound electron-hole pairs in doped organic semiconductors (Sections 5.2 and 5.3) and in organic solar cells (Section

4.4). Previous theoretical studies argued that ICTC dissociation barriers reduce naturally for increased doping concentrations [37–39]. At low doping concentrations, the distance between the deep Coulomb potentials of the ICTCs is large, reflecting in large dissociation barriers. At high doping concentrations, the distance between ICTCs is reduced and their electrostatic potentials can overlap. With increasing concentration the potentials smear out and the depth of the Coulomb wells significantly reduces. This effect leads to a decrease of the (effective) ICTC dissociation barrier with increasing doping concentration [38].

Limitation by Intrinsic Traps

Apart from large ICTC binding energies, deep trap states within the energy gap can reduce the doping efficiency. Such trap states originate from impurities and the amount depends on the degree of purification of the material [114, 115]. Tietze *et al.* proved the existence of intrinsic deep traps for several matrix/dopant combinations by measuring the Fermi level position as a function of doping concentration [41, 42, 94, 114]. The shift of the Fermi level with doping concentration for different doped semiconductors could be described by Fermi-Dirac statistics only when deep intrinsic traps with a fixed concentration of up to 0.2 % were introduced into the DOS. The energy of this trap level with respect to the transport level was set larger than the donor (E_D) or acceptor (E_A) level of the dopant in case of n- and p-doping, respectively.

Within this classical model, the Fermi level change was divided into three regions: At doping concentrations that are smaller than the trap concentration, the doping efficiency is very low because dopants only fill deep trap states instead of generating mobile charge carriers. When the doping concentration exceeds the trap concentration, charge carriers are generated from the respective donor and acceptor levels with high probabilities, which leads to an increase in doping efficiency. At very large concentrations, the Fermi level is pinned between the donor/acceptor level and the transport level. In this dopant reserve regime, the doping efficiency decreases again with increasing doping concentration. According to these results, the doping efficiency increases with decreasing trap concentration, smaller offset of the donor/acceptor level from the transport states and increasing width of the density of states distribution [94]. In case of efficient charge transfer from the dopant to the matrix molecule, the donor and acceptor levels were connected to the release probability of a charge from the matrix/dopant ICTC state [41].

2.3.3 Transport in Doped Organic Semiconductors

Efficient optoelectronic devices necessitate highly conductive films. Therefore, it is crucial to understand the influence of molecular doping on charge carrier transport in organic semiconductors. A common way to describe charge transport in doped organic

semiconductors is to consider the induced changes of doping to the density of states and apply the same hopping formalism to it as discussed for intrinsic semiconductors (see Section 2.2). This section summarizes some of the previous considerations which are relevant for the discussion of the experimental results of this thesis.

First, the case of very low intrinsic energetic disorder is discussed. At very low doping concentrations ($\ll 1\%$), charged dopants introduce deep Coulomb wells into the semiconductor DOS, acting as charge carrier traps [37, 39, 111]. The reduction of the (mean) mobility caused by these traps depends on their energetic depth, which is supposed to be connected to the Coulomb binding energy of the ICTC. This effect reduces the charge carrier mobility from its intrinsic value to a minimum with increasing doping concentration [39, 116]. Furthermore, the width of the density of states increases with doping concentration due to the introduction of electric dipoles, leading to a further reduction of the mobility [39, 117].

After its minimum value, the mobility increases with doping concentration because charge carriers can fill more and more deep states within the DOS. Furthermore, the distance between the Coulomb wells reduces with doping concentration and their electrostatic potentials can overlap. With increasing concentration, the potentials smear out and the effective depth of the Coulomb wells reduces [37–39]. This leads to a steep increase of the charge carrier mobility and conductivity with doping concentration [39, 116]. After reaching its maximum typically around 10 mol%, the conductivity decreases again due to an increase of energetic disorder originating from large amounts of electrical dipoles and a disruption of the structural order in the film [118–120].

In case of a very large intrinsic energetic disorder, the negative impact of Coulomb traps from dopants at low doping concentrations is reduced. Therefore, the mobility increases with doping concentration already at low doping levels because the positive effect of filling of deep states dominates [39]. A steep increase of the conductivity at higher doping concentrations also occurs for this disordered systems. However, the maximum of the conductivity is typically at larger concentrations than 10 mol% because the impact of additional disorder by dopants is less pronounced in such disordered semiconductors [102]. Additionally to the introduced Coulomb traps, intrinsic deep trap states can also deteriorate charge transport in doped organic semiconductors. The impact of these traps on the mobility depends strongly on their concentration and energetic depth. If the trap depth and concentration is larger compared to the introduced Coulomb traps, the mobility can substantially be reduced by these deep traps. In contrast to Coulomb traps, the concentration of these intrinsic traps does not increase with doping concentration. When the doping concentration increases above the trap concentration, the traps are compensated by charge carriers and the mobility strongly increases with doping concentration [40, 115].

2.3.4 Air-stable n-Doping

The basis for long-term stable organic semiconductor devices are air stable organic materials. The redox potentials of water and oxygen are expected to set an approximate limit to the electronic levels of stable compounds. If the EA is smaller than 5.7 eV and the IE larger than 4 eV, neutral organic molecules are supposed to be insensitive to exposure to oxygen or water [34, 121, 122]. However, n-doping of many organic molecules that are typically used in organic devices necessitates n-dopants with an IE smaller than 4 eV, making these compounds highly air sensitive [20]. To overcome this problem, the actual n-doping species can be incorporated in an air-stable precursor compound with a sufficiently high IE . This approach was demonstrated for cationic salt and dimer precursors that split up in solution or during thermal evaporation in vacuum and release a strongly reducing n-doping radical [45, 123–126]. Recent studies revealed for various 1,3-Dimethyl-2-phenyl-2,3-dihydro-1H-benzoimidazole (DMBI) derivatives strong n-doping of C_{60} and achieved record conductivities as high as 12 S/cm [47, 49, 103]. Section 5.1 investigates the n-doping properties of DMBI salts and DMBI dimers in more detail. Apart from the actual n-dopants, also the n-doped layers can be highly sensitive to air exposure [20, 94, 127]. The results of these recent studies suggest a dependence of the air sensitivity on the EA of the matrix molecule. Section 5.4 investigates the correlation between the electronic levels and the air stability for a variety of n-doped semiconductors and draws conclusions on a general limit for air stable n-doping of organic semiconductors.

2.4 Organic Solar Cells

Although this thesis concentrates on basic studies on the electronic properties of organic semiconductors, Section 4.4 exemplary demonstrates how the basic findings can be used to improve organic semiconductor devices, i.e. organic solar cells. Compared to their inorganic counterparts, organic semiconductors offer a variety of new design possibilities such as semi-transparent, large-area, and flexible devices produced at low-cost in roll-to-roll processes [2, 6, 128]. The device efficiencies of organic solar cells recently increased above 10%, being necessary for a broad usage on the market [32, 129–131]. This section describes briefly the basic mechanisms of organic solar cells in Section 2.4.1 and 2.4.2 and further summarizes the known dependencies of solar cell parameters on physical properties in Section 2.4.3. This section is mostly based on references [61, 132].

2.4.1 p-n-Junction

An inorganic solar cell typically consists of a junction of a p-doped and an n-doped semiconductor. A diffusion current of majority charge carriers (holes for p-side and electrons for n-side) towards the other side of the junction leads to the formation of a space charge region. The potential drop over this space charge region causes a drift current of minority carriers in the opposite direction. In thermal equilibrium, the magnitude of diffusion current and drift current are equal and given by the potential barrier across the junction. This barrier decreases by applying a high potential to the p-side and a low potential to the n-side, resulting in an exponential increase of the diffusion current with voltage (V). As a first approximation, the drift current does not change with voltage and is equal to the saturation current j_s at low voltages. The jV -characteristic of such a p-n-diode is:

$$j(V) = j_s \left[\exp\left(\frac{eV}{nk_B T}\right) - 1 \right], \quad (2.18)$$

with n as the ideality factor of the diode. Without illumination, the magnitude of the drift current depends on the thermal generation of charge carriers. Illumination of the p-n-junction generates additional *excitons*, i.e. electron-hole pairs, which can be split by the thermal energy in inorganic semiconductors. This creates additional minority charge carriers and increases the drift current by the generated photocurrent (j_{ph}):

$$j(V) = j_s \left[\exp\left(\frac{eV}{nk_B T}\right) - 1 \right] - j_{ph}. \quad (2.19)$$

Figure 4.12 shows the jV -characteristic of such an ideal solar cell according to Equation 2.19. Important parameters for the determination of the solar cell efficiency are the *short-circuit current density* (j_{sc}) at $V = 0$, the *open-circuit voltage* (V_{oc}) at $j = 0$ and the *fill-factor*

(FF) at the maximum power point (mpp). These values directly determine the power conversion efficiency of the solar cell (η):

$$\eta = \frac{j_{sc} V_{oc} FF}{P_{in}}, \quad FF = \frac{j_{max} V_{max}}{j_{sc} V_{oc}}, \quad (2.20)$$

with P_{in} as the power density of the light illumination.

In a real device, parasitic resistances deteriorate the performance of a solar cell, which can be described by a serial (R_s) and a parallel resistance (R_p) in an equivalent circuit picture. While R_s can for example arise from energy barriers at contacts or small electrical conductivities of the semiconductor layers, a finite R_p can originate from recombination processes.

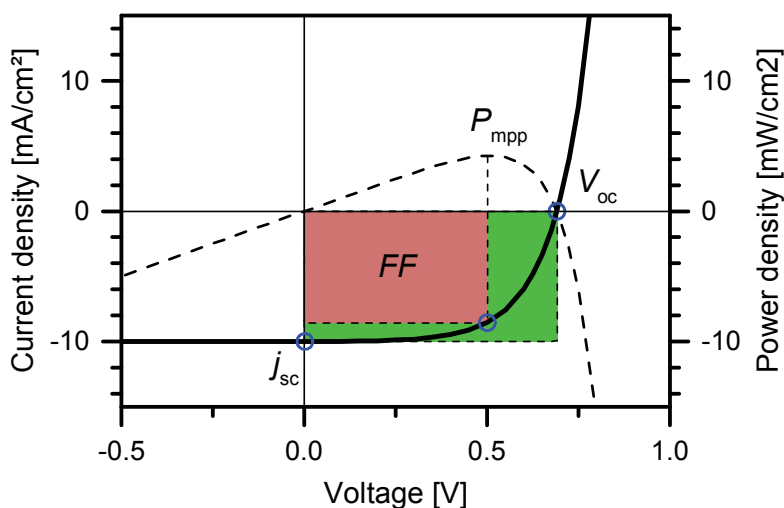


Figure 2.10: jV -characteristic of a solar cell: The solid line displays the change of current density (j) with voltage (V) under light illumination according to Equation 2.19 (left axis). The dashed line depicts the generated power density P (right axis), which has its maximum at the maximum power point (MPP). The ratio between the red and the green rectangle is the fill-factor FF , which determines together with V_{oc} and j_{sc} the power conversion efficiency of the solar cell. The figure is adapted from reference [61].

2.4.2 Basic Mechanism of Organic Solar Cells

After the observation of photoconduction in organic molecules, organic materials were introduced as active layer in solar cells [133–135]. However, the power conversion efficiencies of these solar cells were well below 1%. The introduction of the *donor-acceptor concept* by Tang was a crucial step towards higher efficiencies in organic solar cells [136]. Due to the low relative dielectric permittivities of around 3 to 4 in organic semiconductors, exciton binding energies are much larger than in inorganic semiconductors [137]. Therefore, excitons cannot be efficiently split by the thermal energy. Here, the energy

offset between the electron donor and the electron acceptor provides the required energy for exciton splitting.

Devices with the donor-acceptor active area sandwiched between two metal contacts show a strong dependence of their performance on work functions of the metal contacts [138, 139]. Therefore, it was another important step to introduce the so-called *pin-concept* in organic solar cells. An implementation of doped transport layers between the photoactive layer and the metal contacts removes the dependence on the work function of the contact and enables ohmic extraction of charge carriers at the contacts [34].

The basic principle of a pin-type organic solar cell is depicted in the energy level diagram of Figure 2.11a. Photons enter the device through a transparent electrode and excite an exciton for example in the donor phase (1). The exciton has to diffuse to the donor-acceptor interface for exciton splitting (2). By applying an energy offset between the electron affinities or ionization energies of donor and acceptor, excitons can split and form energetically lower lying charge transfer (CT) states at the interface (3). Note that this CT state forms similarly to the ICTC in molecularly doped semiconductors, as discussed in Section 2.3.2. The only difference is the larger offset of the electronic energies in the case of molecular doping. Analogous to molecular doping, the CT binding energy has to be overcome to dissociate the CT state into separate charge carriers (4). Finally, the charge carriers need to be extracted at the metal contacts to contribute to the photocurrent of the solar cell (5).

2.4.3 Solar Cell Parameters

The efficiency of a solar cell depends on the generated photocurrent and photovoltage. The generation efficiency of photocurrent (η_{gen}) can be divided into four different contributions, which are explained in the following:

$$\eta_{\text{gen}} = \eta_{\text{abs}} \cdot \eta_{\text{CT}} \cdot \eta_{\text{diss}} \cdot \eta_{\text{ex}} \quad (2.21)$$

η_{abs} depends on the amount of absorbed photons and is already very high for the thin films of a variety of organic molecules exhibiting high absorption coefficients. Suitable donor-acceptor combinations can already strongly absorb over a broad spectral range and produce high photocurrents [130, 140]. η_{CT} depends on the amount of created excitons that reach the donor-acceptor interface and form CT states. Here, a crucial parameter is the exciton diffusion length, which is typically only several nanometers in organic semiconductors [141, 142]. Only excitons generated at a distance from the interface that is smaller or similar to the diffusion length are able to reach the donor-acceptor interface. This problem could be solved by intermixing of donor and acceptor within the active layer [143, 144]. This so-called bulk heterojunction (BHJ) concept significantly increased device efficiencies and is used nowadays as standard. The CT state energy has to be smaller

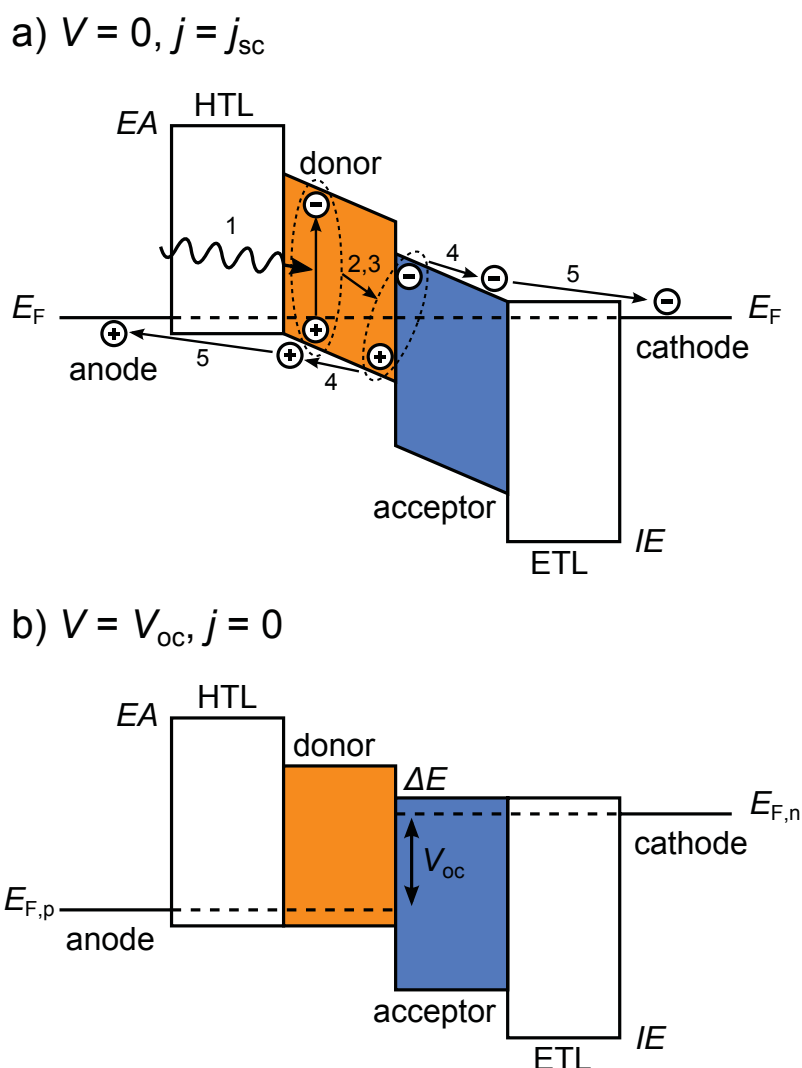


Figure 2.11: Energy level diagram of an organic solar cell in pin-architecture: Energy level diagram at short-circuit (**a**) and open-circuit (**b**) condition. While j_{sc} is given by the extracted charge carriers (**a**), V_{oc} is defined by the quasi Fermi level splitting (**b**). The lower and upper lines of each box depict the IE and EA of the materials. The figure is adapted from reference [94].

than the exciton energy for efficient CT state formation from excitons, which can be for example achieved by tuning the energy offset ΔE between donor and acceptor molecule (Figure 2.11b).

η_{diss} describes the splitting efficiency of CT states into single charge carriers and directly correlates with the difference between the CT state energy and the energy of (free) separated charges [145]. Section 4.4 of this thesis investigates how electrostatic interactions can be used to decrease the energy barrier for CT state dissociation [64]. The extraction efficiency η_{ex} of these charge carriers can be affected by several effects, such as energy barriers between the active layer and contacts, small charge carrier mobilities, or recomb-

nation of charge carriers. The implementation of doped transport layers can for example circumvent the problem of extraction barriers at metal contacts [34]. The efficiency of one or more of these processes can change with the applied electric field, making η voltage dependent. Accordingly, the generated photocurrent decreases with increasing voltage, which reduces FF .

The second important parameter that characterizes the power conversion efficiency is the open-circuit voltage (V_{oc}). As shown in Figure 2.11b, the difference of the quasi Fermi levels of donor and acceptor determines V_{oc} :

$$eV_{oc} = E_{F,n} - E_{F,p}. \quad (2.22)$$

The Fermi level splitting can also be described in dependence of the number of holes in the donor (p) and electrons in the acceptor (n):

$$eV_{oc} = V_0 + k_B T \cdot \ln \left[\frac{np}{N_n N_p} \right], \quad (2.23)$$

where N_n and N_p are the effective density of states in the donor HOMO and acceptor LUMO, respectively. As no charge carriers are extracted at V_{oc} , the generation rate G and recombination rate R of charge carriers must be equal [146, 147]. While G increases with light intensity, R depends on the number of charge carriers: $R = \gamma np$, where γ is the recombination rate coefficient. Therefore Equation 2.23 can be written as:

$$eV_{oc} = V_0 + k_B T \cdot \ln \left[\frac{G}{\gamma N_n N_p} \right]. \quad (2.24)$$

As recently shown, a reduction of the interfacial area between the donor and the acceptor phase can reduce the recombination rate and increase V_{oc} [148]. V_0 denotes the upper limit of V_{oc} and is reached for $T = 0$ K. Widmer *et al.* observed a correlation of V_0 with the *effective gap* of the donor-acceptor system, which is the difference between the *EA* of the acceptor and the *IE* of the donor [149]. The results in Section 4.4 demonstrate how a precise control of the effective gap can enable a continuous tuning of V_{oc} .

After charge transfer at the donor-acceptor interface, the CT state relaxes quickly to its ground state energy (E_{CT}), which is the required energy to excite the relaxed CT state directly from the ground state of the neutral donor-acceptor pair. This energy can differ strongly from the effective gap due to energy shifts by geometrical relaxation, Coulomb binding between electron and hole, and different polarization energies of CT states and single charges. Furthermore, energetic disorder at the donor-acceptor interface can reduce E_{CT} and V_{oc} with respect to the effective gap because electron-hole pairs preferably occupy CT states at low energies [150, 151]. Therefore, it seems more appropriate to describe V_0 in Equation 2.23 and 2.24 by E_{CT} directly instead of using the effective gap [152, 153].

3. Experimental Methods

This chapter provides details on the organic materials as well as on the experimental and simulation methods used for this thesis. Section 3.1 gives general information on organic small molecules and sample preparation. Photoelectron spectroscopy as the most important method of this thesis is described in Section 3.2, including subsections on ultraviolet, X-ray, and inverse photoelectron spectroscopy. Sections 3.3 and 3.4 summarize details on conductivity measurements and solar cell fabrication, respectively. Finally, Section 3.5 briefly gives details on the density functional theory simulations performed for this thesis.

3.1 Materials and Sample Preparation

The major aim of this thesis is to derive general conclusions on structure-property-relationships by investigating a large variety of small organic molecules. Figure 3.1 exemplarily shows four molecules playing a decisive role in different parts of the discussions. The model system of ZnPc and its fluorinated derivatives is used in Chapter 4 to investigate the impact of quadrupole moments on thin film energies. Specific properties, such as the quadrupole moment or the electronic levels, can be selectively adjusted with the degree of fluorination in this material system. As donor in blends with the standard acceptor C₆₀, the basic findings are tested in solar cells. In Chapter 5, electronic levels, charge transport properties, and air sensitivity of n-doped organic semiconductors are studied. Figure 3.1b exemplarily displays bis-HFI-NTCDI as electron transport material, which is routinely employed in organic solar cells of IAPP. (2-Cyc-DMBI)₂, shown in Figure 3.1c, is used as highly efficient and air-stable n-dopant for most of the investigations on molecular n-doping. Table 7.1 of the Appendix summarizes the chemical structures and names of all molecules discussed in this thesis.

An important goal is to connect electronic characteristics of organic thin films to molecular parameters that can be directly obtained from the chemical structures. The results in Chapter 4 demonstrate that molecular quadrupole moments, in particular the out-of-plane components (Q_{π}) of planar molecules, crucially affect the ionization energy (IE) and electron affinity (EA) in thin crystalline films. Another example are molecular relaxation energies of ions (λ_{+} , λ_{-}), which play a decisive role for hole and electron transport in doped organic semiconductors (see Section 5.3). Both parameters are accessible by density functional theory (DFT) simulations. Where available, Table 7.2 of the Appendix lists the most important material properties, namely mass density, molar mass, and experimental values for ionization energy (IE) and electron affinity (EA) in thin films.

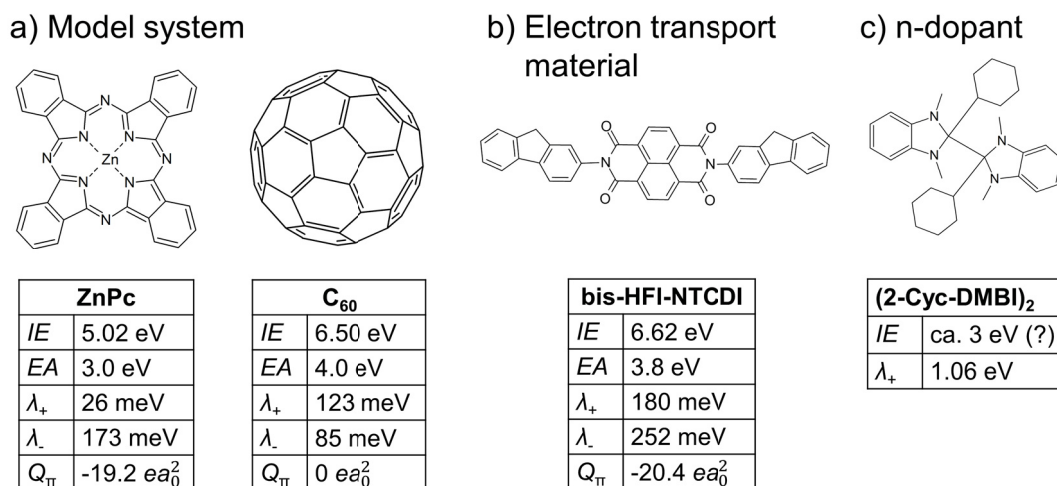


Figure 3.1: Selection of important organic small molecules for this thesis: *IE* and *EA* denote the ionization energy and electron affinity of thin films processed on weakly interacting substrates, respectively. The given *IE* value of the actual n-doping species provided by the precursor (2-Cyc-DMBI)₂ is not a direct measure but only a rough estimate. λ_+ and λ_- are the molecular relaxation energies of cations and anions, respectively. Q_π denotes the quadrupole component perpendicular to the molecular plane.

Project collaborators provide DFT values for *IE* and *EA* in gas-phase (IE_0 , EA_0), molecular quadrupole moments, relaxation energies, and Coulomb binding energies of different donor-acceptor pairs. The values are listed in Tables 7.3 and 7.4 of the Appendix.

The organic materials, typically delivered as powders, are purified by repeated 3-zone gradient sublimation before processing the samples. Only the DMBI derivatives utilized as air-stable n-dopant precursors are used as delivered (see Section 5.1). All materials investigated in this thesis are thermally evaporated in ultra-high vacuum (UHV) at base pressures between 10^{-7} and 10^{-9} mbar. Intrinsic, p-doped and n-doped organic layers as well as metal layers are evaporated in separate UHV chambers, which are each connected to the measurement chamber of the photoelectron spectroscopy (PES) setup. These experimental conditions reduce contamination of the samples during processing to a minimum and enable highly sensitive PES measurements at the surface of organic thin films.

Figure 3.2 sketches the thermal evaporation process typically used at IAPP. While gold is evaporated from molybdenum boats, the organic materials are evaporated from ceramic crucibles at rates between 0.1 and 0.3 Å/s. The evaporation rate of the organic materials is controlled by the heating current, i.e. the temperature of the crucibles. Individual quartz crystal microbalances (QCM) for each crucible monitor the evaporation rate¹ of each material, enabling a precise control of the layer thickness and additionally the mixing ratio in blends when co-evaporating different materials. A rotating shutter located between sample and crucible causes a tenfold reduction of the deposition rate, enabling the fabri-

¹ Technically spoken, the QCMs measure a frequency change originating from the increasing mass of the evaporated material, which is calculated into a deposition rate.

cation of doped samples with low doping ratios down to 10^{-5} [94]. For blends, the relative content of each material can be specified by its fraction measured in weight (wt% - weight percent), volume (vol% - volume percent), or as number of molecules (mol% - mole percent). Accordingly, the weight, volume, and molar ratio denote the ratio between two or more materials. Finally, placing a shadow mask in front of the sample enables deposition of structured layers on the substrate.

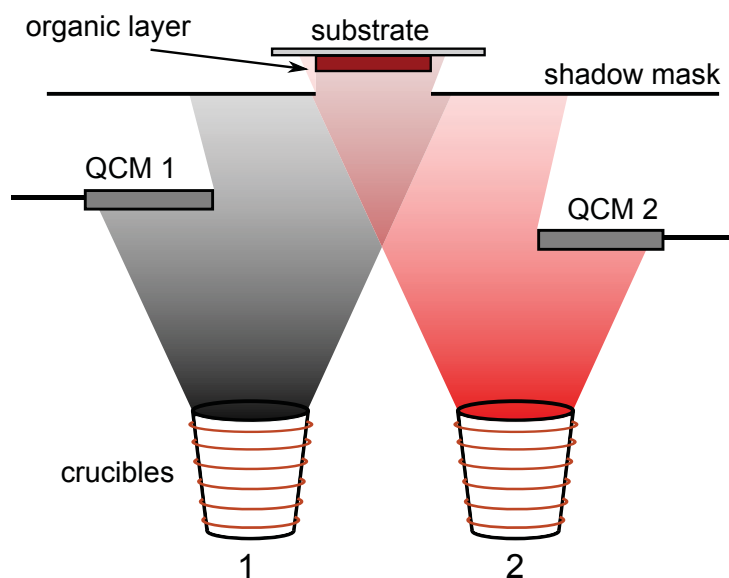


Figure 3.2: Sketch of the thermal evaporation process used at IAPP: Single quartz crystal microbalances monitor the evaporation rate for each material, enabling a precise control of the layer thickness as well as the mixing ratio in blends. This figure is adapted from reference [94].

3.2 Photoelectron Spectroscopy

This section describes the predominantly used measurement technique of this thesis, *photoelectron spectroscopy* (PES). It is based on references [54, 55, 94, 154–157]. PES directly probes the occupied electronic states at the surface of sufficiently conductive materials. Figure 3.3a sketches the working principle of photoelectron spectroscopy. Illuminating a sample with photons with an energy of E_{ph} leads to electron release from occupied electronic states of the material when the sample work function is smaller than E_{ph} .

A complex lens system collects and focuses the photoelectrons to the entrance slit of a hemispherical analyzer, measuring the kinetic energy of these photoelectrons. The lens system can be adjusted to meet specific requirements of the measurements, such as high intensity or good spatial resolution. The applied electric field and the radius of the hemispherical analyzer define the energy (pass energy E_p) at which photoelectrons can pass

the hemisphere and reach the detector. Instead of varying E_p to scan different kinetic energies, a retardation voltage can be applied to reduce different kinetic energies of photoelectrons to a fixed E_p , which ensures an equal resolution for all kinetic energies. This mode is called *Fixed Analyzer Transmission Mode*. The energetic resolution of the analyzer improves with decreasing pass energy, smaller widths of entrance and exit slits, and larger radius of the hemispherical analyzer. The resolution can be further improved by using a detector array instead of a single detector.

In order to ensure charge neutrality during the measurement, a negative sample current compensates the positive charging of the sample surface due to emission of photoelectrons. Since the conductivity of most intrinsic organic semiconductors is comparably small, the thickness of investigated organic layers is limited to a few 10 nm. PES is typically performed in ultra-high vacuum with a base pressure below 10^{-9} mbar to avoid contamination of the sample surface.

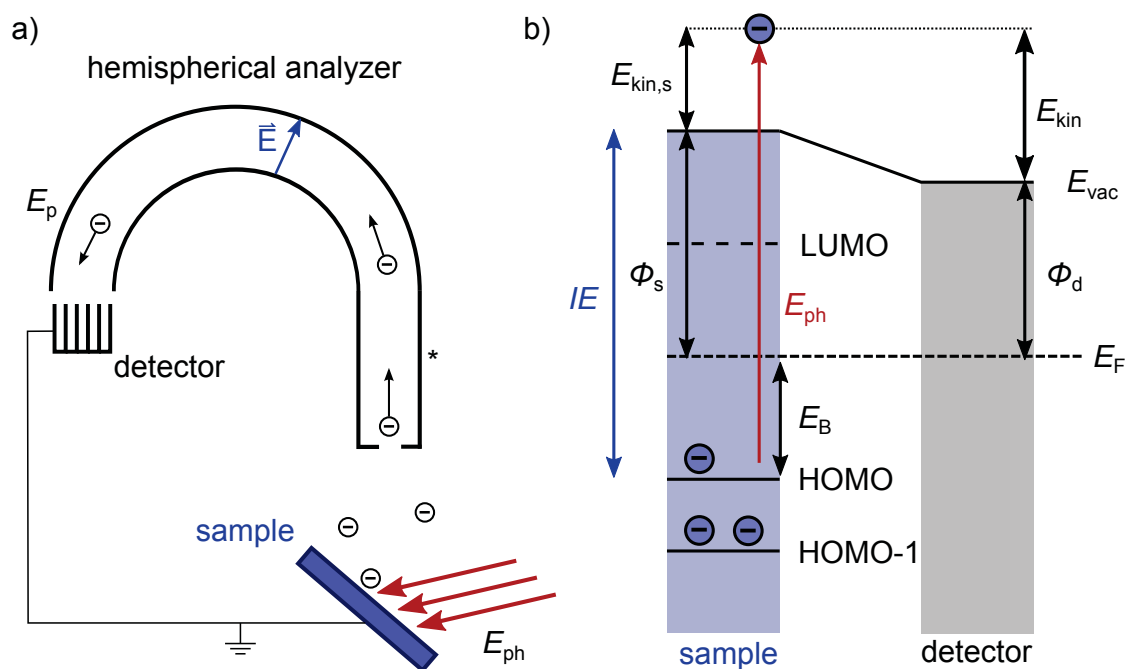


Figure 3.3: Basic principle of photoelectron spectroscopy: (a) Sketch of the geometry of sample, hemispherical analyzer, and detector within ultra-high vacuum. *For reasons of simplicity, the lens system, which defines acceptance area/angle for photoelectrons, is not shown here. (b) Energy level diagram of sample and detector.

Figure 3.3b shows the energy level diagram of sample and detector in equilibrium. An electric connection between sample and detector ensures an alignment of their Fermi levels. As noted in Section 2.1.1, the HOMO and LUMO levels obtained by PES do not belong to orbital energies of neutral molecules, but refer to the energies of holes in the HOMO and electrons in the LUMO of cations and anions in the organic thin film, respectively [54, 55]. This distinction is important because the energies of ionized molecules consider-

ably change in a solid due to polarization and relaxation effects. The (local) vacuum level (E_{vac}) is defined as the energy of an electron at rest just above the surface of the sample [54, 55]. The (local) work function (Φ_s) is defined as the difference between E_{vac} and the Fermi level (E_F). Note that E_F has a binding energy of zero by definition. A previous study on multicomponent surfaces showed that PES can not detect the local variation of Φ_s due to the large distance between sample and analyzer [158]. In that case the measurement only gives a mean value for Φ_s . The ionization energy IE (electron affinity EA) is defined as the difference between E_{vac} and the HOMO (LUMO) level.

Excitation of electrons with a binding energy of E_B (with respect to E_F) from a sample with a work function of Φ_s generates photoelectrons at the sample surface with a kinetic energy of:

$$E_{\text{kin},s} = E_{\text{ph}} - \Phi_s - E_B \quad (3.1)$$

The kinetic energy in the measured spectrum² depends on the work function of the detector (Φ_d):

$$E_{\text{kin}} = E_{\text{kin},s} + \Phi_s - \Phi_d - eV_{\text{bias}} \quad (3.2)$$

Typically, an additional bias voltage (V_{bias}) of around 10 V between sample and detector ensures that also electrons with low kinetic energy can reach the detector, particularly for the case of $\Phi_s < \Phi_d$.

Combining Equation 3.1 and 3.2 leads to:

$$E_B = E_{\text{ph}} - E_{\text{kin}} - \Phi_d - eV_{\text{bias}} \quad (3.3)$$

Φ_d can be obtained with a reference measurement of the Fermi edge of a metal sample. Consequently, the binding energy of electronic states with respect to E_F can be directly calculated from the measured kinetic energy of photoelectrons without knowing the sample work function.

PES typically probes only the first 1...10 nm of the sample surface, depending on the photon energy. The surface sensitivity originates from electron-electron scattering processes and is, therefore, directly connected to the mean free path (λ_{mfp}) of photoelectrons within the sample. λ_{mfp} depends on the kinetic energy of photoelectrons and on material parameters, such as the density. Figure 3.4 shows a typical dependence of λ_{mfp} on the kinetic energy, where a minimum is expected to occur between 50 and 100 eV for organic materials [159, 160]. According to Equation 3.1, the kinetic energy of photoelectrons within the sample depends on the photon energy and the binding energy of the electronic states

² The actual kinetic energy at the surface of the detector is smaller because photoelectrons are retarded down to the pass energy of the analyzer.

from which the electron is emitted. Due to this surface sensitivity, PES does not measure the electronic levels within the bulk but mainly those of the first monolayers of the sample. It was shown that the surface levels of organic semiconductors typically differ from the bulk levels by a few 100 meV [24, 161].

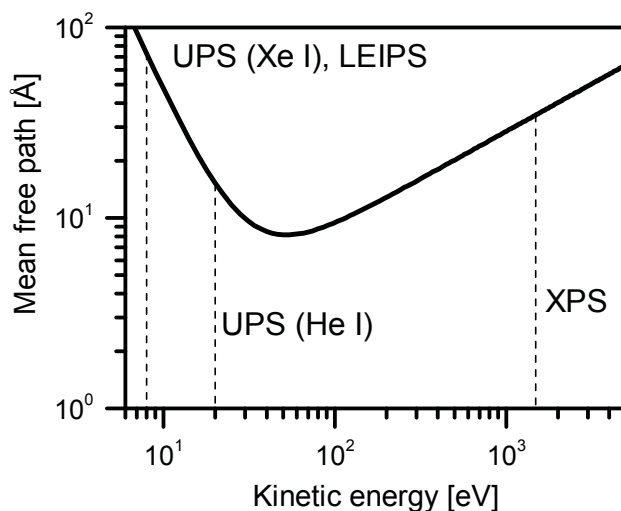


Figure 3.4: Dependence of the mean free path of electrons on kinetic energy: The underlying formula of the solid line is extracted from reference [162] and describes the qualitative dependence for organic solids.

3.2.1 Ultraviolet Photoelectron Spectroscopy

Ultraviolet photoelectron spectroscopy (UPS) is used to investigate the valence states of organic samples at low binding energies, for example providing values for the ionization energy (IE). Figure 3.5 shows a high-resolution spectrum³ of a thin ZnPc layer measured with an incident photon energy of 8.44 eV. The binding energy scale of UPS spectra is typically set to zero at the Fermi level position. In several cases of this thesis however, the vacuum level is set to zero to allow a direct comparison of IE values for different samples. The first peak below the Fermi level corresponds to photoelectrons originating from the highest occupied molecular orbital (HOMO). Therefore, the sum of the binding energy position of this peak and the sample work function is a direct measure of the ionization energy (IE) at the surface of the sample.

Krause *et al.* suggested that the HOMO peak onset rather than its maximum is a better estimation of the transport level for holes in organic semiconductors [17]. Accordingly, reported IE values mostly refer to the onset energies of UPS peaks. However, this definition is rather arbitrary as the onset value changes with the width of the UPS peak and depends on the energetic disorder of the sample as well as the experimental resolution of

³ The measurement was performed by Fabio Bussolotti at the Institute for Molecular Science in Okazaki, Japan.

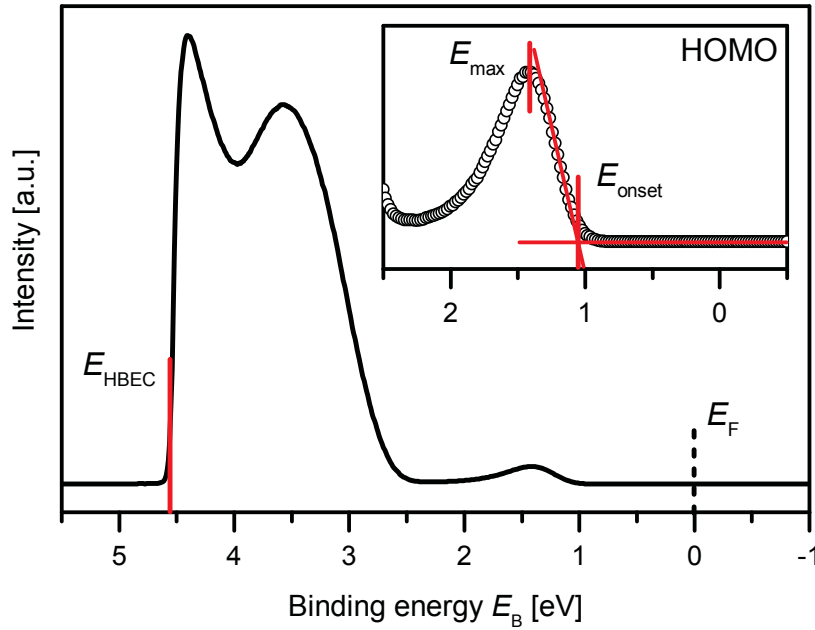


Figure 3.5: Typical highly-sensitive ultraviolet photoelectron spectrum: The spectrum shows a ZnPc layer thermally evaporated on silicon with native oxide. The measurement was performed with the UPS setup in Okazaki by Dr. Fabio Bussolotti using Xe I excitation lines ($E_{\text{ph}} = 8.44 \text{ eV}$). The inset shows a zoom into the spectrum at the HOMO emission peak.

the setup. If possible, this thesis therefore takes the maximum positions of the respective UPS peaks for comparing the electronic levels of different materials.

As seen in Figure 3.5, the underground intensity of the spectrum increases with increasing binding energy. When photoelectrons lose kinetic energy in inelastic scattering processes, they appear at higher binding energies in the spectrum. These secondary electrons can only leave the sample (and finally reach the detector), if their kinetic energy is larger or equal to the work function Φ_s of the sample. Therefore, Φ_s can be directly determined from the onset of the so-called *high binding energy cut-off* (HBEC):

$$\Phi_s = E_{\text{ph}} - E_{\text{HBEC}}. \quad (3.4)$$

UPS setup at IAPP, Dresden

Two different UPS setups are utilized in this thesis. The first setup is located at IAPP and is used for the majority of the experiments. This setup is directly connected to a ultra-high vacuum multi-chamber cluster tool, which enables transferring freshly prepared samples to the measurement chamber without exposing them to ambient conditions. The spectra are acquired at a base pressure of $1 \dots 5 \cdot 10^{-11} \text{ mbar}$ with a PHOIBOS 100 analyzer system (Specs, Berlin, Germany) exhibiting a detector containing five channeltrons (PCU 300, Specs). As photon source, He I excitation lines from a Helium discharge lamp with

an energy of 21.22 eV are used (UVS 10/35, Specs). The analyzer settings are optimized to achieve high signal-to-noise ratios⁴. The energetic resolution of the measurements is 150 meV, as obtained from the width of the Fermi edge of a gold spectrum. The reproduction of samples under equal experimental conditions gives an estimated experimental error of around 50 meV. The angle between the normal of the sample surface and the analyzer is 20°. The Fermi level positions of all spectra are calibrated to the Fermi edges of respective gold or silver substrates. Work functions are obtained from HBECs of the UPS spectra by applying a bias voltage of 8 V. Before evaporation of organic layers, the metal substrates are sputter-cleaned by Argon ions from a discharge lamp directly in the measurement chamber. A more comprehensive description of the setup can be found in references [94, 155, 156]. The exact layer stacks of all UPS samples measured at IAPP and presented in this thesis are given in Section 7.4 of the Appendix.

UPS setup at the IMS, Okazaki

Highly sensitive UPS measurements are performed by Fabio Bussolotti at the Institute for Molecular Science (IMS) in Okazaki (Japan) for sensitive investigation of electronic levels in n-doped ZnPc and C₆₀. This setup is also directly connected to the evaporation chamber where the samples are fabricated. The UPS spectra are acquired at a base pressure of $2 \cdot 10^{-10}$ mbar with an MBS-A1 analyzer system, using monochromatic Xe I excitation lines ($E_{\text{ph}} = 8.44$ eV) from a Xenon discharge lamp. The system was constructed at Chiba University [90, 163]. The energetic resolution is estimated to be around 30 meV. The Fermi level positions of the spectra are calibrated by a measurement of a clean silver sample. The work functions are obtained from the HBEC of the UPS spectra by applying a bias voltage of 5 V. The organic layers are evaporated at low rates of 0.05 Å/s at a base pressure of 10^{-9} mbar on silicon substrates covered with native oxide.

3.2.2 X-ray Photoelectron Spectroscopy

X-ray photoelectron spectroscopy (XPS) is utilized to analyze the core levels of organic materials, possessing much higher binding energies than the valence states. The main difference to UPS is the larger photon energy (1...20 keV). Core levels measurements deliver information on the chemical composition of molecules because the core levels of each atomic species have distinct binding energies. These binding energies change with the bonding partners of the respective atoms, allowing to distinguish different bonding conditions. For example, the C1s binding energy is higher for a carbon atom within a C=O bond in comparison to a C-C bond. Comprehensive databases of core level binding energies are available for a large variety of compounds. In this thesis, the database of reference

⁴ For most measurements, a pass energy of 3 eV, the *Low Angular Dispersion* lens mode, and the largest sizes for entrance and exit slits (7 x 20 mm) are used.

[164] is mostly used for the analysis of XPS spectra. To obtain relative concentrations of atomic species within a material, the measured emission intensities need to be weighted by atomic sensitivity factors (ASF), accounting for different photoemission cross sections. In this thesis, the ASFs of reference [165] are used.

The XPS measurements for this thesis are performed with the same setup as used for the UPS measurements at IAPP. Instead of UV light, Al K_{α} irradiation from a X-ray source (XR50, Specs, Berlin, Germany) with a photon energy of 1486.6 eV is used. Similar to UPS measurements, the analyzer settings are optimized to high signal-to-noise ratios⁵. The energetic resolution of the measurement is estimated to be around 0.9 eV and originates predominantly from the line width of the X-ray source of 0.85 eV [157]. The experimental error is around 0.1-0.2 eV. The spot size of the measurement area is roughly 5 mm. The angle between analyzer and sample surface is 90° (normal emission). A more comprehensive description of the setup can be found in references [94, 156, 157].

3.2.3 Inverse Photoelectron Spectroscopy

Inverse photoelectron spectroscopy (IPES) probes the unoccupied electronic states above the Fermi level in organic semiconductors and, therefore, is able to directly measure the electron affinity at the surface of organic semiconductors. An incident beam of electrons with a fixed energy fills empty electronic states, causing emission of photons. Their energy is given by the energy of the incident electrons and the binding energy of the electronic states. The binding energy of unoccupied states with respect to the Fermi level can be directly calculated from the photon energy spectrum. IPES has a cross section being orders of magnitude lower compared to UPS and therefore exhibits much lower signal-to-noise ratios than UPS.

The low-energy inverse photoelectron spectroscopy (LEIPS) setup at the Institute for Molecular Science (IMS, Okazaki, Japan) is placed in the same vacuum chamber as the high-sensitivity UPS setup. Compared to other IPES setups, the kinetic energy is reduced to below 8 eV, allowing long measurement times without sample degradation. LEIPS measurements are performed for a long time of around 12 h to ensure an improved signal-to-noise ratio. The energy resolution of the setup is 420 meV⁶. Fermi level positions of the spectra are calibrated by measuring a clean silver sample. Intensities of the spectra are normalized by the sample current during the measurement. The measurements are performed by Dr. Fabio Bussolotti. More detailed information on the LEIPS system can be found in reference [166].

⁵ For most measurements, a pass energy of 20 eV, the *Large Area* lens mode, and the largest sizes for entrance and exit slits (7 x 20 mm) are used.

⁶ Personal information from Fabio Bussolotti.

3.3 Conductivity Measurements

Electrical conductivity measurements are performed to investigate the transport properties of charge carriers in doped organic semiconductors. The measurements are conducted directly in vacuum during evaporation of the organic layers to avoid degradation of the organic layers over time and to avoid structural changes, oxygen doping, or dopant degradation due to air exposure. The conductivity is measured laterally between two gold contacts evaporated on glass as a non-conductive substrate. The sensitivity of the conductivity measurement is limited by the lowest current which can be measured by the Source Measurement Unit (SMU). This is typically between 10^{-11} and 10^{-10} A. To achieve higher sensitivities, a meander-type structure is used for the gold contacts (Figure 3.6a), enabling the measurement of conductivity values down to $1 \cdot 10^{-8}$ S/cm. A thin chrome layer (1 nm) underneath the gold contacts (40 nm) ensures a better sticking on glass substrates.

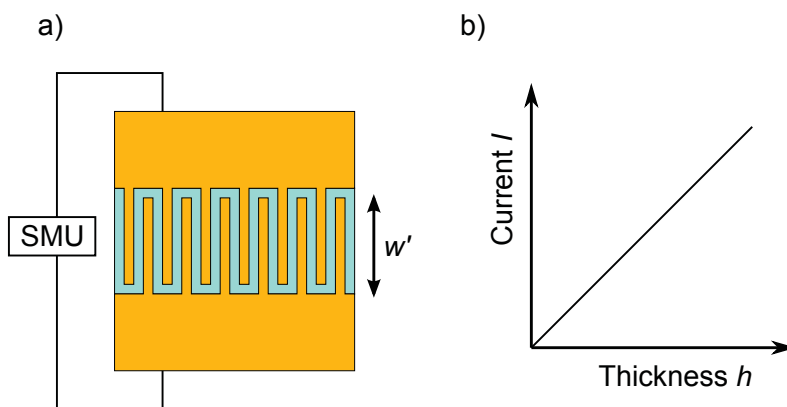


Figure 3.6: Basic principle of conductivity measurements: (a) Sketch of the top view of the gold contact structure evaporated on glass. (b) The (lateral) sample current between the two contacts increases linearly with the thickness of the organic layer when the layer growth is perfectly homogeneous. The conductivity is obtained from the slope of the linear increase.

To measure the conductivity, a voltage of 10 V is applied and the doped organic semiconductor layer (up to 20 nm) is evaporated into the channel between the gold contacts. The resistance between the gold contacts is given by the geometry of the organic channel: $R = \rho_{\text{spec}} \cdot l / (w \cdot h)$, where ρ_{spec} is the specific resistivity, l the channel length (0.5 mm), w the channel width (111 mm) and h the channel height. Note that due to the meander structure, the channel width is significantly larger than the channel length, as $w = w' \cdot n$ with n as the number of bends of the channel. The channel height is given by the thickness of the organic layer, which increases during the measurement. As the electrical conductivity σ_{el} is the inverse of ρ_{spec} , the measured current between the contacts during evaporation of the organic layer is given by:

$$I = \frac{U \cdot \sigma_{\text{el}} \cdot w}{l} \cdot h, \quad (3.5)$$

where U is the applied voltage. Ideally, the measured current increases linearly with the thickness of the evaporated layer and the conductivity can be extracted from the slope (Figure 3.6b). The advantage of this technique is that only the resistance of the organic layer is measured, as the contact resistance is expected to stay constant with layer thickness. By repetition of experiments, the experimental error is estimated to be between 10 and 20 %.

In order to measure the temperature dependence of the conductivity, a glass substrate covered by indium-tin-oxide (ITO) is mounted below the sample. An adjustable current through the ITO layer, causing resistive heating, can control the temperature of the sample. The temperature sensor is either placed between the sample and the glass/ITO or on top of the gold contact at the edge of the sample. The latter leads to systematically lower measured temperatures during heating. Therefore, the mean value of both temperature sensor positions is used for data evaluation. The conductivity measurements are mostly performed by Olka Kaveh and Daniel Schütze at IAPP.

3.4 Solar Cells

The basic findings on the impact of molecular properties on the electronic levels in thin films are tested in organic solar cells to verify the relevance for devices. The solar cells are built and characterized by Dr. Beatrice Beyer (Fraunhofer Institute for Electron Beam, Plasma Technology and COMEDD, Dresden, Germany). The devices are fabricated on glass substrates (thickness: 0.7 mm) covered with indium-tin-oxide (ITO) contacts structured by laser ablation. After cleaning the substrates with acetone and isopropanol, organic layers and aluminum are thermally evaporated in a ultra-high vacuum chamber with a base pressure of 10^{-7} mbar. The complete solar cell stack is: ITO (130 nm), BPAPF:NDP-9 (50 nm, 3 wt%), ZnPc:F₄ZnPc:C₆₀ (38 nm), C₆₀ (20 nm), C₆₀:NDN-26 (15 nm, 4 wt%), Al (200 nm). The proprietary materials NDP-9 and NDN-26 are purchased from Novaled GmbH (Dresden, Germany). The size of the active area is 0.15 cm². After deposition of the solar cells, the substrates are encapsulated under nitrogen atmosphere with a cavity glass.

The current density vs. voltage (j - V) characteristics are recorded using a source measurement unit including a digital multimeter (Keithley 2000 DMM), a Kepco power supply, and a silicon reference solar cell. A metal halide lamp is used to simulate the solar spectrum for global irradiation (AM 1.5). The illumination intensity and the temperature are kept constant at 100 mW/cm² and 25 °C, respectively. An additional mask ensures a defined illumination area of 0.12 cm². Further information on the fabrication and characterization of the devices can be found in references [167–169].

3.5 Density Functional Theory

Density functional theory (DFT) is a quantum mechanical modeling method utilized to investigate the electronic structure of many-electron systems, such as the organic molecules investigated in this thesis. In a first step, the spatially dependent electron density of the ground state is approximated by using so-called Kohn-Sham functions. On the basis of this electron density, different properties of the system can be calculated, such as the total energy, the quadrupole moment, or the reorganization energy. The modeling is performed by Dr. Reinhard Scholz (IAPP) as well as Karl Sebastian Schellhammer and Dr. Christopher Gaul (Dr. Frank Ortmann's group, Institute for Material Science, Dresden, Germany).

The gas-phase ionization energy (IE_0), gas-phase electron affinity (EA_0), quadrupole moment (QPM), and molecular relaxation energy ($\lambda_{+,-}$) are calculated by using the M06-2x exchange-correlation functional [170] and the correlation-consistent basis set cc-pVTZ [171] as implemented in the computational chemistry package NWChem [172]. IE_0 is determined as the difference between the total energies of the positively charged molecule and the neutral molecule both being in the relaxed geometry of the neutral molecule. Accordingly, EA_0 is determined as the difference between the total energies of the negatively charged molecule and the neutral molecule. Both values, IE_0 and EA_0 , are defined positively in this thesis. The relaxation energy of the cation after charging (λ_+) is determined as the difference between the total energies of the cation in its optimized geometry and the cation in the optimized geometry of the neutral molecule. Accordingly, the relaxation energy of the anion (λ_-) is determined as the difference between the total energies of the anion in its geometric ground state and the anion in the geometric ground state of the neutral molecule. All calculated values are listed in Table 7.3 of the Appendix.

A complete charge transfer of one electron from donor to acceptor is assumed for the calculation of Coulomb binding energies between the ions in charge transfer (CT) states as well as in integer charge transfer complexes (ICTC). First, the dimer geometries, i.e. of donor cation and acceptor anion, are optimized with dispersion-corrected DFT to find the minimum in total energy. In these model geometries, a Mullikan charge is assigned to each atom of the oppositely charged ions. The Coulomb binding energy ($E_{\text{coul,CT}}$ or $E_{\text{coul,ICTC}}$) is then obtained from the Mullikan charge distribution. This computationally simple approach leads to similar results like more advanced approaches, such as constrained DFT calculations and Hartree-Fock-based configuration interaction of singles (CIS) [173]. Coulomb interactions are screened by the inverse of the dielectric constant (ϵ_r) to obtain values for the solid state. The ϵ_r value of the matrix is used for ICTCs and the mean between the values of donor and acceptor is used for CT states. It is assumed that $\epsilon_r = 3$ for all non-fullerene matrix molecules and $\epsilon_r = 4.4$ for C_{60} [173]. The values for the Coulomb binding energies in vacuum are listed in Table 7.4 of the Appendix.

4. Impact of Quadrupole Moments on Thin Film Energy Levels

The working mechanism of most organic electronic devices depends essentially on an optimized energy level alignment of different organic semiconductors, consisting of weakly bonded organic molecules. The transport energies of the rather localized charge carriers, i.e. holes and electrons, are associated to the ionization energy (IE) and the electron affinity (EA) of the organic semiconductors, respectively [16, 17]. The IE and EA of molecules in organic films are not universal, but depend on film morphology and composition [20–22]. Furthermore, previous studies showed that charge-quadrupole interactions can induce large electrostatic shifts of the electronic levels in crystalline films [27–30].

In this chapter, the influence of the molecular quadrupole moment (QPM) on the energy levels at the surface of thin solid films is investigated using ultraviolet photoelectron spectroscopy (UPS). Section 4.1 summarizes the special properties of the model system comprising ZnPc and its fluorinated derivatives, serving as a basis for all studies in this chapter. In Section 4.2, the dependence of surface energy levels on molecular orientation is investigated for a variety of crystalline films of planar molecules and correlated with molecular QPMs obtained from density functional theory (DFT) simulations. In Section 4.3, the impact of the mixing ratio of two molecules with different QPMs on the energy levels is analyzed for intermixed blends and for blends exhibiting phase separation. The findings of the first sections are used to demonstrate in Section 4.4 how an adjustment of QPMs can optimize device parameters in organic solar cells, such as the open-circuit voltage or the short-circuit current. Most of the experimental and simulation results of this chapter as well as their discussion are included in references [168, 174].

4.1 Model System of $F_n\text{ZnPc}$

Phthalocyanines belong to the most investigated small organic molecules due to their good absorption and transport properties. In particular, the system zinc phthalocyanine (ZnPc) with C_{60} was intensively used in the past as a model donor-acceptor system in organic solar cells at IAPP [175–180]. Furthermore, ZnPc was utilized as a model matrix material for basic investigations on molecular p- and n-doping [42, 84, 181]. By substituting hydrogen with fluorine atoms, it becomes possible to stepwise increase the ionization energy [57, 182] and alter the molecular quadrupole moment (QPM). In addition, the availability of studies about structural properties [182–186] makes ZnPc and its fluorinated derivatives an ideal model system to investigate the impact of QPMs on the energy levels of thin molecular films. Apart from the changes of the energy levels and the QPMs, other properties such as structural or optical characteristics remain similar for all derivatives [57, 182].

Figure 4.1a shows the structural formulas of the five ZnPc derivatives used in this thesis. Stepwise fluorination of the side groups results in a gradual increase of the gas-phase ionization energy (IE_0), as calculated by density functional theory (DFT) simulations¹ (see Figure 4.1b). Furthermore, the fluorine atoms pull negative charge density to the edges of the planar molecules, altering the charge distribution on the molecules. The variation of charge distribution leads to significant changes to the respective quadrupole tensors of the molecules. The quadrupole tensors obtained from DFT simulations are transformed into diagonalized tensors with their traces equal to zero to obtain the molecular quadrupole moments. Apart from some isomers of $F_4\text{ZnPc}$ ² (see Section 7.2.1 for all structural formulas), the quadrupole tensors of the symmetric ZnPc derivatives consist of two equal components parallel to the molecular plane ($Q_1 = Q_2$) and one component perpendicular to the molecular plane (Q_π), with $Q_\pi = -2 \cdot Q_1$. As shown in Figure 4.1c, Q_π increases gradually with the amount of fluorination and changes its sign. Apart from the number of fluorine atoms, also their positions determine the magnitudes of Q_π and IE_0 , as observed for $F_4\text{ZnPc}$ and $F_4\text{-ZnPc}$. Except some isomers of $F_4\text{ZnPc}$, the dipole moment of all ZnPc derivatives is zero and the impact of interactions of charges with permanent molecular dipole moments on the energy levels of ZnPc derivatives can be excluded for this class of molecules.

¹ Values for IE_0 and QPMs were calculated by Dr. Christopher Gaul and Karl Sebastian Schellhammer in the group of Dr. Frank Ortmann at TU Dresden. The obtained values are included in reference [174].

² Note that $F_4\text{ZnPc}$ is sometimes named ZnF_4Pc in other publications [169, 187].

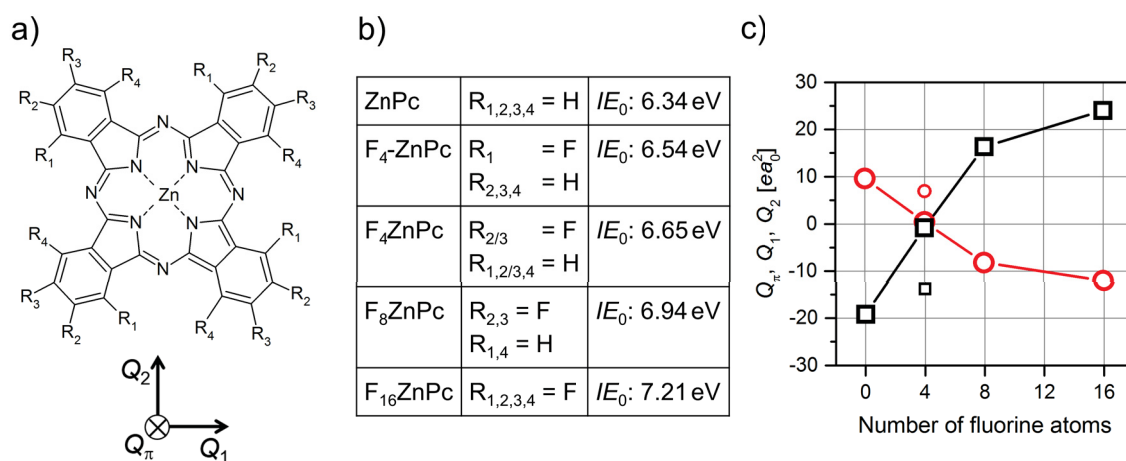


Figure 4.1: Molecular properties of the model system $F_n\text{ZnPc}$: (a) Structural formulas of ZnPc and its fluorinated derivatives. (b) Compilation of the fluorine atom positions of all $F_n\text{ZnPc}$ derivatives. $F_4\text{ZnPc}$ consists of different isomers with the fluorine atom being either at position R_2 or R_3 . The chemical structures of all $F_4\text{ZnPc}$ isomers can be found in Section 7.2.1. $|E_0|$ denotes the gas phase ionization energy of single molecules, as calculated by density functional theory. (c) In-plane (Q_1 and Q_2 , red circles) and out-of-plane (Q_π , black squares) quadrupole components considerably change with the degree of fluorination. Small symbols depict the values for $F_4\text{-ZnPc}$.

4.2 Energy Level Dependence on Molecular Orientation

The molecular orientation plays an essential role for the energetics at surfaces and interfaces of organic thin films [21, 27, 188]. Underlying electrostatic interactions can lead to large energy shifts with varying orientation and can induce driving forces for charge separation at specific organic interfaces [26, 31, 64]. In this section, the dependence of surface energy levels of crystalline films on the molecular orientation is directly connected to the molecular quadrupole moment, in particular the tensor component perpendicular to the molecular plane. For this purpose, the model system of $F_n\text{ZnPc}$ with its tunable quadrupole moments is used as a basis for the investigations.

Schünemann *et al.* showed for ZnPc that the molecular orientation depends on the substrate on which the film is grown on [184, 185]. In particular, weakly interacting substrates such as glass, indium tin oxide, amorphous organic films (BPAPF or BF-DPB), or polycrystalline C_{60} induced an edge-on orientation of ZnPc with a mean angle of 90° between molecular plane and substrate plane. Brendel *et al.* also observed edge-on orientation of fluorinated ZnPc derivatives on weakly interacting substrates [182]. Only $F_{16}\text{ZnPc}$ showed a film structure with the occurrence of two phases. On the other hand, gold and silver substrates resulted in a more face-on orientation of ZnPc with a composition of different orientations and crystal structures [184, 185]. For gold, a mean angle of 36° with respect to the substrate was determined.

The impact of molecular orientation on energy levels is now investigated for thin layers (20 nm) of ZnPc and its fluorinated derivatives, each thermally evaporated on dif-

ferent types of substrates and analyzed by ultraviolet photoelectron spectroscopy (UPS). For edge-on oriented films, silver substrates covered by p-doped BPAPF (5 nm, 2 wt%, p-dopant: NDP-9) were used as substrates. To favor face-on orientation, the layers were directly evaporated on gold substrates. Figure 4.2 exemplarily shows the spectra of ZnPc and F_8 ZnPc, each evaporated on both types of substrates. As expected from the larger gas-phase ionization energy (IE_0) of F_8 ZnPc (6.94 eV compared to 6.34 eV for ZnPc), the F_8 ZnPc films have a higher ionization energy (IE) compared to the ZnPc films. However, the dependence of IE on the substrate differs for both derivatives. While the IE of ZnPc is smaller by 0.22 eV for edge-on orientation, it is larger by 0.37 eV for F_8 ZnPc films exhibiting edge-on orientation. As shown in Figure 4.2, the electrostatic correction of holes ($\Delta_+ = IE - IE_0$) is similar for ZnPc and F_8 ZnPc films in face-on orientation. On the contrary, the films in edge-on orientation exhibit a large difference in Δ_+ . It is shown in the following section that the difference in Δ_+ between ZnPc and F_8 ZnPc originates from their different QPMs.

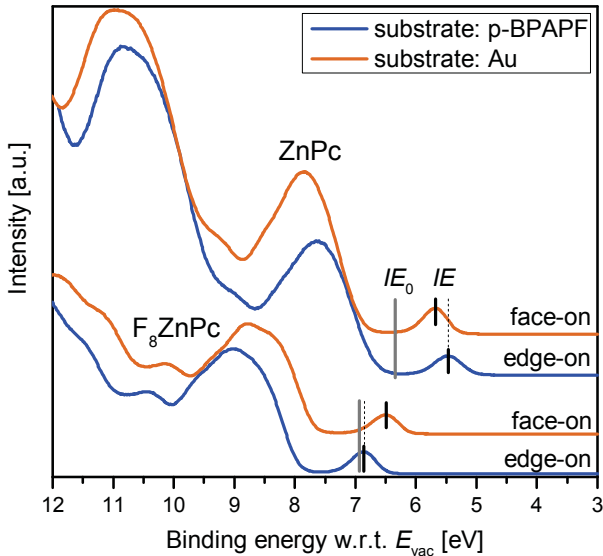


Figure 4.2: Ultraviolet photoelectron spectra of ZnPc and F_8 ZnPc at different molecular orientations: While p-doped BPAPF ensures edge-on orientation, Au substrates cause a more face-on orientation. The gray lines denote the ionization energies of single molecules in the gas phase (IE_0), calculated by density functional theory. An adapted form of this figure is included in reference [174].

4.2.1 Connection to the Quadrupole Component Q_π

The impact of molecular orientation and quadrupole moments on electrostatic interactions in the films is now discussed in a simplified sketch to understand the behavior of ZnPc and F_8 ZnPc on different substrates. As discussed in Section 2.1.2, the electrostatic correction for holes (Δ_+) consists of a polarization part (P_+) and a contribution which accounts for the interaction with permanent charge distributions in the surrounding (Δ_{perm}). The latter is dominated by charge-quadrupole interactions in many crystalline films because molecules with large permanent dipole moments often stack alternately, canceling the dipole contribution [27, 28]. This holds particularly true for the

symmetric ZnPc derivatives whose dipole moments are zero (see Section 7.2.1 for their structural formulas).

The charge-quadrupole interaction energy (Δ_{q-Q}) of an excess charge q with surrounding quadrupole moments \mathbf{Q} at distances \vec{r}_i is given by:

$$\Delta_{q-Q} = \frac{q}{4\pi\epsilon_0\epsilon_r} \sum_i \left[\frac{1}{2} \frac{\vec{r}_i \cdot \mathbf{Q} \cdot \vec{r}_i}{r_i^5} \right], \quad (4.1)$$

where i sums over all molecules in the surrounding. Note that the approximation of the charge distribution by quadrupole moments and the assumption of point charges become invalid particularly at short distances in the range of molecular dimensions. Furthermore, Poelking *et al.* recently presented a case where an integration over the whole thin film geometry is necessary to correctly determine the thin film energy levels [27]. Nevertheless, all experimental results discussed in this chapter can qualitatively be explained within a short-range scheme, where interactions with nearby molecules predominantly contribute to the electrostatic shifts.

Figure 4.3a and 4.3b sketch the geometries of F_n ZnPc films in edge-on and face-on orientation, respectively. Like most other planar molecules, ZnPc molecules typically arrange in a π - π -stacking geometry, where the intermolecular distance along the π - π -stacking direction (ca. 4 Å) is significantly smaller compared to the other two directions (ca. 13 Å) [183, 184]. For the fluorinated derivatives, the latter value increases slightly with degree of fluorination up to 14.5 Å for F_{16} ZnPc. As Δ_{q-Q} decreases strongly with distance, the component of the quadrupole tensor pointing along π - π -stacking direction (Q_π) might be the dominating one among all tensor components (see Equation 4.1).

Figure 4.3c shows that Δ_+ linearly increases with Q_π from ZnPc to F_{16} ZnPc for both types of molecular orientations³, in good agreement with the above considerations. However, the slope of the increase is reduced by a factor of around 4 for the films in face-on orientation. This can be partly explained by the fact that UPS probes predominantly the molecules at the thin film surface (see red circles in Figure 4.3a and 4.3b). While for edge-on orientation, surface molecules of a perfectly smooth film have two direct neighbors along the π - π -stack, they have only one neighbor for face-on orientated films, which should reduce Δ_{q-Q} by a factor of 2. This should even be the case when the molecules are slightly tilted, as it is expected for ZnPc films. The observation that the slope for face-on orientated films is even reduced by factor of 4 compared to edge-on orientation can have several reasons. For example, neglecting in-plane quadrupole components Q_1 and Q_2 as a contribution to Δ_{q-Q} might be erroneous specifically for face-on orientation, where the excess charge can interact with such components in four spatial directions. Another possible effect that would reduce the slope for both orientations is a reduction of

³ The UPS measurement for F_4 -ZnPc in edge-on orientation was performed by Katrin Ortstein at IAPP. The IE values for the F_4 -ZnPc and the F_{16} ZnPc film in face-on orientation are taken from references [178] and [189], respectively.

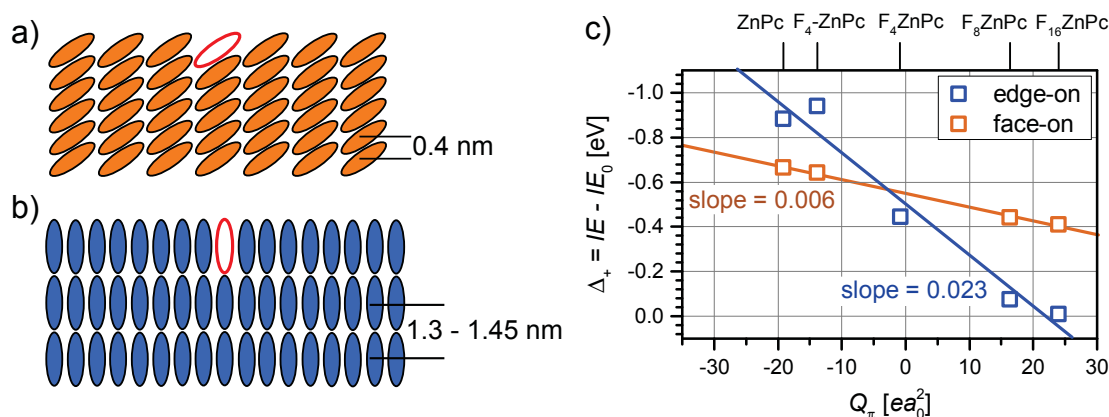


Figure 4.3: Dominant role of the quadrupole component Q_π for thin film energy levels: Sketch of two thin films of $F_n\text{ZnPc}$ molecules in face-on (a) or edge-on (b) orientation. The intermolecular distances are extracted from references [182, 183]. Note that the face-on film might be a composition of different polymorphs where the orientation of molecules with respect to the substrate is not equal. Part (a) of this figure sketches one possible film structure for face-on orientation. The red circles denote surface molecules typically probed by UPS. (c) IE_0 and Q_π denote calculated values for the gas phase ionization energy and the quadrupole moment, respectively. IE denotes the thin film ionization energy, as measured by UPS. The slopes are extracted from linear fits. This figure is partly included in reference [174].

the polarization energy P_+ from ZnPc to $F_{16}\text{ZnPc}$ ⁴. Indeed, a previous study on the similar system of fluorinated CuPc revealed that the transport gap reduces with the degree of fluorination [57]. This suggests that P_+ also varies between the $F_n\text{ZnPc}$ derivatives.

Film Thickness Dependence of Energy Levels

The IE of $F_n\text{ZnPc}$ is now investigated at very small coverages below the monolayer thickness to verify that charge-quadrupole interactions along the π - π -stacking direction dominate the variation of Δ_+ among the ZnPc derivatives. IE values for different thicknesses of $F_n\text{ZnPc}$ films in edge-on orientation were obtained from UPS measurements⁵ on films stepwise deposited on p-doped BPAPF. Figure 4.4a shows several representative UPS spectra of ZnPc films at different thicknesses. The respective ZnPc content of the UPS spectra is obtained by subtracting the substrate spectrum from the superimposed spectra. The IE values of $F_n\text{ZnPc}$ films presented in 4.4b are obtained from the HOMO peak positions of the respective difference spectra. As a result, the IE of ZnPc changes considerably with film thickness. First, it decreases by 400 meV from very low coverages to a layer thickness of 30 Å and then increases by 100 meV when the thickness is further increased to 200 Å.

The change of IE with thickness can be explained by the evolving structure during film deposition. At very small coverages, many possible scenarios of the “film” structure can

⁴ Note that P_+ is always negative as IE is defined positive in this thesis.

⁵ The measurements were partly performed by Katrin Ortstein at IAPP.

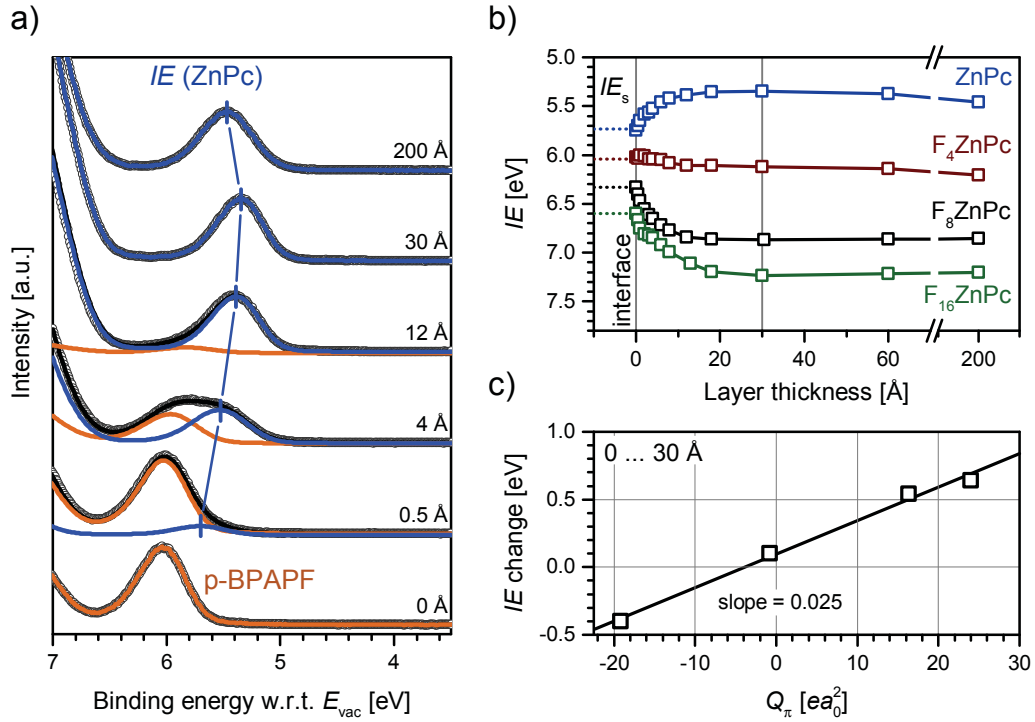


Figure 4.4: Development of IE with layer thickness for F_n ZnPc films: (a) UPS spectra of ZnPc stepwise deposited onto p-doped BPAPF. The contribution of ZnPc to each spectrum (blue line) is obtained by subtracting the substrate spectrum from the superimposed spectra. (b) Thickness-dependent IE of F_n ZnPc on p-BPAPF obtained from the HOMO peak positions in difference spectra. IE_s is the extrapolated ionization energy of F_n ZnPc at 0 Å. (c) Difference between IE at 30 Å and IE_s scales with Q_π . The slope is obtained from a linear fit. The figure is included in reference [174].

explain the Δ_+ value, differing from the thick edge-on oriented films presented in Figure 4.3. The existence of only single ZnPc molecules or small islands on the (rough) surface of the BPAPF film effectively reduces the number of neighboring ZnPc molecules compared to thick crystalline ZnPc films. This directly reduces charge-quadrupole interactions along the π - π -stacking direction of ZnPc molecules and results in a lower absolute value of the charge-quadrupole interaction energy Δ_{q-Q} . Furthermore, a different molecular orientation at small coverages [190], would also reduce $|\Delta_{q-Q}|$. Therefore, it is assumed that the extrapolated IE value at 0 Å, which is denoted as IE_s , corresponds to molecules with a Δ_{q-Q} close to zero⁶. In good agreement, IE_s is equally reduced by 0.6 eV compared to IE_0 for all ZnPc derivatives, indicating a similar polarization energy P_+ at such small coverages.

The IE of ZnPc (F_8 ZnPc, F_{16} ZnPc) decreases (increases) with evolving layer thickness until a layer thickness of 30 Å, which can be explained by the formation of the first ordered monolayer in edge-on orientation. The monolayer thicknesses were previously obtained by X-ray diffraction measurements to vary between 13 Å and 14.5 Å [182]. The formation

⁶ A contribution of BPAPF to Δ_{q-Q} is neglected due to its small Q_π value and its amorphous film structure.

of the first monolayer in edge-on orientation leads to a change of Δ_{q-Q} , depending on the magnitude of the respective quadrupole moment. In good agreement, the shift of IE until 30 Å scales linearly as a function of Q_π with the slope being very similar to the observation in Figure 4.3c. A further increase of the layer thickness from 30 to 200 Å changes the IE slightly, which might be due to an increased interaction with other quadrupole components than Q_π , a change of polarization (P_+), or an increased film roughness with film thickness [183]. However, these changes are comparatively small and it can be concluded that the variation of Δ_+ between the F_n ZnPc films in Figure 4.3c originate primarily from different charge-quadrupole interactions along the π - π -stacking direction.

4.2.2 Extension to other Systems

A dependence of IE on molecular orientation is not restricted to the model system F_n ZnPc, but was observed before for several other systems [21, 94, 188, 191]. Table 4.1 summarizes for several compounds the IE values of films in edge-on and face-on orientation obtained by UPS as well as the respective Q_π value obtained from DFT simulations. As shown in Figure 4.5, the difference between both IE values scales linearly with Q_π for a broad variety of materials. The slope of $0.022 \text{ eV}/ea_0^2$ is only slightly larger than the slope observed for fluorinated ZnPc derivatives ($0.017 \text{ eV}/ea_0^2$, Figure 4.3c). Note that some of the investigated molecules do not have such a high degree of symmetry as F_n ZnPc with $Q_1 = Q_2$, such as 6T, DH6T, DIP, or pentacene. The fact that the observed correlation also holds true for such molecules suggests that the magnitude of Q_π controls the orientation dependence of IE for a large variety of planar molecules forming crystalline films.

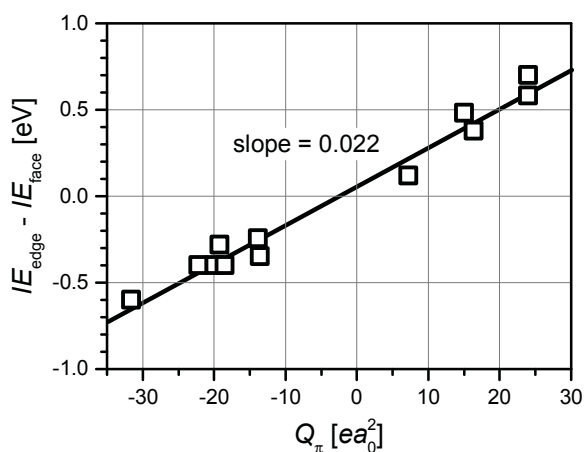


Figure 4.5: Orientation dependence of IE correlates with Q_π : The difference in IE between edge-on and face-on orientated films scales with the respective Q_π value for several small planar molecules. The underlying values of this graph are summarized in Table 4.1. The slope is obtained from a linear fit to the data. This figure is included in reference [174].

Table 4.1: Ionization energies of thin films with face-on and edge-on molecular orientation, as obtained from the low binding energy onset of the HOMO peaks in UPS spectra. DFT values for Q_π were calculated by Dr. Christopher Gaul and Karl Sebastian Schellhammer in the group of Dr. Frank Ortman at TU Dresden. The values are included in reference [174].

| Material | $Q_\pi [ea_0^2]$ | $IE_{\text{face}} [\text{eV}]$ | $IE_{\text{edge}} [\text{eV}]$ |
|-----------------------|------------------|--------------------------------|--------------------------------|
| 6T | -22.2 | 5.4 [21] | 5.0 [21] |
| CuPc | -19.9 | 5.2 [188] | 4.8 [188] |
| DH6T | -31.6 | 5.3 [21] | 4.7 [21] |
| DIP | -18.5 | 5.60 [191] | 5.20 [191] |
| F ₄ -ZnPc | -13.9 | 5.46 [178] | 5.22 ¹ |
| F ₈ ZnPc | 16.3 | 6.10 | 6.48 |
| F ₁₆ CuPc | 24.0 | 5.9 [188] | 6.6 [188] |
| F ₁₆ ZnPc | 24.0 | 6.3 [189] | 6.78 |
| HATNA-F ₆ | 7.3 | 7.72 [192] | 7.84 ¹ |
| HATNA-F ₁₂ | 15.1 | 7.73 [192] | 8.21 ¹ |
| Pentacene | -13.6 | 5.25 [90, 193] | 4.90 [90] |
| ZnPc | -19.2 | 5.30 | 5.02 |

¹Acquired by Katrin Ortstein at IAPP

Conclusion

The results of this section showed that charge-quadrupole interactions along the π - π -stacking direction of planar molecules induce large energy level shifts in crystalline films. These electrostatic interactions can explain the dependence of the ionization energy on molecular orientation observed at the film surface of a variety of planar molecules. This energy dependence on quadrupole moments and on molecular orientation is particularly relevant for understanding and predicting the energy level alignment at the interface between different organic layers. In the next section, the impact of charge-quadrupole interactions on the energy levels in blends are investigated.

4.3 Impact of Mixing Ratio on Blend Energy Levels

Blends of different organic molecules play an important role for the photoactive or emissive areas as well as for molecularly doped transport layers in organic optoelectronic devices [7, 34, 143, 144]. For example in organic solar cells, an optimization of the energy level alignment between donor and acceptor of the bulk-heterojunction is crucial to obtain high device efficiencies. This optimization is often done by using the energies obtained for intrinsic layers of donor and acceptor, which however can lead to large errors because the energies of blends can substantially differ from neat layers [22, 179]. In this section, the impact of quadrupole moments on the energy levels in blends of different molecules is investigated. The section is divided in a discussion of blends comprising structurally similar molecules, intermixing on a molecular scale, and blends of sterically incompatible molecules, forming separated phases. Section 4.3.1 discusses the first case on the basis of blends of different fluorinated ZnPc derivatives, allowing for a continuous tuning of energy levels with their mixing ratio. In Section 4.3.2, the case of phase separated blends is studied by comparing ZnPc:C₆₀ and F₈ZnPc:C₆₀ blends.

4.3.1 Intermixed Blends

Salzmann *et al.* revealed large ionization energy (*IE*) changes with varying mixing ratio in blends of pentacene and perfluoropentacene [194]. The observed changes were, however, not uniform and did not allow for a precise tuning of *IE* with mixing ratio. This observation was explained by an undesired phase separation within the blended films, originating from the formation of a new co-crystal phase with a different molecular orientation [194]. On the other hand, phthalocyanines were shown to be suitable components for blends with fine scale intermixing, as they are structural compatible due to their flat molecule structure [195–197]. Therefore, the model system F_nZnPc seems to be ideal for studying the impact of quadrupole moments (QPM) on the energy levels in such blends. The energy levels in blends of molecules with edge-on orientation are investigated in this section because they should exhibit a larger influence of charge-quadrupole interactions. For that purpose, the blends were built under equal preparation conditions as used for the pure edge-on oriented films investigated in Section 4.2.

Figure 4.6a-c shows the UPS spectra of different ZnPc:F_nZnPc (*n* = 4, 8, 16) blend layers with varying mixing ratios. The spectra reveal monotonous shifts of the HOMO emission peaks to higher binding energies with increasing F_nZnPc content, corresponding to increasing *IE* values. To obtain the respective energy levels of ZnPc and F_nZnPc in the blends, the spectra are fitted by two Gaussian functions after subtracting a Shirley background [198]. The intensity ratio of the two Gaussian functions is set equal to the molar ratio of ZnPc and F_nZnPc in the blends, as obtained from the intensity ratio of fluorine and zinc emission peaks in X-ray photoelectron spectra.

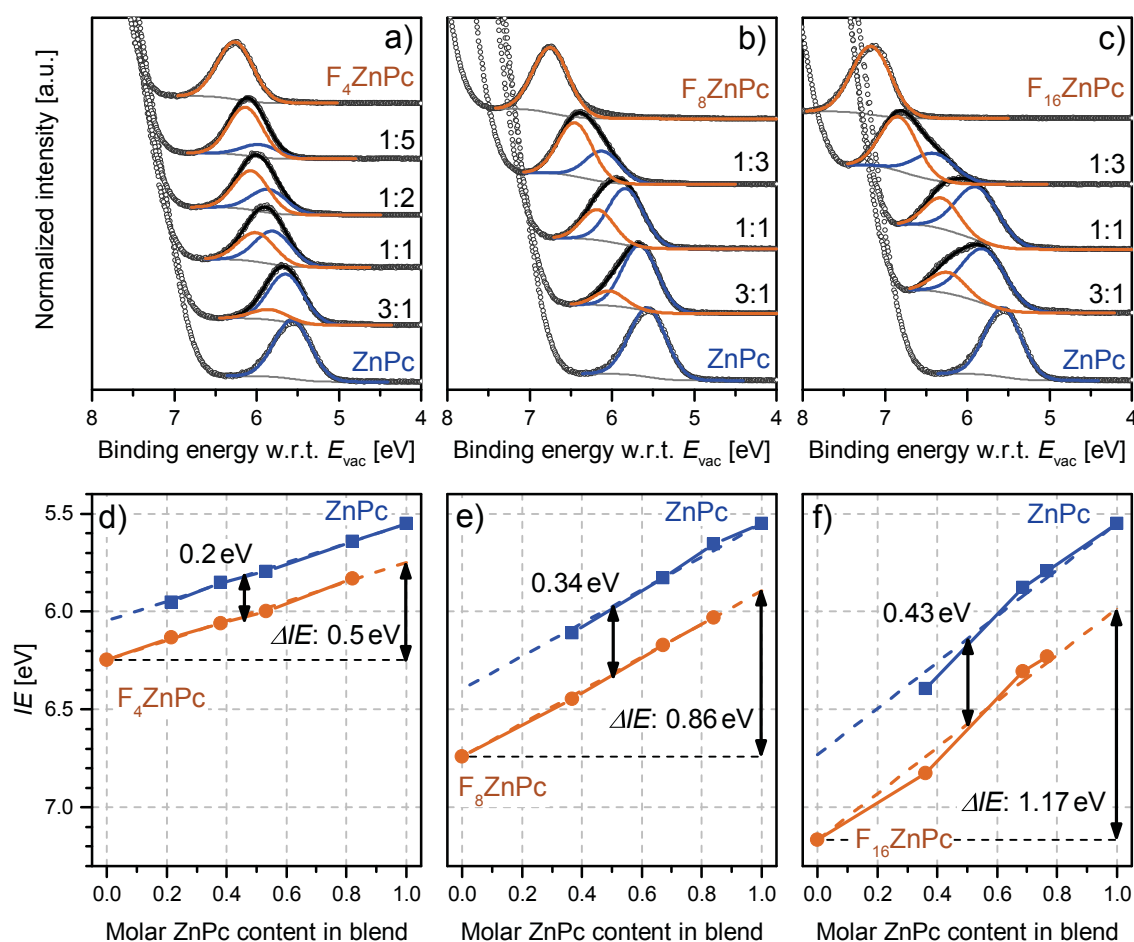


Figure 4.6: Continuous energy level of F_n ZnPc blends: (a-c) HOMO regions of UPS spectra of ZnPc: F_n ZnPc blend layers (20 nm) evaporated on silver substrates covered by p-doped BPAPF. After subtracting a Shirley background, the emission peaks are fitted by two Gaussian functions whose intensity ratio is given by the relative molar content of ZnPc and F_n ZnPc, as extracted from XPS measurements. The given ratios on the right of each spectrum are weight ratios, as obtained from quartz crystal monitors during evaporation. (d-e) The IE of ZnPc and F_n ZnPc in the blends are extracted from the peak positions of the Gaussian fits. Dashed lines are linear fits with the slopes kept equal for ZnPc and F_n ZnPc. This figure is an adapted version of Figure 2 published in reference [168].

The variation of IE with mixing ratio in ZnPc: F_n ZnPc blends, as extracted from the Gaussian fits, is shown in Figure 4.6d-e. Remarkably, the IE of ZnPc and F_n ZnPc both increase (decrease) linearly with increasing content of F_n ZnPc (ZnPc) with their energy difference being constant. Only for ZnPc: F_{16} ZnPc blends, the change of IE is not as uniform as observed for the other material combinations. A phase separation between ZnPc: F_{16} ZnPc co-crystals and pure phases of the excess compound, as observed for blends of pentacene and perfluorinated pentacene [194], might explain this behavior.

The continuous change of IE with mixing ratio can be explained by a varying (mean) charge-quadrupole interaction energy Δ_{q-Q} , changing with the mixing ratio of two molecules exhibiting different quadrupole components Q_π . In a long-range picture, the excess

charge interacts with a mean quadrupole field and Δ_{q-Q} continuously changes with the mixing ratio. The continuous shift in the spectra can also be understood when only short-range charge-quadrupole interactions are considered. In such a short-range scheme, the Δ_{q-Q} value of a distinct site depends on the Q_π of neighboring molecules within a short range. The integrated signal of all sites at a sample surface should exhibit a discrete distribution of Δ_{q-Q} values, which changes with mixing ratio. However, due to spatial and energetic disorder as well as experimental broadening, both scenarios would lead to the same Gaussian spectra in experiment. Accordingly, it is not possible to obtain from the experimental data the relevant range of charge-quadrupole interactions dominating Δ_{q-Q} .

If the (mean) interaction energy Δ_{q-Q} and the polarization energy P_+ are equal for both components of the ZnPc:F_nZnPc blends, the energy difference of their *IE* should be equal to the difference of their gas-phase ionization energy (IE_0). However, the differences in IE_0 are 0.31, 0.60, and 0.87 eV, respectively, and therefore considerably larger than the *IE* differences in the intermixed blends (see Figure 4.6). A possible explanation is that the magnitude of P_+ for the fluorinated derivatives is larger. This consideration is supported by the observations made on a similar material system, F_nCuPc. In that case, the difference between *IE* and *EA* reduced from CuPc to F₁₆CuPc by 400 meV [57], indicating larger magnitudes of P_+ and P_- for F₁₆CuPc.

The *IE* in blends of ZnPc with F₄ZnPc, F₈ZnPc, or F₁₆ZnPc can be continuously tuned with the mixing ratio over a tuning range (ΔIE) of 0.5 eV, 0.86 eV, or 1.17 eV, respectively. As shown in Figure 4.7, the magnitude of ΔIE directly scales with the difference between the Q_π values of both compounds, which also holds true when two fluorinated ZnPc derivatives are mixed (F₄ZnPc:F₁₆ZnPc blends depicted as red square in Figure 4.7). The slope of this dependence ($0.027 \text{ eV}/ea_0^2$) is only slightly higher compared to the observed slope of $0.023 \text{ eV}/ea_0^2$ extracted for the dependence of Δ_+ on Q_π in neat films (see Figure 4.3). The higher slope can be explained by a change of polarization and is in line with the observation that the *IE* difference in blends is reduced compared to the IE_0 difference between single molecules.

To check if these results can be applied to other material combinations, UPS experiments were performed on SubPc:Cl₆SubPc and HATNA-F₆:HATNA-F₁₂ blends⁷ with varying mixing ratios and prepared under equal conditions as used for F_nZnPc blends. These two systems show a tuning of *IE* with mixing ratio being less pronounced compared to F_nZnPc blends. This can partly be explained by the smaller difference in Q_π for these material combinations. Nevertheless, their tuning ranges slightly deviate from the trend observed for F_nZnPc blends (Figure 4.7), indicating weaker charge quadrupole interactions between the molecules of the different blend components. This deviation might have structural reasons, such as phase separation, other molecular orientations than edge-on,

⁷ Part of the UPS experiments were performed by Katrin Ortstein at IAPP.

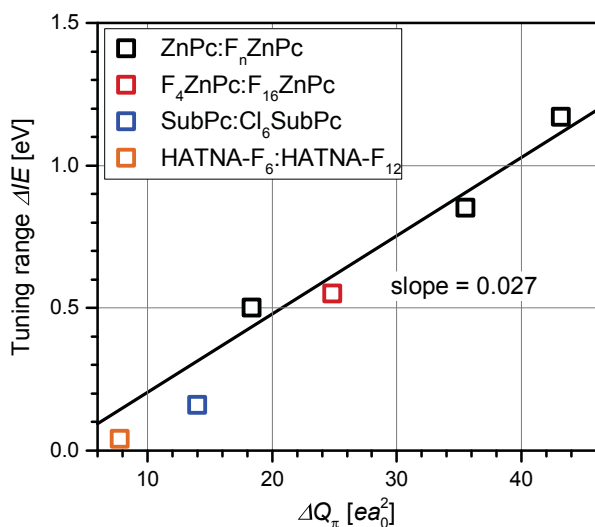


Figure 4.7: Tuning range in intermixed blends of planar molecules: The tuning range of IE with mixing ratio increases with larger differences between the respective Q_π values. The tuning range is given by the IE difference between the two materials in neat films subtracted by the difference in blends. The line depicts a linear fit to the data of F_n ZnPc blends. The data of this figure are included in reference [174].

or a larger intermolecular distance. Nevertheless, the measurements demonstrate that the tuning effect can be transferred to other systems and is not a unique property of ZnPc and its fluorinated derivatives. However, the model system of F_n ZnPc seems to match the preconditions of a tunable ionization energy, i.e. a defined crystalline structure in edge-on orientation and molecular mixing without phase separation, at its best.

4.3.2 Blends with Phase Separation

The results presented in the last section showed how molecular quadrupole moments can enable a continuous shift of IE with the mixing ratio in intermixed blends. However, such types of blends are typically not utilized in organic solar cells, where a certain degree of phase separation between donor and acceptor molecules is an essential necessity for efficient devices. This section focuses on such more phase separated systems.

Model System of F_n ZnPc:C₆₀

Due to their structural and sterical incompatibility, the solar cell model system comprising the planar ZnPc molecule as donor and the spherical C₆₀ molecule as acceptor exhibits significant structural disorder and phase separation that both can further change with the mixing ratio [177, 180]. Tietze *et al.* showed that the structural changes with donor-acceptor mixing ratio are accompanied by shifts of the electronic levels and the open-circuit voltage [179]. Graham *et al.* observed varying electronic levels with mixing ratio also for other donor molecules blended with C₆₀ and suggested that interactions of charges with permanent charge distributions are a possible origin, however without demonstrating a quantitative correlation with the respective molecular quadrupole moments [22].

The energy levels of previously reported ZnPc:C₆₀ blends [179] are now compared to the energies of F₈ZnPc:C₆₀ blends to investigate the impact of quadrupole moments on the energy levels in donor-acceptor blends exhibiting a certain degree of phase separation. Figure 4.8a shows UPS spectra of F₈ZnPc:C₆₀ blends with different donor-acceptor mixing ratios evaporated on p-doped BPAPF. To obtain the respective parts in the blend spectra that belong to F₈ZnPc and C₆₀, the spectra are fitted by a superposition of spectra obtained for neat films.

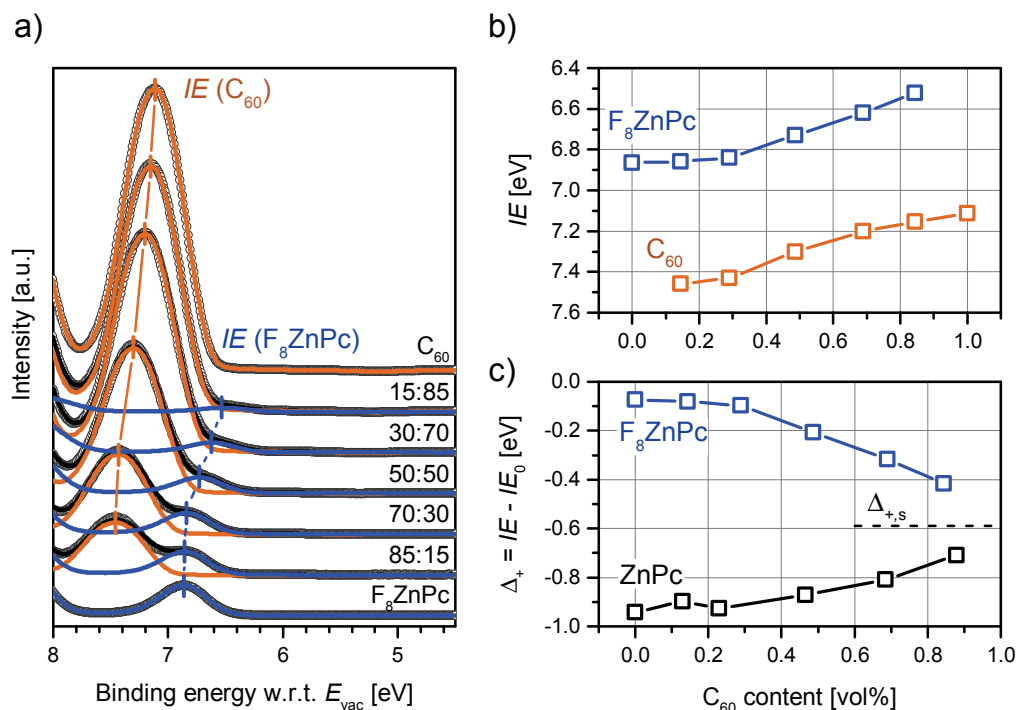


Figure 4.8: Energy levels in phase separated donor:acceptor blends: (a) HOMO region of UPS spectra of F₈ZnPc:C₆₀ blends (20 nm) deposited on silver substrates covered by p-doped BPAPF. The respective parts of F₈ZnPc and C₆₀ are obtained by fitting the blend spectra with superimposed spectra of neat films. The relative contents are given as weight ratios. (b) *IE* values of F₈ZnPc and C₆₀ in blends are extracted from the peak positions of the superimposed spectra. (c) The solid-state correction Δ_+ is obtained from the difference of experimental *IE* values and calculated gas-phase ionization energies (*IE*₀). $\Delta_{+,s}$ denotes the solid state correction for $\Delta_{q-Q} = 0$, as extracted from Figure 4.4b. Experimental values of ZnPc:C₆₀ blends are taken from reference [179]. The content of this figure is included in reference [174].

As shown in Figure 4.8b, both the *IE* of F₈ZnPc and C₆₀ decrease with increasing C₆₀ content, which can be directly explained by the different quadrupole moments of donor and acceptor as well as a change of the film structure with mixing ratio. While F₈ZnPc has a Q_π of $16.3 ea_0^2$, it is zero for C₆₀. The positive Q_π causes an increase of *IE* in neat F₈ZnPc films (see Section 4.2.1). From previous structural studies on similar systems, it is expected that the (average) size of the F₈ZnPc phases continuously decreases with increasing C₆₀ content [199]. Accordingly, the relative amount of molecules within F₈ZnPc phases that are located at the interface to C₆₀ molecules increases for larger C₆₀ contents.

These interface molecules have a reduced magnitude of Δ_{q-Q} compared to “bulk” molecules of the donor phase. Therefore, the mean Δ_{q-Q} value within the whole F_8ZnPc phase decreases with increasing C_{60} content and should reach values close to zero at very high C_{60} contents. In contrast to $ZnPc:F_nZnPc$ blends, the IE change with mixing ratio deviates from a perfectly linear behavior. Due to the phase separation, F_8ZnPc only experience a significant change in Δ_{q-Q} and IE at high C_{60} contents when more F_8ZnPc molecules get into contact with C_{60} . Equally, an increasing charge-quadrupole interaction explains the increase in IE for C_{60} with larger F_8ZnPc content.

$ZnPc$ and F_8ZnPc exhibit a similar magnitude but a different sign of Q_π . Therefore, the energies of $F_8ZnPc:C_{60}$ blends are now compared to the energies of $ZnPc:C_{60}$ blends to verify that the magnitude of Q_π controls the observed energy shifts with mixing ratio. The solid-state correction Δ_+ of $ZnPc$ and F_8ZnPc in blends with C_{60} is calculated from the experimentally measured IE and the calculated IE_0 . As shown in Figure 4.8c, the large difference in Δ_+ between pure layers reduces continuously with increasing C_{60} concentration, indicating a reduction of charge-quadrupole interactions, i.e. of $|\Delta_{q-Q}|$. In good agreement, the Δ_+ values of both molecules approach the values observed for very small coverages of $(F_8)ZnPc$ on p-doped BPAPF (see Figure 4.4b). These values are attributed to molecules with Δ_{q-Q} close to zero.

Extension to other Systems

To generalize these findings, the investigation is extended to two other donor molecules, namely 6T and bDIP [22]. Graham *et al.* showed that they also form neat crystalline layers like F_nZnPc and exhibit a reduction of crystallinity with increasing content of C_{60} [22]. Figure 4.9 displays the difference between the IE of the donors, $ZnPc$, F_8ZnPc , 6T, and bDIP, within blends with high contents of C_{60} and the IE of neat donor films. This difference directly scales with the respective quadrupole component Q_π of the donor molecules. Note that bDIP exhibits an additional dipole moment that, apparently, does not significantly affect the general trend. The slope of this correlation is slightly lower than the slope observed for intermixed blends in Figure 4.7. The reason is probably the fact that the investigated donor concentrations are still too high to observe the full change in IE . In good agreement, the two samples with a lower donor concentration show a larger IE difference to the neat films. Nevertheless, these findings demonstrate that charge-quadrupole interactions crucially affect the electronic levels also in blends with phase separation showing a dependence of the blend energy levels on the respective quadrupole component Q_π , which is similar to the observation on intermixed blends. The strength of this effect is expected to depend on the degree of phase separation and should be the weakest for planar heterojunctions when the interface area is reduced to a minimum.

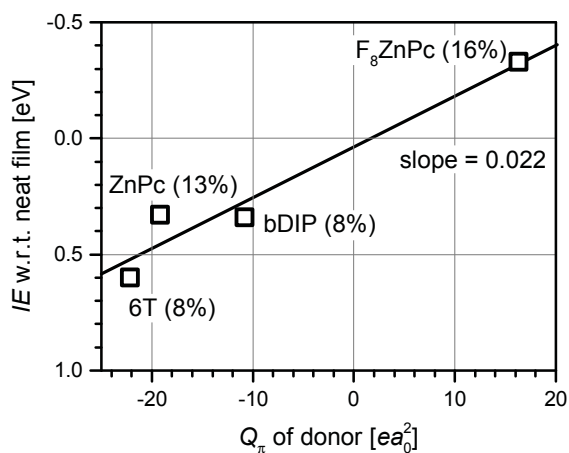


Figure 4.9: Tuning range in blends with phase separation: The difference in IE between donor molecules in neat films and molecules in blends with C_{60} changes with the quadrupole component Q_π of the respective donor molecule. To compare with literature results, the onset values of the HOMO emission peaks are used to determine IE . The content of this figure is included in reference [174].

Conclusion

The investigations of this section demonstrated for intermixed blends a continuous tuning of energy levels with the mixing ratio of two molecules with different quadrupole components Q_π . As shown for several material combinations, the tuning range scales with the difference of the respective Q_π values. The change of the energy levels with mixing ratio is also present in blends exhibiting some degree of phase separation, showing a similar dependence of the tuning range on Q_π . The observation that the energy levels do not shift perfectly linear indicate that due to the phase separation molecules in the “bulk” of the phase of one compound are less affected by quadrupole moments of the other compound. The next section will demonstrate how this effect can be utilized in solar cells to implement driving forces for charge separation at the donor-acceptor interface.

4.4 Application to Organic Solar Cells

In the preceding sections, the impact of molecular quadrupole moments on the energy levels in neat and blended organic films was investigated. To prove the relevance of charge-quadrupole interactions for electronic devices, the dependence of photovoltaic characteristics, such as the open-circuit voltage (V_{oc}) and the short-circuit current (j_{sc}), on quadrupole moments and other molecular parameters is investigated in this section. In the simplified energy level diagram in Figure 4.10a, the generation of charge carriers is described by three subsequent steps [18, 145]. First, a photon is absorbed creating an excited singlet state (S_1) for example of a donor molecule. This exciton needs to diffuse to the donor-acceptor interface to form a charge transfer (CT) state of a donor cation and an acceptor anion. While the CT formation efficiency in general increases with the difference of the optical gap of the donor ($E_{D,opt}$) and the CT state energy (E_{CT}), the minimum energetic difference necessary for efficient CT state formation varies among different material systems [18, 200]. Finally, the CT state needs to split into separated charges (CS state with energy E_{CS}) for generation of photocurrent. It was shown that the splitting efficiency of CT states depends on the difference between E_{CS} and E_{CT} [145]. To increase device efficiency, it is therefore important to optimize E_{CT} and E_{CS} for achieving high charge carrier generation efficiencies while keeping energy losses as low as possible (Figure 4.10b).

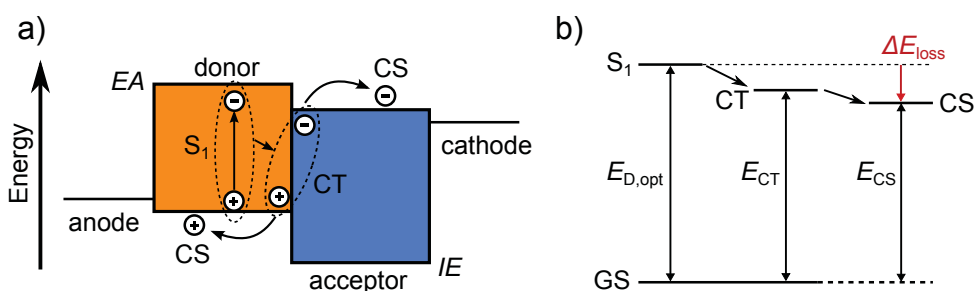


Figure 4.10: Important energies of photovoltaic donor-acceptor systems: (a) Energy level alignment of donor, acceptor, and electrodes at flat-band conditions. The energies of the charge transfer (CT) state and the charge separated (CS) state depend directly on the ionization energy (IE) of the donor and the electron affinity (EA) of the acceptor. (b) The charge carrier generation efficiency and the energy losses vary with the energy offset between CT and CS state.

The large Coulomb binding energy of CT states of several 100 meV generally leads to a reduction of E_{CT} with respect to E_{CS} . Previous theoretical studies discussed how charge-quadrupole interactions can reduce this dissociation barrier [31, 64]. In this section, the influence of the molecular quadrupole moment and the gas phase ionization energy of donor molecules on E_{CT} and E_{CS} is investigated. For this purpose, a ternary mixture of ZnPc and F_4 ZnPc as donors together with C_{60} as acceptor is used for the bulk heterojunction of the photoactive layer. Based on the discussion of Section 4.3, it is expected that the three molecular species separate in a donor and an acceptor phase, where the donor phase consists of an intermixed blend of two structurally similar molecules, i.e. ZnPc and

F_4ZnPc . As a consequence, the (mean) quadrupole moment and the (mean) ionization energy of the donor phase can be tuned with the mixing ratio of the two donor molecules.

4.4.1 Energy Levels in Ternary Blends

In the following, UPS measurements on $ZnPc:F_4ZnPc:C_{60}$ blend layers are analyzed to obtain the (mean) ionization energies of donor and acceptor (IE_D , IE_A) and a qualitative measure of E_{CS} for different donor ratios between $ZnPc$ and F_4ZnPc . The ternary blend layers (thickness: 40 nm) were evaporated on silver substrates covered by p-doped BPAPF. The UPS spectra in Figure 4.11a exhibit distinct HOMO emission peaks from the donor molecules at around 6 eV and from the acceptor molecules at around 7 eV. The emission from the two donor molecules appears as one single peak in the spectrum and the peak onset is used to determine the ionization energy of the donor (IE_{onset}). Although $ZnPc$ and F_4ZnPc exhibit some emission also in the region around 7 eV, its intensity is expected not to be high enough to affect the determination of the HOMO peak onset of C_{60} ⁸ (see also spectra in Figure 4.8 or reference [179] for comparison).

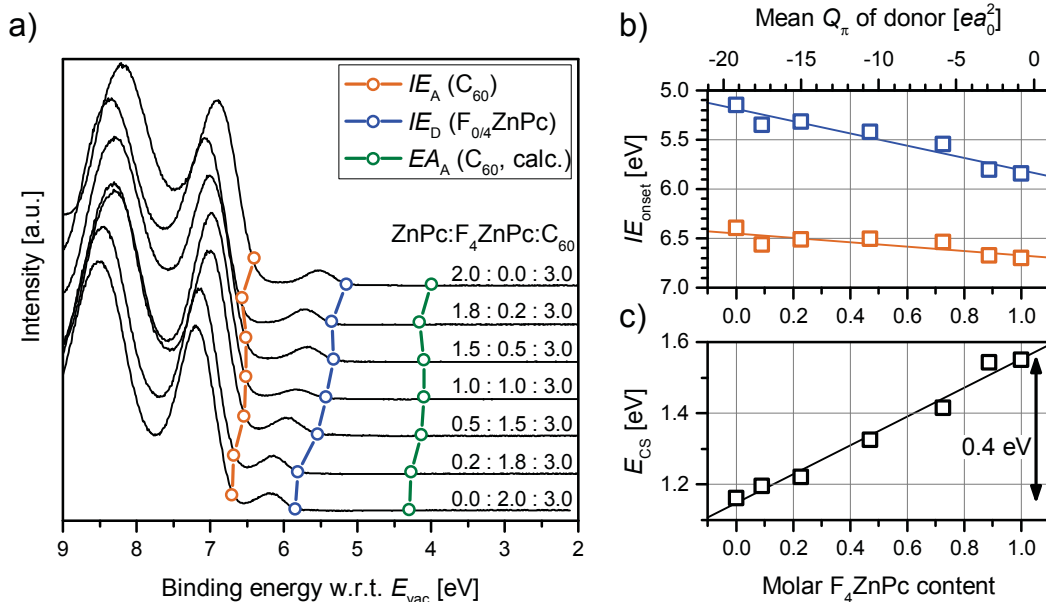


Figure 4.11: UPS spectra of $ZnPc:F_4ZnPc:C_{60}$ blends: (a) Spectra with varying weight ratio of the two donor molecules. EA_A is determined with the assumption of a constant transport gap of C_{60} (2.41 eV, [179]). (b) Values for IE_D and IE_A extracted from the HOMO peak onsets of the spectra in (a). (c) The energy of the charge separated state (E_{CS}) is calculated from the difference between IE_D and EA_A . The lines in (b) and (c) are linear fits to the data. The experimental data of this figure are published in reference [168].

As shown in Figure 4.11b, IE_{onset} of $(F_4)ZnPc$ and C_{60} each continuously increase with larger F_4ZnPc contents, i.e. with an increased mean value of the quadrupole component

⁸ The intensity of the HOMO emission peak of C_{60} is generally higher compared to $(F_4)ZnPc$ because its HOMO orbital is five times degenerated [201].

$Q_{\pi,D}$ of the donor. IE_D increases from ZnPc to F₄ZnPc by 0.7 eV, similar to the enhancement observed in Figure 4.6 for intermixed blends of these molecules. The increase of IE_A by 0.3 eV indicates that the energy levels of a large amount of C₆₀ molecules are affected by the change in $Q_{\pi,D}$ despite the occurrence of phase separation between donor and acceptor. The onset difference between IE_A and the electron affinity of the acceptor (EA_A) was experimentally obtained before to be 2.41 eV for a ZnPc:C₆₀ blend with an acceptor content of approximately 60 wt% [179]. Assuming that this value does not change strongly with the ZnPc:F₄ZnPc ratio, E_{CS} can be determined for different donor ratios with following expression:

$$E_{CS} = IE_D - EA_A \quad (4.2)$$

The results shown in Figure 4.11c reveal that E_{CS} monotonously increases by up to 0.4 eV when adjusting the ratio between ZnPc and F₄ZnPc.

4.4.2 Tuning of Open-Circuit Voltage

Organic solar cells with ternary ZnPc:F₄ZnPc:C₆₀ blends as active layers⁹ are now analyzed to investigate how a variation of the donor properties affects the photovoltaic parameters. The current-voltage characteristics in Figure 4.12a reveal an increase of the open-circuit voltage (V_{oc}) with higher contents of F₄ZnPc within the donor phase, which can be directly explained by the increase of IE_D . Unfortunately, the short-circuit current density and the fill factor decrease simultaneously, leading to an overall lower power conversion efficiency for high F₄ZnPc contents. Possible origins of these decreases are discussed in Section 4.4.3.

The magnitude of V_{oc} is directly connected to E_{CT} [18, 152, 187]. Tress *et al.* studied the CT state absorption properties of ZnPc:F₄ZnPc:C₆₀ solar cells by sensitive measurements of the external quantum efficiency (EQE) onset, which they fitted by Gaussian functions [169]. E_{CT} for different ratios between the two donors can be estimated from the peak position (E_0) and the standard deviation (σ) of these Gaussian functions by using following expression:

$$E_{CT} = E_0 - \lambda_{CT}, \quad (4.3)$$

⁹ The solar cells were built and characterized by Dr. Beatrice Beyer from the Fraunhofer Institute for Electron Beam, Plasma Technology and COMEDD (FEP) in Dresden, Germany. Detailed information on the production and characterization of the devices can be found in Section 3.4.

with λ_{CT} as the reorganization energy of the CT state [18]. λ_{CT} is calculated from the standard deviation of the Gaussian fits with following expression:

$$\lambda_{CT} = \sigma^2 / (2k_B T). \quad (4.4)$$

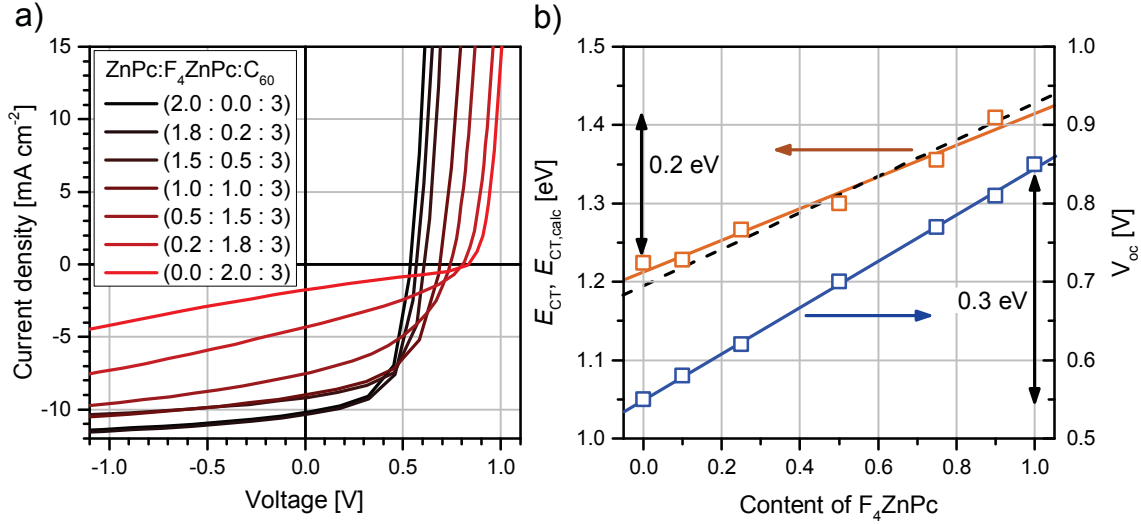


Figure 4.12: Characteristics of ternary solar cells: (a) Current-voltage characteristics of ZnPc:F₄ZnPc:C₆₀ solar cells with varying ratio between the two species of donor molecules. (b) Charge transfer state energy (E_{CT}) and open-circuit voltage (V_{oc}) increase with the F₄ZnPc content. E_{CT} values are obtained from the maximum positions and widths of Gaussian peaks fitted to sensitive external quantum efficiency spectra in reference [169]. The dashed line depicts charge transfer state energies calculated from molecular parameters ($E_{CT,calc}$) by using Equation 4.5. The content of this figure is included in references [168, 174].

The results in Figure 4.12b reveal that E_{CT} continuously increases from ZnPc to F₄ZnPc by 0.2 eV. The increase in E_{CT} can be attributed to the variation of three molecular parameters, namely the gas phase ionization energy of donor molecules ($IE_{0,D}$), the relaxation energy of donor cations ($\lambda_{D,+}$), and the Coulomb binding energy between donor cations and acceptor anions ($E_{coul,CT}$). All three parameters can be calculated by density functional theory (DFT) simulations¹⁰. $E_{coul,CT}$ was obtained from an optimized geometry of the donor-acceptor pair and by assuming a mean value of $\epsilon_r = 3.6$ for the dielectric constant [173]. The reader is referred to Section 3.5 for further details on the DFT simulations. Values for the CT state energy at different donor mixing ratios can be estimated from the mean values of $IE_{0,D}$, $\lambda_{D,+}$, and $E_{coul,CT}$:

$$E_{CT,calc} = IE_{0,D} - EA_{0,A} - (\lambda_{D,+} + \lambda_{A,-}) - E_{coul,CT} - \Delta_{solid}, \quad (4.5)$$

¹⁰ IE , EA and λ values were calculated by Dr. Christopher Gaul and Karl Sebastian Schellhammer as a part of the group of Dr. Frank Ortman at TU Dresden. $E_{coul,CT}$ values were obtained by Dr. Reinhard Scholz at IAPP.

where $EA_{0,A}$ is the electron affinity of an acceptor molecule in the gas phase and $\lambda_{A,-}$ denotes the relaxation energy of an acceptor anion. Δ_{solid} comprises all solid state effects, such as polarization effects or energetic disorder, and is assumed to be constant for all donor ratios.

The dashed line in Figure 4.12b depicts $E_{CT,\text{calc}}$ for $\Delta_{\text{solid}} = 2.15$ eV, showing an increase of 0.23 eV being only slightly larger than the one observed in experiment. Apparently, other influences to E_{CT} , such as changes in the electrostatic environment, energetic disorder, or relaxation effects, only have a minor impact on the variation of E_{CT} when replacing ZnPc by $F_4\text{ZnPc}$. The increase of E_{CT} from ZnPc to $F_4\text{ZnPc}$ originates mainly from the enhancement of $IE_{0,D}$ by 0.31 eV. This increase is compensated by an increase of $E_{\text{coul},CT}$, being 0.43 eV for ZnPc: C_{60} and 0.50 eV for $F_4\text{ZnPc}:C_{60}$. The DFT simulations show that the increase of $E_{\text{coul},CT}$ from ZnPc to $F_4\text{ZnPc}$ is due to the different charge distribution on the two donor molecules since the distance between $(F_4)\text{ZnPc}$ and C_{60} is similar. ZnPc has more negative charge distribution in the middle of the molecule compared to $F_4\text{ZnPc}$, reflecting in a more negative $Q_{\pi,D}$. This leads to a larger effective distance between the positive charge distribution on the ZnPc cation and the negative charge distribution on the adjacent C_{60} anion, resulting in a smaller Coulomb binding energy. The results of the more comprehensive study on several matrix-dopant combinations presented in Section 5.2.4 suggest a general relationship between $E_{\text{coul},CT}$ and Q_{π} of planar donor or acceptor molecules.

As seen in Figure 4.12b, V_{oc} increases by 0.3 eV from ZnPc to $F_4\text{ZnPc}$, which is 0.1 eV larger compared to the enhancement of E_{CT} , implying that the difference between E_{CT} and V_{oc} decreases with larger $F_4\text{ZnPc}$ contents. This might be due to a reduction of voltage losses originating from non-radiative recombination (ΔV_{nr}), which were observed to decrease with increasing E_{CT} for a variety of donor-acceptor combinations [187]. ΔV_{nr} can be calculated from the quantum yield of the electroluminescent emission (EQE_{EL}) data published in reference [169] with following formula [187, 202]:

$$\Delta V_{nr} = -\frac{k_B T}{q} \cdot \ln(\text{EQE}_{\text{EL}}). \quad (4.6)$$

Equation 4.6 yields $\Delta V_{nr} = 403$ meV for ZnPc: C_{60} and $\Delta V_{nr} = 328$ meV for $F_4\text{ZnPc}:C_{60}$, serving as an explanation for the observation that V_{oc} increases stronger than E_{CT} .

4.4.3 Splitting Efficiency of CT States

In this section, the influence of QPMs on the difference between E_{CS} and E_{CT} is investigated, as this energetic difference ($\Delta_{CT,\text{diss}}$) is supposed to act as barrier for free charge carrier generation [145]. The ternary ZnPc: $F_4\text{ZnPc}:C_{60}$ solar cells are an ideal model system to investigate the impact of $\Delta_{CT,\text{diss}}$ on the short-circuit current density (j_{sc}) and the fill factor (FF) and to correlate the magnitude of $\Delta_{CT,\text{diss}}$ with molecular parameters.

While E_{CS} is taken from the UPS spectra¹¹ presented in Figure 4.11, E_{CT} shown in Figure 4.12 is obtained from the sensitive EQE measurements in reference [169]. As shown in Figure 4.13a, $\Delta_{CT,diss}$ linearly increases with $Q_{\pi,D}$ by up to 0.2 eV when replacing ZnPc with F₄ZnPc.

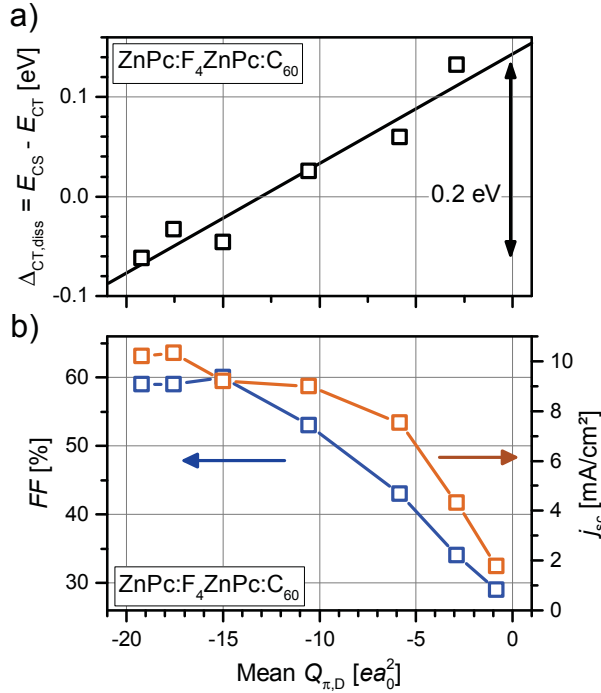


Figure 4.13: Dependence of photovoltaic parameters on the CT dissociation barrier: (a) Dependence of the CT state dissociation barrier ($Q_{\pi,D}$) on the mean quadrupole component of donor molecules ($Q_{\pi,D}$). E_{CS} is obtained from the UPS spectra presented in Figure 4.11. (b) A large CT dissociation barrier leads to a reduction of the short-circuit current (j_{sc}) and the fill factor (FF). The content of this figure is included in reference [174].

The increase of $Q_{\pi,D}$ and $\Delta_{CT,diss}$ directly reflects in the solar cell parameters presented in Figure 4.13b. At $Q_{\pi,D}$ values larger than $-15 ea_0^2$, both j_{sc} and FF continuously decrease with increasing $Q_{\pi,D}$. Apparently, $Q_{\pi,D}$ becomes to large for $Q_{\pi,D} > -15 ea_0^2$, significantly reducing the generation efficiency of free charges. The decrease in FF can be explained by a field-dependent free charge carrier generation [145]. The mobility measurements in reference [168] show a reduction of the mobility in ZnPc:F₄ZnPc blends due to the energy offset between both molecular species. Such a mobility decrease could partly cause the decrease of FF [203].

Impact of Charge Quadrupole Interactions

As the results in Figure 4.13 indicate that the magnitude of $Q_{\pi,D}$ is important for efficient CT dissociation, it is interesting to discuss the impact of $Q_{\pi,D}$ on E_{CT} and E_{CS} . E_{CT} is reduced with respect to E_{CS} due to the Coulomb binding energy of the CT state ($E_{coul,CT}$). The DFT simulations revealed that $E_{coul,CT}$ is lower for ZnPc:C₆₀ by 70 meV in comparison to F₄ZnPc:C₆₀ due to the negative $Q_{\pi,D}$ of ZnPc. Partly, this can already explain the reduction of $\Delta_{CT,diss}$ from F₄ZnPc:C₆₀ to ZnPc:C₆₀. In the following, it is dis-

¹¹The surface sensitive UPS measurements give only an estimation for E_{CS} and there is probably an offset between the real dissociation barrier and the one plotted in Figure 4.13a.

cussed how molecular quadrupole moments can induce local driving forces for charge separation at the donor-acceptor interface when the donor and acceptor molecules form separated phases. Figure 4.14a illustrates the case of a flat heterojunction between donor and acceptor, being the border case of a large degree of phase separation. For focusing the discussion, it is assumed that $Q_{\pi,D}$ and $E_{\text{coul,CT}}$ are the only parameters inducing a spatial gradient of the energy levels at the donor-acceptor interface. In the first case, $Q_{\pi,D}$ is zero and the Coulomb binding between the donor cation and acceptor anion leads to a shift of the energy levels at the interface (Figure 4.14b). In such a case, $\Delta_{\text{CT,diss}}$ is given by the Coulomb binding energy at the interface: $\Delta_{\text{CT,diss}} = E_{\text{CS}} - E_{\text{CT}} = E_{\text{coul,CT}}$.

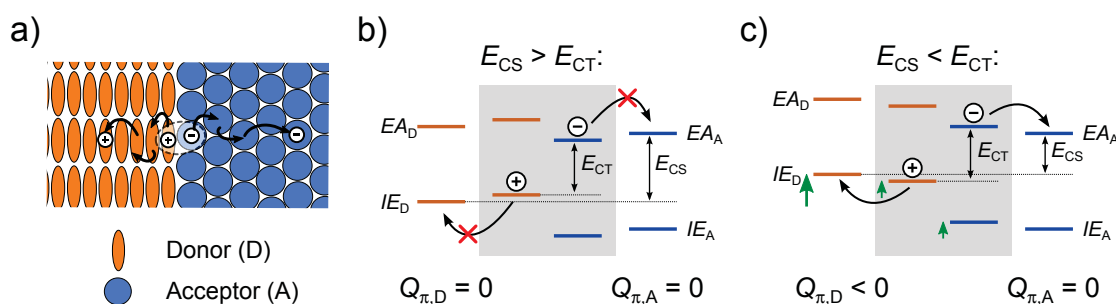


Figure 4.14: Impact of molecular quadrupole moments on CT state dissociation: (a) Sketch of a planar heterojunction between donor and acceptor. (b,c) Simplified sketch of the energy levels in the donor phase (left), at the interface (middle, grey), and in the acceptor phase (right) for vanishing QPMs (b) and a negative $Q_{\pi,D}$ (c). This figure is included in reference [174].

In the second case, a negative $Q_{\pi,D}$ leads to a decrease of IE_D and EA_D in the bulk of the donor phase due to charge-quadrupole interactions along the π - π -stacking direction of the planar donor molecules (Figure 4.14c). The induced energy shift at the interface is weaker due to the reduced number of neighbors with negative $Q_{\pi,D}$. When the shift is equal for donor and acceptor molecules at the interface, E_{CT} remains unchanged. The energy of the molecules in the bulk of the acceptor phase remain unaffected by the change of $Q_{\pi,D}$. This results in an electrostatic gradient from the donor to the acceptor phase, reducing the dissociation barrier: $\Delta_{\text{CT,diss}} = E_{\text{CS}} - E_{\text{CT}} = E_{\text{coul,CT}} + k \cdot Q_{\pi,D}$. k is a positive parameter is expected to depend on the degree of phase separation between donor and acceptor. For example, blends intermixed on a molecular scale, such as the ZnPc:F_nZnPc blends in Section 4.3.1, both molecular species experience the same electrostatic shifts by charge-quadrupole interactions ($k = 0$). Equally to these considerations, a positive $Q_{\pi,A}$ of the acceptor would further reduce the dissociation barrier, which might be important for developing efficient non-fullerene acceptors.

These considerations might explain the observation in previous studies that F₄-ZnPc (see Figure 4.1 for structural formula) outperforms ZnPc and F₄ZnPc as a donor molecule in solar cells [178]. F₄-ZnPc delivers a V_{oc} increased by around 0.2 eV compared to ZnPc [178], which can be attributed to its higher $IE_{0,D}$. In contrast to F₄ZnPc however, F₄-ZnPc yields similar values for j_{sc} and FF like ZnPc [178] because its $Q_{\pi,D}$ ($= -13.87 \text{ ea}_0^2$)

is sufficiently small to allow for efficient CT state dissociation. While a variety of parameters, such as mobility, morphology, charge carrier delocalization, or energetic disorder, are known to affect the generation efficiency of charge carriers in organic solar cells, the molecular quadrupole moment seems to be another important parameter that should be taken into account for the design of new donor and acceptor materials.

Conclusion

It was investigated in this section how molecular parameters affect device characteristics of organic solar cells. The open-circuit voltage (V_{oc}) is directly connected to the charge transfer (CT) state energy at the donor-acceptor interface, which was continuously tuned with the mixing ratio of two donor molecules, ZnPc and F₄ZnPc, in a ternary blend with the acceptor C₆₀. Simulation results suggested that the tuning effect mainly originates from the change of two molecular parameters, the ionization energy and the quadrupole moment of the donor. Furthermore, the short-circuit current density changed strongly with the donor mixing ratio due to a change of the CT state dissociation barrier. The reduction of this barrier from F₄ZnPc to ZnPc was attributed to the negative out-of-plane quadrupole component of ZnPc, inducing local driving forces for charge separation at the donor-acceptor interface.

4.5 Summary

The impact of molecular quadrupole moments on the energy levels in organic films was investigated on the basis of ZnPc and its fluorinated derivatives, where the quadrupole moment can be adjusted by the degree of fluorination. The results demonstrated that charge-quadrupole interactions along the π - π -stacking geometry induce large energy shifts in many crystalline films of planar molecules. The difference in ionization energy between films with edge-on or face-on oriented molecules directly scaled with the quadrupole component perpendicular to the molecular plane. The electrostatic interactions were utilized to continuously tune energy levels with the mixing ratio of two molecules, where the tuning range increased with the difference of their quadrupole moments. Such a tuning even worked in donor-acceptor blends typically used in organic solar cells, where the compounds are not intermixed, but exhibit some degree of phase separation. This tuning mechanism was applied to ternary blends in organic solar cells to show how relevant device parameters can be optimized by adjusting molecular parameters. This allowed for a continuous tuning of the open-circuit voltage with the mixing ratio of two donor molecules having different quadrupole moments and ionization energies. It was further demonstrated that adjusting quadrupole moments can induce driving forces for charge separation at the donor-acceptor interface, reflecting in larger short-circuit currents.

5. Investigations on Molecular n-Doping

Molecular doping is suitable to precisely control the electronic properties of organic semiconductors, such as conductivity, charge carrier density, or Fermi level position. Particularly in optoelectronic devices made of small molecules, molecularly doped transport layers play an important role in device design [34, 35]. In this chapter, molecular n-doping is investigated where n-dopants with small ionization energies provide electrons to the matrix material. The necessity of small ionization energies typically makes these n-dopants sensitive to air exposure. In Section 5.1, two newly developed air stable n-dopants are compared to established n-dopants regarding their doping properties. The doping mechanism of one air stable n-dopant is investigated in more detail to find the origin of its low doping efficiency. In Section 5.2, the highly efficient and air stable n-dopant (2-Cyc-DMBI)₂ is used to analyze the electronic states in n-doped semiconductors by direct and inverse photoelectron spectroscopy. For highly n-doped organic semiconductors, the electronic states and their energetic disorder are discussed with the model of integer charge transfer complexes of matrix anions and dopant cations. The results of Section 5.3 reveal that the electrical conductivity at room temperature of doped organic semiconductors correlates with the Arrhenius-type thermal activation energy, obtained from temperature-dependent conductivity measurements. After discussion of transport mechanisms explaining the concentration dependence of the activation energy, the variation of its magnitude between different materials is directly correlated to respective molecular parameters, obtained from density functional theory simulations. Finally, the sensitivity of the conductivity and the position of the Fermi level to air exposure is investigated for various n-doped semiconductors to draw conclusions on a general limit of air stable n-doping (Section 5.4).

5.1 Comparison of Different n-Dopants

In this section, different n-dopants are compared regarding their doping efficiency and electrical conductivity in an established electron transport material for organic solar cells, with the goal to choose an n-dopant for further basic investigations on electronic states, electrical conductivity, and air stability of n-doped semiconductors in Sections 5.2-5.4. The state-of-the-art but air sensitive n-dopant Cr₂(hpp)₄ is compared to two classes of air stable n-dopants, namely the DMBI dimer (2-Cyc-DMBI)₂ and the DMBI salt o-MeO-DMBI-X, where X can be substituted by chlorine, bromine, or iodine. Finally, the doping mechanism of the air stable n-dopant o-MeO-DMBI-Cl is analyzed in more detail (Section 5.1.2). Most of the results presented in this section are published in reference [204].

Figure 5.1 shows the expected doping mechanisms of these n-dopants in blends with bis-HFI-NTCDI, which is a standard electron transport material in organic solar cells processed at IAPP [32, 128, 205, 206]. The matrix/dopant combination of bis-HFI-NTCDI and $\text{Cr}_2(\text{hpp})_4$ is expected to show an integer electron transfer from dopant to matrix without any change of their chemical structures. Efficient electron transfer is expected to necessitate an ionization energy of the dopant (IE_D) being similar or lower than the electron affinity of the matrix (EA_M). Inverse or direct photoelectron spectroscopy measurements on neat films of bis-HFI-NTCDI and $\text{Cr}_2(\text{hpp})_4$ resulted in values of 4.0 eV and 3.8 eV for IE_D and EA_M , respectively. The fact that n-doping works for this combination [207] can be explained by a reduced IE_D when the dopant is distributed within the matrix with a large quadrupole moment, as seen for various blends investigated in Section 4.3.

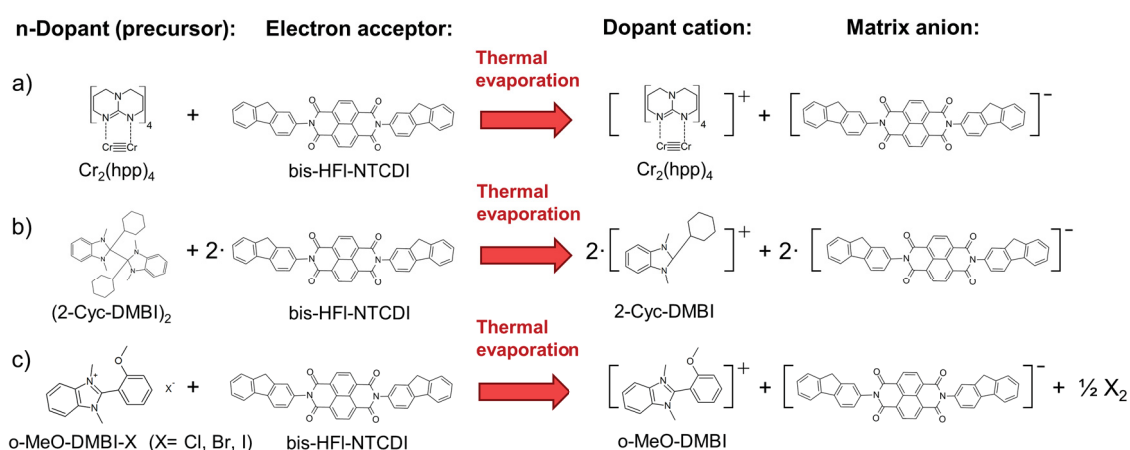


Figure 5.1: Doping mechanisms of different n-dopants: (a) “Classical” n-doping mechanism with an integer electron transfer without any change of the chemical structures. (b,c) The precursor molecules of the air stable dopants split upon thermal evaporation, releasing highly reducing radicals as actual n-doping species.

The small IE_D of $\text{Cr}_2(\text{hpp})_4$ makes such n-dopants typically sensitive to air exposure. The air stable molecules $(2\text{-Cyc-DMBI})_2$ and o-MeO-DMBI-X have been developed to act as air stable precursor molecules of n-dopants, having a large IE which resists oxidation at air. Upon thermal evaporation, these precursor molecules split and release the actual n-doping species. As shown in Figure 5.1b, $(2\text{-Cyc-DMBI})_2$ splits into two equal radicals, each providing an electron [46, 47]. Therefore, the doping concentration is twice as large as the precursor concentration for efficient precursor splitting. Upon thermal evaporation, a neutral halogen atom is expected to split from the precursor o-MeO-DMBI-X , producing a highly reducing o-MeO-DMBI radical [49]. In the following section, the performance of these n-dopants in bis-HFI-NTCDI is investigated in terms of electrical conductivity and Fermi level position.

5.1.1 Doping Characteristics

The doping characteristics of different n-dopants are compared in this section. An important parameter is the ionization energy IE_D because the n-dopant should be only able to dope matrix molecules with an EA_M that is similar or larger than IE_D . Therefore, a smaller value for IE_D is beneficial. As noted before, ultraviolet photoelectron spectroscopy (UPS) measurements on a neat $Cr_2(hpp)_4$ film revealed an IE_D of 4.0 eV. IE_D values are not accessible by standard UPS experiments for the air stable DMBI dopants because the actual n-doping species, i.e. highly reactive radicals, probably dimerize in a pure dopant film. Therefore, the conductivity of matrix materials with varying EA_M n-doped by these dopants was measured¹ to obtain an estimation for IE_D . ZnPc has the lowest EA_M ($= 3.0 \text{ eV}^2$) of all matrix materials investigated in this study that can be doped by (2-Cyc-DMBI)₂. Blending of (2-Cyc-DMBI)₂ into pentacene ($EA_M = 2.7$ [193]) does not show a stable doping effect. Therefore, IE_D of the n-doping radical of (2-Cyc-DMBI)₂ is expected to be in between 2.7 eV and 3.0 eV, being sufficiently low for typical electron transport materials. IE_D is expected to be larger for o-MeO-DMBI-X as it does not show any doping effect in ZnPc. In the following, bis-HfI-NTCDI is used as a matrix material for a detailed comparison of different dopants because it can be doped by all n-dopants and serves as an electron transport layer in devices.

Electrical Conductivity

First, the lateral conductivity of n-doped bis-HfI-NTCDI layers (thickness: 20 nm) at different molar doping ratios is investigated. The results in Figure 5.2 reveal that $Cr_2(hpp)_4$ and (2-Cyc-DMBI)₂ lead to similar conductivities up to a molar doping ratio of 0.05. While the conductivity of $Cr_2(hpp)_4$ doped films decreases above this doping ratio, the conductivity of (2-Cyc-DMBI)₂ doped films has a plateau for ratios between 0.1 and 0.3. A conductivity decrease at higher concentrations was previously observed and mostly attributed to an increasing structural disorder in this concentration regime [102, 120]. The structural disorder might effectively be larger for $Cr_2(hpp)_4$ as the molar mass of this dopant is roughly three times larger. As discussed in Section 5.2.4, matrix anions and dopant cations form electrical dipoles, introducing energetic disorder into the doped film. The larger and sterically more demanding dopant $Cr_2(hpp)_4$ might introduce larger dipole moments and hence might cause an increased energetic disorder.

The o-MeO-DMBI-X dopants result in lower conductivities compared to the other two dopants. Nevertheless, the conductivity of o-MeO-DMBI-Cl doped layers is only slightly lower than of $Cr_2(hpp)_4$ doped films and follows the same trend with a decrease at molar

¹ The conductivity measurements of this section were mostly performed by Dr. Paul Pahner, Olka Kaveh, and Daniel Schütze at IAPP.

² The LEIPS measurements were performed by Dr. Fabio Bussolotti in the group of Prof. Satoshi Kera at the Institute for Molecular Science in Okazaki, Japan.

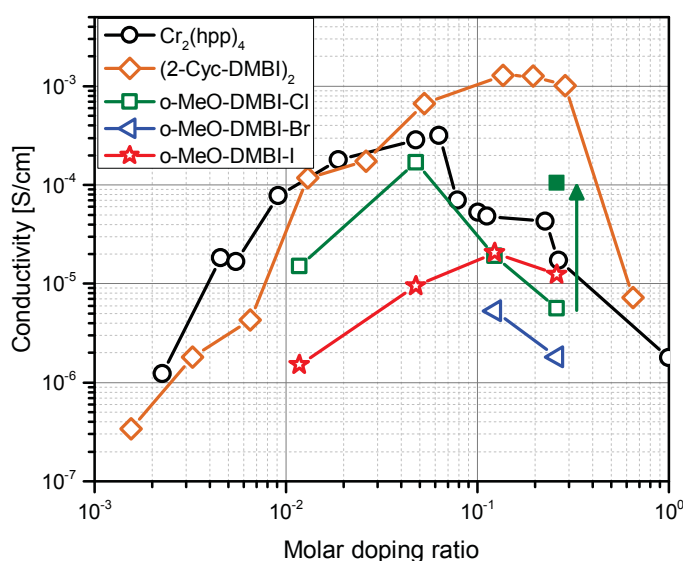


Figure 5.2: Lateral conductivity of n-doped bis-HFI-NTCDI layers: While the reduced conductivity of $\text{Cr}_2(\text{hpp})_4$ doped films at large doping ratios is attributed to an increased energetic disorder, the reduced conductivity of o-MeO-DMBI-X doped films probably originates from the unique precursor decomposition mechanism. The conductivity of the o-MeO-DMBI-Cl doped sample at a concentration of 21 mol% can be significantly increased by thermal annealing to 100 °C for 40 min. Note that the doping concentration is twice the precursor concentration for $(2\text{-Cyc-DMBI})_2$, as one precursor provides two n-doping radicals. The conductivity data are published in reference [204].

doping ratios above 0.05. Post annealing of a bis-HFI-NTCDI: o-MeO-DMBI-Cl (21 mol%) layer can increase the conductivity by more than one order of magnitude to a value even higher than obtained with $\text{Cr}_2(\text{hpp})_4$ at the same doping concentration (see green arrow in Figure 5.2). This strong increase is not possible for $\text{Cr}_2(\text{hpp})_4$ doped layers, indicating that the origin for the reduction of the conductivity at higher doping ratios is different between o-MeO-DMBI-Cl and $\text{Cr}_2(\text{hpp})_4$. As shown below, the conductivity decrease does not originate from an increased energetic disorder, but arises from undesired decomposition products in the film, which can be removed by annealing.

Fermi Level Position

The position of the Fermi level (E_F) within a doped film is directly connected to the doping efficiency [41, 42]. E_F of n-doped bis-HFI-NTCDI layers with varying concentrations is now analyzed to investigate whether the differences in conductivity are related to a variation in doping efficiency. The position of E_F in thin films of intrinsic organic semiconductors is determined by the substrate work function and the density of states of the organic semiconductor, including trap states within the energy gap [208, 209]. The substrate work function of gold can be increased by a thin interlayer (3 nm) of the p-dopant $\text{C}_{60}\text{F}_{36}$ to set E_F into the energy gap for an intrinsic bis-HFI-NTCDI sample. Figure 5.3a

shows the change of E_F with molar doping ratio with respect to the HOMO peak positions in UPS spectra (HOMO_{max}). When the doping concentration increases above the concentration of trap states, the distance between E_F and HOMO_{max} increases strongly due to the occupation of electron transport states [41, 42]. In the high concentration region, E_F is pinned between occupied states of matrix anions within integer charge transfer complexes (ICTC) and unoccupied LUMO states of neutral matrix molecules. Section 5.2 provides further information on these states. At very high molar doping ratios approaching 1, the concentration of neutral matrix molecules vanishes and E_F shifts towards higher unoccupied states.

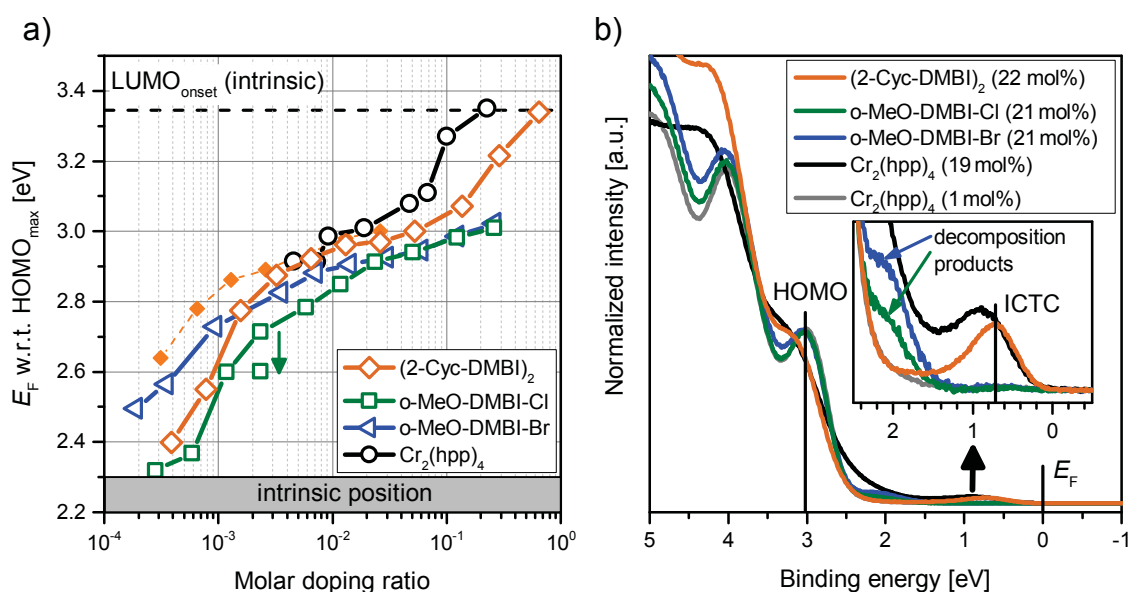


Figure 5.3: Doping characteristics of different n-dopants: (a) Change of Fermi level position with doping concentration, as measured by UPS. The green arrow depicts the reduction of doping efficiency at an increased dopant evaporation rate. The orange dashed line and filled squares belong to a bis-HFI-NTCDI:(2-Cyc-DMBI)₂ run performed after evaporation of o-MeO-DMBI-X. Due to large peak broadening at high concentrations, E_F is plotted with respect to HOMO peak positions. The black dashed line depicts the LUMO onset position for the case that the LUMO onset (EA onset) with respect to the HOMO_{max} (IE_{max}) of the doped samples is equal to that of an intrinsic sample. (b) UPS spectra of bis-HFI-NTCDI doped by different n-dopants at around 20 mol%. The peak at 0.8 eV is attributed to photoemission from matrix anions within integer charge transfer complexes (ICTCs) with dopant cations. A similar version of this figure is published in reference [204].

The position of E_F at molar doping ratios below 10^{-2} significantly differs between samples doped by (2-Cyc-DMBI)₂, o-MeO-DMBI-Br, or o-MeO-DMBI-Cl, where the latter exhibits the lowest values. A simple explanation would be that o-MeO-DMBI-Cl provides the n-doping species, the o-MeO-DMBI radical, less efficiently at low evaporation temperatures and rates used for lower doping concentrations. However, applying a ten times

higher dopant evaporation rate³ results in an even weaker n-doping effect, as exemplarily investigated for MR=0.003 (see green arrow in Figure 5.3a). As shown in Section 5.1.2, the weaker n-doping effect at higher evaporation rates is due to an evaporation temperature dependence of the decomposition mechanism of the n-dopant precursor.

Another reason for the different E_F positions at lower doping concentrations might be unintentional doping by gas-phase impurities present in the evaporation chamber whose intensity was larger for the o-MeO-DMBI-Br run in comparison to the o-MeO-DMBI-Cl run. This explanation is supported by the change of electronic properties during the exposure of an intrinsic C₆₀ film to the dopant chamber in which o-MeO-DMBI-Cl was evaporated before. The conductivity of the intrinsic sample considerably increased during exposure to the chamber and UPS measurements revealed a E_F shift away from the HOMO peak during the exposure step, indicating an n-doping effect. Comparing two different measurement runs of bis-HFI-NTCDI:(2-Cyc-DMBI)₂ samples further verifies this effect. The samples processed after o-MeO-DMBI-Cl evaporation exhibit a stronger n-doping effect at low doping concentrations in comparison to the run processed in a cleaned chamber (see dashed orange line in Figure 5.3a). This background doping effect also occurred after evaporation of (2-Cyc-DMBI)₂, but it was considerably weaker and lasted only for a few days. Apparently, the DMBI n-dopants are volatile and stay in the gas phase of the chamber after evaporation, hence acting as unintentional n-dopants. This makes it challenging to precisely control the Fermi level position at low doping concentrations.

At high doping concentrations, E_F seems to shift closer towards the LUMO peak when the dopants Cr₂(hpp)₄ and (2-Cyc-DMBI)₂ are used, indicating a higher doping efficiency (Figure 5.3a). However, such a strong shift of E_F already at a molar doping ratio of 0.1 as observed for Cr₂(hpp)₄ is not expected. This shift can be explained by an increased $IE-EA$ difference of the matrix at very high concentrations [210], whose origin can be for example a decreased dielectric constant or an increased structural disorder. The UPS spectra of bis-HFI-NTCDI samples each doped by one of the four n-dopants at around 20 mol% are shown in Figure 5.3b to investigate the origin of the differences in E_F at high concentrations. The spectra of the films doped by Cr₂(hpp)₄ and (2-Cyc-DMBI)₂ clearly show emission from occupied LUMO states of anions just below E_F . Furthermore, these spectra are broadened due to an increased amount of charge transfer complexes, acting as electrical dipoles (see also Section 5.2). The spectra of the films doped by o-MeO-DMBI-Cl and o-MeO-DMBI-Br do not show these features and look similar to the spectrum of a Cr₂(hpp)₄ doped film at a doping concentration of 1 mol%, indicating a much lower charge transfer efficiency from dopant to matrix and explaining the weaker E_F shift for these dopants.

The spectra of o-MeO-DMBI-Cl/Br doped films exhibit an additional feature at around 2 eV (6 eV with respect to E_{vac}), which might belong to an undesired decomposition prod-

³ A rotational shutter between dopant source and sample was used to decrease the deposition rate at the sample by a factor of 10.

uct of the precursor molecule, acting as doping-inactive impurity. Such decomposition products might be the origin for the reduced conductivities at high doping concentrations for these dopants. Therefore, the conductivity increase by thermal annealing observed in Figure 5.2 could originate from a removal of these impurities. Figure 5.4 shows the spectra of a bis-HfI-NTCDI:o-MeO-DMBI-Br layer before and after thermal annealing at 50°C. The spectra clearly reveal the removal of the shoulder at 6 eV by annealing. As the E_F position is equal in both spectra, the n-doping effect seems to be unaffected by annealing. Apparently, these volatile impurities can be removed by thermal annealing without destroying the doping effect, resulting in an increase of the conductivity to a value observed at 1 mol% for the efficient dopants $\text{Cr}_2(\text{hpp})_4$ and $(2\text{-Cyc-DMBI})_2$ (see Figure 5.2). The decomposition mechanism of the precursor molecule o-MeO-DMBI-Cl is investigated in more detail in the next section to find the molecular species causing the shoulder in UPS spectra.

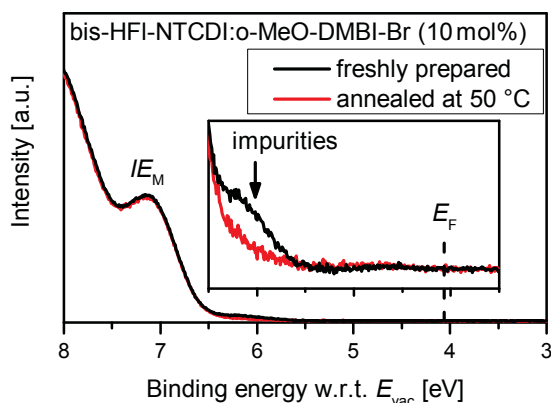


Figure 5.4: Removal of impurities in doped layers by thermal annealing: The UPS spectra of a bis-HfI-NTCDI:o-MeO-DMBI-Br (10 mol%) layer before and after thermal annealing at 50°C reveal a reduction of the shoulder at 6 eV, which is assigned to doping inactive decomposition products of the precursor molecule. This figure is published in reference [204].

5.1.2 Doping Mechanism of o-MeO-DMBI-Cl

Mass Spectroscopy

Mass spectroscopy measurements (QMS200 prisma, Pfeiffer Vacuum) during thermal evaporation of o-MeO-DMBI-Cl at high evaporation rates of several Å/s were performed to identify the decomposition products of o-MeO-DMBI-Cl acting as impurity. The mass spectrum in Figure 5.5 exhibits pronounced peaks indicating the presence of a large amount of chloromethane (CH_3Cl) besides pure chlorine. These results suggest that one or more methyl groups split from the precursor molecule at high evaporation temperatures, resulting in undesired decomposition products. The small peak at $238 u^4$ probably belongs to o-MeO-DMBI molecules where one of the methyl groups is removed from the main molecule. As methyl groups can split from the oxygen or one of the two nitro-

⁴ unified atomic mass unit

gen atoms, the core level energies of the decomposition products are investigated in the following.

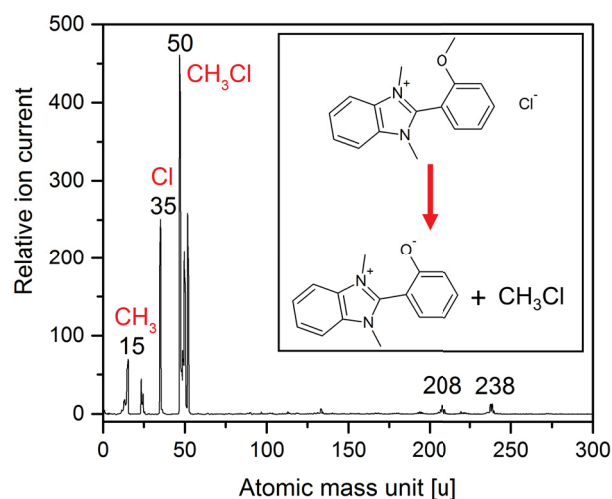


Figure 5.5: Analysis of decomposition products of o-MeO-DMBI-Cl by mass spectroscopy: The precursor molecule was evaporated at high evaporation rates and temperatures to investigate the decomposition mechanism relevant at large doping concentrations. The inset shows the most probable decomposition mechanism. This figure is published in reference [204].

Core Level Analysis

In the following, the effect of evaporation rate and temperature on the core level energies of o-MeO-DMBI-Cl decomposition products is investigated. Therefore, X-ray photoelectron spectroscopy (XPS) was performed on three layers (thickness: ca. 4 nm) processed on gold foils at varying dopant evaporation rates that are typically used for molar doping ratios of 0.02, 0.1, and 1. A sample processed via spin coating from ethanol solution at room temperature represents the intact precursor molecule o-MeO-DMBI-Cl before decomposition. The Cl2p, O1s, C1s, and N1s emission spectra of o-MeO-DMBI-Cl in Figure 5.6 exhibit peak positions which agree well with the chemical structure of the precursor molecule [164]. In good agreement to the expected splitting of chlorine from the precursor molecule, the intensity of its chlorine emission, denoted as Cl2p (1), vanishes for the evaporated samples. However, the spectra of the evaporated samples reveal a new chlorine peak at higher binding energies, denoted as Cl2p (2), which might indicate the presence of ClCH₃ in the evaporated films and further supports the consideration that a demethylation from the precursor molecule occurs at high evaporation temperatures. The shapes of the C1s and N1s emission are very similar among the four samples under investigation. In contrast, the O1s emission changes substantially with the processing condition. The peak of the precursor molecule at 534.0 eV, denoted as O1s (1), vanishes after thermal evaporation and two new peaks appear at 533.3 eV and 530.6 eV, named as O1s (2a) and O1s (2b), respectively.

Figure 5.7a shows the intensities of the Cl2p, O1s, and C1s emissions, each scaled by the respective N1s intensity and corrected by atomic sensitivity factors [165]. While the relative Cl2p (1) intensity fits well to the chemical structure of the precursor molecule, the C1s and O1s (1) intensities are slightly too large. As purification of the precursor

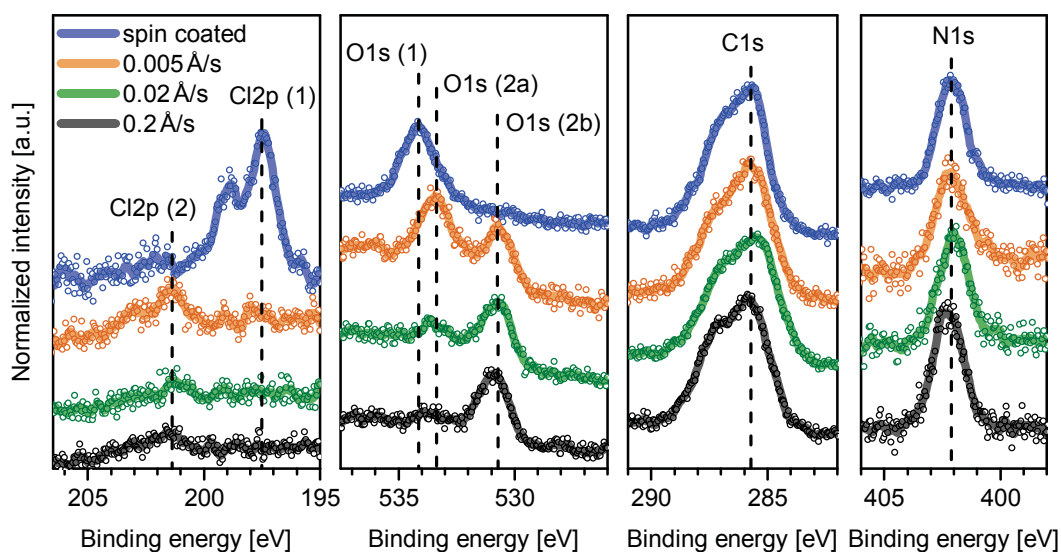


Figure 5.6: Chemical composition of o-MeO-DMBI-Cl layers with different fabrication conditions: Cl2p (1) belongs to intact precursor molecules, while Cl2p (2) refers to decomposition products. The change from O1s (2a) to O1s (2b) indicates a demethylation at the oxygen position at higher evaporation rates. A similar version of this figure is published in reference [204].

molecule by sublimation was not possible, the increased intensities might originate from impurities. The reduction of the C1s intensity with evaporation rates agrees well with a demethylation from the precursor molecule. Simultaneously, the O1s (2b) emission at lower binding energy increases with evaporation rate, while the O1s (2a) emission at high binding energies decreases. The O1s (2b) emission might belong to decomposition products where the methyl group at the oxygen atom is removed.

Figure 5.7b shows corresponding UPS spectra of the four samples. The precursor exhibits a large ionization energy (IE) of 6.75 eV, making it stable against air exposure. All evaporated samples have a lower IE than the precursor. However, even the evaporated sample with the lowest rate does not have an IE below 4 eV, which should be necessary for efficient n-doping of bis-HfI-NTCDI or C_{60} . Probably, the n-doping radicals form dimers in a neat film, having higher IE values compared to single radicals.

Experimental core level energies and IE values obtained with XPS and UPS are now compared to energies calculated with density functional theory (DFT) simulations⁵, in particular the energies of the precursor, the n-doping radical, and the three possible decomposition products with one methyl group removed. For a better analysis of the energy shifts, all experimental and simulated energy values are subtracted by the respective energy of the precursor molecule. As a result, the core level energies and the IE of the sample with the largest evaporation rate exhibit the best agreement with the simulated energies for the decomposition product where a methyl group is split from the oxygen atom (Table

⁵ The DFT simulations were performed by Dr. Reinhard Scholz at IAPP.

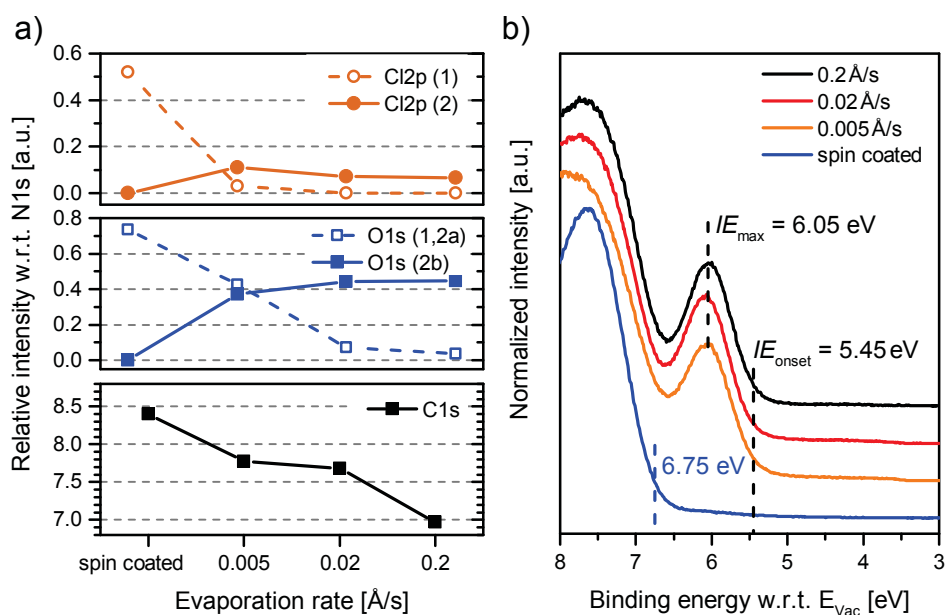


Figure 5.7: (a) Dependence of the chemical composition of o-MeO-DMBI-Cl layers on evaporation rate. The relative intensities with respect to the N1s intensity are corrected by atomic sensitivity factors taken from reference [165]. (b) Corresponding UPS spectra of o-MeO-DMBI-Cl films, where the zero of the binding energy scale is set to the vacuum level E_{vac} . A similar version of this figure is published in reference [204].

5.1). The IE of this sample is very similar to the energy of the impurities observed in bis-HfI-NTCDI:o-MeO-DMBI-Cl/Br layers in Figures 5.3b and 5.4. These results suggest that at high evaporation temperatures, the precursor molecule splits into CH_3Cl and a doping inactive zwitterion, acting as a charge carrier trap, which can be removed by thermal annealing (see inset of Figure 5.5). While the energy of the O1s (2a) emission peak agrees well with the energy of the n-doping radical obtained from calculation, the N1s emission and the IE are expected to appear at lower binding energies. As noted before, this disagreement might be due to the low stability of the radicals, which probably form dimers in a neat film so that the radicals are not detectable by UPS. Apart from the undesired decomposition mechanism, the formation of o-MeO-DMBI dimers might further reduce the doping efficiency at high concentrations.

Table 5.1: Relative core level and ionization energies: All measured (XPS, UPS) and calculated (DFT) values are given relative to the energy of the precursor molecule. A positive relative value implies a binding energy being larger than for the precursor molecule. The XPS/UPS binding energies are given with respect to the vacuum level. The (vertical) ionization energy (*IE*) calculated by DFT is obtained for single molecules in the gas phase. The O1s and N1s binding energies calculated by DFT refer to orbital energies. N (1) belongs to the N atom located closer to the oxygen atom. The DFT simulations were performed by Dr. Reinhard Scholz at IAPP. The data are published in reference [204].

| | O1s (XPS) [eV] | N1s (XPS) [eV] | <i>IE</i> (UPS) [eV] | O1s (DFT) [eV] | N1s (DFT) [eV] | <i>IE</i> (DFT) [eV] |
|-------------|-------------------|-------------------|-------------------------|-------------------|-------------------|-------------------------|
| spin coated | 0 | 0 | 0 | 0 | 0 | 0 |
| 0.005 Å/s | -0.8/-3.4 | 0/? | -1.3 | | | |
| 0.2 Å/s | -3.6 | -0.2 | -1.3 | | | |
| radical | | | | -0.8 | -1.0/-1.0 | -2.7 |
| demeth. at: | | | | | | |
| O | | | | -3.8 | 0.1/0.0 | -0.9 |
| N (1) | | | | -0.5 | -3.1/-0.8 | 0.2 |
| N (2) | | | | -0.3 | -0.9/-3.1 | 0.2 |

Conclusion

In conclusion, the air stable precursor (2-Cyc-DMBI)₂ showed the best performance in bis-HfI-NTCDI among all n-dopants investigated and, therefore, it is mainly used for the basic investigations in the following sections of this chapter. At high doping concentrations, (2-Cyc-DMBI)₂ led to higher conductivities in comparison to the reference dopant Cr₂(hpp)₄. The larger conductivity was attributed to the small molecular mass of this dopant, introducing less energetic disorder to the doped films in comparison to the large dopant Cr₂(hpp)₄. bis-HfI-NTCDI films doped by the air stable precursor molecules o-MeO-DMBI-X (X = Cl, Br, I) exhibited lower conductivities and lower doping efficiencies at high concentrations. The core level analysis indicated that this is due to a change of the decomposition mechanism at high evaporation temperatures, providing a large amount undesired doping-inactive decomposition products. These products, reducing the electrical conductivity, were removable by thermal annealing.

Both species of air stable n-dopant precursors, (2-Cyc-DMBI)₂ and o-MeO-DMBI-X, introduced n-doping species into the vacuum chamber, resulting in an background n-doping effect even days after the last dopant evaporation. Furthermore, preliminary measurements indicated that 2-Cyc-DMBI can diffuse within the doped films or evaporate from the surface of the sample at elevated sample temperatures. Therefore, despite its good doping characteristics, (2-Cyc-DMBI)₂ does not seem to fulfill the requirements for device application. However, it is a good basis for the design of new molecules and ideal for basic investigations on n-doping due to its high doping efficiency.

5.2 Analysis of Electronic States

The density of states in organic semiconductors plays an important role for charge carrier transport. Before the discussion of the electrical conductivity in Section 5.3, the occupied and unoccupied density of states of n-doped semiconductors are analyzed in this section using ultraviolet and inverse photoelectron spectroscopy. The experimental data are discussed within the framework of an integer charge transfer model, which assumes an integer charge transfer from dopant to matrix molecule and neglects any hybridization of molecular orbitals of matrix and dopant molecules [44]. In such a case, integer charge transfer complexes (ICTCs) determine the density of states of doped semiconductors. The variation of energy levels among several matrix molecules n-doped with (2-Cyc-DMBI)₂ is correlated with respective molecular parameters obtained with density functional theory simulations, namely the relaxation energy of matrix anions, the Coulomb binding energy of ICTCs and the quadrupole moment of matrix molecules. Most of the results discussed in this section are included in references [211, 212].

5.2.1 Integer Charge Transfer Complexes

After integer charge transfer from a dopant to a matrix molecule, the two ions form a (ground state) *integer charge transfer complex* (ICTC), whose energy levels considerably differ from the levels of neutral molecules. In contrast to the excited charge transfer (CT) state of donor and acceptor molecules in solar cells, the ICTC comprising a donor cation and an acceptor anion is the ground state for matrix-dopant combinations with an efficient initial charge transfer. An efficient charge transfer is expected to occur when the ionization energy IE_D of the donor molecule is smaller than the electron affinity EA_A of the acceptor. The energy levels of an ICTC can be qualitatively understood by considering a separation of the ICTC formation into several subsequent steps. As this chapter mostly covers n-doping, the following discussion focuses on the energy levels of the acceptor, i.e. the matrix molecule for n-doping.

Figure 5.8 depicts the change of energy levels of donor and acceptor within a simplified sketch. After electron transfer from donor to acceptor, the (former) LUMO of the acceptor is occupied by one electron. The IE of the acceptor anion ($IE_{A,\text{anion}}$) corresponds to the removal of this electron. Without geometrical relaxation of the anion, $IE_{A,\text{anion}}$ is equal to the EA of the neutral acceptor (EA_A). Due to on-site Coulomb repulsion, the EA of the acceptor anion ($EA_{A,\text{anion}}$) is reduced with respect to EA_A [213]. The presence of the additional electron also shifts the other electronic levels of the anion to higher energies, corresponding to a reduction of the binding energy of the electronic states. As the anion is still in the ground state geometry of the neutral molecule directly after ionization, it loses its relaxation energy $\lambda_{A,-}$ in a subsequent geometric relaxation process (see Section 2.1.1). Removing the electron from the relaxed anion leads to a neutral molecule being in the

ground state geometry of the anion. It is assumed that the energy lost in the subsequent relaxation to the ground state of the neutral molecule is equal to $\lambda_{A,-}$. In that case, $IE_{A,\text{anion}}$ of the relaxed anion is increased by $2\lambda_{A,-}$ with respect to EA_A of the neutral molecule [59, 60]. The other levels of the acceptor anion may also change with geometric relaxation. However, they are less relevant for the n-doping process.

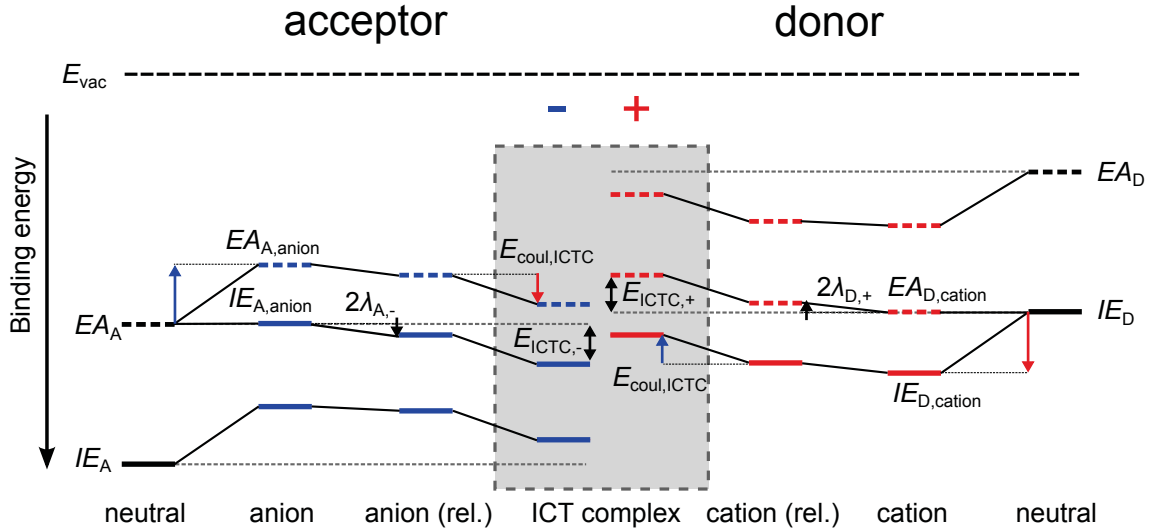


Figure 5.8: Sketch of the energy levels of an integer charge transfer complex (ICTC): The Coulomb binding energy ($E_{\text{coul,ICTC}}$) and the relaxation energy ($\lambda_{A,-}$, $\lambda_{A,+}$) result in an increase of $IE_{A,\text{anion}}$ and a decrease of $EA_{D,\text{cation}}$, respectively. $E_{\text{ICTC,-}}$ and $E_{\text{ICTC,+}}$ denote the binding energies of electrons and holes within ICTCs, respectively.

Since the acceptor anion is located next to a donor cation within an ICTC, the electronic states typically shift by a few 100 meV due to the Coulomb binding energy ($E_{\text{coul,ICTC}}$). Accordingly, all levels of the anion shift to higher binding energies, causing an increase of $IE_{A,\text{anion}}$ and $EA_{A,\text{anion}}$. All of the described effects equally apply to the donor molecule within the ICTC and shift its electronic levels in the opposite direction (Figure 5.8). Note that the difference between $IE_{A,\text{anion}}$ and $EA_{D,\text{cation}}$ is larger than the difference between EA_A and IE_D due to the geometrical relaxation process. This might decrease the probability of a electron transfer back to the dopant for large values of $\lambda_{D,+}$ or $\lambda_{A,-}$.

In a simple picture, the charge on the matrix ion located in an ICTC has to be separated from the dopant ion for charge transport. Therefore, the binding energy of charges in an ICTC can be defined as the difference between bound and free charge carriers. According to the sketch in Figure 5.8, the binding energy of electrons in an ICTC for n-doping is:

$$E_{\text{ICTC,-}} = IE_{A,\text{ICTC}} - EA_A = E_{\text{coul,ICTC}} + 2\lambda_{A,-}, \quad (5.1)$$

where $IE_{A,ICTC}$ is the IE of the acceptor anion within the ICTC. Accordingly, the binding energy of holes for p-doping is:

$$E_{ICTC,+} = IE_D - EA_{D,ICTC} = E_{coul,ICTC} + 2\lambda_{D,+}, \quad (5.2)$$

with $EA_{D,ICTC}$ being the EA of the donor cation within the ICTC.

5.2.2 Example of n-Doped ZnPc and C₆₀

To validate the considerations of Section 5.2.1, highly sensitive ultraviolet photoelectron spectroscopy (UPS) and low-energy inverse photoelectron spectroscopy (LEIPS) results on ZnPc and C₆₀ each n-doped by (2-Cyc-DMBI)₂ are discussed in the following⁶. Figure 5.9 shows the spectra of intrinsic and highly n-doped ZnPc and C₆₀, where the occupied states below E_F were probed by UPS and the unoccupied states above E_F were probed by LEIPS. Apart from a shift of E_F towards the LUMO peak, new emission peaks emerge in the spectra of the n-doped films. Furthermore, the spectra of n-doped films are considerably broadened due to an increase of energetic disorder. In the following, the peaks of the spectra are analyzed using Gaussian functions to obtain values for $IE_{A,ICTC}$ and EA_A .

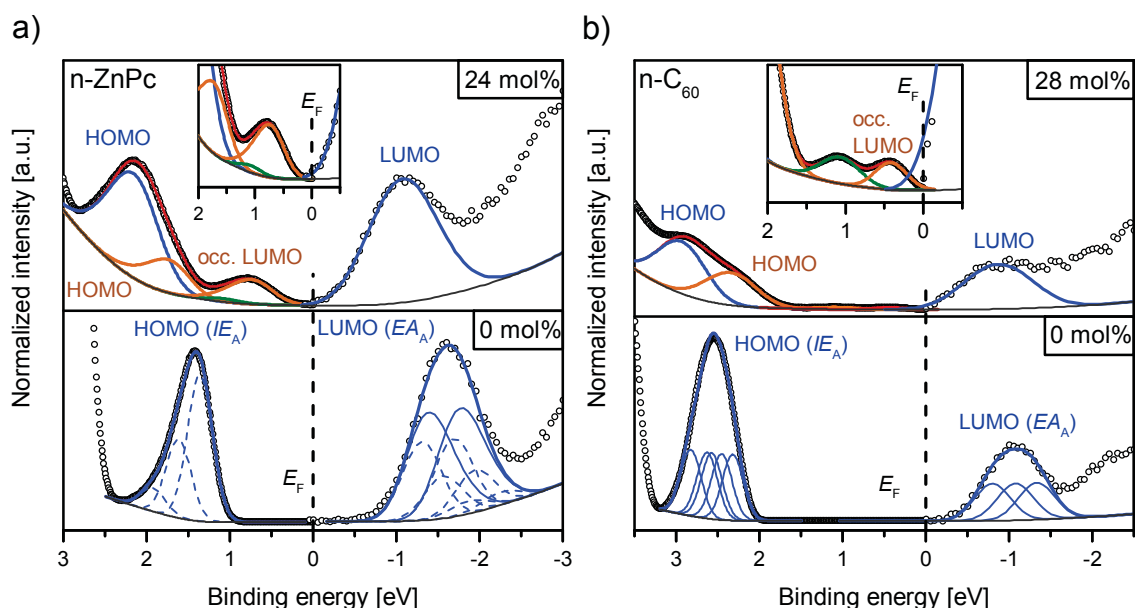


Figure 5.9: UPS and LEIPS spectra of n-doped ZnPc and C₆₀: After subtraction of a Tougaard background (gray), fitting the experimental data (circles) by a set of Gaussian functions yield the energies of neutral (blue) and negatively charged (orange) molecules. The green peaks are attributed to intact precursor molecules of the n-dopant. The samples with a thickness around 20 nm were evaporated at rates around 0.05 Å/s on silicon substrates covered by a native oxide. The data are included in references [211, 212].

⁶ The highly sensitive UPS and LEIPS measurements were performed by Dr. Fabio Bussolotti in the lab of Prof. Satoshi Kera at the Institute for Molecular Science in Okazaki, Japan.

Analysis of Electronic States

First, the UPS and LEIPS spectra of an intrinsic ZnPc layer are analyzed. The peaks of the spectra can be fitted each with a set of Gaussian functions to obtain the energy of the electronic states. After subtracting a Tougaard background beforehand, at least three Gaussian functions are necessary to fit the HOMO peak of ZnPc (Figure 5.9a). The three Gaussian functions at different binding energies correspond to different vibrational modes of the ionized molecule [214–216]. The distance and intensity of the smaller Gaussian functions relative to the largest Gaussian function are 0.26 eV and 0.56 eV as well as 54% and 16%, respectively. The full width at half maximum (FWHM) is 350 meV and set equal for all Gaussian functions. When the same triple set of Gaussian functions with the same intensity ratio and relative distances is used for fitting the LUMO peak, the FWHM needs to be increased to 550 meV due to the experimental error of LEIPS (= 420 meV). Although the two LUMO states of ZnPc are degenerate in density functional theory (DFT) simulations⁷, two triple sets of Gaussian functions with a relative distance of 380 meV are necessary for fitting the peak. This can be explained by a symmetry breaking in the solid state, specifically at the surface. In particular, the splitting of the LUMO peak in LEIPS might be due to the different charge distribution on the anion when either one or the other LUMO state is occupied.

Three new peaks emerge in the UPS spectrum of the n-doped ZnPc layer (Figure 5.9a). According to the sketch in Figure 5.8, two of these new peaks originate from ZnPc anions located close to n-dopant cations. The peak just below E_F is attributed to emission from occupied LUMO states of anions, while the peak at around 1.7 eV indicate emission from (former) HOMO states. The peak at 1.1 eV probably belongs to n-dopant precursor molecules that were not split upon evaporation. The triple set of Gaussian functions obtained from the intrinsic spectrum is also used to fit the spectrum of n-doped ZnPc. However, the FWHM of the functions need to be increased to fit the peaks of neutral molecules and anions of n-doped ZnPc. The broadening indicates an increase of energetic disorder due to the introduction of n-dopants.

A similar fitting procedure can be applied to the spectra of intrinsic and n-doped C₆₀ (Figure 5.9b). Instead of a triple set of Gaussian functions with varying intensity, five (three) Gaussian functions with equal intensity can fit the HOMO (LUMO) peak, accounting for the large degeneracy of these states. The high degeneracy of the HOMO also reflects in a large intensity ratio between the HOMO peak and the occupied LUMO peak in the UPS spectrum.

The Gaussian fits and the sample work functions obtained from the spectra can be used to calculate values of $IE_{A,ICTC}$ and EA_A for different doping concentrations. The results plotted in Figure 5.10 reveal an increase of $E_{ICTC,-}$ with molar doping ratio for n-doped ZnPc and C₆₀. This increase correlates with an increase of the FWHM of occupied LUMO

⁷ Simulations are performed by Dr. Christopher Gaul of the group of Dr. Frank Ortman at TU Dresden.

peaks. Apparently, larger energetic disorder of ICTCs increases $E_{\text{ICTC},-}$, which seems reasonable as electrons preferably occupy ICTCs with the lowest energy around a dopant cation. Apart from the dependence on energetic disorder, a reduction of the dielectric constant with doping concentration might be another reason for the increase of $E_{\text{ICTC},-}$. In any case, n-doped ZnPc layers have values for $E_{\text{ICTC},-}$ increased by roughly 0.5 eV in comparison to n-doped C_{60} . In the following, this difference is correlated to molecular parameters.

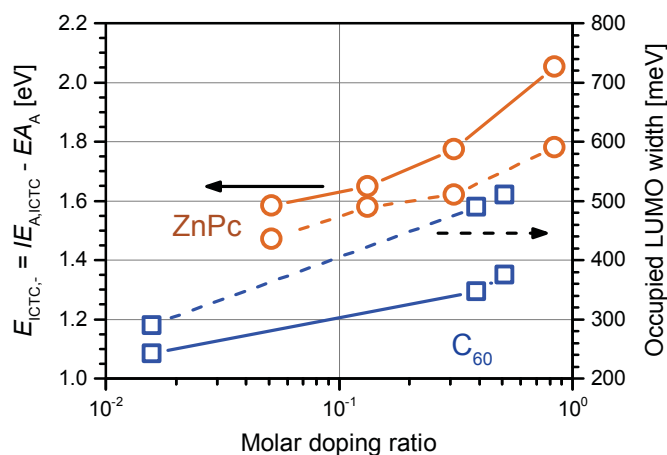


Figure 5.10: Increase of ICTC binding energy with energetic disorder: The binding energy of electrons in an ICTC ($E_{\text{ICTC},-}$, solid lines) and the FWHM of occupied LUMO peaks (dashed lines) are obtained from Gaussian fits applied to the UPS and LEIPS spectra shown in Figure 5.9. The data are included in reference [212].

Correlation with Molecular Parameters

Molecular parameters obtained from density functional theory (DFT) simulations are now utilized to explain the difference in $E_{\text{ICTC},-}$ between n-doped ZnPc and n-doped C_{60} . The molecular relaxation energies of matrix anions ($\lambda_{\text{A},-}$) obtained from DFT calculations⁸ are $\lambda_{\text{A},-} = 173 \text{ meV}$ for ZnPc and $\lambda_{\text{A},-} = 85 \text{ meV}$ for C_{60} . Furthermore, the Coulomb binding energy of ICTCs ($E_{\text{coul,ICTC}}$) in their optimized geometry can be calculated by DFT⁹. As a result, the dimer configuration with the lowest energy exhibits an $E_{\text{coul,ICTC}}$ of 0.93 eV for ZnPc:2-Cyc-DMBI and 0.45 eV for C_{60} :2-Cyc-DMBI when dielectric constants of $\epsilon_r = 2.8$ (ZnPc) and $\epsilon_r = 4.4$ (C_{60}) are used, respectively [173].

The molecular contributions of molecular relaxation and Coulomb binding energy to $E_{\text{ICTC},-}$ are expected to add up like: $E_{\text{coul,ICTC}} + 2\lambda_{\text{A}}$ (Figure 5.8). This leads to values of 1.28 eV and 0.62 eV as molecular contributions to $E_{\text{ICTC},-}$ in n-doped ZnPc and C_{60} , respectively. Their difference is only slightly larger than the difference between the

⁸ All $\lambda_{\text{A},-}$ values presented in this thesis were calculated by Dr. Christopher Gaul or Sebastian Schellhammer in the group of Dr. Frank Ortmann (TU Dresden).

⁹ All $E_{\text{coul,ICTC}}$ values used for the discussion in this thesis were obtained by Dr. Reinhard Scholz at IAPP.

$E_{\text{ICTC},-}$ values observed in experiment (Figure 5.10). Apart from a different energetic disorder, the surface sensitivity of the experimental techniques can explain this deviation. Weaker screening effects at the sample surface compared to the bulk can induce energy shifts of few 100 meV in experiment [24, 161]. Similarly, the Coulomb binding energy is probably increased at the sample surface, causing larger $E_{\text{ICTC},-}$ values at the sample surface. Nevertheless, the difference in molecular parameters, particularly in $E_{\text{coul,ICTC}}$, can qualitatively explain the large difference in $E_{\text{ICTC},-}$ between n-doped ZnPc and n-doped C₆₀.

5.2.3 Highly Efficient Charger Transfer from 2-Cyc-DMBI

As filled LUMO states of anions appear just below the Fermi level, the degree of charge transfer from n-dopant to matrix molecule can be qualitatively analyzed by UPS. The degree of charge transfer is expected to depend on the relative position of the ionization energy of the n-dopant (IE_{D}) and the electron affinity of the accepting matrix molecule (EA_{A}). ZnPc is the matrix molecule with the lowest EA_{A} ($= 3.0$ eV) which still experiences a significant conductivity increase upon n-doping with (2-Cyc-DMBI)₂. The results in Chapter 4 indicated that EA_{A} of F_nZnPc can be increased¹⁰ stepwise by the degree of fluorination, making n-doped F_nZnPc an ideal model system to investigate the impact of EA_{A} on the charge transfer efficiency.

Figure 5.11 displays the UPS spectra of ZnPc, F₈ZnPc and C₆₀ each n-doped by (2-Cyc-DMBI)₂ with varying doping concentration. All spectra reveal an increasing intensity of the occupied LUMO peak with molar doping ratio. Remarkably, all three matrix-dopant combinations exhibit a vanishing emission from neutral matrix molecules at high molar doping ratios above 1, indicating a high charge transfer efficiency for all combinations. Apparently, the variation of EA_{A} in this range does not have a significant influence on the charge transfer efficiency. Furthermore, the high charge transfer efficiencies suggest that these systems do not exhibit a substantial negative impact of dopant clustering even at high doping concentrations. This is remarkable because the measurements on neat (2-Cyc-DMBI)₂ films in Section 5.1 indicated that 2-Cyc-DMBI radicals, i.e. the actual n-doping species, tend to form dimers.

While the IE of neutral ZnPc and C₆₀ molecules changes only slightly with molar doping ratio, the IE of neutral F₈ZnPc molecules substantially decreases with molar doping ratio. The origin of the different behavior is not clear. As shown in Section 4.2, the quadrupole moment of ZnPc (F₈ZnPc) induces a decrease (increase) of IE in neat layers. This effect seems to become weaker with increasing molar doping ratio. The solid state correction Δ_+ for the IE of intrinsic F_nZnPc layers increased linearly with Q_{π} with a slope of $0.023 \text{ eV}/ea_0^2$. For ZnPc, F₄ZnPc, and F₈ZnPc n-doped with 10 mol% of (2-Cyc-DMBI)₂,

¹⁰ As previous studies observed for the similar system of F_nCuPc only a slight change in the IE - EA difference with fluorination [57], it is also expected for F_nZnPc that IE and EA similarly increase with fluorination.

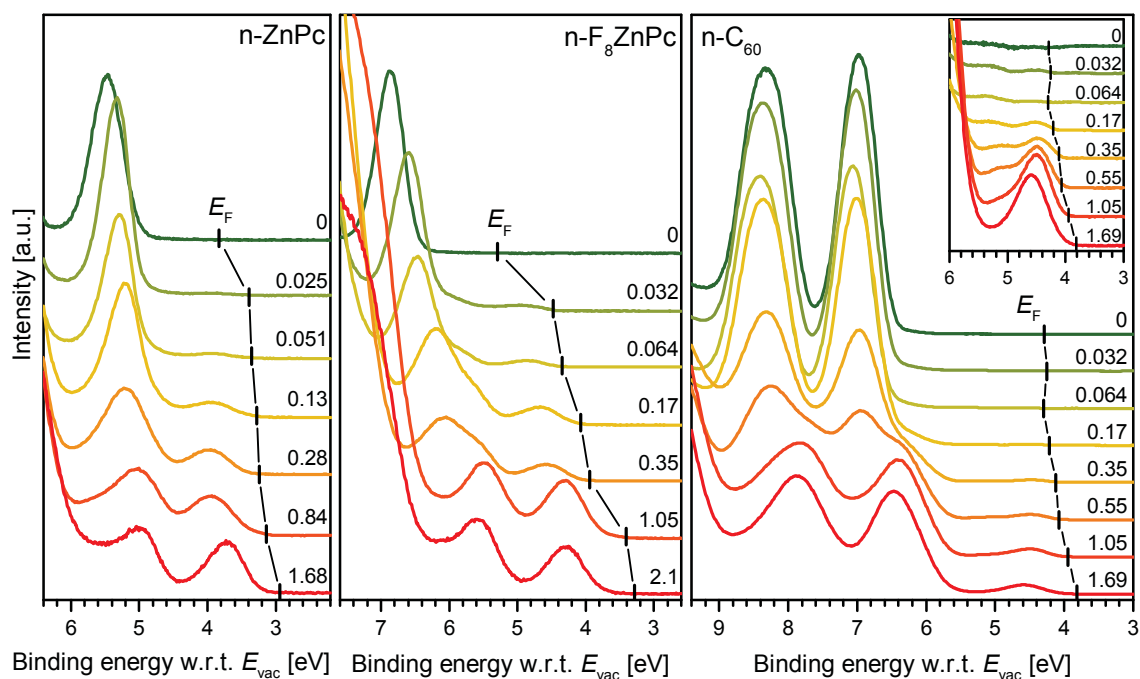


Figure 5.11: UPS spectra at different doping concentrations: The spectra indicate a high charge transfer efficiency from 2-Cyc-DMBI to ZnPc, F_8 ZnPc, and C_{60} as seen by the vanishing emission from neutral molecules at large molar doping ratios. The numbers on the low binding energy side of each spectrum denote the respective molar doping ratio. The spectra were obtained with the UPS setup at IAPP. The figure is included in reference [212].

the slope is reduced to around $0.017 \text{ eV}/ea_0^2$. Apart from this, the spectra of n-doped F_8 ZnPc and C_{60} show a larger HOMO peak difference between neutral molecules and anions. According to the sketch in Figure 5.8, this could originate from a smaller Coulomb binding energy of the ICTC. In fact, F_8 ZnPc:2-Cyc-DMBI reveals a value for $E_{\text{coul,ICTC}}$ which is 0.24 eV lower than for ZnPc:2-Cyc-DMBI.

5.2.4 Importance of Energetic Disorder at 10 mol%

As shown in Section 5.3, the conductivity at a doping concentration of 10 mol% is typically close to the maximum achievable conductivity of the respective material combination. Therefore, it is particularly interesting to investigate the electronic states at a doping concentration of 10 mol% in more detail. In particular, the position of E_F with respect to the highest occupied electronic states in n-doped semiconductors is expected to crucially affect charge carrier activation and transport. This energy difference is directly obtained from the peak position of occupied LUMO states in UPS spectra. This value describes the energy necessary to excite electrons from occupied LUMO states of matrix anions within ICTCs to E_F , being equal to $IE_{A,ICTC}$ subtracted by the sample work function. From the molecular picture in Figure 5.8, one might expect that the distance between occupied LUMO states and E_F increases with a larger Coulomb binding energy

of ICTCs ($E_{\text{coul,ICTC}}$). Figure 5.12a shows both parameters for different matrix molecules n-doped with 10 mol% of (2-Cyc-DMBI)₂. A clear correlation, however, is not visible. Apparently, $E_{\text{coul,ICTC}}$ is not the only parameter determining the position of the occupied LUMO states at such high concentrations.

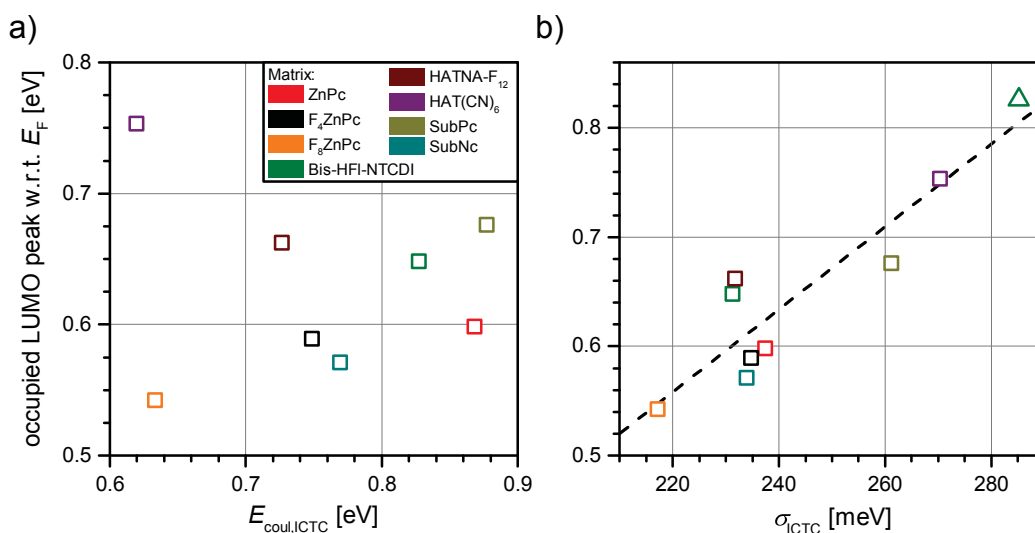


Figure 5.12: Impact of energetic disorder on occupied LUMO states: (a) No clear correlation between $E_{\text{coul,ICTC}}$ and occupied LUMO peak positions as obtained from UPS spectra. All matrix molecules are n-doped by (2-Cyc-DMBI)₂. (b) The distance of occupied LUMO states to E_F increases with the energetic disorder of ICTCs (σ_{ICTC}). The green triangle depicts a bis-HFI-NTCDI sample n-doped with $\text{Cr}_2(\text{hpp})_4$. The data are included in reference [212].

Apart from $E_{\text{coul,ICTC}}$, the energetic disorder significantly affects $IE_{\text{A,ICTC}}$ (Figure 5.10). In a Gaussian density of states (DOS), the relative distance between occupied DOS and E_F increases for larger widths of the Gaussian DOS [81]. If the density of accessible ICTC configurations is Gaussian like, the position of the occupied LUMO states in UPS spectra should shift to larger binding energies when the energetic disorder of possible ICTC configurations increases. A qualitative measure for the energetic disorder of occupied ICTCs can be obtained from the width of the occupied LUMO peaks in UPS spectra (σ_{ICTC}). As shown in Figure 5.12b, the distance between occupied LUMO states and E_F increases with σ_{ICTC} for the matrix materials investigated in this study. These results indicate that at a doping concentrations of 10 mol%, charge carriers need to be thermally activated over large energy barriers when the energetic disorder of ICTCs is increased. In good agreement, the results in Section 5.3 show that the electrical conductivity at such high concentrations crucially depends on the energetic disorder of ICTCs.

Correlation with Molecular Parameters

In the following, the molecular origin of the energetic disorder of ICTCs is discussed. In addition to the intrinsic disorder of the neat matrix material, the introduction of dopants

typically results in an increase of energetic disorder. On the one hand, dopant molecules can disrupt the local structure of the matrix film, which is relevant particularly for crystalline matrix materials and large dopant molecules [119]. As the n-dopant (2-Cyc-DMBI)₂ has a very low molar mass, the increase of structural disorder might be reduced compared to larger n-dopants. Furthermore, the charged matrix-dopant pairs have large dipole moments, introducing electrostatic disorder into the film. Previous studies observed an increase of energetic disorder with increasing density and magnitudes of dipole moments [217]. This can explain the increase of energetic disorder with molar doping ratio, as observed for n-doped ZnPc and C₆₀ (Figure 5.10).

The energetic disorder might further increase due to varying Coulomb binding energies among different ICTC configurations originating from varying distances and relative orientations of the respective matrix anions and dopant cations. Therefore, the energetic disorder of ICTCs might be connected to $E_{\text{coul,ICTC}}$, which belongs to the ICTC configuration with the lowest total energy. Indeed, σ_{ICTC} increases linearly with $E_{\text{coul,ICTC}}$ for six out of eight matrix materials investigated here (Figure 5.13a). The deviation of two matrix materials from the trend can be explained by their low molar masses below 500 u , resulting in a large ICTC density. Apparently, the electrostatic disorder induced by surrounding dipole moments further increases σ_{ICTC} for such high ICTC densities. The electrostatic disorder is also expected to increase for large ICTC dipole moments. Therefore, a large distance between electron and hole in a ICTC might result in a higher energetic disorder, although it probably helps to decrease $E_{\text{coul,ICTC}}$. A large ICTC dipole moment serves as a possible explanation for the much higher energetic disorder for bis-HfI-NTCDI n-doped by the sterically more demanding n-dopant Cr₂(hpp)₄ compared to the planar dopant (2-Cyc-DMBI)₂ (see Figure 5.3 in Section 5.1).

As the binding energy of electrons in ICTCs ($E_{\text{ICTC,-}}$) and the energetic disorder of ICTCs (σ_{ICTC}) correlate with $E_{\text{coul,ICTC}}$, it is interesting which parameters determine the magnitude of $E_{\text{coul,ICTC}}$. Intuitively, an increase of the distance between matrix and dopant molecule should directly reduce $E_{\text{coul,ICTC}}$ but might be difficult to realize particularly for planar small molecules. Although the distance between the centers of charge of matrix anion and dopant cation varies among the different matrix molecules, $E_{\text{coul,ICTC}}$ does not reduce with increasing distance (Figure 5.13b).

As shown in Section 4.4, the donor-acceptor combination ZnPc:C₆₀ has a smaller value for $E_{\text{coul,CT}}$ compared to F₄ZnPc:C₆₀ due to the different quadrupole components Q_{π} of ZnPc and F₄ZnPc. The correlation in Figure 5.13c indicates that $E_{\text{coul,ICTC}}$ also depends on Q_{π} for the case of molecular doping. The deviation of SubNc from the general trend can be explained by its large intrinsic dipole moment, reducing $E_{\text{coul,ICTC}}$. Larger positive values of Q_{π} for matrix (acceptor) molecules imply a relocation of negative charge to the edge of the molecule, which increases the effective distance between the negative and positive charge distribution, resulting in a reduced $E_{\text{coul,ICTC}}$. A negative Q_{π} value for n-dopants or matrix molecules in the case of p-doping should reduce $E_{\text{coul,ICTC}}$ in the same way.

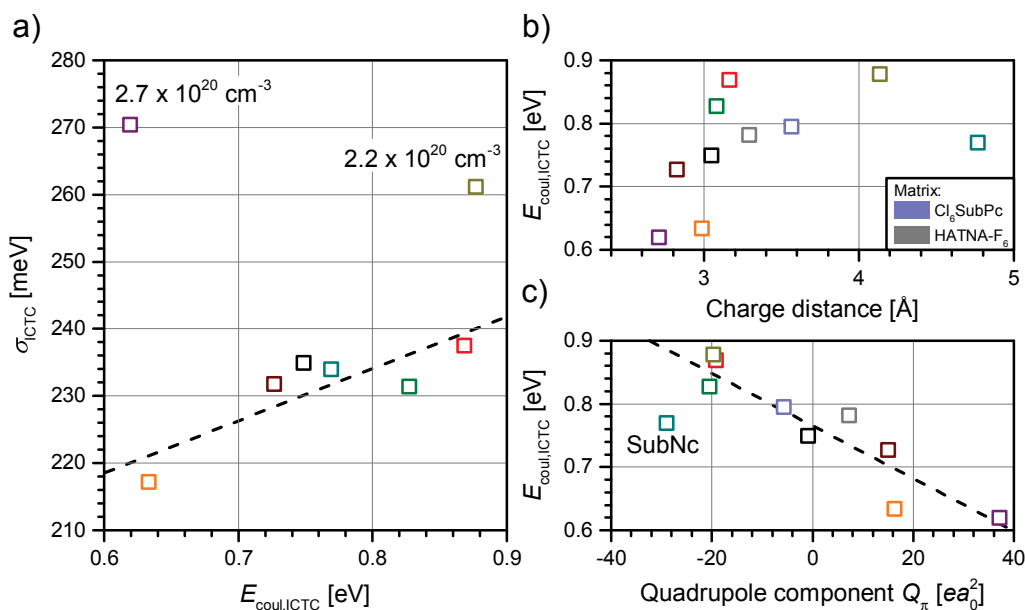


Figure 5.13: Correlation of energetic disorder with molecular parameters: (a) Energetic disorder of ICTCs increases with $E_{\text{coul,ICTC}}$ for small ICTC densities. The two matrix materials with increased σ_{ICTC} have comparably large ICTC densities above $2 \cdot 10^{20} \text{ cm}^{-3}$. (b) $E_{\text{coul,ICTC}}$ does not decrease with larger distance between the centers of charge of the two ions. (c) $E_{\text{coul,ICTC}}$ decreases with the quadrupole component Q_{π} of matrix molecules. The symbol/color code is the same as used in Figure 5.12. In (b) and (c), the matrix materials Cl₆SubPc and HATNA-F₆ are additionally included. The data are included in reference [212].

Conclusion

In this section, the electronic states in doped organic semiconductors were discussed within the model of integer charge transfer complexes (ICTCs). In n-doped ZnPc and C₆₀, the difference between the ionization energy of matrix anions in ICTCs and the electron affinity of neutral matrix molecules increased with the energetic disorder, the relaxation energy of matrix anions, and the Coulomb binding energy of ICTCs ($E_{\text{coul,ICTC}}$). The distance between the highest occupied states and the Fermi level is expected to be an important parameter determining thermally activated transport. At high doping concentrations, this value scaled with the width of occupied LUMO peaks in UPS spectra, indicating that the energy barrier for thermal activation of charge carriers depends on the energetic disorder of ICTCs in this concentration regime. The energetic disorder was found to be proportional to $E_{\text{coul,ICTC}}$ for materials with a moderate ICTC density. A comparison of different matrix molecules revealed that a variation of the charge distribution on matrix molecules can reduce $E_{\text{coul,ICTC}}$ significantly, probably resulting in lower energy barriers for charge carrier activation. As shown in the next section, the magnitude of the electrical conductivity in n-doped semiconductors essentially depends on the magnitude of $E_{\text{coul,ICTC}}$.

5.3 Electrical Conductivity

The electrical conductivity of doped organic semiconductors typically increases with doping concentration and often reaches its maximum at concentrations above 10 mol% [40, 42, 85, 102, 120]. However, the absolute values of the conductivity as well as the concentration where the maximum is reached vary considerably among different material combinations. Therefore, the aim of this section is to correlate the variation in conductivity to material specific molecular parameters. In Section 5.3.1, the relationship between the room temperature conductivity and the thermal activation energy (E_A) obtained from temperature-dependent conductivity measurements is analyzed. Section 5.3.2 discusses possible transport mechanisms and the impact of material parameters within different concentration regimes. In Section 5.3.3, an empirical function is used for a doping concentration of 10 mol% to correlate the variation of E_A among different materials directly with material specific parameters, such as charge relaxation or energetic disorder. Most of the content of this section is included in reference [212].

5.3.1 Arrhenius-type Thermal Activation of the Conductivity

A multitude of previous studies observed an Arrhenius-type thermal activation of the conductivity in doped organic semiconductors with a reduction of the activation energy with increasing doping concentration [40, 84, 85, 102, 103, 120, 218, 219]. The conductivity at room temperature (σ_e) can be described by two parameters, the thermal activation energy (E_A) and an exponential prefactor ($\sigma_{e,\infty}$):

$$\sigma_e = \sigma_{e,\infty} \cdot \exp\left(-\frac{E_A}{k_B T}\right). \quad (5.3)$$

Doping Concentration of 10 mol%

To understand the variation of σ_e among different matrix/dopant combinations, σ_e and E_A are extracted from temperature-dependent conductivity measurements for several n- and p-doped organic semiconductors with a fixed doping concentration of 10 mol%¹¹. The results in Figure 5.14 reveal that σ_e varies between 10^{-6} S/cm and 10 S/cm and that σ_e directly scales with the respective E_A value. The n-doped fullerenes deviate from the general trend and systematically exhibit higher values for σ_e , which might be due to the higher dielectric constant or due to the special symmetry of these molecules allowing for a higher isotropy of charge transport. Apart from n-doped fullerenes, HAT(CN)₆:(2-Cyc-DMBI)₂ also exhibits a higher σ_e in comparison to other non-fullerene matrix molecules.

¹¹Most of the conductivity measurements presented in this section were performed by Olka Kaveh and Daniel Schütze at IAPP. Furthermore, part of the experimental data is taken from literature, as indicated in the figure captions.

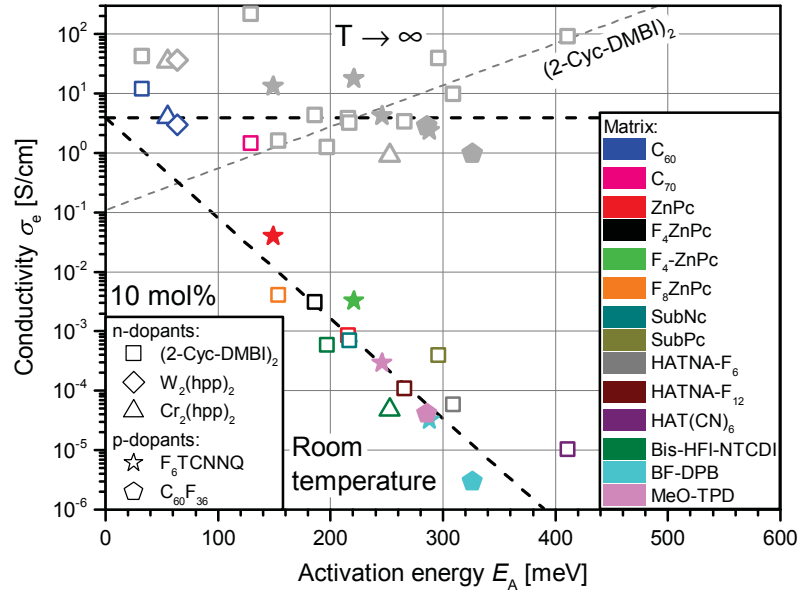


Figure 5.14: Thermally activated conductivity at 10 mol%: The Arrhenius-type thermal activation energy (E_A) controls the magnitude of the conductivity at room temperature (σ_e). Empty (filled) symbols belong to n-doped (p-doped) samples. The gray symbols correspond to $\sigma_{e,\infty}$ values calculated from σ_e and E_A using Equation 5.3. Black dashed lines are linear fits to all data excluding n-doped fullerenes. The gray dashed line is a fit to $\sigma_{e,\infty}$ values of samples n-doped with (2-Cyc-DMBI)₂. The experimental data of C₆₀:W₂(hpp)₄ and C₆₀:Cr₂(hpp)₄ as well as p-doped MeO-TPD and BF-DPB are taken from references [102, 120]. A similar version of this figure is included in reference [212].

The prefactor $\sigma_{e,\infty}$ can be calculated from σ_e and E_A with Equation 5.3. While most values lie between 1 and 20 S/cm, n-doped fullerenes and n-doped HAT(CN)₆ again have higher values due to the increased E_A . At first sight, a clear correlation between $\sigma_{e,\infty}$ and E_A for all material combinations is not observable. However, when only planar molecules n-doped with (2-Cyc-DMBI)₂ are taken into account, $\sigma_{e,\infty}$ increases exponentially with E_A , following the *Meyer-Neldel rule* observed before in previous studies [81, 82]. The trend can be fitted by following expression:

$$\sigma_{e,\infty} = \sigma_0 \cdot \exp(E_A/E_{MN}) \quad (5.4)$$

where E_{MN} is the Meyer-Neldel energy. Hence, the reduction of σ_e due to the increase of E_A is compensated by an enhancement of $\sigma_{e,\infty}$ [81, 82]. As a consequence, the conductivity of HAT(CN)₆:(2-Cyc-DMBI)₂ is still as high as 10⁻⁵ S/cm, despite the high E_A of more than 400 meV.

For the p-doped samples, $\sigma_{e,\infty}$ seems to decrease with E_A . However, the reduction of $\sigma_{e,\infty}$ from the crystalline planar matrix molecules (ZnPc, F₄-ZnPc) to the amorphous non-planar matrix molecules (BF-DPB, MeO-TPD) might be due to weaker intermolecular coupling. Therefore, it is suggested for future studies that more material combinations

with similar structural properties are used to draw conclusions about the dependence of $\sigma_{e,\infty}$ on E_A for p-doping.

With E_{MN} obtained from Equation 5.4, values for σ_0 can be obtained for the planar molecules n-doped with (2-Cyc-DMBI)₂. As a result, the variation of σ_0 is less than one order of magnitude, indicating that the change of σ_e over nearly three orders of magnitude is driven by the change in E_A . The small sensitivity of σ_0 on the matrix molecule is remarkable because this parameter is expected to depend on several material-specific properties, such as the intermolecular electronic coupling or the degree of charge carrier delocalization [82]. Apparently, the variation of these parameters is relatively small for this selection of materials or their impact is lower at such high doping concentrations.

Variation of Doping Concentration

In the following, the relation between σ_e and E_A at varying doping concentration is investigated. Figure 5.15a displays the change of σ_e with concentration for various matrix-dopant combinations. While all material combinations investigated show an increase of σ_e with increasing doping concentration below concentrations of 10 mol%, the behavior above 10 mol% considerably differs between the materials. Most of them exhibit a maximum value just above 10 mol% and a subsequent decrease of σ_e with increasing concentration. As discussed in Section 5.3.2, the decrease could originate from an increase of energetic disorder at high doping concentrations. Only MeO-TPD and BF-DPB p-doped by F₆TCNNQ show a strong increase of σ_e up to concentrations of 30 mol%. These non-planar molecules form amorphous neat films with a high energetic disorder, which might be larger than the doping-induced energetic disorder even at large concentrations.

Figure 5.15b shows the corresponding values of E_A and $\sigma_{e,\infty}$ for the material combinations presented in Figure 5.15a. The increase of σ_e correlates with a reduction of E_A with doping concentration, indicating that the strong correlation between E_A and σ_e observed for 10 mol% is remarkably independent of doping ratio. In good agreement, Figure 5.15c reveals that the prefactor $\sigma_{e,\infty}$ changes only slightly with doping concentrations. Apparently, the change of σ_e mainly originates from a change of E_A within the concentration regime investigated here. The trends observed in Figure 5.14 and Figure 5.15b indicate that it is crucial to identify material parameters that influence E_A to increase σ_e at room temperature in doped organic semiconductors.

5.3.2 Concentration Dependence of the Activation Energy

In this section, possible reasons for the change of E_A with doping concentration are discussed. Previous studies observed a negative impact of intrinsic trap states located within the energy gap on doping efficiency and charge transport at low doping concentrations below 1 mol% [40–42, 114]. As most samples investigated in this section have higher dop-

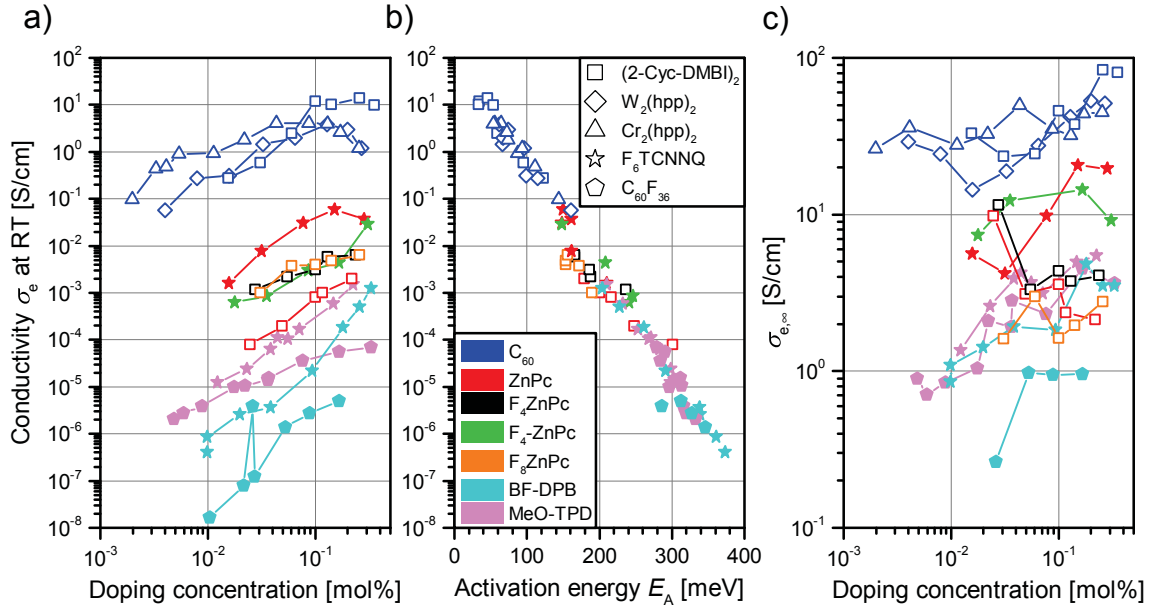


Figure 5.15: Conductivity and thermal activation energy at varying doping concentration: (a) Change of conductivity with doping concentration. (b) The conductivity change with concentration scales with the change of the activation energy. (c) The prefactor $\sigma_{e,\infty}$ varies less strongly with doping concentration compared to the change of σ_e induced by the varying E_A . The experimental data of C₆₀:W₂(hpp)₄ and C₆₀:Cr₂(hpp)₄ as well as p-doped MeO-TPD and BF-DPB are taken from references [102, 120]. The data are included in reference [212].

ing concentrations than 1 mol%, the influence of these intrinsic traps is neglected here. Instead, the following discussion focuses on the impact of integer charge transfer complexes (ICTCs) on E_A (see Section 5.2.1 for more details on ICTCs). Figure 5.16a sketches the mechanism of charge transport in the regime of low doping concentrations where the distance between ICTCs is very large. In a simple scheme, bound charges in ICTCs need to be thermally activated to transport states at higher energies to contribute to charge transport. For the case that the energetic disorder of the transport states is much smaller than the binding energy of charges in ICTCs, charge transport should be limited by the dissociation probability of ICTCs. The energy barrier for creating mobile charge carriers from bound charges in ICTCs should be mostly given by the Coulomb binding energy of ICTCs ($E_{\text{coul,ICTC}}$). The investigations of CT state dissociation in solar cells presented in Section 4.4.3 suggest that charge-quadrupole interactions with surrounding molecules might be able to further modify the ICTC dissociation barrier.

At high doping concentrations, the distance between ICTCs is reduced and interactions between charge carriers become more relevant. In such a case, transport can be described in an idealized picture by electron transport directly between different ICTC configurations, where single charge carriers are always located close to dopant ions (Figure 5.16b). At such high carrier concentrations, where the potential landscape continuously changes due to moving carriers in the surrounding, multi-electron hops may also play a role, as suggested before [220]. Thus, bound charge carriers in ICTCs might turn into mo-

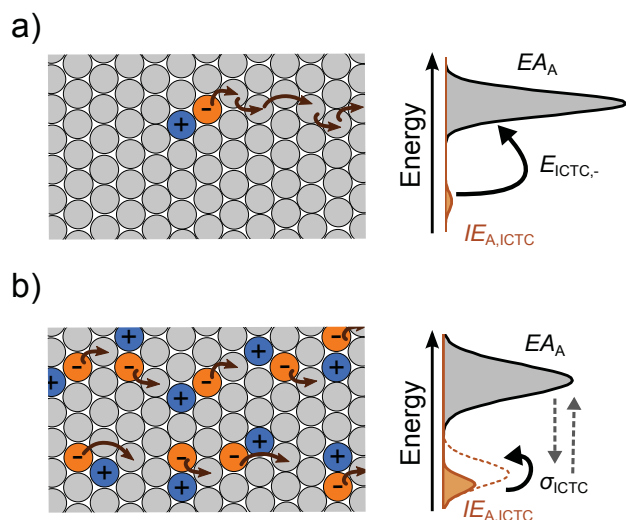


Figure 5.16: Sketch of two border cases for electron transport in n-doped organic semiconductors: (a) At low doping concentrations, ICTCs need to be dissociated for a subsequent transport of mobile charge carriers. **(b)** Due to the small distance between ICTCs at high doping concentrations, charge transport can be described by electron transport between different ICTC configurations whose local energies change continuously. A similar version of this figure is included in reference [212].

mobile charge carriers with increasing doping concentration and do not have to overcome $E_{\text{coul,ICTC}}$ towards higher-lying mobile transport states. In such a case, the energetic disorder of accessible ICTC configurations should be the limiting parameter for charge transport. Indeed, the results in Section 5.3.3 indicate that E_A at high concentrations depend on the energetic disorder of ICTCs. The analysis of electronic states at 10 mol% in Section 5.2.4 indicated that the energetic disorder of ICTCs is proportional to $E_{\text{coul,ICTC}}$ when the ICTC density is not too large. Hence, these considerations suggest that the magnitude of E_A essentially depends on $E_{\text{coul,ICTC}}$ at low and moderate doping concentrations.

Impact of the ICTC Coulomb Binding Energy on the Activation Energy

In the following, $E_{\text{coul,ICTC}}$ is systematically varied by either substituting the matrix or the dopant molecule to investigate its impact on E_A . In particular, the change of E_A with doping concentration is investigated for ZnPc, $F_4\text{ZnPc}$, and $F_8\text{ZnPc}$ doped with $(2\text{-Cyc-DMBI})_2$ as well as C_{60} doped with $(2\text{-Cyc-DMBI})_2$, $W_2(\text{hpp})_4$, or $Cr_2(\text{hpp})_4$. The increase of fluorination of $F_n\text{ZnPc}$ gradually decreases $E_{\text{coul,ICTC}}$ ¹² due to the change of the quadrupole component Q_π (see Section 5.2.4). The relaxation energies for the anions of ZnPc, $F_4\text{ZnPc}$, and $F_8\text{ZnPc}$ is very similar and should not substantially affect E_A . For n-doped C_{60} , $E_{\text{coul,ICTC}}$ decreases from the planar dopant $(2\text{-Cyc-DMBI})_2$ to the sterical dopants $W_2(\text{hpp})_4$ and $Cr_2(\text{hpp})_4$ due to the increase of the distance between matrix anion and dopant cation within the ICTC¹³. As shown in Figure 5.17 for both cases, E_A at concentrations around 1 mol% decreases when $E_{\text{coul,ICTC}}$ is reduced, supporting the consideration

¹²The DFT simulations to obtain $E_{\text{coul,ICTC}}$ were performed by Dr. Reinhard Scholz at IAPP. All values can be found in Table 7.4 of the Appendix. Note that the values always refer to an optimized dimer geometry.

¹³ $E_{\text{coul,ICTC}}$ was not calculated for the dimer of C_{60} and $Cr_2(\text{hpp})_4$. However, the group of Dr. Frank Ortmann at TU Dresden performed comprehensive DFT simulations, suggesting that $E_{\text{coul,ICTC}}$ for $C_{60}:Cr_2(\text{hpp})_4$ is smaller than for $C_{60}:W_2(\text{hpp})_4$ (see reference [211] for details).

that a low $E_{\text{coul,ICTC}}$ is necessary for efficient generation of mobile charges at low doping concentrations and for a low energetic disorder at moderate concentrations.

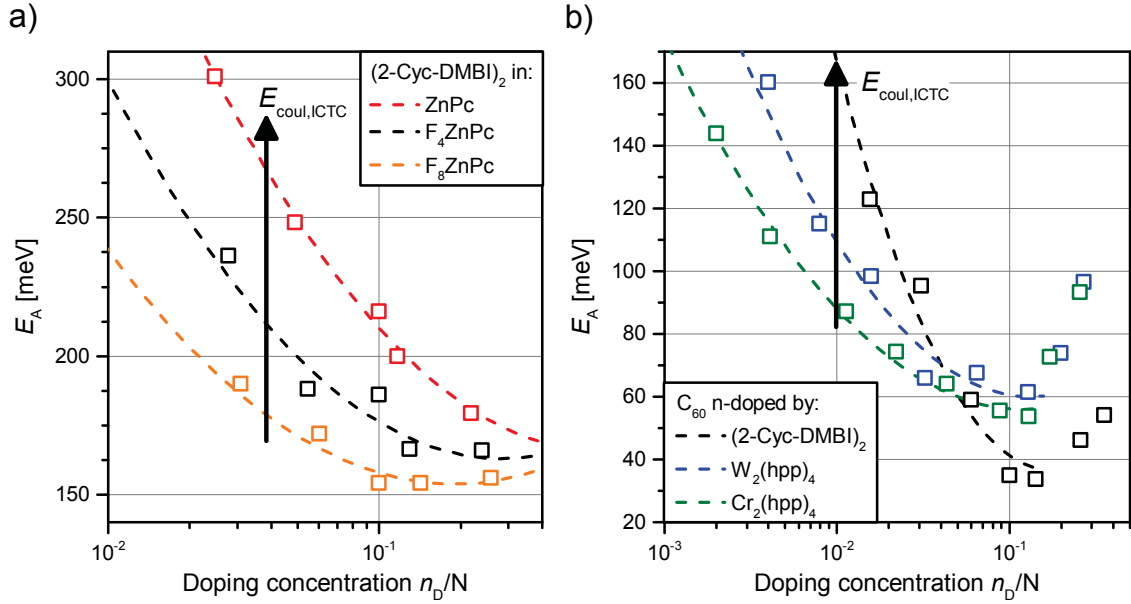


Figure 5.17: Concentration dependence of the thermal activation energy: At low and moderate concentrations, the activation energy (E_A) of n-doped F_n ZnPc (a) and n-doped C_{60} (b) increases with the Coulomb binding energy of the respective ICTC ($E_{\text{coul,ICTC}}$). At large doping concentrations, the large density of ICTCs induces additional energetic disorder and increases E_A , particularly for n-doped C_{60} whose ICTCs have large dipole moments. Experimental data for C_{60} doped with $W_2(\text{hpp})_4$ or $Cr_2(\text{hpp})_4$ are taken from reference [120]. The dashed lines depict quadratic fits using Equation 5.5. The data are included in reference [212].

Different effects can explain the decrease of E_A with doping concentration observed in Figure 5.17. One explanation is a reduction of the effective energetic barrier for ICTC dissociation due to the reduced distances between ICTCs. It was argued that ICTCs can interact electrostatically with each other at higher densities, resulting in a smear out of the electrostatic potential and an increase of energetic disorder [37–39]. Another origin for the reduction of E_A might be an improved (mean) charge carrier mobility at higher charge carrier densities. It was shown in previous studies that in a Gaussian density of states the hopping mobility increases with charge carrier concentration when the Fermi level is above the so-called equilibrium level at σ/kT [76, 80]. In this high charge concentration regime, the mobility exhibits an Arrhenius-type thermal activation energy, which decreases with carrier concentration. This effect should become dominant when the conductivity is not limited by the activation from deep ICTC traps, but by the energetic disorder of the transport states. This would be the case for a very large intrinsic disorder even higher than $E_{\text{coul,ICTC}}$ or for a direct transport between different ICTC configurations as sketched in Figure 5.16b.

The high resolution UPS spectra in Section 5.2 suggest that the energetic distribution of ICTC configurations can be described by a Gaussian density of states. Therefore, it

is interesting to compare the experimental results on doped semiconductors to previous simulation results on hopping transport within a Gaussian density of states (DOS). Simulations of Fishchuk *et al.* revealed that the thermal activation energy of the conductivity and mobility decreases with charge carrier concentration [81, 82]. The dependence of E_A on charge carrier concentration was fitted by a quadratic function, such as:

$$E_A = A \cdot \log^2(n/N) + B \cdot \log(n/N) + C, \quad (5.5)$$

with n/N as the relative charge carrier concentration and A , B , and C as fitting parameters. A similar empirical quadratic function can be used to fit the dependence of E_A on n_D/N for the n-doped semiconductors presented in Figure 5.17.

Fishchuk *et al.* observed an increase of E_A with energetic disorder [81, 82]. Therefore, the strong increase of E_A at large doping concentrations for n-doped C_{60} can be explained by an increased disorder (Figure 5.17b). Compared to the ICTCs of planar F_nZnPc molecules with 2-Cyc-DMBI, the combinations of the spherical C_{60} molecule and different n-dopants have larger ICTC dipole moments (see Table 7.4), resulting in a larger doping-induced electrostatic disorder at the same ICTC density. The increase of energetic disorder is expected to be larger for the n-dopants $W_2(hpp)_4$ and $Cr_2(hpp)_4$ compared to (2-Cyc-DMBI)₂ due to their larger dipole moment. In good agreement, $C_{60}:(2\text{-Cyc-DMBI})_2$ has a lower minimum value of E_A and a less steep increase of E_A at very large concentrations¹⁴.

5.3.3 Important Molecular Parameters at 10 mol%

After investigating the concentration dependence of E_A in the preceding section, the impact of material parameters on E_A is now investigated for a fixed doping concentration of 10 mol%. The results presented in the previous section already indicate that electron transport within a Gaussian energetic distribution of different ICTC configurations is a realistic scenario for charge transport at high doping concentrations. Therefore, the previous simulation results of Fishchuk *et al.* [82] on hopping transport within a Gaussian DOS are extracted and analyzed to obtain an empirical fit function for E_A . Fishchuk *et al.* found that E_A of the (mean) mobility and conductivity at a fixed carrier concentration can be described by two parameters, namely the energetic disorder (σ), i.e. the width of the Gaussian DOS, and the (small) polaron activation energy ($E_{A,pol}$), which is equal to half of the polaron binding energy ($E_{A,pol} = E_p/2$). Values for E_A , σ , and $E_{A,pol}$ are extracted from reference [82] for relative charge carrier concentrations between 10^{-3} and 10^{-1} . It is

¹⁴The same effect of a larger ICTC dipole moment can explain the lower conductivities and higher energetic disorder at large concentrations for bis-HFI-NTCDI: $Cr_2(hpp)_4$ compared to bis-HFI-NTCDI:(2-Cyc-DMBI)₂ films, as observed in Section 5.1.1.

found that the following empirical function can describe the dependence of E_A on σ and $E_{A,\text{pol}}$ for $\sigma/E_{A,\text{pol}}$ ratios between 1 and 4:

$$E_A = E_{A,\text{pol}} + A \cdot \sigma + B \cdot \frac{\sigma^2}{E_{A,\text{pol}}}, \quad (5.6)$$

where A and B depend on the relative charge carrier concentration.

The parameters $E_{A,\text{pol}}$ and σ are replaced by $\lambda/4$ [52] and σ_{ICTC} to obtain an empirical fit function of E_A for the n-doped organic semiconductors investigated here. Here, the reorganization energy λ is approximated by twice the molecular relaxation energy of matrix anions¹⁵ ($\lambda = 2\lambda_A$). Furthermore, it is assumed that the width of the occupied DOS of ICTCs as measured by UPS (σ_{ICTC}) is proportional to the width of the energetic distribution of all accessible ICTC configurations relevant for charge transport [81]. With that assumptions, Equation 5.6 changes to:

$$E_A = \lambda/4 + A' \cdot \sigma_{\text{ICTC}} + B' \cdot \frac{\sigma_{\text{ICTC}}^2}{\lambda/4}, \quad (5.7)$$

where A' and B' are assumed to be constant at a fixed doping concentration of 10 mol% and therefore serve as material independent fitting parameters.

Figure 5.18a shows that Equation 5.7 can describe the dependence of E_A on σ_{ICTC} and λ for a variety of n-doped semiconductors very well when $A = -0.14$ and $B = 0.23$ are used. To further verify Equation 5.7, the impact of σ_{ICTC} and λ on E_A is investigated separately by choosing a set of material combinations for each case where one of the two parameters is relatively constant. Figure 5.18b shows the dependence of $E_A - \lambda/4$ on σ_{ICTC} for systems with a variation of λ between 330 meV and 380 meV. In agreement with Equation 5.7, these systems exhibit an increase of $E_A - \lambda/4$ with σ_{ICTC} . The question if the trend is linear (second term) or quadratic (second term) is difficult to answer because the variation of λ by more than 10% is too large for this selection of materials. Equation 5.7 predicts an increase of $E_A - \lambda/4$ with $1/\lambda$ when σ_{ICTC} is constant. Selections of material combinations with either high (261... 285 meV) or medium (231... 238 meV) σ_{ICTC} values show the expected dependence on $1/\lambda$ (Figure 5.18c). Also in agreement with Equation 5.7, the slope and offset are larger for higher σ_{ICTC} values.

According to Equation 5.7, a reduction of σ_{ICTC} generally yields smaller E_A values. On the other hand, the magnitude of the optimum value for λ resulting in the lowest E_A is not obvious. Figure 5.19a displays the relationship of E_A on λ for a large number of matrix/dopant combinations at a fixed doping concentration of 10 mol%. In addition to the planar matrix molecules doped by (2-Cyc-DMBI)₂, n-doped fullerenes as well as p-doped MeO-TPD and BF-DPB are further included. The thick (thin) solid line represents the fit obtained in Figure 5.18c for medium (high) σ_{ICTC} values, respectively. For a

¹⁵All λ_A values calculated by DFT presented in this thesis were provided by Dr. Christopher Gaul and Sebastian Schellhammer in the group of Dr. Frank Ortmann (TU Dresden).

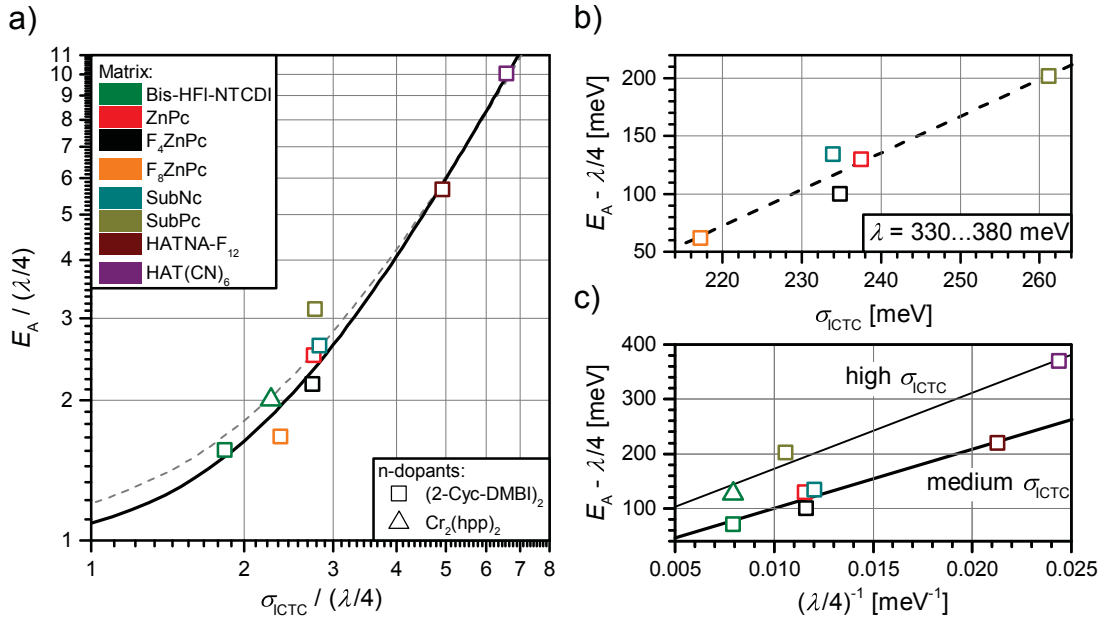


Figure 5.18: Dependence of E_A on energetic disorder and reorganization energy: (a) The empirical approach of Equation 5.7 (black line) can describe the correlation of E_A with the reorganization energy (λ) calculated by DFT and the width of the occupied DOS of ICTCs (σ_{ICTC}) obtained by UPS. The gray dashed line depicts an empirical fit using Equation 5.7 with $B' = 0$. (b) A set of material combinations with a small variation of λ shows an increase of E_A with σ_{ICTC} as expected from Equation 5.7. (c) For combinations with high (261...285 meV) or medium (231...238 meV) values of σ_{ICTC} , the expected inverse dependence of $E_A - \lambda/4$ on λ is observed. The data are included in reference [212].

constant σ_{ICTC} , E_A strongly decreases with increasing λ and reaches a minimum at λ_{min} . For $\lambda > \lambda_{\text{min}}$, E_A increases with λ . λ_{min} can be directly obtained from the derivative of Equation 5.7:

$$\lambda_{\text{min}} = 4\sqrt{B'} \cdot \sigma_{\text{ICTC}}. \quad (5.8)$$

As a result, the actual λ value of most material combinations investigated here is below λ_{min} and an increase of λ would decrease E_A . The remarkably low E_A of $F_8\text{ZnPc}:(2\text{-Cyc-DMBI})_2$ can be explained on the one hand by the low energetic disorder and on the other hand by the fact that λ of $F_8\text{ZnPc}$ is very close to λ_{min} .

The observed behavior of Equation 5.7 in experiments can be attributed to the nature of the Marcus hopping rate [73] which is

$$\kappa_{\text{ET}} \propto \exp \left[-\frac{(\lambda + \Delta G^0)^2}{4\lambda k_B T} \right] \quad (5.9)$$

with ΔG^0 as the difference in free energy between final and initial state. When λ is small compared to the energetic disorder (σ_{ICTC}), molecular reorganization supports hopping between transport states separated by large energy differences. Apparently, transport for

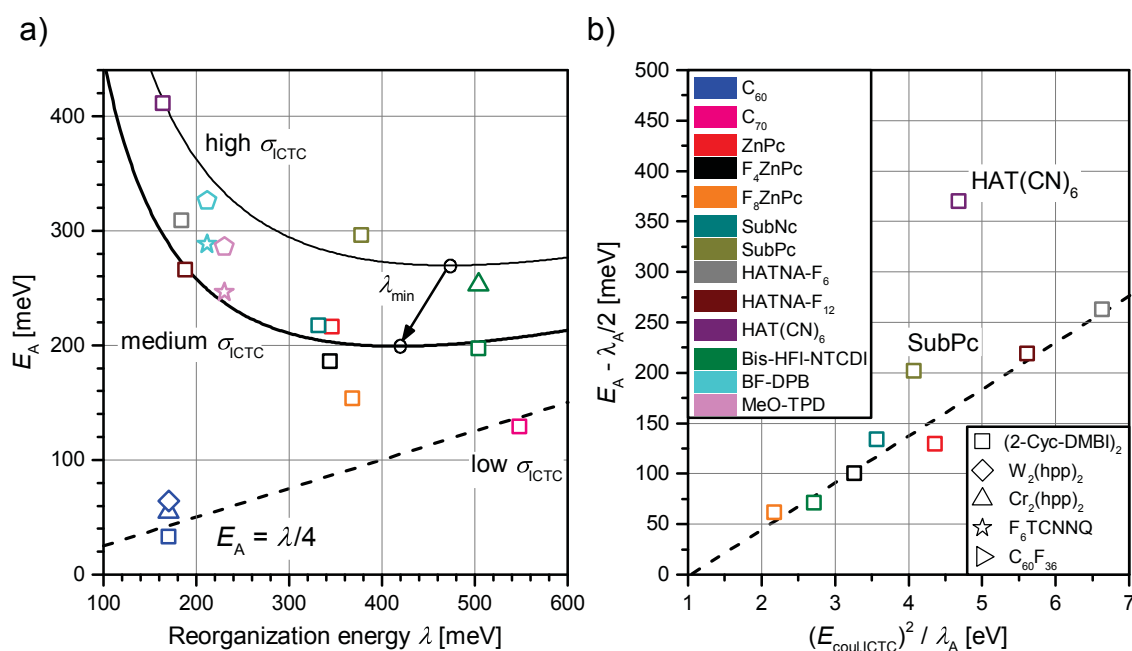


Figure 5.19: Correlation between E_A and molecular parameters (a) Change of E_A with reorganization energy for several n- and p-doped organic semiconductors at 10 mol%. The thin and thick solid line refers to the fits in Figure 5.18c for high and medium values of σ_{ICTC} , respectively. The dashed line represents the expected behavior for pure polaronic transport with $E_A = \lambda/4$. (b) For most samples, E_A can be described as a function of the Coulomb binding energy of ICTCs ($E_{\text{coul,ICTC}}$) and the relaxation energy of matrix anions (λ_A). The deviation of n-doped HAT(CN)₆ and SubPc from the trend might be due to their large ICTC density. The dashed line depicts a linear fit excluding n-doped SubPc and HAT(CN)₆. The experimental data of C₆₀:W₂(hpp)₄ and C₆₀:Cr₂(hpp)₄ as well as p-doped MeO-TPD and BF-DPB are taken from references [102, 120]. The data are included in reference [212].

most of the n-doped non-fullerenes in Figure 5.19a is dominated by this effect. On the other hand, when λ is large compared to the energetic disorder, polaron relaxation effects dominate transport and E_A increases with λ . This regime is observed for n-doped fullerenes (dashed line in Figure 5.19a), where E_A is very close to $\lambda/4$. This observation can be partly attributed to the low energetic disorder of n-doped fullerenes, supported by the low σ_{ICTC} values observed in experiment. Furthermore, unique properties of fullerenes such as a more isotropic transport or a larger charge delocalization might generally reduce the impact of energetic disorder on E_A for this class of materials [78, 82]. The results indicate that a reduction of energetic disorder is in general a promising route towards lower E_A values and larger conductivities in doped organic semiconductors. The analysis of the electronic states in Section 5.2.4 revealed a correlation of σ_{ICTC} and $E_{\text{coul,ICTC}}$ for low ICTC densities. As shown in Figure 5.19b, the variation of E_A between

different matrix molecules doped by (2-Cyc-DMBI)₂ can be described by the change of two molecular parameters by using following empirical fit function:

$$E_A = \lambda_A/2 + A'' \cdot \frac{E_{\text{coul,ICTC}}^2}{\lambda_A} + B'', \quad (5.10)$$

with $A'' = 0.046$ and $B'' = 48$ meV. Both the molecular relaxation energy of matrix anions (λ_A) as well as the Coulomb binding energy of ICTCs ($E_{\text{coul,ICTC}}$) can be calculated by DFT directly from the molecular structure. As seen in Figure 5.19b, n-doped HAT(CN)₆ and SubPc deviate from the general trend. This can be attributed to the fact that these materials exhibit the largest ICTC densities of all investigated n-doped molecules, probably inducing an increased energetic disorder (see Figure 5.13 in Section 5.2.4). The large ICTC densities originate from the comparably low molar masses of these molecules, another parameter obtainable from the chemical structure.

Conclusion

In conclusion, the thermal activation energy (E_A) controls the electrical conductivity of doped organic semiconductors at room temperature. While at low and moderate doping concentrations, E_A crucially depends on the Coulomb binding energy of integer charge transfer complexes ($E_{\text{coul,ICTC}}$), an increased energetic disorder induced by the large number of electrical dipole moments leads to an increase of E_A at very high doping concentrations. It was possible to describe E_A at a concentration of 10 mol% by an empirical function of the reorganization energy and the energetic disorder of ICTCs. As a result, the reorganization energy of most of the material combinations investigated is too low to obtain the lowest achievable value for E_A . Besides a reduction of $E_{\text{coul,ICTC}}$, low values for the ICTC density and the dipole moment of ICTCs seem to be essential to obtain low energetic disorder in doped organic semiconductors. The n-doped fullerenes exhibited a remarkably low impact of energetic disorder and showed a very low E_A at 10 mol%, mainly given by the magnitude of their reorganization energy.

5.4 Air Stability of n-Doped Semiconductors

Efficient n-doping of organic semiconductors necessitates n-dopants with a low ionization energy (IE), making these dopants often sensitive to air exposure [20]. As discussed in Section 5.1, air stable dopant compounds can be made by incorporating the actual n-doping species in an air stable precursor molecule with a large IE . In particular, the air stable precursor (2-Cyc-DMBI)₂ exhibits high doping efficiencies in a variety of matrix materials with electron affinities down to 3 eV (see Section 5.2.3). Apart from the chemical stability of n-dopants, a high air stability of n-doped layers is crucial to avoid degradation at air during device processing. Furthermore, the air stability of these layers is one of the factors determining device lifetime. Therefore, the sensitivity of the electronic properties of several organic semiconductors n-doped with (2-Cyc-DMBI)₂ to air exposure is investigated in this section. In Section 5.4.1, the magnitude of the conductivity decrease upon air exposure is compared to the electron affinity of the respective matrix molecules. In Section 5.4.2, the Fermi level change upon air exposure obtained by ultraviolet photoelectron spectroscopy (UPS) is correlated with the observed conductivity decrease. Finally, a universal electron trap energy introduced upon air exposure is determined by extracting the ionization energy of integer charge transfer complexes from UPS spectra (Section 5.4.3). The investigations of this section are based on the results of reference [127] and will be included in reference [221].

5.4.1 Conductivity Decrease Upon Air Exposure

Previous studies suggested that electron transport in organic semiconductors is air stable when the EA of the semiconductor is larger than 4 eV [34, 121, 122]. In a recent study, an universal trap for electron transport in polymers was determined to be at around 3.6 eV and was related to adsorbance of O₂(H₂O)₂ complexes [89, 222]. The results presented in reference [127] indicated the presence of such a trap also in n-doped semiconductors after exposing them to air. Furthermore, the study revealed that the energy levels of the matrix rather than of the dopant predominantly determine whether the n-doping effect is sensitive to air exposure or not. In this section, the dependence of the air stability on the EA of the matrix material (EA_A) is systematically investigated by comparing the sensitivity of the conductivity to air exposure for different n-doped organic semiconductors.

The results in Chapter 4 of this thesis demonstrated that the IE and EA of crystalline films of planar molecules in edge-on orientation typically increase with a larger degree and strength of electron withdrawing side groups. In particular, the IE increases by more than 1 eV when ZnPc and HATNA are fluorinated (see Table 7.2 for values), which are hence chosen as matrix materials. Figure 5.20a shows the reduction in conductivity¹⁶ (σ_e) under air exposure for the different matrix materials n-doped with 10 mol% of (2-Cyc-DMBI)₂.

¹⁶Most of the conductivity data of this section were measured by Olka Kaveh and Daniel Schütze at IAPP.

The drop of σ_e during 60 min of air exposure is less pronounced for n-doped F_4ZnPc and HATNA- F_{12} as compared to n-doped ZnPc and HATNA- F_6 , respectively, which can be explained by the higher EA_A . However, n-doped F_8ZnPc and HAT(CN) $_6$ with even larger EA_A exhibit lower relative conductivities after air exposure in comparison to n-doped F_4ZnPc and HATNA- F_{12} , respectively. The stronger decrease of σ_e at short exposure times for n-doped F_8ZnPc in comparison to n-doped F_4ZnPc might indicate that adsorbates diffuse faster into the n-doped F_8ZnPc film. Another explanation would be that air exposure causes structural disorder in these materials, resulting in further trap states in the transport gap [90]. This effect of an increased disorder might be more pronounced for n-doped HAT(CN) $_6$ due to its low molar mass, serving as a possible explanation for the stronger reduction of σ_e compared to n-doped HATNA- F_{12} .

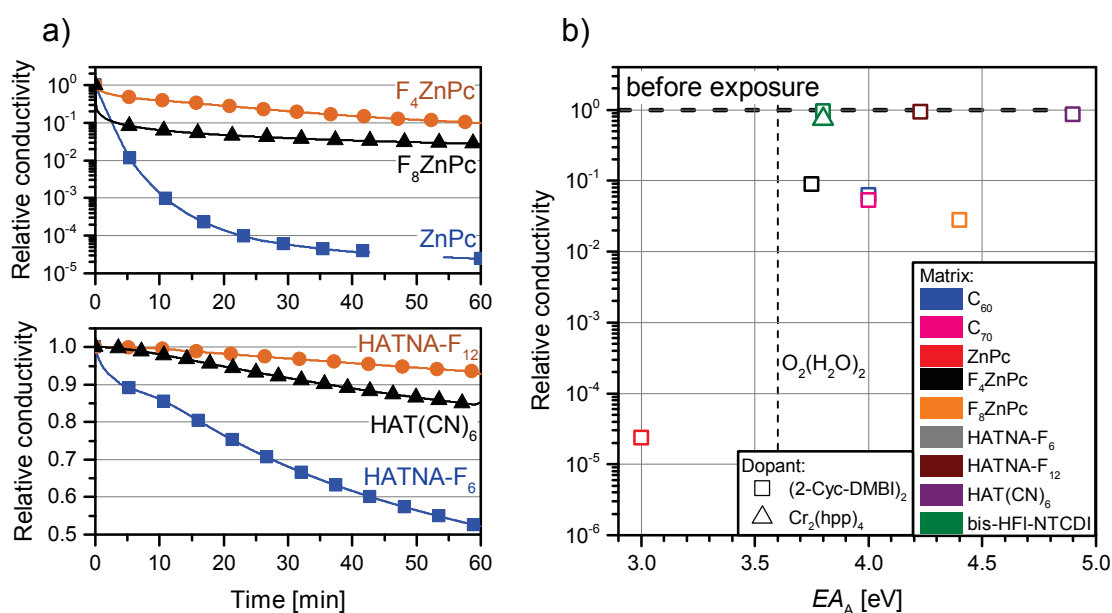


Figure 5.20: Decrease of conductivity upon air exposure: (a) Ratio between the conductivities (σ_e) before and after air exposure for different matrix molecules n-doped with 10 mol% of $(2-Cyc-DMBI)_2$. (b) Dependence of the conductivity decrease on the electron affinity of different matrix molecules (EA_A). The vertical dashed line depicts the universal electron trap at 3.6 eV observed in reference [89]. The σ_e values before and after air exposure as well as the EA_A values of intrinsic matrix layers are summarized in Table 5.2. This data will be included in reference [221].

Figure 5.20b shows the ratio between σ_e before and after 60 min of air exposure plotted versus the respective EA_A . The low EA_A of ZnPc is considerably below the universal electron trap of 3.6 eV observed before in reference [89], explaining the low stability of n-doped ZnPc against air exposure. However, the reduction of σ_e for the other matrix materials does not seem to correlate with the respective EA_A . Furthermore, the higher sensitivity of bis-HFI-NTCDI doped with $Cr_2(hpp)_4$ (9 mol%) in comparison to the sample doped with $(2-Cyc-DMBI)_2$ cannot be explained by a difference in EA_A . Apparently, the variation of the degree of conductivity decrease between the materials with similar EA_A is due to other parameters.

Table 5.2: Electronic properties of n-doped semiconductors and their sensitivity to air exposure: Unless stated otherwise, EA_A and $IE_{A,ICTC}$ were obtained from inverse and direct photoelectron spectroscopy experiments using weakly interacting substrates, respectively. $\sigma_{e,0}$ and $\sigma_{e,air}$ denote the conductivities before and after exposure to air for 60 min, respectively. ΔE_F denotes the Fermi level shift upon air exposure for 10 min, obtained from the HOMO peak positions in UPS spectra. All matrix materials are doped with 10 mol% of (2-Cyc-DMBI)₂. Furthermore, a bis-HFI-NTCDI sample n-doped with 9 mol% of Cr₂(hpp)₄ is added at the end of the table for comparison. The data of this table will be included in reference [221].

| Matrix | EA_A [eV] | $IE_{A,ICTC}$ [eV] | $\sigma_{e,0}$ [S/cm] | $\sigma_{e,air}$ [S/cm] | ΔE_F [eV] |
|----------------------------|------------------|--------------------|-----------------------|-------------------------|-------------------|
| C ₆₀ | 4.0 ² | 4.53 | 11 | $7.0 \cdot 10^{-1}$ | 0.16 |
| C ₇₀ | 4.0 [223] | 4.61 | $5.2 \cdot 10^{-3}$ | $2.8 \cdot 10^{-4}$ | 0.15 |
| ZnPc | 3.0 ² | 3.92 | $6.6 \cdot 10^{-4}$ | $1.6 \cdot 10^{-8}$ | 0.36 |
| F ₄ ZnPc | $\sim 3.75^3$ | 4.50 | $3.3 \cdot 10^{-3}$ | $3.0 \cdot 10^{-4}$ | 0.22 |
| F ₈ ZnPc | $\sim 4.4^3$ | 4.87 | $2.1 \cdot 10^{-3}$ | $5.8 \cdot 10^{-5}$ | 0.10 |
| HATNA-F ₆ | - | 4.89 | $4.8 \cdot 10^{-5}$ | $2.4 \cdot 10^{-5}$ | 0.10 |
| HATNA-F ₁₂ | $\sim 4.23^4$ | 5.40 | $9.0 \cdot 10^{-5}$ | $8.4 \cdot 10^{-5}$ | 0.03 |
| HAT(CN) ₆ | >4.9 [224] | 5.85 | $4.7 \cdot 10^{-4}$ | $3.9 \cdot 10^{-4}$ | -0.02 |
| bis-HFI-NTCDI | 3.8 ² | 4.71 | $6.9 \cdot 10^{-4}$ | $6.7 \cdot 10^{-4}$ | 0.03 |
| bis-HFI-NTCDI ¹ | 3.8 ² | 4.51 | $6.5 \cdot 10^{-5}$ | $4.8 \cdot 10^{-5}$ | - |

¹Doped with 9 mol% of Cr₂(hpp)₄.

²Obtained by Dr. Fabio Bussolotti in the lab of Prof. Satoshi Kera at IMS.

³Estimated by assuming an equal $IE_A - EA_A$ difference for ZnPc, F₄ZnPc, and F₈ZnPc.

⁴In case of an equal $IE_A - EA_A$ difference for edge-on and face-on orientation [225].

5.4.2 Analysis of Fermi Level Shift Upon Air Exposure

Apart from the conductivity decrease, the Fermi level (E_F) typically shifts towards its intrinsic position upon air exposure [20]. Figure 5.21 displays UPS spectra of the n-doped semiconductors presented in Figure 5.20a before and after exposure to air for 10 min. The spectra in Figure 5.21a-c reveal that the shift of E_F decreases from n-doped ZnPc to n-doped F₈ZnPc, indicating improved air stable n-doping for the fluorinated matrices as expected from the enhanced EA_A . The occupied LUMO peak and the HOMO shoulder of matrix anions located in integer charge transfer complexes (ICTC) vanish in all cases after air exposure, indicating a deoccupation of matrix anions and an occupation of trap states (see also reference [127]), which is in line with the reduction of σ_e by at least one order of magnitude in all cases.

In accordance with the conductivity reduction observed in Figure 5.20, the spectra of n-doped HATNA derivatives reveal a considerably smaller sensitivity to air exposure. The

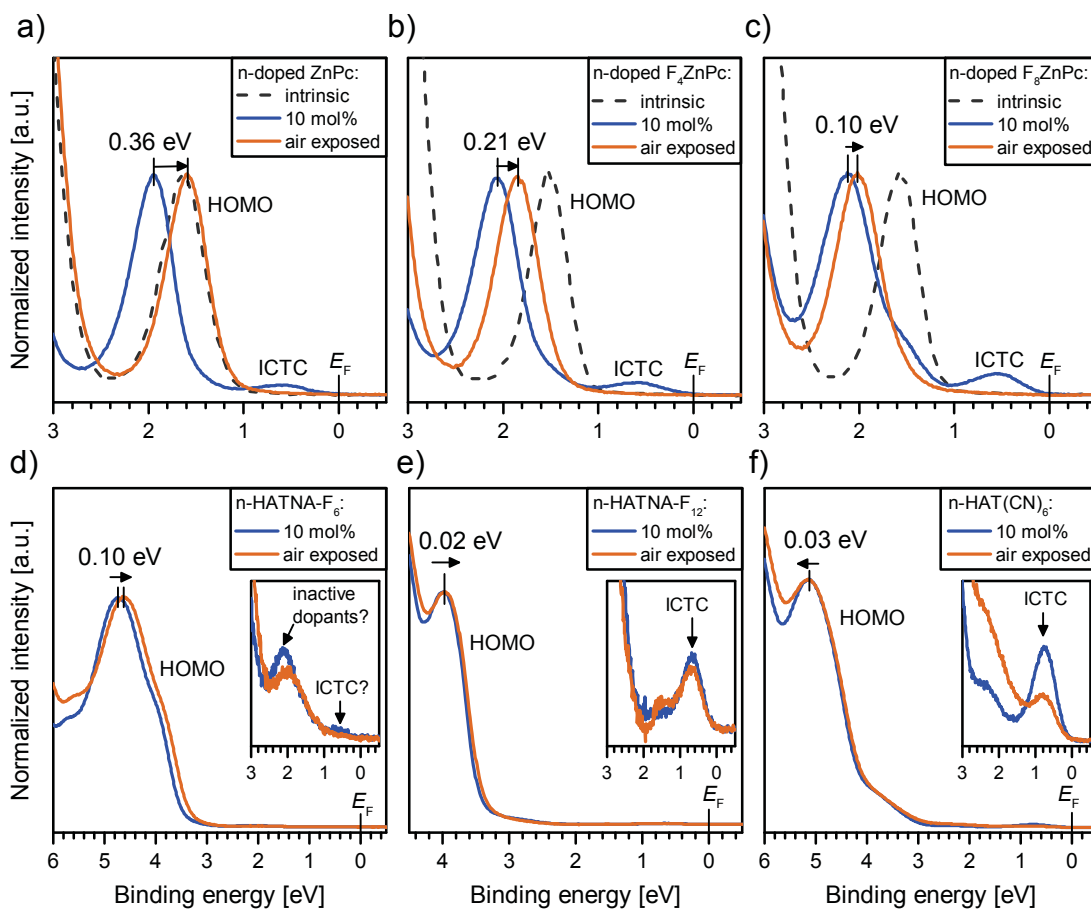


Figure 5.21: Fermi level shift during air exposure: (a-f) UPS spectra before and after air exposure (10 min) for different matrix molecules n-doped with $(2\text{-Cyc-DMBI})_2$. A shift of the HOMO peak to lower binding energies corresponds to a Fermi Level (E_F) shift towards lower energies. The peak denoted as ICTC belongs to the emission of electrons from matrix anions located within integer charge transfer complexes. The data will be included in reference [221].

spectrum of n-doped HATNA-F₆ in Figure 5.21d exhibits a slightly larger E_F shift compared to n-doped HATNA-F₁₂ and n-doped HAT(CN)₆, in agreement with the larger drop of σ_e for n-doped HATNA-F₆. The large peak in the spectrum of n-doped HATNA-F₆ at around 2 eV, which is much larger than the ICTC peak, might belong to unsplitted precursor molecules, indicating a poor charge transfer efficiency. For n-doped HATNA-F₁₂, the small shift of E_F and the nearly unchanged intensity of the ICTC peak after air exposure (Figure 5.21e) is in good agreement with the very small reduction of σ_e . The spectra of n-doped HAT(CN)₆ in Figure 5.21f reveal a fractional deoccupation of matrix anions, agreeing with the observed larger reduction of σ_e during air exposure as compared to n-doped HATNA-F₁₂. Furthermore, the spectrum after air exposure is broader, indicating an increased energetic disorder, which might be due to the small molar mass of HAT(CN)₆. An increase of energetic disorder can further explain the reduction of σ_e .

Correlation with Conductivity Reduction

The decrease in conductivity and the shift of E_F can be explained by the introduction of trap states in the energy gap below the transport level. As presented in Section 2.2.3, the *Hoesterey-Letson* formula was used to describe the mobility in organic crystals when traps with a relative concentration (c) and a discrete trap energy (E_T) with respect to the transport level are introduced [86–88]:

$$\mu(c) = \mu_0 \left[1 + c \cdot \exp\left(\frac{E_T}{k_B T}\right) \right]^{-1}, \quad (5.11)$$

where μ_0 is the mobility without traps.

Although Equation 5.11 was developed for organic crystals with negligible energetic disorder, the reduction of σ_e in n-doped semiconductors might qualitatively exhibit a similar dependence on depth and concentration of traps introduced upon air exposure. The trap energy is not directly accessible by UPS. However, when the trap energy is below the transport level, trap states become occupied upon air exposure. This results in a shift of E_F to lower energies, which is detectable by UPS. The magnitude of the Fermi level shift (ΔE_F) upon air exposure should depend on E_T , the trap density, and the distribution of transport and trap states [41]. Assuming that ΔE_F increases linearly with E_T and that the available charge carrier concentration, i.e. the number of dopant cations, remains constant¹⁷, Equation 5.11 can be rewritten to obtain a relation between the conductivities before ($\sigma_{e,0}$) and after air exposure ($\sigma_{e,\text{air}}$):

$$\sigma_{e,\text{air}}(c) = \sigma_{e,0} \left[1 + c^* \cdot \exp\left(\frac{a \cdot \Delta E_F}{k_B T}\right) \right]^{-1}, \quad (5.12)$$

where c^* and a are fitting parameters and ΔE_F is obtained from UPS spectra.

Equation 5.12 can roughly describe the trend of the experimental data in Figure 5.22, if $a = 1.09$ and $c^* = 0.02$ are used. Although two material combinations deviate from the trend, this result suggests that the introduction of trap states below the transport level is the main origin for the reduction of σ_e during air exposure. A physical interpretation of the fitting parameters c^* and a is challenging because they depend on several parameters such as the exposure time and the energetic distribution of trap states. Furthermore, ΔE_F is measured at the sample surface and is used to fit the behavior of σ_e , being a bulk property. The trap density at the surface might be higher than in the bulk because of a limited diffusion of impurities from the surface into the bulk. In good agreement, the conductivity still decreases even after 60 min of air exposure for most samples (see Figure 5.20a).

¹⁷The large charge transfer efficiencies observed in Section 5.2.3 suggest that the the activation energies of dopants is much smaller than the trap energy.

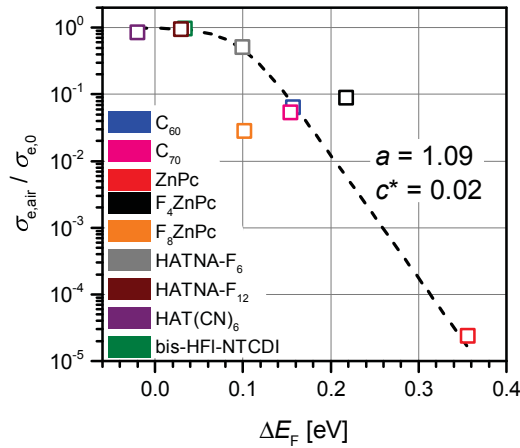


Figure 5.22: Correlation of conductivity decrease with Fermi level shift: The reduction of conductivity and the Fermi Level shift ΔE_{F} upon air exposure can be explained by the introduction of trap states below the transport level. The dashed line is a fit using Equation 5.12. The data of this figure will be included in reference [221].

5.4.3 Universal Air Trap as a Limit for Air Stable n-Doping

The results of Section 5.3 indicated that charge transport in highly doped organic semiconductors occurs via integer charge transfer complexes (ICTCs). In such a case, the transport level should be related to $IE_{\text{A,ICTC}}$, being the ionization energy of matrix anions located in ICTCs and can be obtained with UPS. If there is an universal trap energy introduced upon air exposure, n-doped semiconductors with $IE_{\text{A,ICTC}}$ larger than this trap energy would be air stable because electron donation from the matrix anion to the trap becomes unlikely. Indeed, Figure 5.23a shows that the E_{F} shift during air exposure decreases when $IE_{\text{A,ICTC}}$ becomes larger. According to this trend, $IE_{\text{A,ICTC}} > 5.1$ eV seems to be a precondition for air stable n-doped semiconductors.

Compared to recent studies which suggested values between 3.6 eV and 4.0 eV for the electron affinity as a lower limit for air stable electron transport in intrinsic semiconductors, the value of 5.1 eV seems to be rather large [34, 89, 121, 122]. However, the Coulomb binding energy $E_{\text{coul,ICTC}}$ between matrix anions and dopant cations substantially increases $IE_{\text{A,ICTC}}$ with respect to EA_{A} (see Section 5.2). Although the exact species causing the charge carrier trap is not known so far, it is likely that its energy is also affected by Coulomb interactions with dopant cations. Furthermore, the energy of trapped charges might experience a shift due to charge-quadrupole interactions. As shown in Section 5.2.3 for n-doped F_nZnPc (10 mol%), the energy levels in crystalline films of n-doped planar molecules change linearly with the quadrupole component Q_{π} of the matrix molecule. A subtraction of both contributions, i.e. the ICTC Coulomb attraction and the charge-quadrupole interactions with matrix molecules, leads to the following correction of $IE_{\text{A,ICTC}}$:

$$IE_{\text{A,ICTC,corr}} = IE_{\text{A,ICTC}} - E_{\text{coul,ICTC}} - \Delta_{\text{q-Q}}, \quad (5.13)$$

where the charge-quadrupole interaction energy is $\Delta_{q-Q} = 0.017 \cdot Q_{\pi}$ (see Section 5.2.3). The $E_{\text{coul,ICTC}}$ values obtained from DFT simulations¹⁸ in vacuum are corrected by an effective dielectric constant at the sample surface ($\epsilon_{r,\text{sur}}$), which is assumed to be the mean value between the bulk and the vacuum value. This results in $\epsilon_{r,\text{sur}} = 2$ for planar molecules and $\epsilon_{r,\text{sur}} = 2.7$ for C_{60} .

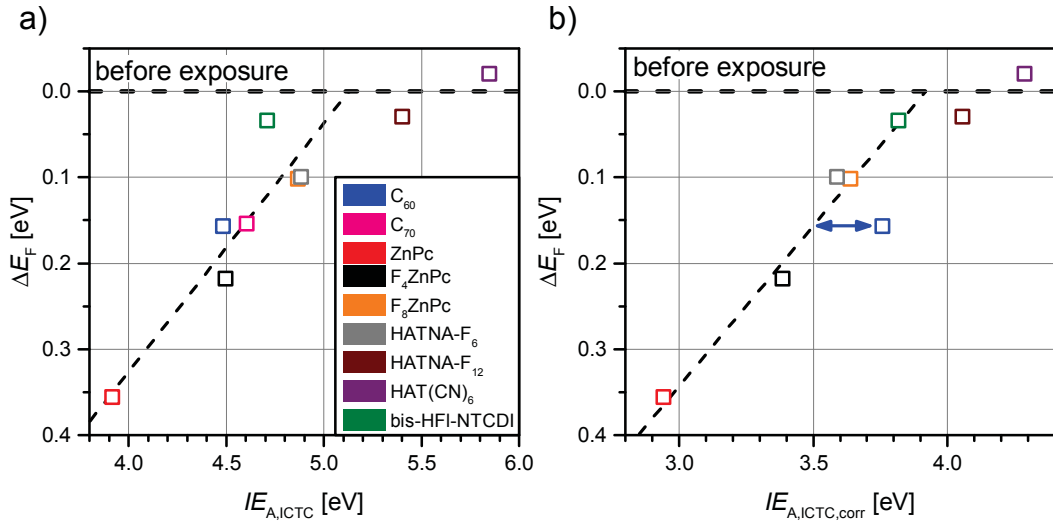


Figure 5.23: Universal trap as a limit for air stable n-doping: (a) The E_F shift upon air exposure for 10 min increases with decreasing $IE_{A,ICTC}$ for $IE_{A,ICTC} < 5.1$ eV. (b) $IE_{A,ICTC}$ values corrected with Equation 5.13 correlate well with the magnitude of the Fermi level shift. For $IE_{A,ICTC,corr} > 3.9$ eV, the n-doped semiconductors are found to be air-stable. The thin dashed lines represent linear fits to the experimental data excluding n-doped HATNA- F_{12} and HAT(CN) $_6$. The data of this figure will be included in reference [221].

The Fermi level shift (ΔE_F) upon air exposure is plotted versus $IE_{A,ICTC,corr}$ in Figure 5.23b, revealing that ΔE_F scales with $IE_{A,ICTC,corr}$. The deviation of n-doped C_{60} can be explained by its larger dielectric constant, resulting in an increased polarization energy and hence an enhanced $IE_{A,ICTC}$ [173, 226]. A linear fit gives an EA of 3.9 eV for the presumed universal trap, which increases to around 5 eV at the surface of n-doped semiconductors due to Coulomb interactions with dopant cations and quadrupole moments of neutral matrix molecules. This value is very close to the trap energy of 3.6 eV observed before for electron transport in polymers, indicating a similar origin of the electron traps in intrinsic polymers and n-doped small molecules [89, 127].

Conclusion

In this section, the air stability of several n-doped organic semiconductors was investigated. In good agreement to previous studies, an increase of the electron affinity of the matrix molecule generally improved the air stability for most n-doped semiconductors.

¹⁸ The simulations were performed by Dr. Reinhard Scholz at IAPP. Details can be found in Section 3.5.

The observed correlation between conductivity drop and Fermi level shift upon air exposure was attributed to the introduction of charge carrier traps below the transport level. The comprehensive analysis of the energies of integer charge transfer complexes indicated that a trap with an universal energy is introduced upon air exposure. By accounting for electrostatic interactions with dopant cations and quadrupole moments of matrix molecules, an universal trap energy of $EA=3.9$ eV was obtained. Although this number is similar to the previously determined EA of $O_2(H_2O)_2$ complexes, the chemical origin of this trap is not clear yet, as the films were exposed to ambient air, consisting of various gaseous substances. For clarification, future investigations could expose n-doped layers to pure gases and further analyze the degradation products of unstable compounds.

5.5 Summary

First, the doping mechanism and the doping efficiency of novel air stable n-dopants were investigated and compared to the reference air sensitive n-dopant $Cr_2(hpp)_4$. While the precursor o-MeO-DMBI-Cl exhibited a reduced doping efficiency at high concentration due to an undesired decomposition mechanism, (2-Cyc-DMBI)₂ showed an even better performance than $Cr_2(hpp)_4$ and provided large electrical conductivities in matrix materials with electron affinities down to 3 eV. Therefore, (2-Cyc-DMBI)₂ was used to comprehensively analyze the electronic states of different n-doped small molecules, which were described by the formation of integer charge transfer complexes (ICTC) of matrix anions and dopant cations. The ionization energy of matrix anions in ICTCs corresponds to the highest occupied states, determining the transport level of electrons. A systematic variation of matrix molecules revealed that the energetic disorder of these transport states increases with the Coulomb binding energy of ICTCs ($E_{\text{coul,ICTC}}$) and further enhances with doping concentration in the regime of very large ICTC dipole densities. DFT simulation results on different ICTCs demonstrated that $E_{\text{coul,ICTC}}$ can be reduced by adding electron withdrawing side groups to planar matrix molecules. For a fixed doping concentration of 10 mol%, it was found that the thermal activation energy of the conductivity can be described by an empirical function of the energetic disorder of ICTCs and the relaxation energy of matrix anions. Due to the remarkably small energetic disorder, the activation energies of n-doped fullerenes reached very low values down to 35 meV, only limited by their relaxation energy. On the other hand, the results indicated that an increase of the relaxation energies of most of the non-fullerene matrix materials would result in smaller activation energies and larger conductivities. In the last section, it was found that the sensitivity of the electronic properties to air exposure reduces when the ionization energy of matrix anions in ICTCs increases, indicating the introduction of a charge carrier trap upon air exposure. An universal trap energy of 3.9 eV was determined, in good agreement with previous studies.

6. Conclusion and Outlook

6.1 Conclusion

The aim of this thesis was to connect electronic properties of thin organic films with parameters of single molecules, helping to provide design rules for novel organic compounds. In the first part, the changes of energy levels with molecular orientation in neat films or with mixing ratio in blends were investigated on the basis of the model system comprising ZnPc and its fluorinated derivatives. Correlations of the observed energy shifts with molecular parameters were verified for other compounds, indicating that charge-quadrupole interactions along the π - π -stacking geometry induce large energy shifts in many crystalline films of planar molecules. Consequently, the quadrupole component perpendicular to the molecular plane (Q_π) of such molecules is an ideal tuning parameter, allowing a systematic adjustment of the energy levels of organic thin films. This enabled a continuous tuning of the energy levels in intermixed blends of two molecules with different Q_π . This effect was also observed for typical donor/acceptor blends exhibiting some degree of phase separation. However, the shift with mixing ratio was not perfectly linear, which was attributed to the formation of an electrostatic gradient from the donor to the acceptor phase.

The impact of specific molecular parameters on device characteristics was demonstrated in organic solar cells by employing a ternary mixture of two intermixing donor molecules with varying Q_π and one phase separating acceptor molecule. The change of the open-circuit voltage with the mixing ratio of the two donor molecules was driven by the change of three parameters obtainable from the chemical structures of the donor molecules, namely the ionization energy, the relaxation energy, and Q_π . Furthermore, these devices demonstrated how an adjustment of quadrupole moments can induce driving forces for charge separation at the donor-acceptor interface to achieve larger short-circuit currents and fill factors.

The topic of the second part of this thesis was the investigation of molecular n-doping of organic semiconductors. First, the doping properties of two novel air stable n-dopants in the electron transport material bis-HfI-NTCDI were investigated. While (2-Cyc-DMBI)₂ yielded high conductivities, even larger than the reference air sensitive dopant Cr₂(hpp)₄, o-MeO-DMBI-Cl doped films exhibited a reduced doping efficiency particularly at high doping concentrations. A comprehensive analysis of the doping mechanism of o-MeO-DMBI-Cl revealed that the decomposition mechanism of the precursor changes with evap-

oration temperature, providing predominantly doping-inactive decomposition products at high concentrations.

The analysis of the electronic states of ZnPc and C₆₀ each n-doped with (2-Cyc-DMBI)₂ using direct and inverse photoelectron spectroscopy indicated that these states are determined by the formation of integer charge transfer complexes (ICTC) of matrix anions and dopant cations. The thermal activation energy of the conductivity at 10 mol% increased with the energetic disorder of these ICTCs, indicating that electron transport at high doping concentrations occurs directly between different ICTC configurations. Due to the remarkably small energetic disorder, the activation energy of n-doped fullerenes reached very low values down to 35 meV, only limited by the relaxation energy of the matrix anions. The other matrix molecules exhibited a considerably larger energetic disorder, which was higher for larger Coulomb binding energies of the ICTCs and further increased for large ICTC densities. As a consequence, the activation energy at 10 mol% could be described for most compounds by an empirical function of the Coulomb binding energy of ICTCs and the relaxation energy of matrix anions. A systematic variation of the matrix molecule revealed that the adjustment of the charge distribution on the matrix molecule by adding electron withdrawing side groups can substantially decrease the Coulomb binding energy and increase the conductivity.

Finally, the sensitivity of the conductivity and of the Fermi level position to air exposure was investigated for several matrix molecules n-doped with (2-Cyc-DMBI)₂. It was found that the air stability increases with the ionization energy of matrix anions in ICTCs. As this energy correlates with the transport energy of electrons, this relationship was explained by the introduction of an impurity upon air exposure with an universal energy, acting as charge carrier trap. The energy of this electron trap was determined to be 3.9 eV, in good agreement with previous studies.

6.2 Outlook

The results of this thesis demonstrated the impact of charge-quadrupole interactions on the thin film energy levels of a variety of planar small molecules. The changes of energy levels with film morphology or composition could be explained within a short-range scheme, considering only the interaction with the closest neighbors of a molecule. In contrast, a previous study showed for the donor molecule DCV5T-Me(3,3) that long-range charge-quadrupole interactions along the whole thin film geometry need to be taken into account to correctly predict the thin film energies [27, 30]. The dominant impact of long-range interactions might be due to the acceptor-donor-acceptor molecule architecture of DCV5T-Me(3,3), being substantially different to the molecules investigated in this thesis. Therefore, it is suggested to probe the ionization energies of thin films of DCV5T-Me(3,3) at different layer thicknesses and molecular orientations and compare them to the behav-

ior of F_n ZnPc films. Furthermore, it remains unclear how relevant long-range interactions are in DCV5T-Me(3,3):C₆₀ blends exhibiting a distinct degree of phase separation between the two different compounds. A systematic analysis of the energies and structural properties of such blends with varying degree of phase separation between the two compounds using experimental and simulation methods might give useful insight into the range of these interactions.

While ZnPc:F₄ZnPc and ZnPc:F₈ZnPc blends showed a linear change of energy levels with mixing ratio, previously investigated blends of pentacene and perfluorinated pentacene only showed inhomogeneous tuning, which was explained by a phase separation originating from the formation of co-crystals [194]. The same effect could also explain the nonlinear shift in ZnPc:F₁₆ZnPc blends, as observed in Section 4.3.1 of this thesis. These examples indicate an impact of quadrupole moments on the layer growth behavior. Another example are DCV5T derivatives, where the donor-acceptor-donor architecture of the molecules causes a large quadrupole moment and results in a specific layer growth [227]. Future studies could investigate in more detail how the magnitude of the quadrupole moments, or in general the charge distribution on the molecules, change the layer structure of neat films and blends and whether the growth behavior changes with temperature.

The study of ternary mixtures of ZnPc, F₄ZnPc, and C₆₀ revealed how tuning the quadrupole component of the donor can adjust the dissociation barrier of charge transfer states. In contrast to C₆₀, non-fullerene acceptor molecules do generally not exhibit a vanishing quadrupole moment. In such a case, the difference between the quadrupole components of donor and acceptor should be the important parameter determining the dissociation barrier. Previous studies on non-fullerene acceptors already presented several efficient compounds exhibiting electron withdrawing sidegroups [228–237], suggesting that the quadrupole moment is also one of the important parameters in the design of novel acceptor molecules. However, further DFT simulations should be performed to verify the impact of the quadrupole moment of these novel acceptor molecules on photovoltaic characteristics. This might help to further optimize their chemical structures to achieve efficient charge generation and minimize voltage losses at the same time.

In addition to the strong energy shifts due to the interaction of charges with permanent charge distributions, the interaction with induced charge distributions leads to a reduction of the difference between ionization energy and electron affinity in organic films. For molecular design, it is interesting how these polarization energies depend on molecular parameters, such as the size, the polarizability, or the charge distribution. A better knowledge would not only enable an improved prediction of the energy levels of organic films, but might also facilitate a tuning of the optical gap, being particularly interesting for the optimization of optoelectronic devices.

Another possibility to tune the energy gap might be the incorporation of molecules in a matrix consisting of two compounds with a different dielectric constant. An incorpora-

tion of molecules into a matrix could also change other properties, for example reducing their energetic disorder and improving charge transport. Apart from electrostatic effects, band gap engineering might be also possible in blends of molecules with different energy gaps and with strong intermolecular electronic coupling. Bandwidths of a few 100 meV were measured for example in pentacene and rubrene crystals [67, 68]. To achieve a band gap engineering effect in organic semiconductors, it might be necessary to find two molecules with very similar structures to obtain an intermixed crystal structure and with (slightly) different energy gaps. It seems challenging to find suitable candidates because molecules which vary in their energy gap due to a different molecular size, i.e. the size of π -electron system, might not form an intermixed crystal in most cases.

The investigations of the doping mechanisms of air stable n-dopants indicated that the usage of dimers of two n-doping radicals is the most promising route towards efficient and air stable n-dopants. Unfortunately, the precursor (2-Cyc-DMBI)₂, which efficiently n-doped several matrix materials, exhibits a comparably low thermal stability and preliminary results indicated that the dopant diffuses within the matrix material. Furthermore, the n-dopant remained in the gas phase of the vacuum chamber for some time after evaporation, resulting in unintentional doping of organic layers processed in the same chamber. Therefore, this dopant seems not to be useful for practical device application despite its high doping efficiency. An increase of the dimer's molar mass might help to overcome these issues [238]. There are already other DMBI dimers available [46, 47]. Although they yielded lower conductivities, they might have a higher thermal stability due to their larger molar mass. These dimers could be used in a future study to investigate how the diffusion properties and the thermal stability change with the size of the dopant.

The correlation of the thermal activation energy with the molecular parameters of several matrix molecules n-doped with 10 mol% of (2-Cyc-DMBI)₂ indicated a crucial impact of the relaxation energy of matrix anions and the energetic disorder of transport states on electron transport. Preliminary measurements on other systems suggested that this correlation is not restricted to these systems. Nevertheless, further studies should be done to verify the generality of this correlation. The results on n-doped F_nZnPc and C₆₀ revealed that the conductivity at moderate doping concentrations is larger for smaller Coulomb binding energies of ICTCs. However, the impact of the relaxation energy on the conductivity in this doping regime was not investigated. It is suggested to measure the activation energy at different doping concentrations for compounds which have a similar Coulomb binding energy but differ in their relaxation energy, for example n-doped C₆₀ and C₇₀. Large relaxation energies might facilitate the high dissociation barriers of electron-hole pairs at low concentrations.

A similar dependence of the charge carrier mobility on the relaxation energy and the energetic disorder is also expected for high charge carrier concentrations in intrinsic semi-

conductors [81]. Temperature-dependent mobility measurements in field-effect transistors on intrinsic organic semiconductors with varying relaxation energy and energetic disorder would shed light on this question. As the energetic disorder is usually lower compared to doped semiconductors, the dependencies on these two parameters might be different for intrinsic semiconductors. Probably, the optimum relaxation energy yielding the highest mobility is lower compared to the highly n-doped semiconductors investigated in this thesis.

The investigations revealed a correlation between macroscopic thin film parameters (conductivity and energetic disorder) and microscopic molecular parameters (Coulomb binding energy of ICTCs, relaxation energy). To understand the origin of this correlation, the microscopic transport mechanism need to be investigated in more detail by simulations in addition to further experimental transport studies. Additional investigations of the microscopic structure within the doped layers could assist such transport simulations. These simulations might answer the question whether electron transfer occurs directly between different ICTCs or via states of “free” matrix molecules and how the transport mechanism changes with doping concentration.

In the last section, an universal electron trap introduced upon air exposure was observed for several n-doped semiconductors. To connect the energy of this trap to a molecular species, further experiments and simulations are necessary. Instead of the exposure to ambient air, the samples could be exposed to pure gases involving only one gaseous species. In addition, simulations might be able to provide electron affinities of potential compounds acting as charge carrier trap within the n-doped semiconductors by accounting for polarization effects and electrostatic interactions. Similarly, the occurrence of an universal trap energy is also expected for p-doped semiconductors [239]. An equal investigation of the air stability of p-doped semiconductors would necessitate a molecular p-dopant with an electron affinity of 6 eV or even larger, which is however not available yet.

7. Appendix

7.1 List of Abbreviations and Symbols

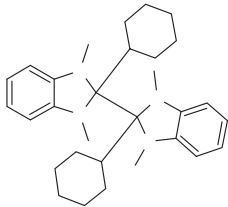
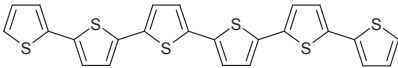
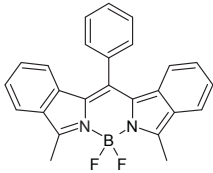
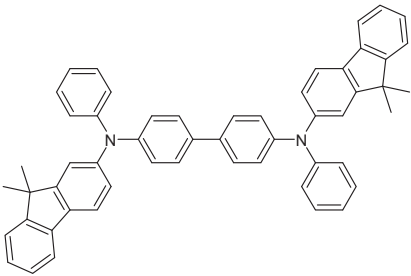
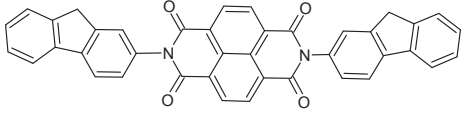
| | |
|-------------------------------|--|
| A | Acceptor |
| a.u. | arbitrary units |
| BHJ | Bulk heterojunction |
| CT | Charge transfer (state) |
| D | Donor |
| $\Delta_{+,-}$ | Solid-state correction of <i>IE</i> and <i>EA</i> |
| Δ_{perm} | Interaction energy with permanent charge distributions |
| $\Delta_{\text{q-Q}}$ | Charge-quadrupole interaction energy |
| DFT | Density functional theory |
| DOS | Density of states |
| <i>EA</i> | Electron affinity |
| <i>EA</i> ₀ | Gas-phase electron affinity (calculated by DFT) |
| <i>E</i> _{coul,CT} | Coulomb binding energy of CT state |
| <i>E</i> _{coul,ICTC} | Coulomb binding energy of ICTC |
| <i>E</i> _{CS} | Energy of separated/free charges |
| <i>E</i> _{CT} | Energy of CT state |
| <i>E</i> _T | (Charge carrier) trap energy |
| <i>FF</i> | Fill factor |
| FWHM | Full width at half maximum |
| HBEC | High binding energy cut-off |
| HOMO | Highest occupied molecular orbital |
| IAPP | Dresden Integrated Center for Applied Physics and Photonic Materials, TU Dresden, www.iapp.de |
| ICTC | Integer charge transfer complex |
| <i>IE</i> | Ionization energy |
| <i>IE</i> ₀ | Gas-phase ionization energy (calculated by DFT) |
| <i>IE</i> _{A,ICTC} | <i>IE</i> of an acceptor anion within an ICTC |
| IMS | Institute for Molecular Science, Okazaki, Japan |

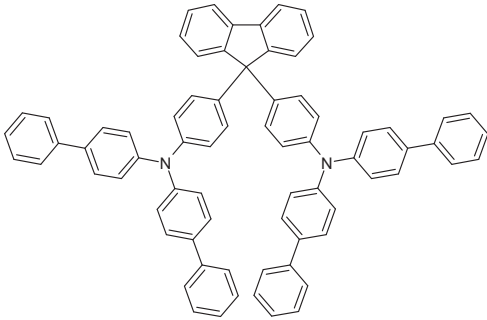

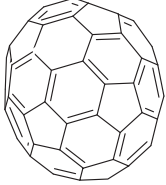
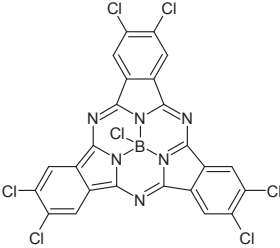
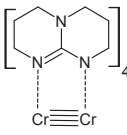
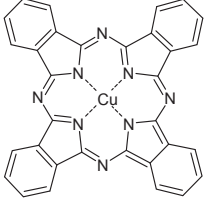
| | |
|-----------------|--|
| ITO | Indium tin oxide |
| IPES | Inverse photoelectron spectroscopy |
| j_{sc} | Short-circuit current density |
| λ | (Molecular) reorganization energy |
| $\lambda_{+,-}$ | (Molecular) relaxation energy of cations or anions |
| LEIPS | Low-energy inverse photoelectron spectroscopy |
| LUMO | Lowest unoccupied molecular orbital |
| mol% | Molar percent |
| μ | (Mean) charge carrier mobility |
| $P_{+,-}$ | Polarization energy of holes and electrons |
| PES | Photoelectron spectroscopy |
| Φ_s | Work function of sample |
| QPM | Quadrupole moment |
| $Q_{1/2}$ | Quadrupole component parallel to the molecular plane |
| Q_π | Quadrupole component vertical to the molecular plane |
| σ | (Static) energetic disorder |
| σ_{ICTC} | Energetic disorder of occupied ICTCs measured with UPS |
| σ_e | Electrical conductivity |
| UHV | Ultra-high vacuum |
| UPS | Ultraviolet photoelectron spectroscopy |
| V_{oc} | Open-circuit voltage |
| vol% | Percent per volume |
| wt% | Percent per weight |
| XPS | X-ray photoelectron spectroscopy |

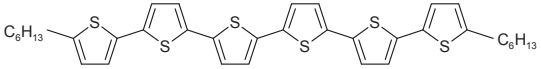
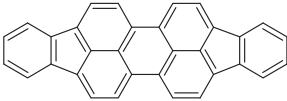

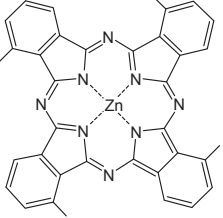
7.2 List of Materials

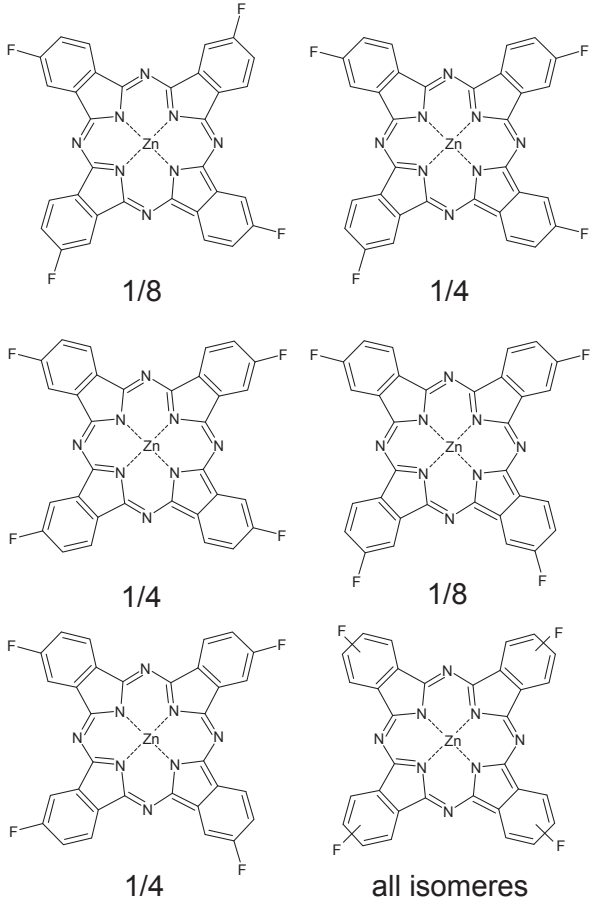
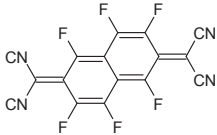
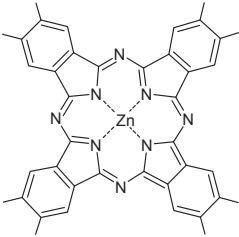
7.2.1 Chemical Structures and Names

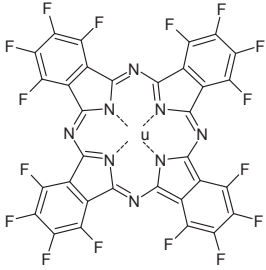
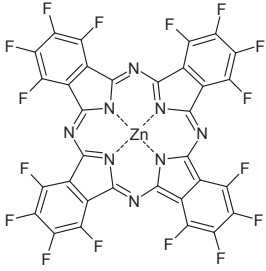
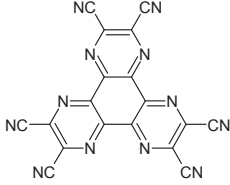
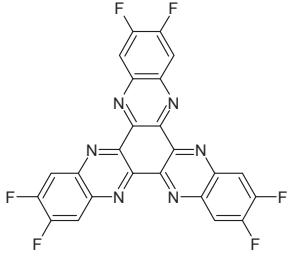
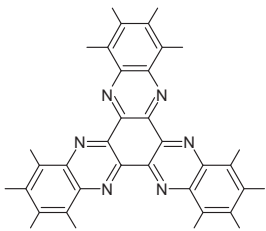
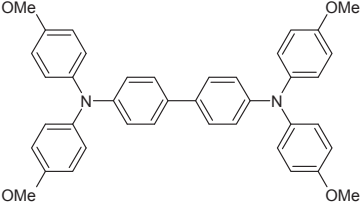
Table 7.1: Chemical structures and names of the molecules used in this thesis. Most of the names and structures are extracted from the OSOL database of IAPP [240].

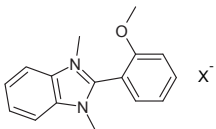
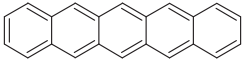
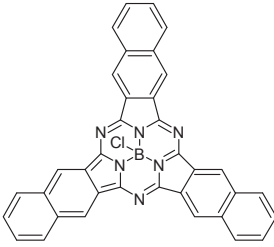
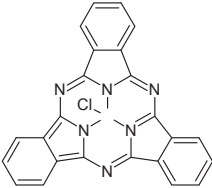
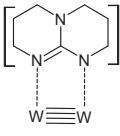
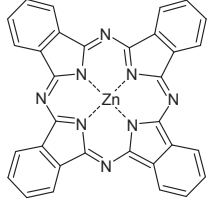
| Name & Supplier | Chemical structure |
|---|---|
| <p>(2-Cyc-DMBI)₂:</p> <p>2,2'-dicyclohexyl-1,1',3,3'-tetramethyl-2,2',3,3'-tetrahydro-1H,1'H-2,2'-bibenzo[d]imidazole</p> <p>Supplier: Zhenan Bao group (Stanford, CA, US)</p> |  |
| <p>6T:</p> <p>2,2':5',2'':5'',2''':5''',2''':5''',2''''-sexithiophene</p> <p>Supplier information in references [21, 22]</p> |  |
| <p>bDIP:</p> <p>benzannulated boron dipyrromethane</p> <p>Supplier information in reference [22]</p> |  |
| <p>BF-DPB:</p> <p>N,N'-((Diphenyl-N,N'-bis(9,9-dimethylfluoren-2-yl))-benzidine</p> <p>Supplier information in reference [102]</p> |  |
| <p>bis-HFI-NTCDI:</p> <p>N,N-Bis(fluoren-2-yl)-naphthalenetetracarboxylic diimide</p> <p>Synthesized by Markus Hummert (IAPP)</p> |  |

| | |
|--|--|
| <p>BPAPF:</p> <p>9,9-bis[4-(N,N-bis-biphenyl-4-yl-amino)phenyl]-9H-fluorene</p> <p>Supplier: Lumtec (New Taipei City, Taiwan)</p> |  |
| <p>C₆₀:</p> <p>Buckminster Fullerene</p> <p>Supplier: IPMS, CreaPhys (Dresden, Germany)</p> |  |
| <p>C₇₀:</p> <p>buckminster fullerene C70</p> <p>Supplier: CreaPhys (Dresden, Germany)</p> |  |
| <p>Cl₆SubPc:</p> <p>2,3,9,10,16,17-Hexachlorinated boron subphthalocyanine chloride</p> <p>Supplier: Lumtec (New Taipei City, Taiwan)</p> |  |
| <p>Cr₂(hpp)₄:</p> <p>tetrakis(1,3,4,6,7,8-hexahydro-2H-pyrimido[1,2-a]pyrimidinato)dichromium (II)</p> |  |
| <p>CuPc:</p> <p>copper(II) phthalocyanine</p> <p>Supplier information in reference [188]</p> |  |

| | |
|---|--|
| <p>DH6T:</p> <p>5,5''''-Dihexyl- 2,2':5',2'':5'',2''':5''',2''':5''',2''''- sexithiophene</p> <p>Supplier information in reference [21]</p> |  |
| <p>DIP:</p> <p>Diindeno[1,2,3-cd:1',2',3'-lm]perylene Periflanthen</p> <p>Supplier information in reference [191]</p> |  |
| <p>F₄TCNQ:</p> <p>2,3,5,6-Tetrafluoro-7,7,8,8- tetracyanoquinodimethane</p> <p>Supplier information in reference [241]</p> |  |
| <p>F₄-ZnPc:</p> <p>1,1',1'',1'''-tetrafluorophthalocyaninato zinc(II)</p> <p>Supplier: BASF (Ludwigshafen, Germany)</p> |  |

| | |
|---|---|
| <p>F₄ZnPc:</p> <p>Compound consists of different isomers, where the numbers below depict their relative occurrences in the mixture. The last structure symbolizes all five isomers by one structure.</p> <p>Supplier: Beatrice Beyer (Fraunhofer FEP, COMEDD, Dresden, Germany)</p> |  <p>The image shows five chemical structures of F₄ZnPc isomers. Each structure is a zinc phthalocyanine with four fluorine atoms at different positions on the four phenyl rings. The relative occurrences are: 1/8, 1/4, 1/4, 1/8, and a structure labeled 'all isomers'.</p> |
| <p>F₆TCNNQ:</p> <p>2,2'-(perfluoronaphthalene-2,6-diylidene)dimalononitrile</p> <p>Supplier: Novaled GmbH (Dresden, Germany)</p> |  <p>The image shows the chemical structure of F₆TCNNQ, which is 2,2'-(perfluoronaphthalene-2,6-diylidene)dimalononitrile. It consists of a central naphthalene ring system with two malononitrile groups attached at the 2 and 2' positions, and six fluorine atoms at the 2, 3, 4, 5, 6, and 7 positions.</p> |
| <p>F₈ZnPc:</p> <p>2,2',2'',2''',3,3',3'',3'''- Octafluorophthalocyaninato zinc(II)</p> <p>Synthesized by Matthias Lau (IAPP); supplied by Dieter Wöhrle (Uni Bremen, Germany)</p> |  <p>The image shows the chemical structure of F₈ZnPc, which is octafluorophthalocyaninato zinc(II). It consists of a central zinc atom coordinated to four nitrogen atoms in a phthalocyanine ring, with eight fluorine atoms attached to the four phenyl rings.</p> |

| | |
|---|---|
| <p>$F_{16}CuPc$:</p> <p>1,1',1'',1''',2,2',2'',2''',3,3',3'',3''',4,4',4'',4'''-hexadecafluorophthalocyaninato copper(II)</p> <p>Supplier information in reference [188]</p> |  |
| <p>$F_{16}ZnPc$:</p> <p>1,1',1'',1''',2,2',2'',2''',3,3',3'',3''',4,4',4'',4'''-hexadecafluorophthalocyaninato zinc(II)</p> <p>Supplier: Beatrice Beyer (Fraunhofer FEP, COMEDD, Dresden, Germany)</p> |  |
| <p>$HAT(CN)_6$:</p> <p>2,3,6,7,10,11-hexacyano-1,4,5,8,9,12-hexaazatriphenylene</p> <p>Supplier: Lumtec (New Taipei City, Taiwan)</p> |  |
| <p>$HATNA-F_6$:</p> <p>2,3,8,9,14,15-Hexafluoro-5,6,11,12,17,18-hexaazatrinaphthylene</p> <p>Supplier: MPI Mainz, Germany [192]</p> |  |
| <p>$HATNA-F_{12}$:</p> <p>1,2,3,4,7,8,9,10,13,14,15,16-Dodecafluoro-5,6,11,12,17,18-hexaazatrinaphthylene</p> <p>Supplier: MPI Mainz, Germany [192]</p> |  |
| <p>$MeO-TPD$:</p> <p>N,N,N',N'-Tetrakis(4-methoxyphenyl)-benzidine</p> <p>Supplier information in references [41, 102]</p> |  |

| | |
|--|--|
| <p>NDP9:</p> <p>Supplier: Novald GmbH (Dresden, Germany)</p> | |
| <p>o-MeO-DMBI-X:</p> <p>2-(2-Methoxyphenyl)-1,3-dimethyl-1H-benzimidazol-3-ium X</p> <p>X=iodide, bromide, chloride</p> <p>Supplier: Zhenan Bao group (Stanford, CA, US)</p> |  |
| <p>Pentacene:</p> <p>Supplier information in reference [94]</p> |  |
| <p>SubNc:</p> <p>Boron sub-2,3-naphthalocyanine chloride</p> <p>Supplier: Lumtec (New Taipei City, Taiwan)</p> |  |
| <p>SubPc:</p> <p>Boron subphthalocyanine chloride</p> <p>Supplier: Lumtec (New Taipei City, Taiwan)</p> |  |
| <p>W₂(hpp)₄:</p> <p>tetrakis(1,3,4,6,7,8-hexahydro-2H-pyrimido[1,2-a]pyrimidinato)ditungsten (II)</p> <p>Supplier: Novald GmbH (Dresden, Germany)</p> |  |
| <p>ZnPc:</p> <p>zinc(II) phthalocyanine</p> <p>Supplier: CreaPhys (Dresden, Germany)</p> |  |

7.2.2 Material Properties

Table 7.2: Thin-film parameters of the molecules used in this thesis. Density values and most of the molar masses are taken from the OSOL database of IAPP [240]. Ionization energy (IE) values are obtained by the low-binding-energy onsets of the respective emission profiles obtained from ultraviolet photoelectron spectroscopy measurements. Equally, the high-binding-energy-onsets of the (low-energy) inverse photoelectron spectroscopy peaks give the respective values for the electron affinity (EA). IE_{weak} and EA_{weak} denote the usage of weakly interaction substrates such as glass, ITO or amorphous organic layers. IE_{strong} and EA_{strong} denote the usage of strongly interaction substrates such as gold or silver substrates.

| Material | Density [g/cm ³] | Mol. mass [g/mol] | IE_{strong} [eV] | IE_{weak} [eV] | EA_{strong} [eV] | EA_{weak} [eV] |
|------------------------------------|---------------------------------|----------------------|------------------------------|----------------------------|------------------------------|----------------------------|
| 2-Cyc-DMBI | | 229.3 | | | | |
| 6T | 1.4 | 494.8 | 5.4 [21] | 5.0 [21] | | 2.04 [242] |
| bDIP | | 396.2 | | | | |
| BF-DPB | 1.21 | 720.9 | 5.23 ¹ | 5.21 ² | | |
| bis-HfI-NTCDI | 1.25 | 594.6 | | 6.62 | | 3.8 ³ |
| BPAPF | 1.2 | 957.2 | 5.6 ¹ | | | |
| C ₆₀ | 1.63 | 720.6 | | | | 4.0 ³ |
| C ₇₀ | | 840.8 | 6.41 ¹ | | | 4.0 [223] |
| Cl ₆ SubPc | | 637.3 | | 6.34 ² | | |
| Cr ₂ (hpp) ₄ | | 656.8 | 4.0 | | | |
| CuPc | | 576.1 | 5.2 [188] | 4.8 [188] | | |
| DH6T | | 663.1 | 5.3 [21] | 4.7 [21] | | |
| DIP | 1.35 | 400.5 | 5.60 [191] | 5.20 [191] | | |
| F ₄ TCNQ | | 276.1 | | | | |
| F ₄ -ZnPc | | 649.9 | 5.46 [178] | 5.22 ² | | |
| F ₄ ZnPc | | 649.9 | | 5.82 | | |
| F ₆ TCNNQ | | 362.2 | | | | |
| F ₈ ZnPc | | 721.8 | 6.1 | 6.48 | | |
| F ₁₆ CuPc | | 863.9 | 5.9 [188] | 6.6 [188] | | |
| F ₁₆ ZnPc | | 865.8 | 6.2 [189] | 6.78 | | |
| HAT(CN) ₆ | 1.67 | 384.3 | 9.6 [207] | | | > 4.9 [224] |
| HATNA-F ₆ | 1.58 | 492.3 | 7.72 [192] | 7.84 ² | | |
| HATNA-F ₁₂ | 1.5 | 600.3 | 7.73 [192] | 8.21 ² | 3.75 [225] | |
| MeO-TPD | 1.46 | 608.7 | 5.1 ¹ | | | |
| o-MeO-DMBI | | 253.3 | | | | |

| | | | | | | |
|-----------------------------------|------|-------|-----------|-------------------|------------|------------------|
| Pentacene | 1.32 | 278.4 | 5.25 [90] | 4.90 [90] | 3.0 [243] | 2.7 [193] |
| SubNc | | 580.8 | | 5.35 [242] | | 3.47 [242] |
| SubPc | 1.5 | 430.7 | | 5.78 ² | | 3.26 [242] |
| W ₂ (hpp) ₄ | | 920.4 | 2.4 [127] | | | |
| ZnPc | 1.55 | 577.9 | 5.30 | 5.02 | 3.34 [244] | 3.0 ³ |

¹Acquired by Dr. Selina Olthof at IAPP

²Acquired by Katrin Ortstein at IAPP

³Acquired by Dr. Fabio Bussolotti at IMS in Okazaki, Japan

7.3 Simulation Results

Table 7.3: Properties of single molecules in the gas phase, as calculated by density functional theory: IE_0 and EA_0 are the ionization energy and electron affinity of single molecules without geometrical relaxation, respectively. Q_1 , Q_2 and Q_π are the diagonal components of the quadrupole tensor with the trace being zero. The Q_π component points perpendicular to the molecular plane of the molecule. In-plane quadrupole components of F_4ZnPc change strongly between -21 and 21 ea_0^2 change strongly for the different isomers. λ_+ and λ_- denote relaxation energies of cations and anions, respectively. All values are calculated by Dr. Christopher Gaul and Karl Sebastian Schellhammer as part of the group of Dr. Frank Ortmann at TU Dresden.

| Material | IE_0 [eV] | EA_0 [eV] | $Q_1 / Q_2 / Q_\pi [ea_0^2]$ | λ_+ / λ_- [eV] |
|----------------------|-------------|-------------|------------------------------|------------------------------|
| 2-Cyc-DMBI | 4.64 | | / / | 1.06 / |
| 6T | 6.70 | 1.05 | 21.3 / 0.8 / -22.2 | 0.264 / 0.233 |
| bDIP | 6.55 | 1.45 | 8.0 / 2.9 / -10.8 | 0.078 / 0.127 |
| bis-HFI-NTCDI | 7.89 | 2.21 | 10.7 / 9.7 / -20.4 | 0.180 / 0.252 |
| BPAPF | 6.56 | 0.00 | -6.5 / 8.3 / -1.9 | 0.078 / 0.133 |
| C_{60} | 8.09 | 2.45 | 0 / 0 / 0 | 0.123 / 0.085 |
| C_{70} | 7.95 | 2.52 | 6 / -3 / -3 | 0.051 / 0.274 |
| Cl_6SubPc | 7.28 | 2.51 | 2.9 / 2.8 / -5.7 | 0.068 / 0.190 |
| CuPc | 8.78 | 0.89 | 10.0 / 10.0 / -19.9 | 0.262 / 0.218 |
| DH6T | 6.54 | 0.99 | 44.0 / -12.3 / -31.6 | 0.258 / 0.223 |
| DIP | 7.01 | 1.75 | 7.3 / 11.2 / -18.5 | 0.112 / 0.113 |
| F_4-ZnPc | 6.54 | 2.29 | 6.9 / 6.9 / -13.9 | 0.036 / 0.159 |
| F_4ZnPc | 6.65 | 2.35 | / / -0.8 ¹ | 0.038 / 0.172 ¹ |
| F_8ZnPc | 6.94 | 2.60 | -8.2 / -8.2 / 16.3 | 0.042 / 0.184 |
| $F_{16}CuPc$ | 9.77 | 1.89 | -12 / -12 / 24 | 0.319 / 0.238 |
| $F_{16}ZnPc$ | 7.21 | 2.43 | -12 / -12 / 24 | 0.058 / |
| HAT(CN) ₆ | 11.59 | 3.27 | -18.6 / -18.6 / 37.2 | 0.780 / 0.082 |
| HATNA- F_6 | 8.82 | 2.01 | -3.6 / -3.6 / 7.3 | 0.226 / 0.092 |
| HATNA- F_{12} | 9.25 | 2.48 | -7.5 / -7.5 / 15.1 | 0.110 / 0.094 |
| Pentacene | 6.51 | 1.46 | 6.0 / 7.6 / -13.6 | 0.046 / 0.059 |
| SubNc | 6.23 | 1.72 | 14.6 / 14.4 / -28.9 | 0.043 / 0.166 |
| SubPc | 6.88 | 1.64 | 9.9 / 9.8 / -19.7 | 0.062 / 0.189 |
| ZnPc | 6.34 | 2.04 | 9.6 / 9.6 / -19.2 | 0.026 / 0.173 |

¹Mean value of all isomers.

Table 7.4: Properties of integer charge transfer complexes (ICTC) and charge transfer (CT) states of different pairs of charged molecules, as calculated by density functional theory. $E_{\text{coul,ICTC/CT}}$ describes the Coulomb binding energy of ICTC or CT states. $p_{\text{CT/ICTC}}$ is the distance between the centers of the negative charge on the anion and the positive charge on the cation and describes the dipole moment of the ICTC or CT state. The first twelve material combinations are matrix:dopant systems and the last two are donor:acceptor systems, as used in solar cells.

| Material combination | $E_{\text{coul,ICTC/CT}}$ [eV] | $p_{\text{ICTC/CT}}$ [eÅ] |
|--|--------------------------------|---------------------------|
| Bis-HFI-NTCDI:2-Cyc-DMBI | 2.48 ¹ | 3.08 ¹ |
| C ₆₀ :2-Cyc-DMBI | 1.97 ¹ | 6.20 ¹ |
| C ₆₀ :W ₂ (hpp) ₄ | 1.68 ¹ | 8.01 ¹ |
| Cl ₆ SubPc:2-Cyc-DMBI | 2.38 ¹ | 3.56 ¹ |
| F ₄ ZnPc:2-Cyc-DMBI | 2.25 ¹ | 3.05 ¹ |
| F ₈ ZnPc:2-Cyc-DMBI | 1.90 ¹ | 2.99 ¹ |
| HAT(CN) ₆ :2-Cyc-DMBI | 1.86 ¹ | 2.71 ¹ |
| HATNA-F ₆ :2-Cyc-DMBI | 2.34 ¹ | 3.29 ¹ |
| HATNA-F ₁₂ :2-Cyc-DMBI | 2.18 ¹ | 2.83 ¹ |
| SubNc:2-Cyc-DMBI | 2.31 ¹ | 4.77 ¹ |
| SubPc:2-Cyc-DMBI | 2.63 ¹ | 4.14 ¹ |
| ZnPc:2-Cyc-DMBI | 2.61 ¹ | 3.17 ¹ |
| F ₄ ZnPc:C ₆₀ | 1.79 ¹ | 6.08 ¹ |
| ZnPc:C ₆₀ | 1.56 ¹ | 6.08 ¹ |

¹Calculated by Dr. Reinhard Scholz (IAPP)

7.4 Stack Details for UPS samples

Table 7.5: Layer stack details for ultraviolet photoelectron spectroscopy (UPS) samples processed by thermal evaporation at IAPP. Au and Ag depict freshly sputtered polycrystalline gold and silver foils, respectively.

| Section | Figure | Stack Details |
|---------|--------|---|
| 4.2 | 4.2 | Ag, BPAPF:NDP9 (2 wt%, 5 nm), ZnPc (20 nm) Au, ZnPc (20 nm) Ag, BPAPF:NDP9 (3 wt%, 5 nm), F ₈ ZnPc (20 nm) Au, F ₈ ZnPc (20 nm) |
| 4.2 | 4.3 | Ag, BPAPF:NDP9 (2 wt%, 5 nm), ZnPc (20 nm) Au, ZnPc (20 nm) Ag, BF-DPB (5 nm), F ₄ -ZnPc (20 nm) Ag, BPAPF:NDP9 (2 wt%, 5 nm), F ₄ ZnPc (20 nm) Ag, BPAPF:NDP9 (3 wt%, 5 nm), F ₈ ZnPc (20 nm) Au, F ₈ ZnPc (20 nm) Ag, BPAPF:NDP9 (2 wt%, 5 nm), F ₁₆ ZnPc (20 nm) |
| 4.2 | 4.4 | Ag, BPAPF:NDP9 (2 wt%, 5 nm), ZnPc (0...20 nm) Ag, BPAPF:NDP9 (2 wt%, 5 nm), F ₄ ZnPc (0...20 nm) Ag, BPAPF:NDP9 (3 wt%, 5 nm), F ₈ ZnPc (0...20 nm) Ag, BPAPF:NDP9 (2 wt%, 5 nm), F ₁₆ ZnPc (0...20 nm) |
| 4.2 | 4.5 | Ag, BPAPF:NDP9 (2 wt%, 5 nm), ZnPc (20 nm) Au, ZnPc (20 nm) Ag, BF-DPB (5 nm), F ₄ -ZnPc (20 nm) Ag, BPAPF:NDP9 (2 wt%, 5 nm), F ₄ ZnPc (20 nm) Ag, BPAPF:NDP9 (3 wt%, 5 nm), F ₈ ZnPc (20 nm) Au, F ₈ ZnPc (20 nm) Ag, BPAPF:NDP9 (2 wt%, 5 nm), F ₁₆ ZnPc (20 nm) Au, C ₆₀ (5 nm), HATNA-F ₆ (20 nm) Au, C ₆₀ (5 nm), HATNA-F ₁₂ (20 nm) |
| 4.3 | 4.6 | Ag, BPAPF:NDP9 (2 wt%, 5 nm), ... ZnPc:F ₄ ZnPc (1:0...0:1, 20 nm) ZnPc:F ₈ ZnPc (1:0...0:1, 20 nm) ZnPc:F ₁₆ ZnPc (1:0...0:1, 20 nm) |

| | | |
|-----|------|--|
| 4.3 | 4.7 | Ag, BPAPF:NDP9 (2 wt%, 5 nm), ... ZnPc:F ₄ ZnPc (1:0...0:1, 20 nm) ZnPc:F ₈ ZnPc (1:0...0:1, 20 nm) ZnPc:F ₁₆ ZnPc (1:0...0:1, 20 nm) F ₄ ZnPc:F ₁₆ ZnPc (1:0...0:1, 20 nm) Ag, BPAPF:NDP9 (3 wt%, 5 nm), SubPc:Cl ₆ SubPc (1:0...0:1, 20 nm) Au, C ₆₀ (5 nm), HATNA-F ₆ :HATNA-F ₁₂ (1:0...0:1, 20 nm) |
| 4.3 | 4.8 | Ag, BPAPF:NDP9 (3 wt%, 5 nm), F ₈ ZnPc:C ₆₀ (1:0...0:1, 20 nm) |
| 4.4 | 4.11 | Ag, BPAPF:NDP9 (2 wt%, 20 nm), ZnPc:F ₄ ZnPc:C ₆₀ (2:0:3...0:2:3, 39 nm) |
| 5.1 | 5.3 | Au, C ₆₀ F ₃₆ (3 nm), bis-HfI-NTCDI (3 nm), ... bis-HfI-NTCDI (3 nm), bis-HfI-NTCDI:o-MeO-DMBI-Cl (20 nm) bis-HfI-NTCDI:o-MeO-DMBI-Br (20 nm) bis-HfI-NTCDI:(2-Cyc-DMBI) ₂ (20 nm) bis-HfI-NTCDI:Cr ₂ (hpp) ₄ (20 nm) |
| 5.1 | 5.4 | Au, C ₆₀ F ₃₆ (3 nm), bis-HfI-NTCDI (3 nm), ... bis-HfI-NTCDI:o-MeO-DMBI-Br (10 mol%, 20 nm) |
| 5.2 | 5.11 | Ag, BPAPF:NDP9 (3 wt%, 5 nm), ... ZnPc (5 nm), ZnPc:(2-Cyc-DMBI) ₂ (20 nm) F ₄ ZnPc (5 nm), F ₄ ZnPc:(2-Cyc-DMBI) ₂ (20 nm) F ₈ ZnPc (5 nm), F ₈ ZnPc:(2-Cyc-DMBI) ₂ (20 nm) Au, C ₆₀ F ₃₆ (3 nm), C ₆₀ (3 nm), C ₆₀ :(2-Cyc-DMBI) ₂ (20 nm) |
| 5.2 | 5.12 | Ag, BPAPF:NDP9 (2 wt%, 5 nm), ... ZnPc (5 nm), ZnPc:(2-Cyc-DMBI) ₂ (10 mol%, 20 nm) F ₄ ZnPc (5 nm), F ₄ ZnPc:(2-Cyc-DMBI) ₂ (10 mol%, 20 nm) F ₈ ZnPc (5 nm), F ₈ ZnPc:(2-Cyc-DMBI) ₂ (10 mol%, 20 nm) Ag, BPAPF:NDP9 (3 wt%, 3 nm), ... SubPc (3 nm), SubPc:(2-Cyc-DMBI) ₂ (10 mol%, 20 nm) SubNc (3 nm), SubNc:(2-Cyc-DMBI) ₂ (10 mol%, 20 nm) Au, C ₆₀ (5 nm), ... HATNA-F ₁₂ (3 nm), HATNA-F ₁₂ :(2-Cyc-DMBI) ₂ (10 mol%, 20 nm) HAT(CN) ₆ (3 nm), HAT(CN) ₆ :(2-Cyc-DMBI) ₂ (10 mol%, 20 nm) Au, C ₆₀ F ₃₆ (3 nm), bis-HfI-NTCDI (3 nm), ... bis-HfI-NTCDI:(2-Cyc-DMBI) ₂ (10 mol%, 20 nm) bis-HfI-NTCDI:Cr ₂ (hpp) ₄ (9 mol%, 20 nm) |
| 5.2 | 5.13 | see Figure 5.12 for details |

| | | |
|-----|------|--|
| 5.3 | 5.18 | see Figure 5.12 for details |
| 5.4 | 5.21 | Ag, BPAPF:NDP9 (2 wt%, 5 nm), ... ZnPc (5 nm), ZnPc:(2-Cyc-DMBI) ₂ (10 mol%, 20 nm) F ₄ ZnPc (5 nm), F ₄ ZnPc:(2-Cyc-DMBI) ₂ (10 mol%, 20 nm) F ₈ ZnPc (5 nm), F ₈ ZnPc:(2-Cyc-DMBI) ₂ (10 mol%, 20 nm) Au, C ₆₀ (5 nm), ... HATNA-F ₆ (3 nm), HATNA-F ₆ :(2-Cyc-DMBI) ₂ (10 mol%, 20 nm) HATNA-F ₁₂ (3 nm), HATNA-F ₁₂ :(2-Cyc-DMBI) ₂ (10 mol%, 20 nm) HAT(CN) ₆ (3 nm), HAT(CN) ₆ :(2-Cyc-DMBI) ₂ (10 mol%, 20 nm) |
| 5.4 | 5.22 | Ag, BPAPF:NDP9 (2 wt%, 5 nm), ... ZnPc (5 nm), ZnPc:(2-Cyc-DMBI) ₂ (10 mol%, 20 nm) F ₄ ZnPc (5 nm), F ₄ ZnPc:(2-Cyc-DMBI) ₂ (10 mol%, 20 nm) F ₈ ZnPc (5 nm), F ₈ ZnPc:(2-Cyc-DMBI) ₂ (10 mol%, 20 nm) Au, C ₆₀ (5 nm), ... HATNA-F ₆ (3 nm), HATNA-F ₆ :(2-Cyc-DMBI) ₂ (10 mol%, 20 nm) HATNA-F ₁₂ (3 nm), HATNA-F ₁₂ :(2-Cyc-DMBI) ₂ (10 mol%, 20 nm) HAT(CN) ₆ (3 nm), HAT(CN) ₆ :(2-Cyc-DMBI) ₂ (10 mol%, 20 nm) Au, C ₆₀ F ₃₆ (3 nm), ... bis-HFI-NTCDI (3 nm), bis-HFI-NTCDI:(2-Cyc-DMBI) ₂ (10 mol%, 20 nm) C ₆₀ (3 nm), C ₆₀ :(2-Cyc-DMBI) ₂ (10 mol%, 20 nm) C ₇₀ (3 nm), C ₇₀ :(2-Cyc-DMBI) ₂ (10 mol%, 20 nm) |
| 5.4 | 5.23 | see Figure 5.22 for details |

Bibliography

- [1] S. R. Forrest: “The path to ubiquitous and low-cost organic electronic appliances on plastic”. *Nature* **428** (6986), 911 (2004).
- [2] T. Someya, T. Sekitani, S. Iba, Y. Kato, H. Kawaguchi, and T. Sakurai: “A large-area, flexible pressure sensor matrix with organic field-effect transistors for artificial skin applications.” *Proceedings of the National Academy of Sciences of the United States of America* **101** (27), 9966 (2004).
- [3] S. C. B. Mannsfeld, B. C.-K. Tee, R. M. Stoltenberg, C. V. H.-H. Chen, S. Barman, B. V. O. Muir, A. N. Sokolov, C. Reese, and Z. Bao: “Highly sensitive flexible pressure sensors with microstructured rubber dielectric layers”. *Nature Materials* **9** (10), 859 (2010).
- [4] M. Kaltenbrunner, M. S. White, E. D. Głowacki, T. Sekitani, T. Someya, N. S. Sariciftci, and S. Bauer: “Ultrathin and lightweight organic solar cells with high flexibility”. *Nature Communications* **3** (1), 770 (2012).
- [5] S. Berny, N. Blouin, A. Distler, H.-J. Egelhaaf, M. Krompiec, A. Lohr, O. R. Lozman, G. E. Morse, L. Nanson, A. Pron, T. Sauermann, N. Seidler, S. Tierney, P. Tiwana, M. Wagner, and H. Wilson: “Solar Trees: First Large-Scale Demonstration of Fully Solution Coated, Semitransparent, Flexible Organic Photovoltaic Modules”. *Advanced Science* **3** (5), 1500342 (2016).
- [6] R. R. Søndergaard, M. Hösel, and F. C. Krebs: “Roll-to-Roll fabrication of large area functional organic materials”. *Journal of Polymer Science Part B: Polymer Physics* **51** (1), 16 (2013).
- [7] S. Reineke, F. Lindner, G. Schwartz, N. Seidler, K. Walzer, B. Lüssem, and K. Leo: “White organic light-emitting diodes with fluorescent tube efficiency.” *Nature* **459** (7244), 234 (2009).
- [8] D. Baran, R. S. Ashraf, D. A. Hanifi, M. Abdelsamie, N. Gasparini, J. A. Röhr, S. Holliday, A. Wadsworth, S. Lockett, M. Neophytou, C. J. M. Emmott, J. Nelson, C. J.

- Brabec, A. Amassian, A. Salleo, T. Kirchartz, J. R. Durrant, and I. McCulloch: "Reducing the efficiency–stability–cost gap of organic photovoltaics with highly efficient and stable small molecule acceptor ternary solar cells". *Nature Materials* **16** (3), 363 (2017).
- [9] B. Siegmund, A. Mischok, J. Benduhn, O. Zeika, S. Ullbrich, F. Nehm, M. Böhm, D. Spoltore, H. Fröb, C. Körner, K. Leo, and K. Vandewal: "Organic narrowband near-infrared photodetectors based on intermolecular charge-transfer absorption". *Nature Communications* **8**, 15421 (2017).
- [10] T. Riedl, T. Rabe, H.-H. Johannes, W. Kowalsky, J. Wang, T. Weimann, P. Hinze, B. Nehls, T. Farrell, and U. Scherf: "Tunable organic thin-film laser pumped by an inorganic violet diode laser". *Applied Physics Letters* **88** (24), 241116 (2006).
- [11] G. Lanzani: "Organic electronics meets biology". *Nature Materials* **13** (8), 775 (2014).
- [12] T. Someya, Z. Bao, and G. G. Malliaras: "The rise of plastic bioelectronics". *Nature* **540** (7633), 379 (2016).
- [13] T. Yokota, P. Zalar, M. Kaltenbrunner, H. Jinno, N. Matsuhisa, H. Kitanosako, Y. Tachibana, W. Yukita, M. Koizumi, and T. Someya: "Ultraflexible organic photonic skin". *Science Advances* **2** (4), e1501856 (2016).
- [14] C. Goh, R. J. Kline, M. D. McGehee, E. N. Kadnikova, and J. M. J. Fréchet: "Molecular-weight-dependent mobilities in regioregular poly(3-hexyl-thiophene) diodes". *Applied Physics Letters* **86** (12), 122110 (2005).
- [15] J.-F. Chang, J. Clark, N. Zhao, H. Sirringhaus, D. W. Breiby, J. W. Andreasen, M. M. Nielsen, M. Giles, M. Heeney, and I. McCulloch: "Molecular-weight dependence of interchain polaron delocalization and exciton bandwidth in high-mobility conjugated polymers". *Physical Review B* **74** (11), 115318 (2006).
- [16] D. R. Zahn, G. N. Gavrila, and M. Gorgoi: "The transport gap of organic semiconductors studied using the combination of direct and inverse photoemission". *Chemical Physics* **325** (1), 99 (2006).
- [17] S. Krause, M. B. Casu, A. Schöll, and E. Umbach: "Determination of transport levels of organic semiconductors by UPS and IPS". *New Journal of Physics* **10** (8), 085001 (2008).
- [18] K. Vandewal: "Interfacial Charge Transfer States in Condensed Phase Systems". *Annual Review of Physical Chemistry* **67** (1), 113 (2016).

-
- [19] C. Deibel, T. Strobel, and V. Dyakonov: "Role of the Charge Transfer State in Organic Donor-Acceptor Solar Cells". *Advanced Materials* **22** (37), 4097 (2010).
- [20] M. L. Tietze, F. Wölzl, T. Menke, A. Fischer, M. Riede, K. Leo, and B. Lüssem: "Self-passivation of molecular n-type doping during air exposure using a highly efficient air-instable dopant". *Physica Status Solidi A* **210** (10), 2188 (2013).
- [21] S. Duhm, G. Heimel, I. Salzmann, H. Glowatzki, R. L. Johnson, A. Vollmer, J. P. Rabe, and N. Koch: "Orientation-dependent ionization energies and interface dipoles in ordered molecular assemblies." *Nature Materials* **7** (4), 326 (2008).
- [22] K. R. Graham, G. O. N. Ndjawa, S. M. Conron, R. Munir, K. Vandewal, J. J. Chen, S. Sweetnam, M. E. Thompson, A. Salleo, M. D. McGehee, and A. Amassian: "The Roles of Structural Order and Intermolecular Interactions in Determining Ionization Energies and Charge-Transfer State Energies in Organic Semiconductors". *Advanced Energy Materials* **6** (22), 1601211 (2016).
- [23] S. R. Yost and T. Van Voorhis: "Electrostatic Effects at Organic Semiconductor Interfaces: A Mechanism for "Cold" Exciton Breakup". *The Journal of Physical Chemistry C* **117** (11), 5617 (2013).
- [24] E. Tsiper, Z. Soos, W. Gao, and A. Kahn: "Electronic polarization at surfaces and thin films of organic molecular crystals: PTCDA". *Chemical Physics Letters* **360** (1-2), 47 (2002).
- [25] F. Amy, C. Chan, and A. Kahn: "Polarization at the gold/pentacene interface". *Organic Electronics* **6** (2), 85 (2005).
- [26] S. M. Ryno, Y.-T. Fu, C. Risko, and J.-L. Brédas: "Polarization Energies at Organic-Organic Interfaces: Impact on the Charge Separation Barrier at Donor-Acceptor Interfaces in Organic Solar Cells". *ACS Applied Materials & Interfaces* **8** (24), 15524 (2016).
- [27] C. Poelking, M. Tietze, C. Elschner, S. Olthof, D. Hertel, B. Baumeier, F. Würthner, K. Meerholz, K. Leo, and D. Andrienko: "Impact of mesoscale order on open-circuit voltage in organic solar cells." *Nature Materials* **14**, 434 (2015).
- [28] G. D'Avino, L. Muccioli, F. Castet, C. Poelking, D. Andrienko, Z. G. Soos, J. Cornil, and D. Beljonne: "Electrostatic phenomena in organic semiconductors: fundamentals and implications for photovoltaics". *Journal of Physics: Condensed Matter* **28** (43), 433002 (2016).
- [29] H. Yoshida, K. Yamada, J. Tsutsumi, and N. Sato: "Complete description of ionization energy and electron affinity in organic solids: Determining contributions

- from electronic polarization, energy band dispersion, and molecular orientation". *Physical Review B* **92** (7), 075145 (2015).
- [30] C. Poelking and D. Andrienko: "Long-Range Embedding of Molecular Ions and Excitations in a Polarizable Molecular Environment". *Journal of Chemical Theory and Computation* **12** (9), 4516 (2016).
- [31] S. Verlaak, D. Beljonne, D. Cheyns, C. Rolin, M. Linares, F. Castet, J. Cornil, and P. Heremans: "Electronic Structure and Geminate Pair Energetics at Organic-Organic Interfaces: The Case of Pentacene/C60 Heterojunctions". *Advanced Functional Materials* **19** (23), 3809 (2009).
- [32] R. Meerheim, C. Körner, B. Oesen, and K. Leo: "10.4% Efficient triple organic solar cells containing near infrared absorbers". *Applied Physics Letters* **108** (10), 103302 (2016).
- [33] B. Lüssem, M. L. Tietze, H. Kleemann, C. Hoßbach, J. W. Bartha, A. Zakhidov, and K. Leo: "Doped organic transistors operating in the inversion and depletion regime". *Nature Communications* **4**, 2775 (2013).
- [34] K. Walzer, B. Maennig, M. Pfeiffer, and K. Leo: "Highly efficient organic devices based on electrically doped transport layers." *Chemical Reviews* **107** (4), 1233 (2007).
- [35] B. Lüssem, M. Riede, and K. Leo: "Doping of organic semiconductors". *Physica Status Solidi A* **210** (1), 9 (2013).
- [36] J. Blochwitz, T. Fritz, M. Pfeiffer, K. Leo, D. Alloway, P. Lee, and N. Armstrong: "Interface electronic structure of organic semiconductors with controlled doping levels". *Organic Electronics* **2** (2), 97 (2001).
- [37] A. Abate, D. R. Staff, D. J. Hollman, H. J. Snaith, and A. B. Walker: "Influence of ionizing dopants on charge transport in organic semiconductors". *Physical Chemistry Chemical Physics* **16** (3), 1132 (2014).
- [38] A. Mityashin, Y. Olivier, T. Van Regemorter, C. Rolin, S. Verlaak, N. G. Martinelli, D. Beljonne, J. Cornil, J. Genoe, and P. Heremans: "Unraveling the mechanism of molecular doping in organic semiconductors." *Advanced Materials* **24** (12), 1535 (2012).
- [39] V. Arkhipov, E. Emelianova, P. Heremans, and H. Bässler: "Analytic model of carrier mobility in doped disordered organic semiconductors". *Physical Review B* **72** (23), 235202 (2005).

- [40] S. Olthof, S. Mehraeen, S. K. Mohapatra, S. Barlow, V. Coropceanu, J.-L. Bredas, S. R. Marder, and A. Kahn: "Ultralow doping in organic semiconductors: Evidence of trap filling". *Physical Review Letters* **109** (17), 176601 (2012).
- [41] M. L. Tietze, L. Burtone, M. Riede, B. Lüssem, and K. Leo: "Fermi level shift and doping efficiency in p-doped small molecule organic semiconductors: a photoelectron spectroscopy and theoretical study". *Physical Review B* **86** (3), 35320 (2012).
- [42] M. L. Tietze, P. Pahner, K. Schmidt, K. Leo, and B. Lüssem: "Doped Organic Semiconductors: Trap-Filling, Impurity Saturation, and Reserve Regimes". *Advanced Functional Materials* **25** (18), 2701 (2015).
- [43] I. Salzmänn, G. Heimel, S. Duhm, M. Oehzelt, P. Pingel, B. M. George, A. Schnegg, K. Lips, R.-P. Blum, A. Vollmer, and N. Koch: "Intermolecular hybridization governs molecular electrical doping". *Physical Review Letters* **108** (3), 35502 (2012).
- [44] I. Salzmänn, G. Heimel, M. Oehzelt, S. Winkler, and N. Koch: "Molecular Electrical Doping of Organic Semiconductors: Fundamental Mechanisms and Emerging Dopant Design Rules." *Accounts of Chemical Research* **49** (3), 370 (2016).
- [45] S. Guo, S. B. Kim, S. K. Mohapatra, Y. Qi, T. Sajoto, A. Kahn, S. R. Marder, and S. Barlow: "n-Doping of Organic Electronic Materials using Air-Stable Organometallics". *Advanced Materials* **24** (5), 699 (2012).
- [46] S. Zhang, B. D. Naab, E. V. Jucov, S. Parkin, E. G. B. Evans, G. L. Millhauser, T. V. Timofeeva, C. Risko, J.-L. Bredas, Z. Bao, S. Barlow, and S. R. Marder: "n-Dopants Based on Dimers of Benzimidazoline Radicals: Structures and Mechanism of Redox Reactions." *Chemistry - A European Journal* **21** (30), 10878 (2015).
- [47] B. D. Naab, S. Zhang, K. Vandewal, A. Salleo, S. Barlow, S. R. Marder, and Z. Bao: "Effective Solution- and Vacuum-Processed n-Doping by Dimers of Benzimidazoline Radicals". *Advanced Materials* **26** (25), 4268 (2014).
- [48] B. D. Naab, S. Guo, S. Olthof, E. G. B. Evans, P. Wei, G. L. Millhauser, A. Kahn, S. Barlow, S. R. Marder, and Z. Bao: "Mechanistic Study on the Solution-Phase n-Doping of 1,3-Dimethyl-2-aryl-2,3-dihydro-1H-benzimidazole Derivatives". *Journal of the American Chemical Society* **135** (40), 15018 (2013).
- [49] P. Wei, T. Menke, B. D. Naab, K. Leo, M. Riede, and Z. Bao: "2-(2-Methoxyphenyl)-1,3-dimethyl-1H-benzimidazol-3-ium Iodide as a New Air-Stable n-Type Dopant for Vacuum-Processed Organic Semiconductor Thin Films". *Journal of the American Chemical Society* **134** (9), 3999 (2012).
- [50] X. Lin, B. Wegner, K. M. Lee, M. A. Fusella, F. Zhang, K. Moudgil, B. P. Rand, S. Barlow, S. R. Marder, N. Koch, and A. Kahn: "Beating the thermodynamic limit

- with photo-activation of n-doping in organic semiconductors". *Nature Materials* **16** (12), 1209 (2017).
- [51] M. Schwoerer and H. C. Wolf: *Organic Molecular Solids*. Wiley-VCH, Weinheim, Germany (2007).
- [52] A. Köhler and H. Bässler: *Electronic Processes in Organic Semiconductors: An Introduction*. Wiley-VCH, Weinheim, Germany (2015).
- [53] M. Schwarze: *Photoelektronenspektroskopie am lösungsprozessierten Donor-Akzeptor-System P3HT:PCBM*. Master thesis, Universität Heidelberg (2012).
- [54] D. Cahen and A. Kahn: "Electron Energetics at Surfaces and Interfaces: Concepts and Experiments". *Advanced Materials* **15** (4), 271 (2003).
- [55] A. Kahn: "Fermi level, work function and vacuum level". *Materials Horizons* **3** (1), 7 (2016).
- [56] N. Karl: "Organic semiconductors". In "Festkörperprobleme 14", 261–290. Springer, Berlin, Heidelberg, Germany (1974).
- [57] H. Brinkmann, C. Kelting, S. Makarov, O. Tsaryova, G. Schnurpfeil, D. Wöhrle, and D. Schlettwein: "Fluorinated phthalocyanines as molecular semiconductor thin films". *Physica Status Solidi A* **205** (3), 409 (2008).
- [58] A. Klimkåns and S. Larsson: "Reorganization energies in benzene, naphthalene, and anthracene". *Chemical Physics* **189** (1), 25 (1994).
- [59] S. Kera, H. Yamane, and N. Ueno: "First-principles measurements of charge mobility in organic semiconductors: Valence hole-vibration coupling in organic ultrathin films". *Progress in Surface Science* **84** (5-6), 135 (2009).
- [60] E. A. Silinsh, A. Klimk, S. Larsson, and V. Capek: "Molecular polaron states in polyacene crystals. Formation and transfer processes". *Chemical Physics* **198** (3), 311 (1995).
- [61] C. Körner: *Oligothiophene Materials for Organic Solar Cells - Photophysics and Device Properties*. Dissertation, TU Dresden (2012).
- [62] E. V. Tsiper and Z. G. Soos: "Charge redistribution and polarization energy of organic molecular crystals". *Physical Review B* **64** (19), 195124 (2001).
- [63] G. D'Avino, L. Muccioli, C. Zannoni, D. Beljonne, and Z. G. Soos: "Electronic Polarization in Organic Crystals: A Comparative Study of Induced Dipoles and Intramolecular Charge Redistribution Schemes". *Journal of Chemical Theory and Computation* **10** (11), 4959 (2014).

- [64] C. Poelking and D. Andrienko: "Design rules for organic donor-acceptor heterojunctions: pathway for charge splitting and detrapping." *Journal of the American Chemical Society* **137** (19), 6320 (2015).
- [65] V. Coropceanu, J. Cornil, D. A. da Silva Filho, Y. Olivier, R. Silbey, and J.-L. Bredas: "Charge transport in organic semiconductors." *Chemical Reviews* **107** (4), 926 (2007).
- [66] A. Troisi and G. Orlandi: "Charge-Transport Regime of Crystalline Organic Semiconductors: Diffusion Limited by Thermal Off-Diagonal Electronic Disorder". *Physical Review Letters* **96** (8), 086601 (2006).
- [67] S.-i. Machida, Y. Nakayama, S. Duhm, Q. Xin, A. Funakoshi, N. Ogawa, S. Kera, N. Ueno, and H. Ishii: "Highest-Occupied-Molecular-Orbital Band Dispersion of Rubrene Single Crystals as Observed by Angle-Resolved Ultraviolet Photoelectron Spectroscopy". *Physical Review Letters* **104** (15), 156401 (2010).
- [68] S. Ciuchi, R. C. Hatch, H. Höchst, C. Faber, X. Blase, and S. Fratini: "Molecular Fingerprints in the Electronic Properties of Crystalline Organic Semiconductors: From Experiment to Theory". *Physical Review Letters* **108** (25), 256401 (2012).
- [69] F. Ortmann, K. Hannewald, and F. Bechstedt: "Ab initio studies of structural, vibrational, and electronic properties of durene crystals and molecules". *Physical Review B* **75** (19), 195219 (2007).
- [70] N. Karl: "Charge carrier transport in organic semiconductors". *Synthetic Metals* **133-134**, 649 (2003).
- [71] V. Podzorov, E. Menard, J. A. Rogers, and M. E. Gershenson: "Hall Effect in the Accumulation Layers on the Surface of Organic Semiconductors". *Physical Review Letters* **95** (22), 226601 (2005).
- [72] R. Marcus and N. Sutin: "Electron transfers in chemistry and biology". *Biochimica et Biophysica Acta* **811** (3), 265 (1985).
- [73] R. A. Marcus: "Electron transfer reactions in chemistry. Theory and experiment". *Reviews of Modern Physics* **65** (3), 599 (1993).
- [74] H. Bässler: "Charge Transport in Disordered Organic Photoconductors - A Monte Carlo Simulation Study". *Physica Status Solidi B* **175** (1), 15 (1993).
- [75] A. Miller and E. Abrahams: "Impurity Conduction at Low Concentrations". *Physical Review* **120** (3), 745 (1960).
- [76] S. D. Baranovskii: "Theoretical description of charge transport in disordered organic semiconductors". *Physica Status Solidi B* **251** (3), 487 (2014).

- [77] H. Bässler: “Localized states and electronic transport in single component organic solids with diagonal disorder”. *Physica Status Solidi B* **107** (1), 9 (1981).
- [78] I. I. Fishchuk, A. Kadashchuk, S. T. Hoffmann, S. Athanasopoulos, J. Genoe, H. Bässler, and A. Köhler: “Unified description for hopping transport in organic semiconductors including both energetic disorder and polaronic contributions”. *Physical Review B* **88** (12), 125202 (2013).
- [79] R. Coehoorn, W. F. Pasveer, P. A. Bobbert, and M. A. J. Michels: “Charge-carrier concentration dependence of the hopping mobility in organic materials with Gaussian disorder”. *Physical Review B* **72** (15), 155206 (2005).
- [80] N. I. Craciun, J. Wildeman, and P. W. M. Blom: “Universal Arrhenius Temperature Activated Charge Transport in Diodes from Disordered Organic Semiconductors”. *Physical Review Letters* **100** (5), 056601 (2008).
- [81] I. I. Fishchuk, A. K. Kadashchuk, J. Genoe, M. Ullah, H. Sitter, T. B. Singh, N. S. Sariciftci, and H. Bässler: “Temperature dependence of the charge carrier mobility in disordered organic semiconductors at large carrier concentrations”. *Physical Review B* **81** (4), 45202 (2010).
- [82] I. I. Fishchuk, A. Kadashchuk, A. Mityashin, M. M. Gavriluk, A. Köhler, H. Bässler, J. Genoe, H. Sitter, and N. S. Sariciftci: “Origin of Meyer-Neldel type compensation behavior in organic semiconductors at large carrier concentrations: Disorder versus thermodynamic description”. *Physical Review B* **90** (24), 245201 (2014).
- [83] M. C. J. M. Vissenberg and M. Matters: “Theory of the field-effect mobility in amorphous organic transistors”. *Physical Review B* **57** (20), 12964 (1998).
- [84] B. Maennig, M. Pfeiffer, A. Nollau, X. Zhou, K. Leo, and P. Simon: “Controlled p-type doping of polycrystalline and amorphous organic layers: Self-consistent description of conductivity and field-effect mobility by a microscopic percolation model”. *Physical Review B* **64** (19), 195208 (2001).
- [85] Y. Shen, K. Diest, M. H. Wong, B. R. Hsieh, D. H. Dunlap, and G. G. Malliaras: “Charge transport in doped organic semiconductors”. *Physical Review B* **68** (8), 081204 (2003).
- [86] D. Hoesterey and G. Letson: “The trapping of photocarriers in anthracene by anthraquinone, anthrone and naphthacene”. *Journal of Physics and Chemistry of Solids* **24** (12), 1609 (1963).
- [87] I. I. Fishchuk, A. K. Kadashchuk, H. Bässler, and D. S. Weiss: “Nondispersive charge-carrier transport in disordered organic materials containing traps”. *Physical Review B* **66** (20), 205208 (2002).

-
- [88] I. Fishchuk, A. Kadashchuk, A. Vakhnin, Y. Korosko, H. Bässler, B. Souharce, and U. Scherf: "Transition from trap-controlled to trap-to-trap hopping transport in disordered organic semiconductors". *Physical Review B* **73** (11), 115210 (2006).
- [89] H. T. Nicolai, M. Kuik, G. A. H. Wetzelaer, B. de Boer, C. Campbell, C. Risko, J. L. Bredas, and P. W. M. Blom: "Unification of trap-limited electron transport in semi-conducting polymers". *Nature Materials* **11** (10), 882 (2012).
- [90] F. Bussolotti, S. Kera, K. Kudo, A. Kahn, and N. Ueno: "Gap states in Pentacene Thin Film Induced by Inert Gas Exposure". *Physical Review Letters* **110** (26), 267602 (2013).
- [91] A. A. Günther, C. Hossbach, M. Sawatzki, D. Kasemann, J. W. Bartha, and K. Leo: "Controlling threshold voltage and leakage currents in vertical organic field-effect transistors by inversion mode operation". *Applied Physics Letters* **107** (23), 233302 (2015).
- [92] H. Kleemann, R. Gutierrez, F. Lindner, S. Avdoshenko, P. D. Manrique, B. Lüssem, G. Cuniberti, and K. Leo: "Organic Zener Diodes: Tunneling across the Gap in Organic Semiconductor Materials". *Nano Letters* **10** (12), 4929 (2010).
- [93] B. Lüssem, H. Kleemann, D. Kasemann, F. Ventsch, and K. Leo: "Organic Junction Field-Effect Transistor". *Advanced Functional Materials* **24** (7), 1011 (2014).
- [94] M. L. Tietze: *Molecular Doping Processes in Organic Semiconductors investigated by Photoelectron Spectroscopy*. Dissertation, TU Dresden (2014).
- [95] I. Salzmänn and G. Heimel: "Towards a comprehensive understanding of molecular doping organic semiconductors (review)". *Journal of Electron Spectroscopy and Related Phenomena* **204**, 208 (2015).
- [96] S.-J. Yoo and J.-J. Kim: "Charge Transport in Electrically Doped Amorphous Organic Semiconductors". *Macromolecular Rapid Communications* **36** (11), 984 (2015).
- [97] C. K. Chiang, C. R. Fincher, Y. W. Park, A. J. Heeger, H. Shirakawa, E. J. Louis, S. C. Gau, and A. G. MacDiarmid: "Electrical Conductivity in Doped Polyacetylene". *Physical Review Letters* **39** (17), 1098 (1977).
- [98] Y. Yamamoto, K. Yoshino, and Y. Inuishi: "Electrical Properties of Phthalocyanine-Halogen Complexes". *Journal of the Physical Society of Japan* **47** (6), 1887 (1979).
- [99] R. C. Haddon, A. F. Hebard, M. J. Rosseinsky, D. W. Murphy, S. J. Duclos, K. B. Lyons, B. Miller, J. M. Rosamilia, R. M. Fleming, A. R. Kortan, S. H. Glarum, A. V. Makhija, A. J. Muller, R. H. Eick, S. M. Zahurak, R. Tycko, G. Dabbagh, and F. A. Thiel: "Conducting films of C₆₀ and C₇₀ by alkali-metal doping". *Nature* **350** (6316), 320 (1991).

- [100] G. Parthasarathy, C. Shen, A. Kahn, and S. R. Forrest: "Lithium doping of semiconducting organic charge transport materials". *Journal of Applied Physics* **89** (9), 4986 (2001).
- [101] S. Olthof, W. Tress, R. Meerheim, B. Lüssem, and K. Leo: "Photoelectron spectroscopy study of systematically varied doping concentrations in an organic semiconductor layer using a molecular p-dopant". *Journal of Applied Physics* **106** (10), 103711 (2009).
- [102] T. Menke, D. Ray, H. Kleemann, M. P. Hein, K. Leo, and M. Riede: "Highly efficient p-dopants in amorphous hosts". *Organic Electronics* **15** (2), 365 (2014).
- [103] T. Menke, P. Wei, D. Ray, H. Kleemann, B. D. Naab, Z. Bao, K. Leo, and M. Riede: "A comparison of two air-stable molecular n-dopants for C60". *Organic Electronics* **13** (12), 3319 (2012).
- [104] J.-M. Kim, S.-J. Yoo, C.-K. Moon, B. Sim, J.-H. Lee, H. Lim, J. W. Kim, and J.-J. Kim: "N-Type Molecular Doping in Organic Semiconductors: Formation and Dissociation Efficiencies of a Charge Transfer Complex". *The Journal of Physical Chemistry C* **120** (17), 9475 (2016).
- [105] P. Pingel and D. Neher: "Comprehensive picture of p-type doping of P3HT with the molecular acceptor F4TCNQ". *Physical Review B* **87** (11), 115209 (2013).
- [106] J.-H. Lee, H.-M. Kim, K.-B. Kim, R. Kabe, P. Anzenbacher, and J.-J. Kim: "Homogeneous dispersion of organic p-dopants in an organic semiconductor as an origin of high charge generation efficiency". *Applied Physics Letters* **98** (17), 173303 (2011).
- [107] E. F. Aziz, A. Vollmer, S. Eisebitt, W. Eberhardt, P. Pingel, D. Neher, and N. Koch: "Localized charge transfer in a molecularly doped conducting polymer". *Advanced Materials* **19** (20), 3257 (2007).
- [108] H. Méndez, G. Heimel, A. Opitz, K. Sauer, P. Barkowski, M. Oehzelt, J. Soeda, T. Okamoto, J. Takeya, J.-B. Arlin, J.-Y. Balandier, Y. Geerts, N. Koch, and I. Salzmann: "Doping of Organic Semiconductors: Impact of Dopant Strength and Electronic Coupling". *Angewandte Chemie* **125** (30), 7905 (2013).
- [109] H. Méndez, G. Heimel, S. Winkler, J. Frisch, A. Opitz, K. Sauer, B. Wegner, M. Oehzelt, C. Röthel, S. Duhm, D. Többens, N. Koch, and I. Salzmann: "Charge-transfer crystallites as molecular electrical dopants". *Nature Communications* **6** (8560) (2015).
- [110] L. Zhu, E.-G. Kim, Y. Yi, and J.-L. Bredas: "Charge Transfer in Molecular Complexes with 2,3,5,6-Tetrafluoro-7,7,8,8-tetracyanoquinodimethane (F4-TCNQ): A Density Functional Theory Study". *Chemistry of Materials* **23** (23), 5149 (2011).

-
- [111] V. I. Arkhipov, P. Heremans, E. V. Emelianova, and H. Bässler: “Effect of doping on the density-of-states distribution and carrier hopping in disordered organic semiconductors”. *Physical Review B* **71** (4), 045214 (2005).
- [112] F. Castet, G. D’Avino, L. Muccioli, J. Cornil, and D. Beljonne: “Charge separation energetics at organic heterojunctions: on the role of structural and electrostatic disorder”. *Physical Chemistry Chemical Physics* **16** (38), 20279 (2014).
- [113] G. D’Avino, S. Mothy, L. Muccioli, C. Zannoni, L. Wang, J. Cornil, D. Beljonne, and F. Castet: “Energetics of Electron–Hole Separation at P3HT/PCBM Heterojunctions”. *The Journal of Physical Chemistry C* **117** (25), 12981 (2013).
- [114] M. L. Tietze, K. Leo, and B. Lüssem: “Quantification of deep hole-trap filling by molecular p-doping: Dependence on the host material purity”. *Organic Electronics* **14** (9), 2348 (2013).
- [115] S. Olthof, S. Singh, S. K. Mohapatra, S. Barlow, S. R. Marder, B. Kippelen, and A. Kahn: “Passivation of trap states in unpurified and purified C60 and the influence on organic field-effect transistor performance”. *Applied Physics Letters* **101** (25), 253303 (2012).
- [116] X. Jiang, Y. Harima, K. Yamashita, Y. Tada, J. Ohshita, and A. Kunai: “Doping-induced change of carrier mobilities in poly(3-hexylthiophene) films with different stacking structures”. *Chemical Physics Letters* **364** (5), 616 (2002).
- [117] P. Pingel, R. Schwarzl, and D. Neher: “Effect of molecular p-doping on hole density and mobility in poly(3-hexylthiophene)”. *Applied Physics Letters* **100** (14), 143303 (2012).
- [118] H. Kleemann, C. Schuenemann, A. A. Zakhidov, M. Riede, B. Lüssem, and K. Leo: “Structural phase transition in pentacene caused by molecular doping and its effect on charge carrier mobility”. *Organic Electronics* **13** (1), 58 (2012).
- [119] X. Lin, G. E. Purdum, Y. Zhang, S. Barlow, S. R. Marder, Y.-L. Loo, and A. Kahn: “Impact of a Low Concentration of Dopants on the Distribution of Gap States in a Molecular Semiconductor”. *Chemistry of Materials* **28** (8), 2677 (2016).
- [120] T. Menke, D. Ray, J. Meiss, K. Leo, and M. Riede: “In-situ conductivity and Seebeck measurements of highly efficient n-dopants in fullerene C60”. *Applied Physics Letters* **100** (9), 093304 (2012).
- [121] M. Hermenau: *Lebensdaueruntersuchungen an organischen Solarzellen*. Dissertation, TU Dresden (2012).

- [122] D. de Leeuw, M. Simenon, A. Brown, and R. Einerhand: "Stability of n-type doped conducting polymers and consequences for polymeric microelectronic devices". *Synthetic Metals* **87** (1), 53 (1997).
- [123] A. Werner, F. Li, K. Harada, M. Pfeiffer, T. Fritz, K. Leo, and S. Machill: "n-Type Doping of Organic Thin Films Using Cationic Dyes". *Advanced Functional Materials* **14** (3), 255 (2004).
- [124] F. Li, A. Werner, M. Pfeiffer, K. Leo, and X. Liu: "Leuco Crystal Violet as a Dopant for n-Doping of Organic Thin Films of Fullerene C60". *The Journal of Physical Chemistry B* **108** (44), 17076 (2004).
- [125] F. Li, M. Pfeiffer, A. Werner, K. Harada, K. Leo, N. Hayashi, K. Seki, X. Liu, and X.-D. Dang: "Acridine orange base as a dopant for n doping of C60 thin films". *Journal of Applied Physics* **100** (2), 023716 (2006).
- [126] Y. Qi, S. K. Mohapatra, S. B. Kim, S. Barlow, S. R. Marder, and A. Kahn: "Solution doping of organic semiconductors using air-stable n-dopants". *Applied Physics Letters* **100** (8), 83305 (2012).
- [127] M. L. Tietze, B. D. Rose, M. Schwarze, A. Fischer, S. Runge, J. Blochwitz-Nimoth, B. Lüssem, K. Leo, and J.-L. Bredas: "Passivation of Molecular n-Doping: Exploring the Limits of Air Stability". *Advanced Functional Materials* **26** (21), 3730 (2016).
- [128] Y. Park, L. Bormann, L. Müller-Meskamp, K. Vandewal, and K. Leo: "Efficient flexible organic photovoltaics using silver nanowires and polymer based transparent electrodes". *Organic Electronics* **36**, 68 (2016).
- [129] J. Hou, O. Inganäs, R. H. Friend, and F. Gao: "Organic solar cells based on non-fullerene acceptors". *Nature Materials* **17** (2), 119 (2018).
- [130] W. Zhao, D. Qian, S. Zhang, S. Li, O. Inganäs, F. Gao, and J. Hou: "Fullerene-Free Polymer Solar Cells with over 11% Efficiency and Excellent Thermal Stability". *Advanced Materials* **28** (23), 4734 (2016).
- [131] Z. Zheng, O. M. Awartani, B. Gautam, D. Liu, Y. Qin, W. Li, A. Bataller, K. Gundogdu, H. Ade, and J. Hou: "Efficient Charge Transfer and Fine-Tuned Energy Level Alignment in a THF-Processed Fullerene-Free Organic Solar Cell with 11.3% Efficiency". *Advanced Materials* **29** (5), 1604241 (2017).
- [132] S. Hunklinger: *Festkörperphysik*. Oldenbourg Wissenschaftsverlag GmbH, München, 2 edn. (2009).
- [133] R. G. Kepler: "Charge Carrier Production and Mobility in Anthracene Crystals". *Physical Review* **119** (4), 1226 (1960).

-
- [134] C. W. Tang and A. C. Albrecht: "Chlorophyll-a photovoltaic cells". *Nature* **254** (5500), 507 (1975).
- [135] G. Chamberlain: "Organic solar cells: A review". *Solar Cells* **8** (1), 47 (1983).
- [136] C. W. Tang: "Two-layer organic photovoltaic cell". *Applied Physics Letters* **48** (2), 183 (1986).
- [137] M. Knupfer: "Exciton binding energies in organic semiconductors". *Applied Physics A: Materials Science & Processing* **77** (5), 623 (2003).
- [138] C. M. Ramsdale, J. A. Barker, A. C. Arias, J. D. MacKenzie, R. H. Friend, and N. C. Greenham: "The origin of the open-circuit voltage in polyfluorene-based photovoltaic devices". *Journal of Applied Physics* **92** (8), 4266 (2002).
- [139] V. D. Mihailetschi, P. W. M. Blom, J. C. Hummelen, and M. T. Rispen: "Cathode dependence of the open-circuit voltage of polymer:fullerene bulk heterojunction solar cells". *Journal of Applied Physics* **94** (10), 6849 (2003).
- [140] Y. Liu, J. Zhao, Z. Li, C. Mu, W. Ma, H. Hu, K. Jiang, H. Lin, H. Ade, and H. Yan: "Aggregation and morphology control enables multiple cases of high-efficiency polymer solar cells". *Nature Communications* **5** (5293) (2014).
- [141] Y. Terao, H. Sasabe, and C. Adachi: "Correlation of hole mobility, exciton diffusion length, and solar cell characteristics in phthalocyanine/fullerene organic solar cells". *Applied Physics Letters* **90** (10), 103515 (2007).
- [142] R. R. Lunt, J. B. Benziger, and S. R. Forrest: "Relationship between Crystalline Order and Exciton Diffusion Length in Molecular Organic Semiconductors". *Advanced Materials* **22** (11), 1233 (2010).
- [143] M. Hiramoto, H. Fujiwara, and M. Yokoyama: "Three-layered organic solar cell with a photoactive interlayer of codeposited pigments". *Applied Physics Letters* **58** (10), 1062 (1991).
- [144] A. J. Heeger: "25th Anniversary Article: Bulk Heterojunction Solar Cells: Understanding the Mechanism of Operation". *Advanced Materials* **26** (1), 10 (2014).
- [145] S. Albrecht, K. Vandewal, J. R. Tumbleston, F. S. U. Fischer, J. D. Douglas, J. M. J. Fréchet, S. Ludwigs, H. Ade, A. Salleo, and D. Neher: "On the Efficiency of Charge Transfer State Splitting in Polymer:Fullerene Solar Cells". *Advanced Materials* **26** (16), 2533 (2014).
- [146] L. J. A. Koster, V. D. Mihailetschi, R. Ramaker, and P. W. M. Blom: "Light intensity dependence of open-circuit voltage of polymer:fullerene solar cells". *Applied Physics Letters* **86** (12), 123509 (2005).

- [147] J. C. Blakesley and D. Neher: "Relationship between energetic disorder and open-circuit voltage in bulk heterojunction organic solar cells". *Physical Review B* **84** (7), 075210 (2011).
- [148] K. Vandewal, J. Widmer, T. Heumueller, C. J. Brabec, M. D. McGehee, K. Leo, M. Riede, and A. Salleo: "Increased Open-Circuit Voltage of Organic Solar Cells by Reduced Donor-Acceptor Interface Area". *Advanced Materials* **26** (23), 3839 (2014).
- [149] J. Widmer, M. Tietze, K. Leo, and M. Riede: "Open-Circuit Voltage and Effective Gap of Organic Solar Cells". *Advanced Functional Materials* **23** (46), 5814 (2013).
- [150] K. Vandewal, W. D. Oosterbaan, S. Bertho, V. Vrindts, A. Gadisa, L. Lutsen, D. Vanderzande, and J. V. Manca: "Varying polymer crystallinity in nanofiber poly(3-alkylthiophene):PCBM solar cells: Influence on charge-transfer state energy and open-circuit voltage". *Applied Physics Letters* **95** (12), 123303 (2009).
- [151] F. Piersimoni, S. Chambon, K. Vandewal, R. Mens, T. Boonen, A. Gadisa, M. Izquierdo, S. Filippone, B. Ruttens, J. D'Haen, N. Martin, L. Lutsen, D. Vanderzande, P. Adriaensens, and J. V. Manca: "Influence of Fullerene Ordering on the Energy of the Charge-Transfer State and Open-Circuit Voltage in Polymer:Fullerene Solar Cells". *The Journal of Physical Chemistry C* **115** (21), 10873 (2011).
- [152] K. Vandewal, K. Tvingstedt, A. Gadisa, O. Inganäs, and J. V. Manca: "Relating the open-circuit voltage to interface molecular properties of donor:acceptor bulk heterojunction solar cells". *Physical Review B* **81** (12), 125204 (2010).
- [153] K. Vandewal, S. Albrecht, E. T. Hoke, K. R. Graham, J. Widmer, J. D. Douglas, M. Schubert, W. R. Mateker, J. T. Bloking, G. F. Burkhard, A. Sellinger, J. M. J. Fréchet, A. Amassian, M. K. Riede, M. D. McGehee, D. Neher, and A. Salleo: "Efficient charge generation by relaxed charge-transfer states at organic interfaces". *Nature Materials* **13** (1), 63 (2014).
- [154] S. Hüfner: *Photoelectron Spectroscopy - Principles and Applications*. Advanced Texts in Physics. Springer, Berlin, Heidelberg (2003).
- [155] S. Olthof: *Photoelectron Spectroscopy on Doped Organic Semiconductors and Related Interfaces*. Dissertation, TU Dresden (2010).
- [156] SPECS GmbH: *PHOIBOS - Hemispherical Energy Analyzer Series - PHOIBOS 100/150 Manual - Version 2.09*. Berlin (2007).
- [157] SPECS GmbH: *X-ray Source XR50 Manual - Version 1.8*. Berlin (2007).
- [158] T. Schultz, T. Lenz, N. Kotadiya, G. Heimel, G. Glasser, R. Berger, P. W. M. Blom, P. Amsalem, D. M. de Leeuw, and N. Koch: "Reliable Work Function Determination

- of Multicomponent Surfaces and Interfaces: The Role of Electrostatic Potentials in Ultraviolet Photoelectron Spectroscopy". *Advanced Materials Interfaces* **4** (19), 1700324 (2017).
- [159] S. Tanuma, C. J. Powell, and D. R. Penn: "Calculations of electron inelastic mean free paths. - V. Data for 14 organic compounds over the 50-2000 eV range". *Surface and Interface Analysis* **21** (3), 165 (1994).
- [160] Z. Tan, Y. Xia, M. Zhao, X. Liu, F. Li, B. Huang, and Y. Ji: "Electron stopping power and mean free path in organic compounds over the energy range of 20–10,000 eV". *Nuclear Instruments and Methods in Physics Research B* **222** (1), 27 (2004).
- [161] W. R. Salaneck: "Intermolecular Relaxation Energies in Anthracene". *Physical Review Letters* **40** (1), 60 (1978).
- [162] M. P. Seah and W. A. Dench: "Quantitative electron spectroscopy of surfaces: A standard data base for electron inelastic mean free paths in solids". *Surface and Interface Analysis* **1** (1), 2 (1979).
- [163] T. Sueyoshi, H. Fukagawa, M. Ono, S. Kera, and N. Ueno: "Low-density band-gap states in pentacene thin films probed with ultrahigh-sensitivity ultraviolet photoelectron spectroscopy". *Applied Physics Letters* **95** (18), 183303 (2009).
- [164] A. V. Naumkin, A. Kraut-Vass, S. W. Gaarenstroom, and C. J. Powell: "NIST Standard Reference Database 20, Version 4.1" (2012).
- [165] C. D. Wagner, L. E. Davis, M. V. Zeller, J. A. Taylor, R. H. Raymond, and L. H. Gale: "Empirical atomic sensitivity factors for quantitative analysis by electron spectroscopy for chemical analysis". *Surface and Interface Analysis* **3** (5), 211 (1981).
- [166] H. Yoshida: "Near-ultraviolet inverse photoemission spectroscopy using ultra-low energy electrons". *Chemical Physics Letters* **539-540**, 180 (2012).
- [167] B. Beyer: *Architectural Approaches for the Absorption Layer and their Impact on Organic Solar Cells*. Dissertation, TU Dresden (2013).
- [168] M. Schwarze, W. Tress, B. Beyer, F. Gao, R. Scholz, C. Poelking, K. Ortstein, A. A. Günther, D. Kasemann, D. Andrienko, and K. Leo: "Band structure engineering in organic semiconductors". *Science*. **352** (6292), 1446 (2016).
- [169] W. Tress, B. Beyer, N. Ashari Astani, F. Gao, S. Meloni, and U. Rothlisberger: "Extended Intermolecular Interactions Governing Photocurrent–Voltage Relations in Ternary Organic Solar Cells". *The Journal of Physical Chemistry Letters* **7** (19), 3936 (2016).

- [170] Y. Zhao and D. G. Truhlar: "The M06 suite of density functionals for main group thermochemistry, thermochemical kinetics, noncovalent interactions, excited states, and transition elements: Two new functionals and systematic testing of four M06-class functionals and 12 other function". *Theoretical Chemistry Accounts* **120** (1), 215 (2008).
- [171] T. H. Dunning Jr.: "Gaussian basis sets for use in correlated molecular calculations. I. The atoms boron through neon and hydrogen". *The Journal of Chemical Physics* **90** (2), 1007 (1989).
- [172] M. Valiev, E. Bylaska, N. Govind, K. Kowalski, T. Straatsma, H. Van Dam, D. Wang, J. Nieplocha, E. Apra, T. Windus, and W. de Jong: "NWChem: A comprehensive and scalable open-source solution for large scale molecular simulations". *Computer Physics Communications* **181** (9), 1477 (2010).
- [173] R. Scholz, R. Luschtinetz, G. Seifert, T. Jägeler-Hoheisel, C. Körner, K. Leo, and M. Rapacioli: "Quantifying charge transfer energies at donor-acceptor interfaces in small-molecule solar cells with constrained DFTB and spectroscopic methods". *Journal of Physics: Condensed Matter* **25** (47), 473201 (2013).
- [174] M. Schwarze, K. S. Schellhammer, C. Gaul, K. Ortstein, M. Lau, G. Cuniberti, C. Poelking, D. Andrienko, F. Ortman, and K. Leo: "Engineering of Device Energy Levels at Organic Heterojunctions by Charge-Quadrupole Interactions", submitted.
- [175] B. Maennig, D. Gebeyehu, P. Simon, F. Kozlowski, A. Werner, F. Li, S. Grundmann, S. Sonntag, M. Koch, K. Leo, M. Pfeiffer, H. Hoppe, D. Meissner, N. Sariciftci, I. Riedel, V. Dyakonov, J. Parisi, and J. Drechsel: "Organic p-i-n solar cells". *Applied Physics A: Materials Science & Processing* **79** (1), 1 (2004).
- [176] S. Pfuetzner, C. Mickel, J. Jankowski, M. Hein, J. Meiss, C. Schuenemann, C. Elschner, A. A. Levin, B. Rellinghaus, K. Leo, and M. Riede: "The influence of substrate heating on morphology and layer growth in C60:ZnPc bulk heterojunction solar cells". *Organic Electronics* **12** (3), 435 (2011).
- [177] C. Schünemann, D. Wynands, L. Wilde, M. P. Hein, S. Pfützn, C. Elschner, K.-J. Eichhorn, K. Leo, and M. Riede: "Phase separation analysis of bulk heterojunctions in small-molecule organic solar cells using zinc-phthalocyanine and C60". *Physical Review B* **85** (24), 245314 (2012).
- [178] J. Meiss, A. Merten, M. Hein, C. Schuenemann, S. Schäfer, M. Tietze, C. Uhrich, M. Pfeiffer, K. Leo, and M. Riede: "Fluorinated Zinc Phthalocyanine as Donor for Efficient Vacuum-Deposited Organic Solar Cells". *Advanced Functional Materials* **22** (2), 405 (2012).

- [179] M. L. Tietze, W. Tress, S. Pfützner, C. Schünemann, L. Burtone, M. Riede, K. Leo, K. Vandewal, S. Olthof, P. Schulz, and A. Kahn: "Correlation of open-circuit voltage and energy levels in zinc-phthalocyanine: C60 bulk heterojunction solar cells with varied mixing ratio". *Physical Review B* **88** (8), 085119 (2013).
- [180] T. Mönch, T. S. Sherkar, L. J. Anton Koster, P. Friederich, M. Riede, P. Formanek, C. Koerner, K. Vandewal, W. Wenzel, and K. Leo: "Experimental and theoretical study of phase separation in ZnPc:C60 blends". *Organic Electronics* **27**, 183 (2015).
- [181] J. Blochwitz, T. Fritz, M. Pfeiffer, K. Leo, D. Alloway, P. Lee, and N. Armstrong: "Interface electronic structure of organic semiconductors with controlled doping levels". *Organic Electronics* **2** (2), 97 (2001).
- [182] M. Brendel, S. Krause, A. Steindamm, A. K. Topczak, S. Sundarraj, P. Erk, S. Höhla, N. Fruehauf, N. Koch, and J. Pflaum: "The Effect of Gradual Fluorination on the Properties of F_nZnPc Thin Films and F_nZnPc/C60 Bilayer Photovoltaic Cells". *Advanced Functional Materials* **25** (10), 1565 (2015).
- [183] C. Schünemann, C. Elschner, A. Levin, M. Levichkova, K. Leo, and M. Riede: "Zinc phthalocyanine - Influence of substrate temperature, film thickness, and kind of substrate on the morphology". *Thin Solid Films* **519** (11), 3939 (2011).
- [184] C. Schünemann, D. Wynands, K.-J. Eichhorn, M. Stamm, K. Leo, and M. Riede: "Evaluation and Control of the Orientation of Small Molecules for Strongly Absorbing Organic Thin Films". *The Journal of Physical Chemistry C* **117** (22), 11600 (2013).
- [185] C. Schünemann: *Organic Small Molecules: Correlation between Molecular Structure, Thin Film Growth, and Solar Cell Performance*. Dissertation, TU Dresden (2012).
- [186] H. Jiang, P. Hu, J. Ye, Y. Li, H. Li, X. Zhang, R. Li, H. Dong, W. Hu, and C. Kloc: "Molecular Crystal Engineering: Tuning Organic Semiconductor from p-type to n-type by Adjusting Their Substitutional Symmetry". *Advanced Materials* **29** (10), 1605053 (2017).
- [187] J. Benduhn, K. Tvingstedt, F. Piersimoni, S. Ullbrich, Y. Fan, M. Tropiano, K. A. McGarry, O. Zeika, M. K. Riede, C. J. Douglas, S. Barlow, S. R. Marder, D. Neher, D. Spoltore, and K. Vandewal: "Intrinsic non-radiative voltage losses in fullerene-based organic solar cells". *Nature Energy* **2**, 17053 (2017).
- [188] W. Chen, D. C. Qi, Y. L. Huang, H. Huang, Y. Z. Wang, S. Chen, X. Y. Gao, and A. T. S. Wee: "Molecular Orientation Dependent Energy Level Alignment at Organic-Organic Heterojunction Interfaces". *The Journal of Physical Chemistry C* **113** (29), 12832 (2009).

- [189] D. Schlettwein, K. Hesse, N. E. Gruhn, P. A. Lee, K. W. Nebesny, and N. R. Armstrong: "Electronic Energy Levels in Individual Molecules, Thin Films, and Organic Heterojunctions of Substituted Phthalocyanines". *The Journal of Physical Chemistry B* **105** (21), 4791 (2001).
- [190] A. Opitz, A. Wilke, P. Amsalem, M. Oehzelt, R.-P. Blum, J. P. Rabe, T. Mizokuro, U. Hörmann, R. Hansson, E. Moons, and N. Koch: "Organic heterojunctions: Contact-induced molecular reorientation, interface states, and charge redistribution". *Scientific Reports* **6**, 21291 (2016).
- [191] J. Q. Zhong, H. Y. Mao, R. Wang, D. C. Qi, L. Cao, Y. Z. Wang, and W. Chen: "Effect of Gap States on the Orientation-Dependent Energy Level Alignment at the DIP/F16CuPc Donor-Acceptor Heterojunction Interfaces". *The Journal of Physical Chemistry C* **115** (48), 23922 (2011).
- [192] F. Selzer, C. Falkenberg, M. Hamburger, M. Baumgarten, K. Müllen, K. Leo, and M. Riede: "Improved organic p-i-n type solar cells with n-doped fluorinated hexaazatrinaphthylene derivatives HATNA-F6 and HATNA-F12 as transparent electron transport material". *Journal of Applied Physics* **115** (5), 054515 (2014).
- [193] W. Han, H. Yoshida, N. Ueno, and S. Kera: "Electron affinity of pentacene thin film studied by radiation-damage free inverse photoemission spectroscopy". *Applied Physics Letters* **103** (12), 123303 (2013).
- [194] I. Salzmann, S. Duhm, G. Heimel, M. Oehzelt, R. Kniprath, R. L. Johnson, J. P. Rabe, and N. Koch: "Tuning the ionization energy of organic semiconductor films: the role of intramolecular polar bonds." *Journal of the American Chemical Society* **130** (39), 12870 (2008).
- [195] E. A. Lucia and F. D. Verderame: "Spectra of Polycrystalline Phthalocyanines in the Visible Region". *The Journal of Chemical Physics* **48** (6), 2674 (1968).
- [196] A. Opitz, B. Ecker, J. Wagner, A. Hinderhofer, F. Schreiber, J. Manara, J. Pflaum, and W. Brütting: "Mixed crystalline films of co-evaporated hydrogen- and fluorine-terminated phthalocyanines and their application in photovoltaic devices". *Organic Electronics* **10** (7), 1259 (2009).
- [197] A. Hinderhofer and F. Schreiber: "Organic-Organic Heterostructures: Concepts and Applications". *ChemPhysChem* **13** (3), 628 (2012).
- [198] D. A. Shirley: "High-Resolution X-Ray Photoemission Spectrum of the Valence Bands of Gold". *Physical Review B* **5** (12), 4709 (1972).

- [199] R. Banerjee, J. Novák, C. Frank, C. Lorch, A. Hinderhofer, A. Gerlach, and F. Schreiber: "Evidence for Kinetically Limited Thickness Dependent Phase Separation in Organic Thin Film Blends". *Physical Review Letters* **110** (18), 185506 (2013).
- [200] W. Li, K. H. Hendriks, A. Furlan, M. M. Wienk, and R. A. J. Janssen: "High Quantum Efficiencies in Polymer Solar Cells at Energy Losses below 0.6 eV". *Journal of the American Chemical Society* **137** (6), 2231 (2015).
- [201] E. Abad: *Energy Level Alignment and Electron Transport Through Metal/Organic Contacts: From Interfaces to Molecular Electronics*. Springer Theses. Springer, Berlin, Heidelberg (2012).
- [202] U. Rau: "Reciprocity relation between photovoltaic quantum efficiency and electroluminescent emission of solar cells". *Physical Review B* **76** (8), 085303 (2007).
- [203] D. Bartesaghi, I. d. C. Pérez, J. Kniepert, S. Roland, M. Turbiez, D. Neher, and L. J. A. Koster: "Competition between recombination and extraction of free charges determines the fill factor of organic solar cells". *Nature Communications* **6**, 7083 (2015).
- [204] M. Schwarze, B. D. Naab, M. L. Tietze, R. Scholz, P. Pahner, F. Bussolotti, S. Kera, D. Kasemann, Z. Bao, and K. Leo: "Analyzing the n-Doping Mechanism of an Air-Stable Small-Molecule Precursor". *ACS Applied Materials & Interfaces* **10** (1), 1340 (2018).
- [205] L. Bormann, F. Nehm, L. Sonntag, F.-Y. Chen, F. Selzer, L. Müller-Meskamp, A. Eychmüller, and K. Leo: "Degradation of Flexible, ITO-Free Oligothiophene Organic Solar Cells". *ACS Applied Materials & Interfaces* **8** (23), 14709 (2016).
- [206] S. Kraner, J. Widmer, J. Benduhn, E. Hieckmann, T. Jägeler-Hoheisel, S. Ullbrich, D. Schütze, K. Sebastian Radke, G. Cuniberti, F. Ortman, M. Lorenz-Rothe, R. Meerheim, D. Spoltore, K. Vandewal, C. Koerner, and K. Leo: "Influence of side groups on the performance of infrared absorbing aza-BODIPY organic solar cells". *Physica Status Solidi A* **212** (12), 2747 (2015).
- [207] Christiane Falkenberg: *Optimizing Organic Solar Cells - Transparent Electron Transport Materials for Improving the Device Performance*. Dissertation, TU Dresden (2011).
- [208] S. Braun, W. R. Salaneck, and M. Fahlman: "Energy-Level Alignment at Organic/Metal and Organic/Organic Interfaces". *Advanced Materials* **21** (14-15), 1450 (2009).

- [209] J.-P. Yang, L.-T. Shang, F. Bussolotti, L.-W. Cheng, W.-Q. Wang, X.-H. Zeng, S. Kera, Y.-Q. Li, J.-X. Tang, and N. Ueno: "Fermi-level pinning appears upon weak electrode-organic contact without gap states: A universal phenomenon". *Organic Electronics* **48**, 172 (2017).
- [210] J. L. Bredas and G. B. Street: "Polarons, bipolarons, and solitons in conducting polymers". *Accounts of Chemical Research* **18** (10), 309 (1985).
- [211] C. Gaul, S. Hutsch, M. Schwarze, K. S. Schellhammer, F. Bussolotti, S. Kera, G. Cuniberti, K. Leo, and F. Ortman: "Insight into doping efficiency of organic semiconductors from the analysis of the density of states in n-doped C60 and ZnPc". *Nature Materials* **17** (5), 439 (2018).
- [212] M. Schwarze, F. Bussolotti, C. Gaul, R. Scholz, A. Hofacker, K. S. Schellhammer, B. D. Naab, Z. Bao, D. Spoltore, B. Nell, K. Vandewal, S. Kera, N. Ueno, J. Widmer, F. Ortman, and K. Leo: "Molecular Parameters Responsible for Thermally Activated Transport in Doped Organic Semiconductors", submitted.
- [213] S. Winkler, P. Amsalem, J. Frisch, M. Oehzelt, G. Heimel, and N. Koch: "Probing the energy levels in hole-doped molecular semiconductors". *Materials Horizons* **2** (4), 427 (2015).
- [214] S. Kera, H. Yamane, I. Sakuragi, K. K. Okudaira, and N. Ueno: "Very narrow photoemission bandwidth of the highest occupied state in a copper-phthalocyanine monolayer". *Chemical Physics Letters* **364** (1-2), 93 (2002).
- [215] S. Duhm, Q. Xin, S. Hosoumi, H. Fukagawa, K. Sato, N. Ueno, and S. Kera: "Charge Reorganization Energy and Small Polaron Binding Energy of Rubrene Thin Films by Ultraviolet Photoelectron Spectroscopy". *Advanced Materials* **24** (7), 901 (2012).
- [216] S. Kera and N. Ueno: "Photoelectron spectroscopy on the charge reorganization energy and small polaron binding energy of molecular film". *Journal of Electron Spectroscopy and Related Phenomena* **204**, 2 (2015).
- [217] R. H. Young, J. A. Sinicropi, and J. J. Fitzgerald: "Dipole Moments, Energetic Disorder, and Charge Transport in Molecularly Doped Polymers". *The Journal of Physical Chemistry* **99** (23), 9497 (1995).
- [218] A. Higgins, S. K. Mohapatra, S. Barlow, S. R. Marder, and A. Kahn: "Dopant controlled trap-filling and conductivity enhancement in an electron-transport polymer". *Applied Physics Letters* **106** (16), 163301 (2015).
- [219] F. Zhang and A. Kahn: "Investigation of the High Electron Affinity Molecular Dopant F6-TCNNQ for Hole-Transport Materials". *Advanced Functional Materials* **28** (1), 1703780 (2017).

- [220] M. Pollak: "A theory for many-electron hopping rates". *Journal of Physics C: Solid State Physics* **14** (21), 2977 (1981).
- [221] M. Schwarze, A. Hofacker, and K. Leo: "Universal Electron Trap as a General Limit for Air Stable n-Doping of Organic Semiconductors" , in preparation.
- [222] J.-M. Zhuo, L.-H. Zhao, R.-Q. Png, L.-Y. Wong, P.-J. Chia, J.-C. Tang, S. Sivaramakrishnan, M. Zhou, E. C.-W. Ou, S.-J. Chua, W.-S. Sim, L.-L. Chua, and P. K.-H. Ho: "Direct Spectroscopic Evidence for a Photodoping Mechanism in Polythiophene and Poly(bithiophene-alt-thienothiophene) Organic Semiconductor Thin Films Involving Oxygen and Sorbed Moisture". *Advanced Materials* **21** (46), 4747 (2009).
- [223] H. Yoshida: "Low-Energy Inverse Photoemission Study on the Electron Affinities of Fullerene Derivatives for Organic Photovoltaic Cells". *The Journal of Physical Chemistry C* **118** (42), 24377 (2014).
- [224] H. Yoshida and K. Yoshizaki: "Electron affinities of organic materials used for organic light-emitting diodes: A low-energy inverse photoemission study". *Organic Electronics* **20**, 24 (2015).
- [225] S. Barlow, Q. Zhang, B. R. Kaafarani, C. Risko, F. Amy, C. K. Chan, B. Domercq, Z. A. Starikova, M. Y. Antipin, T. V. Timofeeva, B. Kippelen, J.-L. Brédas, A. Kahn, and S. R. Marder: "Synthesis, Ionisation Potentials and Electron Affinities of Hexaazatri-naphthylene Derivatives". *Chemistry - A European Journal* **13** (12), 3537 (2007).
- [226] I. G. Hill, A. Kahn, Z. G. Soos, and R. A. Pascal Jr.: "Charge-separation energy in films of π -conjugated organic molecules". *Chemical Physics Letters* **327** (3-4), 181 (2000).
- [227] R. Fitzner, E. Mena-Osteritz, A. Mishra, G. Schulz, E. Reinold, M. Weil, C. Körner, H. Ziehlke, C. Elschner, K. Leo, M. Riede, M. Pfeiffer, C. Urich, and P. Bäuerle: "Correlation of π -Conjugated Oligomer Structure with Film Morphology and Organic Solar Cell Performance". *Journal of the American Chemical Society* **134** (27), 11064 (2012).
- [228] K. Cnops, G. Zango, J. Genoe, P. Heremans, M. V. Martinez-Diaz, T. Torres, and D. Cheyns: "Energy Level Tuning of Non-Fullerene Acceptors in Organic Solar Cells". *Journal of the American Chemical Society* **137** (28), 8991 (2015).
- [229] H. Lin, S. Chen, Z. Li, J. Y. L. Lai, G. Yang, T. McAfee, K. Jiang, Y. Li, Y. Liu, H. Hu, J. Zhao, W. Ma, H. Ade, and H. Yan: "High-Performance Non-Fullerene Polymer Solar Cells Based on a Pair of Donor-Acceptor Materials with Complementary Absorption Properties". *Advanced Materials* **27** (45), 7299 (2015).

- [230] Y. Lin, J. Wang, Z.-G. Zhang, H. Bai, Y. Li, D. Zhu, and X. Zhan: "An Electron Acceptor Challenging Fullerenes for Efficient Polymer Solar Cells". *Advanced Materials* **27** (7), 1170 (2015).
- [231] S. Li, L. Zhan, F. Liu, J. Ren, M. Shi, C.-Z. Li, T. P. Russell, and H. Chen: "An Unfused-Core-Based Nonfullerene Acceptor Enables High-Efficiency Organic Solar Cells with Excellent Morphological Stability at High Temperatures". *Advanced Materials* **30** (6), 1705208 (2017).
- [232] B. Qiu, L. Xue, Y. Yang, H. Bin, Y. Zhang, C. Zhang, M. Xiao, K. Park, W. Morrison, Z.-G. Zhang, and Y. Li: "All-Small-Molecule Nonfullerene Organic Solar Cells with High Fill Factor and High Efficiency over 10%". *Chemistry of Materials* **29** (17), 7543 (2017).
- [233] W. Zhao, S. Li, H. Yao, S. Zhang, Y. Zhang, B. Yang, and J. Hou: "Molecular Optimization Enables over 13% Efficiency in Organic Solar Cells". *Journal of the American Chemical Society* **139** (21), 7148 (2017).
- [234] H. Bin, Y. Yang, Z.-G. Zhang, L. Ye, M. Ghasemi, S. Chen, Y. Zhang, C. Zhang, C. Sun, L. Xue, C. Yang, H. Ade, and Y. Li: "9.73% Efficiency Nonfullerene All Organic Small Molecule Solar Cells with Absorption-Complementary Donor and Acceptor". *Journal of the American Chemical Society* **139** (14), 5085 (2017).
- [235] Z. Fei, F. D. Eisner, X. Jiao, M. Azzouzi, J. A. Röhr, Y. Han, M. Shahid, A. S. R. Chesman, C. D. Easton, C. R. McNeill, T. D. Anthopoulos, J. Nelson, and M. Heeney: "An Alkylated Indacenodithieno[3,2- b]thiophene-Based Nonfullerene Acceptor with High Crystallinity Exhibiting Single Junction Solar Cell Efficiencies Greater than 13% with Low Voltage Losses". *Advanced Materials*, DOI: 10.1002/adma.201705209 (2018).
- [236] J. Zhang, C. Yan, W. Wang, Y. Xiao, X. Lu, S. Barlow, T. C. Parker, X. Zhan, and S. R. Marder: "Panchromatic Ternary Photovoltaic Cells Using a Nonfullerene Acceptor Synthesized Using C-H Functionalization". *Chemistry of Materials* **30** (2), 309 (2018).
- [237] H. Li, Y. Zhao, J. Fang, X. Zhu, B. Xia, K. Lu, Z. Wang, J. Zhang, X. Guo, and Z. Wei: "Improve the Performance of the All-Small-Molecule Nonfullerene Organic Solar Cells through Enhancing the Crystallinity of Acceptors". *Advanced Energy Materials* 1702377 (2018).
- [238] J. Li, C. W. Rochester, I. E. Jacobs, S. Friedrich, P. Stroeve, M. Riede, and A. J. Moulé: "Measurement of Small Molecular Dopant F4TCNQ and C60F36 Diffusion in Organic Bilayer Architectures". *ACS Applied Materials & Interfaces* **7** (51), 28420 (2015).

- [239] P. Pahner: *Charge Carrier Trap Spectroscopy on Organic Hole Transport Materials*. Dissertation, TU Dresden (2016).
- [240] Dresden Integrated Center for Applied Physics and Photonic Materials (IAPP): *OSOL database*.
- [241] T. Menke: *Molecular Doping of Organic Semiconductors - A Conductivity and Seebeck Study*. Dissertation, TU Dresden (2013).
- [242] J. Endres, I. Pelczer, B. P. Rand, and A. Kahn: "Determination of Energy Level Alignment within an Energy Cascade Organic Solar Cell". *Chemistry of Materials* **28** (3), 794 (2016).
- [243] N. Koch, A. Kahn, J. Ghijsen, J.-J. Pireaux, J. Schwartz, R. L. Johnson, and A. Elschner: "Conjugated organic molecules on metal versus polymer electrodes: Demonstration of a key energy level alignment mechanism". *Applied Physics Letters* **82** (1), 70 (2003).
- [244] W. Gao and A. Kahn: "Controlled p-doping of zinc phthalocyanine by coevaporation with tetrafluorotetracyanoquinodimethane: A direct and inverse photoemission study". *Applied Physics Letters* **79** (24), 4040 (2001).

Acknowledgements/Danksagung

Diesen Moment habe ich schon sehr lange herbeigesehnt. Das Schreiben der Danksagung bedeutet nämlich gleichzeitig die Fertigstellung der Dissertation nach nun mehr als vier-einhalb Jahren. Auch wenn ich diese Dissertation alleine getippt habe, wäre diese ohne die Hilfe zahlreicher Mitmenschen nicht in dieser Form entstanden. Daher möchte ich auf diesem Wege allen herzlich danken, die zum Gelingen dieser Arbeit beigetragen haben.

- Mein besonderer Dank gilt Prof. Dr. Karl Leo, welcher es mir ermöglicht hat, am IAPP mit großen wissenschaftlichen Freiheiten auf dem spannenden und vielseitigen Gebiet der organischen Elektronik zu promovieren. Ich danke Ihnen für das entgegengebrachte Vertrauen und die Geduld, wodurch ich die zwei Themenfelder dieser Arbeit in diesem Umfang bearbeiten konnte.
- Prof. Dr. Elizabeth von Hauff möchte ich für die freundliche Übernahme des Zweitgutachtens danken.
- Ich danke Prof. Dr. Björn Lüssem, Dr. Daniel Kasemann, Dr. Johannes Widmer und Dr. Hans Kleemann, die mich als ODS/ORBAS/NewDev-Gruppenleiter in verschiedenen Phasen meiner Promotion tatkräftig unterstützt haben und immer für eine wissenschaftliche Diskussion zur Verfügung standen.
- Ich danke Dr. Max L. Tietze und Dr. Paul Pahner für die umfangreiche Unterstützung in der Anfangszeit am IAPP und die ausführliche Einweisung in die beiden wichtigsten experimentellen Methoden dieser Arbeit, Photoelektronenspektroskopie und Leitfähigkeitsmessungen, sowie in das Clustertool UFO I.
- Ein besonderer Dank geht an Sven Kunze, der immer schnelle Lösungen bei technischen Problemen im Labor parat hatte. Auch danke ich Andreas Büst für seine technische Unterstützung während der Schlussphase im UFO I.
- Ich danke Dr. Reinhard Scholz für dreieinhalb gemeinsame Jahre im gemütlichen Ofen unter dem Dach des Beyerbaus. Vielen Dank für die vielen erleuchtenden Diskussionen und die zahlreichen DFT-Simulationen.
- I gratefully thank Prof. Dr. Satoshi Kera, Prof. Dr. Nobuo Ueno, Dr. Fabio Bussolotti und Dr. Takahiro Ueba for their kind hospitality during my stay at IMS in Okazaki

(Japan). In particular, I thank Dr. Fabio Bussolotti for performing UPS and LEIPS measurements.

- Ein großer Dank geht an Olka Kaveh, Daniel Schütze und Dr. Paul Pahner, die einen Großteil der Leitfähigkeitsmessungen dieser Arbeit durchgeführt haben.
- Ein besonderer Dank geht an Dr. Beatrice Beyer und Dr. Wolfgang Tress, die die Solarzellendaten zur Verfügung gestellt haben. Ohne diese würde das erste Ergebniskapitel dieser Arbeit nicht in dieser Form existieren.
- Ein großer Teil der Erkenntnisse dieser Arbeit basiert auf der Verbindung von experimentellen Ergebnissen mit Simulationen. Daher möchte ich besonders Dr. Reinhard Scholz, Dr. Carl Poelking, Dr. Denis Andrienko, Dr. Frank Ortmann, Dr. Christopher Gaul, Karl Sebastian Schellhammer und Andreas Hofacker für die Durchführung von Simulationen danken.
- Katrin Ortstein danke ich für die Durchführung von UPS-Messungen und für die Bearbeitung eines anspruchsvollen Masterarbeitsthemas.
- Johanna Katzschner, Dr. Angelika Wolf, Dr. Annette Polte, Kai Schmidt und Peter Leumer danke ich für die Unterstützung bei administrativen und IT-Fragen.
- I thank Dr. Benjamin D. Naab, Prof. Dr. Zhenan Bao, Dr. Beatrice Beyer, Dr. Matthias Lau and Prof. Dr. Dieter Wöhrle for synthesizing and providing essential organic molecules for the studies of this thesis.
- Dr. Alrun A. Hauke (geb. Günther) und Jörn Vahland danke ich für die Durchführung von Beweglichkeitsmessungen in Transistoren.
- Annette Zeika (geb. Petrich) danke ich für die Aufreinigung verschiedener Substanzen.
- Prof. Dr. Ellen Hieckmann danke ich für die engagierte Unterstützung beim Genehmigungsverfahren der XPS-Anlage.
- Ich bedanke mich außerdem bei Dr. Lauren Scholz (geb. Polander), Dr. Max L. Tietze, Dr. Paul Pahner, Dr. Frank Ortmann, Dr. Christopher Gaul, Dr. Janine Kleemann (geb. Fischer), Dr. Ellen Siebert-Henze, Lijia Fang und weiteren für eine fruchtbare Zusammenarbeit in weiteren spannenden Projekten, die nicht oder nur teilweise in dieser Arbeit beschrieben wurden.
- Ein reger Gedankenaustausch ist die Grundlage wissenschaftlicher Erkenntnis. Daher möchte ich mich bei zahlreichen Kollegen für die intensiven Diskussionen bedanken, insbesondere bei Dr. Max L. Tietze, Dr. Paul Pahner, Dr. Reinhard Scholz, Dr. Frank Ortmann, Dr. Fabio Bussolotti, Bernhard Nell und Andreas Hofacker für

Diskussionen über molekulare Dotierung, bei Dr. Christian Körner, Johannes Benduhn, Bernhard Siegmund, Dr. Donato Spoltore und Prof. Dr. Koen Vandewal für Diskussionen zu organischen Solarzellen, bei Dr. Denis Andrienko, Dr. Reinhard Scholz und Dr. Carl Poelking für Diskussionen über molekulare Quadrupolmomente sowie bei Dr. Benjamin D. Naab, Prof. Dr. Zhenan Bao, Dr. Olaf Zeika und Dr. Beatrice Beyer für Diskussionen zu chemischen Themen.

- Trotz größter Mühe schleichen sich immer ein paar Fehler ein. Daher danke ich Hans, Frank, Max, Reinhard, Christian, Bernhard, Johannes und Prof. Leo für das intensive Korrekturlesen dieser Arbeit.
- Das IAPP habe ich durch seine offene und umgängliche Atmosphäre als ein Ort des Miteinanders erlebt. Ich möchte daher hier im speziellen allen Organisatoren der legendären Weihnachtsfeiern und Organic Days bedanken, die immer ein Highlight waren. Außerdem danke ich Felix, Paul, Franz, Ludwig, Annette, Daniel, Donato, Jacob, Lorenz, Olka, Vasilis und vielen mehr, die durch spannende Unterhaltungen manche Wartezeit im UFO I schnell vergehen lassen haben.
- Ein besonderer Dank geht an Freddi, Sven, Uli, Böhmi, Felix D., Felix H., Hannes und vielen mehr für die spaßigen Spieleabende.
- Gemeinsam schmeckt es besser. Daher danke ich dem über die Jahre wechselnden Mensateam für die angenehme Zeit in der alten Mensa, unter anderem mit Felix, Yoonseok, Christian, Stefan, Daniel, Kyung-Geun, Max, Hans, Johannes, Vasilis, Katrin, Ji-Ling, Koen, Jinhan, Jonas, Jakob, Lukasz, Mathias, ...
- Ich bedanke mich bei der Graduiertenakademie der TU Dresden für ihre finanzielle Unterstützung während der Schreibphase dieser Dissertation.
- Außerdem möchte ich mich bei meiner Familie für die Unterstützung nicht nur während der Promotion sondern während meines gesamten bisherigen Lebenswegs bedanken. Ohne Euch hätte ich nicht diesen Weg einschlagen können. Nun kann ich endlich die Frage, wann ich denn endlich fertig sei mit der Doktorarbeit, mit "Jetzt!" beantworten. Die Beantwortung der zweiten Frage, wann ich denn "richtig" zu arbeiten anfangen muss, muss noch warten;).
- Von ganzem Herzen möchte ich Dir, Katrin, für Deine Unterstützung in den letzten acht Jahren bedanken. Vielen Dank, dass Du insbesondere in der Endphase des Schreibens so viel Verständnis gezeigt hast, wenn ich sonntags mal wieder spät nach Hause kam.

Erklärung

Diese Arbeit wurde am “Dresden Integrated Center for Applied Physics and Photonic Materials” (IAPP) / Institut für Angewandte Physik (IAP) an der Fakultät im Bereich Mathematik und Naturwissenschaften an der Technischen Universität Dresden unter wissenschaftlicher Betreuung von Prof. Dr. Karl Leo angefertigt.

Hiermit versichere ich, dass ich die vorliegende Arbeit ohne unzulässige Hilfe Dritter und ohne Benutzung anderer als der angegebenen Hilfsmittel angefertigt habe; die aus fremden Quellen direkt oder indirekt übernommenen Gedanken sind als solche kenntlich gemacht. Die Arbeit wurde bisher weder im Inland noch im Ausland in gleicher oder ähnlicher Form einer anderen Prüfungsbehörde vorgelegt. Weiterhin versichere ich, dass bisher keine Promotionsverfahren stattgefunden haben.

Ich erkenne die Promotionsordnung des Bereichs Mathematik und Naturwissenschaften der Technischen Universität Dresden vom 23.02.2011 inklusive der Änderungsbeschlüsse vom 15.06.2011 und vom 18.06.2014 an.

Martin Schwarze